Loughborough University

Certificate of Originality
Thesis Access Conditions and Deposit Agreement

Students should consult the guidance notes on the electronic thesis deposit and the access conditions in the University's Code of Practice on Research Degree Programmes

Author IOANNIS KARAGIANNIS

Title TRIBO-DYNAMIC ANALYSIS OF HYPOID GEARS IN AUTOMOTIVE DIFFERENTIALS

I [Please insert name and address], "the Depositor",
would like to deposit [Please insert title of dissertation], hereafter referred to as the "Work", once it has successfully been examined in Loughborough University Institutional Repository

Status of access CONFIDENTIAL

Moratorium Period 3 years, ending FEBRUARY/2016

Status of access approved by (CAPITALS):……

Supervisor (Signature)……...……...

School of WOLFSON SCHOOL OF MECHANICAL AND MANUFACTURING ENGINEERING

Author's Declaration *I confirm the following :*

CERTIFICATE OF ORIGINALITY
This is to certify that I am responsible for the work submitted in this thesis, that the original work is my own except as specified in acknowledgements or in footnotes, and that neither the thesis nor the original work therein has been submitted to this or any other institution for a degree

NON-EXCLUSIVE RIGHTS
The licence rights granted to Loughborough University Institutional Repository through this agreement are entirely non-exclusive and royalty free. I am free to publish the Work in its present version or future versions elsewhere. I agree that Loughborough University Institutional Repository administrators or any third party with whom Loughborough University Institutional Repository has an agreement to do so may, without changing content, convert the Work to any medium or format for the purpose of future preservation and accessibility.

DEPOSIT IN LOUGHBOROUGH UNIVERSITY INSTITUTIONAL REPOSITORY
I understand that open access work deposited in Loughborough University Institutional Repository will be accessible to a wide variety of people and institutions - including automated agents - via the World Wide Web. An electronic copy of my thesis may also be included in the British Library Electronic Theses On-line System (EThOS).
I understand that once the Work is deposited, a citation to the Work will always remain visible. Removal of the Work can be made after discussion with Loughborough University Institutional Repository, who shall make best efforts to ensure removal of the Work from any third party with whom Loughborough University Institutional

Repository has an agreement. Restricted or Confidential access material will not be available on the World Wide Web until the moratorium period has expired.

- That I am the author of the Work and have the authority to make this agreement and to hereby give Loughborough University Institutional Repository administrators the right to make available the Work in the way described above.
- That I have exercised reasonable care to ensure that the Work is original, and does not to the best of my knowledge break any UK law or infringe any third party's copyright or other Intellectual Property Right. I have read the University's guidance on third party copyright material in theses.
- The administrators of Loughborough University Institutional Repository do not hold any obligation to take legal action on behalf of the Depositor, or other rights holders, in the event of breach of Intellectual Property Rights, or any other right, in the material deposited.

*The statement below shall apply to **ALL** copies:*

This copy has been supplied on the understanding that it is copyright material and that no quotation from the thesis may be published without proper acknowledgement.

Restricted/confidential work: All access and any copying shall be strictly subject to written permission from the University Dean of School and any external sponsor, if any.

Author's signature……..Date 10 JANUARY 2013

user's declaration: for signature during any Moratorium period (Not Open work): ***I undertake to uphold the above conditions:***			
Date	Name (CAPITALS)	Signature	Address

Tribo-dynamic analysis of hypoid gear pairs in automotive differentials

by

Ioannis Karagiannis

Thesis submitted in partial fulfilment of the requirements for the degree of Doctor of Philosophy

Loughborough University

Wolfson School of Mechanical and Manufacturing Engineering

January 2013

Abstract

Torsional vibrations in differentials of Rear Wheel Drive vehicles are of major importance for the automotive industry. Hypoid transmissions, forming the motion transfer mechanism from the driveshaft to the wheels, suffer from severe vibration issues. The latter are attributed to improper mesh between the mating gear flanks due to misalignments, variation of contact load and shifting of the effective mesh position. For certain operating conditions, the gear pair exhibits high amplitude motions accompanied with separation of the mating surfaces. Ultimately, single or even double-sided vibro-impact phenomena evolve, which have been related to noise generation. This thesis attempts to address these issues by effectively analysing the dynamic behaviour of a hypoid gear pair under torsional motion. The case study considered is focused on a commercial light truck.

The major difference of the employed mathematical model to prior formulations is the usage of an alternative expression for the dynamic transmission error so that the variation of contact radii and transmission error can be accounted for. This approach combined to a correlation of the resistive torque in terms of the angular velocity of the differential enables the achievement of steady state, stable periodic solutions.

The dynamic complexity of systems with gears necessitates the identification of the various response regimes. A solution continuation method (software AUTO) is employed to determine the stable/unstable branches over the operating range of the differential. The ensuing parametric studies convey the importance of the main system parameters on the dynamic behaviour of the transmission yielding crucial design guidelines.

A tribo-dynamic investigation aims at expanding the dynamic model from pure dry conditions to a more integrated elastohydrodynamic (EHL) approach. Analytical and extrapolated solutions are applied for the derivation of the film thickness magnitude based on the kinematic and loading characteristics of the dynamic model. The temperature rise is governed mainly by conduction due to the thin lubricant films. The generated friction is also computed as a function of the viscous shear and asperity interactions. The effective lubricant viscosity is greatly affected by the pressure increase due to the resonant behaviour of the contact load.

The final part of this work is involved with a feasibility study concerning the application of Nonlinear Energy Sinks (NES) as vibration absorbers, exploiting their ability for broadband frequency interaction. Response regimes associated with effective energy absorption are identified and encouraging results are obtained, showing the potential of the method.

To my family and Athena

Στην οικογένειά μου και την Αθηνά

Aknowledgements

I would like to express my gratitude to my supervisor Dr. Stephanos Theodossiades and Prof. Homer Rahnejat, chair of Dynamics Research Group for providing me with the opportunity to undertake this Research Project. Their guidance and assistance throughout the completion of this study is invaluable.

I need to appraise Prof.Patrick Kelly and Mr.Timothy Saunders of FORD Motor Company for their assistance on defining important technical chatacteristics of the project; highlighting its importance from an industrial perception.

I would like to thank all the members of the Dynamics Research Group who were willing to offer their consultation whenever I needed. I shoud refer in specific to Dr. Ramin Rahmani, Dr. Miguel De la Cruz and Dr. George Koronias. The involvement of Dr. Nikolaos Roidos should also be accredited on the verification of certain aspects of the mathematic formulation.

I have to highlight also the inspiration awarded to me by Prof. Alexander Vakakis of University of Illinois at Urbana-Champaign; my decision to pursue a Doctorate Degree should be appointed to him. His lectures on Dynamics during my undergraduate dates at NTUA have been the source of my motivation.

Finally, I am grateful to my family for providing me with their support throughout this demanding task.

Table of Contents

Abstract i

Aknowledgements iv

List of Figures ix

List of Tables xx

Nomenclature xxi

Chapter 1 - Introduction 1

1.1 - Background 1

1.2 - Aims and Objectives 3

1.3 - Hypoid Gears and applications 4

1.4 - Structure of the Thesis 6

Chapter 2 - Literature Review 8

2.1 - Introduction 8

2.2 - Problem Description 9

2.3 - Modelling / Simulation techniques 14

2.3.1 Dynamic modelling 14

2.3.2 Tooth Contact Analysis 19

2.4 - Tribological consideration 21

2.5 - Applied measures 24

2.6 - The concept of Targeted Energy Transfer 30

2.7 - Synopsis 32

Chapter 3 - Global Dynamics 34

3.1 - Introduction 34

3.2 - Dynamic Modelling 34

3.2.1 Gear Pair Dynamics 34

3.2.2 Vehicle and Drivetrain Dynamics 38
3.3 - Formulation of Gear Mesh 42
3.3.1 Kinematic Analysis 43
3.3.2 Load distribution and contact geometry 47
3.4 - Synopsis 63
Chapter 4 - Tribological Consideration 65
4.1 - Introduction 65
4.2 - Dynamic Modelling of Lubricated Contact 65
4.3 - Thermal Elastohydrodynamic Analysis 68
4.3.1 Contact Kinematics 71
4.3.2 Contact properties 75
4.3.3 Film thickness calculation 89
4.3.4 Effect of Temperature and Pressure 97
4.3.5 Calculation of viscous and boundary friction 104
4.4 - Synopsis 106
Chapter 5 - Dynamic Response Analysis 108
5.1 - Introduction 108
5.2 - Solution methodology 108
5.3 - Fundamental Dynamic Model 111
5.3.1 Initial Results – model capabilities under steady state cruising 113
5.3.2 Dynamic transmission error in integral form 118
5.3.3 The dependence of external torque to the axle angular velocity 120
5.3.4 The effect of initial velocities 125
5.3.5 Detection of gear teeth separation (vibro-impacts) 128
5.3.6 Comparison to previous hypoid gear pair models 133

5.3.7 Family of periodic solutions – stability and parametric studies 138
5.3.8 Transient conditions 149
5.4 - Synopsis 157
Chapter 6 - Tribodynamic Analysis 158
6.1 - Introduction 158
6.2 - Computational Algorithm 158
6.3 - Load and film thickness variation under non Newtonian isothermal conditions 160
6.4 - Friction and gear pair efficiency 166
6.5 - Heat balance 169
6.6 - Dynamic interaction 173
6.7 - Model Validation 180
6.8 - Synopsis 181
Chapter 7 - The Concept of Targeted Energy Transfer 183
7.1 - Introduction 183
7.2 - Dynamic Model 183
7.3 - Steady state resonance 186
7.3.1 Problem definition 186
7.3.2 Parametric studies 189
7.3.3 Overview of the energy transfer mechanism 191
7.4 - Breach of dynamic equilibrium 200
7.5 - Synopsis 207
Chapter 8 - Overall conclusions, contribution to knowledge and suggestions for future work 208
8.1 - Overall conclusions 208
8.2 - Novelty – Validation 209

8.3 - Achievements of aims and objectives 210
8.4 - Contributions to knowledge 211
8.5 - Critical assessment of current work and suggestions for future work 212
References 214
Appendix 224

List of Figures

Figure 1.1- Differential Gear vibration and noise generation mechanism (after Saunders, 2005) 2

Figure 1.2- A hypoid gear pair 4

Figure 2.1- Axle whine noise source and transfer paths (source: FORD Motor Company UK Ltd) 10

Figure 2.2:- Correlation of Sound Pressure Level and Torsional Vibration Level for 550Hz (after Nakayashiki et al, 1983) 11

Figure 2.3- Correlation of resonant frequency of noise and vibration amplitudes (after Hirasaka et al, 1991) 12

Figure 2.4- Bearing Forces as a product of Mesh force and Transmisibility function (after Miyauchi et al, 2001) 13

Figure 2.5- General form of a gear pair oscillator (after Blankenship and Kahraman, 1995) 14

Figure 2.6- Mechanical Model of a spur gear pair (after Kahraman and Singh, 1990) 15

Figure 2.7- Dynamic mesh force and Gear pair compliances per unit transmission error (after Sun et al, 2003) 25

Figure 2.8- Optimized designs towards dynamic mesh force reduction (after Lee and Kocer, (2003) 26

Figure 2.9- Noise reduction ring design (after Miyauchi et al, 2001) 27

Figure 2.10- The effect of "noise reduction ring" on the compliance and mesh force magnitude (after Miyauchi et al, 2001) 28

Figure 2.11- View of slip yoke damper ring (after Lee, 2007) 29

Figure 2.12- View of tunable cardboard liner (after Sun et al, 2011) 29

Figure 2.13- Linear substructure and Nonlinear attachment (after Vakakis et al, 2003) 31

Figure 3.1- General hypoid gear pair mesh model 36

Figure 3.2- Free body diagram of the hypoid gear pair 37

Figure 3.3- Torque variation for Equilibrium, Drive and Coasting conditions 42

Figure 3.4- Global and Local Coordinate Systems 45

Figure 3.5- Derivation of linear velocity along the line of action 46

Figure 3.6- The pinion under quasi-static equilibrium 48

Figure 3.7- Distribution of contact pressure (N/mm^2) on the pinion flanks (LTCA by CALYX) 49

Figure 3.8- Determination of the equipollent forcing system. Each force is equivalent to a parallel force and a couple with respect to a reference point 51

Figure 3.9- Dimensionless contact radii with respect to pinion angular rotation for a complete mesh cycle: (a) Pinion contact radius $\hat{R}_p$, (b) Gear contact radius $\hat{R}_g$ 58

Figure 3.10- Dimensionless mesh parameters with respect to pinion angular rotation for a complete mesh cycle: (a) Mesh Stiffness $\hat{k}_m$, (b) kinematic transmission error $\hat{\Delta}\varphi_L$ 59

Figure 3.11- Dependence of mean contact stiffness with input torque 59

Figure 3.12- Comparison of derived mesh properties and the corresponding Fourier expansion for input torque 20Nm: (a) kinematic (unloaded) transmission error (b) pinion contact radius (c) mesh stiffness 62

Figure 4.1- Frictional model of a gearing system 66

Figure 4.2- Free body diagram of lubricated model 67

Figure 4.3- The Elastohydrodynamic Conjunction 70

Figure 4.4- Geometric and kinematic properties at the contact footprint 72

Figure 4.5- Evaluation of contact zone from TCA (after Park and Kahraman, 2009) 76

Figure 4.6- Mesh and engagement cycle 77

Figure 4.7- Velocities and surface velocity radii; (a) velocity across x-direction, (b) velocity across y-direction, (c) surface velocity radius $r_{fr,x}/R_{zx0}$ and (d) surface velocity radius $r_{fr,y}/R_{zx0}$. ____ pinion , ... gear. The pinion torque is equal to 50Nm..... 79

Figure 4.8: Comparison between analytical and CALYX predicted velocities; (a) pinion direction –x, (b) pinion direction –y (c) gear direction –x, (d) gear direction –y ____CALYX , ... analytical. The pinion torque is equal to 50Nm. 80

Figure 4.9- Parameters α and β; ____ tabulated data , ... polynomial fit 82

Figure 4.10- Geometric and load factors; (a) Radii of curvature, ____ $\hat{R}_{zx}$, ... $\hat{R}_{zy}$, (b) ____ β/α , ... $\cos\theta$, (c) ____ a_{axis}, ... b_{axis}, (d) ____ W , ... p_{mean} . The pinion torque is equal to 50Nm..... 83

Figure 4.11- Surface velocity radii with respect to input torque; (a) $r_{fr,x}^{(p)}/R_{zx0}$, (b) $r_{fr,y}^{(p)}/R_{zx0}$, (c) $r_{fr,x}^{(g)}/R_{zx0}$, (d) $r_{fr,y}^{(g)}/R_{zx0}$ ____50Nm, ...100Nm, _ . _200Nm, _ _ _300Nm) 84

Figure 4.12- Radii of curvature with respect to input torque; ____50Nm, ... 100Nm, _ . _200Nm, _ _ _300Nm..... 85

Figure 4.13- Effect of input torque on the applied load, mean pressure and dimensions of contact ellipse; (a) contact ellipse minor semi axis a_{axis}/R_{zx0}, (b) contact ellipse major semi axis b_{axis}/R_{zx0}, (c) contact load W and (d) mean contact pressure p_{mean} ;____50Nm, ...100Nm, _ . _ 200Nm, _ _ _300Nm..... 86

Figure 4.14- Ratio of effective contact ratio to the nominal one 87

Figure 4.15- Load sharing factor for different values of input torque ____50Nm, ...100Nm, _ . _200Nm, _ _ _300Nm..... 88

Figure 4.16- Orientation of the contact ellipse during the engagement cycle; (a) $\varphi = 1/8\varphi_{eng}$, (b) $\varphi = 2/8\varphi_{eng}$, (c) $\varphi = 3/8\varphi_{eng}$, (d) $\varphi = 4/8\varphi_{eng}$, (e) $\varphi = 4/8\varphi_{eng}$, (e)

$\varphi = 5/8\varphi_{eng}$, (f) $\varphi = 6/8\varphi_{eng}$, (g) $\varphi = 7/8\varphi_{eng}$, (h) $\varphi = 8/8\varphi_{eng}$. Lubricant entrainment is taking place on X- direction. ——50Nm, ……100Nm, , – – –300Nm 94

Figure 4.17- Function representing statistical asperity distribution 105

Figure 5.1- Flowchart of the fundamental mechanical model 110

Figure 5.2- Response Characteristics of the gear pair: (a) pinion angular ; (b) gear angular velocity; (c) dynamic mesh force; (d) dynamic transmission error 114

Figure 5.3- (a) Phase plots; (b) Energy ratio; (c) Non conservative work; (d) Mesh force over deflection 117

Figure 5.4- FFT of dynamic mesh force time history 118

Figure 5.5- Illustration of stability issues: (a) pinion angular velocity, (b) dynamic mesh force, (c) phase plots, (d) energy balance; ——— integral form , – . – simplified form 120

Figure 5.6- Angular velocities of gear members at 1100-1120 meshing periods: (a) pinion, (b) gear; ——velocity dependent torque , —— . velocity independent torque 122

Figure 5.7- (a) Dynamic mesh force and (b) phase plots at 1100-1120 meshing periods; ——velocity dependent torque, – . – velocity independent torque 122

Figure 5.8- Angular velocities of gear members at 100100-100120 meshing periods: (a) pinion, (b) gear; ——velocity dependent torque , – . – velocity independent torque 123

Figure 5.9- (a) Dynamic mesh force and (b) phase plots at 100100-100120 meshing periods; ——velocity dependent torque, – . – velocity independent torque 123

Figure 5.10- FFT of the dynamic mesh force at 100100-100120 periods: (a) variant (b) constant resistive torque 124

Figure 5.11- Poincare maps: (a) variant (b) constant resistive torque 124

Figure 5.12- (a) Pinion (b) Gear angular velocity for initial angular velocities below the nominal; ..... $n = 0$, ——$n = 0.5$ – . – $n = 1$ 126

Figure 5.13- (a) Pinion (b) Gear angular velocity for initial angular velocities above the nominal; ..... $n=2$, _____ $n=1.5$, _ . _ $n=1$ 127

Figure 5.14- Dynamic transmission error for initial angular velocities (a) below the nominal; ..... $n=0$, _____ $n=0.5$, _ . _ $n=1$, (b) above the nominal; ..... $n=2$, _____ $n=1.5$, _ . _ $n=1$ 127

Figure 5.15- Response Spectra: (a) Maximum, (b) Minimum Amplitude, (c) Number of single sided impacts, (d) Elastic Energy per 100 cycles; speed * increasing, ■ decreasing..... 129

Figure 5.16- Response at 78kph, constant mesh conditions; (a) Dynamic transmission error, (b) Phase portrait, (c) Dynamic mesh force, (d) FFT of dynamic mesh force 131

Figure 5.17- Response at 78kph, contact loss conditions; (a) Dynamic transmission error, (b) Phase portrait, (c) Dynamic mesh force, (d) FFT of dynamic mesh force 132

Figure 5.18- Dynamic transmission error after Wang et al (2007): (a) maximum (b) minimum amplitude; * single DOF, ▲ double DOF 135

Figure 5.19- Comparison of response characteristics: : (a) Maximum, (b) Minimum Amplitude, (c) Number of single sided impacts, (d) Elastic Energy per 100 cycles; _____current methodology, _ . _ . Wang et al (2007)..... 136

Figure 5.20- (a) Time history of dynamic transmission error and (b) phase portrait at cruising speed of 78kph, input torque of 121.3Nm; current methodology _ _ _ _ upper branch, _____ lower branch, _ . _ Wang et al (2007)..... 137

Figure 5.21- Comparison of response spectra: (a) maximum, (b) minimum amplitude; ▲Wang et al (2007), ■constant contact radii 138

Figure 5.22- Effect of mesh damping coefficient on periodic motions, maximum amplitude: (a) c= 1.9130e+003 Ns/m (b) c= 2.8695e+003 Ns/m (c) 5.7390e+003 Ns/m (d) 1.1478e+004 Ns/m; 140

Figure 5.23- Effect of mesh damping coefficient on periodic motions, minimum amplitude: (a) c= 1.9130e+003 Ns/m (b) c= 2.8695e+003 Ns/m (c) 5.7390e+003

Ns/m (d) 1.1478e+004 Ns/m; _____ stable branch, _ _ _ _ branch with unstable solutions 141

Figure 5.24- Effect of out of phase stiffness variation: (a) maximum (b) minimum amplitude;..... 143

Figure 5.25- Effect of in phase stiffness variation: (a) maximum (b) minimum amplitude;..... 143

Figure 5.26- Effect of contact radii variation: (a) maximum (b) minimum amplitude144

Figure 5.27- Effect of the kinematic transmission error, in phase case: (a) maximum (b) minimum amplitude; _____ stable branch, _ _ _ _ unstable branch 145

Figure 5.28- Effect of kinematic transmission error, $\pi/2$ phase difference: (a) maximum (b) minimum amplitude; _____ stable branch, _ _ _ _ unstable branch.... 146

Figure 5.29- Effect of second mesh stiffness harmonic: (a) maximum (b) minimum amplitude;..... 146

Figure 5.30- Effect of second radii variation harmonic: (a) maximum (b) minimum amplitude; _____ stable branch, _ _ _ _ unstable branch 147

Figure 5.31- Effect of second static transmission error harmonic: (a) maximum (b) minimum amplitude; _____ stable branch, _ _ _ _ unstable branch 148

Figure 5.32- Angular velocities under coasting conditions: normal view, (a) pinion; (b) gear, detailed view, (c) pinion; (d) gear, _ _ _ _SSI , _____DSI..... 150

Figure 5.33- Angular accelerations under coasting conditions: (a) pinion; (b) gear, _ _ _ _ SSI , _____DSI..... 151

Figure 5.34- Dynamic response time histories under coasting conditions: normal view, (a) mesh force; (b) dynamic transmission error, detailed view, (c) mesh force; (d) dynamic transmission error, _ _ _ _ SSI, _____ DSI 152

Figure 5.35- Phase plots: (a) Double Sided Impact (b) Single Sided Impact motion 153

Figure 5.36- FFT of the dynamic mesh force: (a) Double Sided Impact (b) Single Sided Impact motion..... 154

Figure 5.37- Wavelet analysis of pinion acceleration, DSI case 155

Figure 5.38- Wavelet analysis of pinion acceleration, SSI case 155

Figure 5.39- Response Spectra for coasting conditions: (a) Maximum, (b) Minimum Amplitude, (c) Number of double sided (d) Elastic Energy per 100 cycles 156

Figure 6.1- EHL subroutine for Grubin type solution 159

Figure 6.2- Lubrication regime chart; boundaries (black lines) and meshing cycle (blue line) 162

Figure 6.3- Traction map for high viscosity mineral oil (after Evans and Johnson, 1986); non Newtonian boundary (red curve _____), viscoelastic boundary (green curve _ _ _ _) and meshing cycle (blue curve _____). 163

Figure 6.4- Shear stress under Newtonian consideration..... 164

Figure 6.5- Tribological properties for two dimensional flow (Chittenden et al, 1986) at inlet lubricant temperature $\theta_{in} = 40^0 C$; (a) _____ Load (W) , _ _ _ _ central film thickness (h_0) , (b) _____ entraining velocity (U) , _ _ _ _ radius of curvature along the entrainment direction (R_e) 165

Figure 6.6- Comparison of (a) film thickness and (b) entraining velocities for inlet lubricant temperature $\theta_{in} = 40^0 C$; _ _ _ _ Mostofi and Gohar (1982), _ . _ Grubin (1949)..... 166

Figure 6.7--(a) Viscous friction force, (b) shear rate during an engagement cycle; _____Chittenden et al (1986), _ _ _ _ Mostofi and Gohar (1982), _ . _ Grubin (1949) 167

Figure 6.8- Sliding velocity; _ _ _ _two dimensional, _ . _ one dimensional flow ... 167

Figure 6.9- (a) Boundary friction force, (b) friction coefficient; _____Chittenden et al (1986), _ _ _ _ Mostofi and Gohar (1982), _ . _ Grubin (1949) 168

Figure 6.10-- a) Pinion frictional torque and (b) overall gear pair efficiency; _____ Chittenden et al (1986) _ _ _ _ Mostofi and Gohar (1982), _ . _ Grubin (1949) 169

Figure 6.11- (a) Temperature and (b) film thickenss distribution across an engagement cycle $\theta_{in} = 40^0 C$; _____ Chittenden et al (1986) _ _ _ _ Mostofi and Gohar (1982), _ . _ Grubin (1949) 170

Figure 6.12- (a) Coefficient of friction and (b) overall gear pair efficiency $\theta_{in} = 40^0 C$; _____ Chittenden et al (1986) _ _ _ _ Mostofi and Gohar (1982), _ . _ Grubin (1949) 171

Figure 6.13- Dynamic viscosity for Chittenden solution; _____thermal analysis, _ . _ isothermal conditions..... 171

Figure 6.14- Effect of inlet lubricant temperature on (a) temperature rise (b) film thickness; _____ $\theta_{in} = 40^0 C$, _ . _ $\theta_{in} = 100^0 C$ 172

Figure 6.15- (a) Shear rate and (b) viscous friction comparison; _____ $\theta_{in} = 40^0 C$, _ . _ $\theta_{in} = 100^0 C$ 172

Figure 6.16- Friction distribution ($\theta_{in} = 100^0 C$); _____ overall, _ _ _ _ viscous, _ . _ boundary 173

Figure 6.17- Effect of inlet lubricant temperature on (a) friction coefficient (b) transmission efficiency, $\theta_{in} = 40^0 C$, Chittenden type solution; _____ $\theta_{in} = 40^0 C$, _ . _ $\theta_{in} = 100^0 C$ 173

Figure 6.18- (a) Contact Load and (b) film thickness; _____dynamic analysis, _ . _ quasi-static analysis 175

Figure 6.19- (a) Temperature and (b) friction coefficient; _____dynamic analysis, _ . _quasi-static analysis 175

Figure 6.20- Separation effects, Chittenden solution, $\theta_{in} = 40^0 C$; (a) _____ flank contact load, _ _ _ _ film thickness, (b) _____ friction force, _ _ _ _ transmission efficiency 176

Figure 6.21- Mean contact pressure along the engagement cycle, Chittenden solution..... 176

Figure 6.22- Effect of cruising speed for Chittenden solution, $\theta_{in} = 40^0 C$: (a) maximum flank load and (b) minimum value of central lubricant film; _____ acceleration, _ . _ . _ deceleration 178

Figure 6.23- Effect of cruising speed for Chittenden solution, $\theta_{in} = 40^0 C$: (a) maximum entraining velocity and (b) maximum temperature rise; _____ acceleration, _ . _ . _ deceleration 178

Figure 6.24- Effect of cruising speed for Chittenden solution, $\theta_{in} = 40^0 C$: (a) mean friction coefficient and (b) mean efficiency; _____ acceleration, _ . _ . _ deceleration 179

Figure 6.25- Response spectra comparison between dry and lubricated case: (a) acceleration and (b) deceleration; _____ lubricated, _ . _ . _ dry model 179

Figure 6.26- Time histories comparison between dry and lubricated case for nominal case: (a) acceleration (b) deceleration; _____ lubricated, _ . _ . _ dry model 180

Figure 6.27- Mean friction coefficient; (a) acceleration (b) deceleration; _____ current model (Chittenden solution), _ . _ . _ Kolinvand and Kahraman (2010), _ _ _ _ Evans&Johnson (1986) 180

Figure 6.28- Friction coefficient over an engagement cycle; _____ current model (Chittenden solution), _ . _ . _ Kolinvand and Kahraman (2010), _ _ _ _ Evans and Johnson (1986) 181

Figure 7.1- The Nonlinear Energy Sink (NES) configuration 184

Figure 7.2: Free Body Diagram of the NES 185

Figure 7.3: Cruising speed – Maximum Response spectra; ■single sided impacts (decelerating), ● single sided impacts (accelerating), ▲no impacts (decelerating), ▼ no impacts (accelerating) 188

Figure 7.4- Dynamic Response for $\upsilon = 99kph$ and $T_p = 182Nm$ without NES: (a) dynamic transmission error; (b) relative velocity; (c) phase plot 188

Figure 7.5- Steady state response properties for accelerating conditions (59-120kph); (a) maximum amplitude, (b) total number of single sided impacts, (c) work of mesh force, (d) energy damped at NES 190

Figure 7.6- Steady state response properties for decelerating conditions (140-60kph); (a) maximum amplitude, (b) total number of single sided impacts, (c) work of mesh force, (d) energy damped at NES 191

Figure 7.7- Response characteristics of the primary system ($\varepsilon = 0.181$; $k_t = 1.0411 \cdot 10^{13} Nm/rad^3$): (a) number of impacts (b) dimensionless peak to peak amplitude; _ _ _ _without NES, _____ with NES 193

Figure 7.8- Time series of the dynamic response at 62.4kph under vibration attenuation conditions ($\varepsilon = 0.181; k_t = 1.0411 \cdot 10^{13} Nm/rad^3$): (a) Dynamic transmission error (primary system), (b) NES relative motion; _ _ _ _without NES, _____ with NES 193

Figure 7.9- (a) Instantaneous energy exchanges between modes, (b) input energy distribution for effective vibration attenuation at 62.4kph..... 194

Figure 7.10- Response characteristics of the primary system ($\varepsilon = 0.214$; $k_t = 1.2388 \cdot 10^{13} Nm/rad^3$): (a) number of impacts (b) dimensionless peak to peak amplitude; _ _ _ _ without NES, _____ with NES 196

Figure 7.11- Time series of dynamic response at 62.4kph under ineffective vibration attenuation conditions ($\varepsilon = 0.214$; $k_t = 1.2388 \cdot 10^{13} Nm/rad^3$): (a) Dynamic transmission error (primary system) (b) NES relative motion; _ _ _ _ without NES, _____ with NES 197

Figure 7.12- - (a) Instantaneous energy exchanges between modes, (b) input energy distribution for ineffective vibration attenuation at 62.4kph..... 198

Figure 7.13- Response characteristics of the primary system ($\varepsilon = 0.31$; $k_t = 6.429 \cdot 10^{12} Nm/rad^3$) for $u(0) = 0, \dot{u}(0) = -\dot{\phi}_g$: (a) number of impacts (b) dimensionless peak to peak amplitude; _ _ _ _ without NES, _____ with NES 198

Figure 7.14-Time series of the dynamic response at 106.8kph, quasi-periodic response regime ($\varepsilon = 0.31; k_t = 6.429 \cdot 10^{12} Nm/rad^3$): (a) Dynamic transmission error (primary system) (b) NES relative motion; _ _ _ _ without NES, _____ with NES .. 199

Figure 7.15- (a) Instantaneous energy exchanges between modes, (b) input energy distribution for quasi-periodic response at 106.8kph 200

Figure 7.16- Time series of dynamic response at 112.3kph under effective vibration attenuation conditions ($\varepsilon = 0.149$; $k_t = 5.506 \cdot 10^{12} Nm/rad^3$): (a) Dynamic transmission error (primary system) (b) NES relative motion; _ _ _ _ without NES, _____ with NES 202

Figure 7.17- Time series of dynamic response at 112.3kph under ineffective vibration attenuation conditions ($\varepsilon = 0.15; k_t = 1.542 \cdot 10^{12} Nm/rad^3$): (a) Dynamic transmission error (primary system) (b) NES relative motion; _ _ _ _ without NES, _____ with NES..... 203

Figure 7.18- Wavelet analysis of the relative torsional velocity, DSI suppresion.... 204

Figure 7.19- Wavelet analysis of the NES relative motion, DSI suppresion 204

Figure 7.20- Wavelet analysis of the relative torsional velocity, no DSI suppresion205

Figure 7.21- Wavelet analysis of the NES relative motion, no DSI suppression 205

Figure 7.22- Number of double sided impacts over the vehicle speed operating range; _ _ _ _ without NES, _____ with NES..... 206

List of Tables

Table 3.1- Vehicle properties and operating conditions..... 40

Table 3.2- Gear pair parameters and machine/cutter settings (Gleason face hobbed gear set)..... 52

Table 3.3- List of main assumptions..... 62

Table 4.1- Basic parameters in EHL formulation..... 70

Table 4.2- Notation of contact footprint variables..... 72

Table 4.3- Variables used in film thickness expressions..... 96

Table 4.4- Parameters in lubricant rheology-energy balance equation..... 99

Table 5.1- Definition of system parameters..... 115

Table 6.1- Lubricant fluid properties..... 161

Table 6.2- Dimensionless Group definition..... 163

Nomenclature

Latin characters

A	$[m^2]$	Vehicle frontal area
a_{axis}	$[m]$	Minor axis of contact ellipse
b_{axis}	$[m]$	Major axis of contact ellipse
b	$[m]$	Half gear backlash along the line of action
c_m	$[Ns/m]$	Mesh damping along the line of action
e	$[m]$	Kinematic (static) transmission error
E_r	$[Pa]$	Reduced modulus of elasticity
f	$[-]$	Coefficient of rolling resistance
F_{fr}	$[N]$	Overall friction force
h_0	$[m]$	Central lubricant film thickness
i	$[-]$	Transmission ratio
I_i	$[kg \cdot m^2]$	Inertia at each side of the differential gear pair
k_m	$[N/m]$	Mesh stiffness along the instantaneous line of action
$\vec{n}$		Unit vector along the mesh force direction
N_i	$[-]$	Number of teeth of gear wheels
$\vec{r}_M$		Position vector of effective mesh point

$r_{fr,i,x}$	$[m]$	Arm of frictional moment along x-direction
$r_{fr,i,x}$	$[m]$	Arm of frictional moment along y-direction
R_i	$[m]$	Contact radius of gear wheel
R_{zx}	$[m]$	Radius of curvature along the minor axis of contact ellipse
R_{zy}	$[m]$	Radius of curvature along the major axis of contact ellipse
T_i	$[Nm]$	External load
v_i	$[m/s]$	Velocity component alonf the line of action
u_i	$[m/s]$	Gear surface velocity at the tangential plane of contact
W	$[N]$	Flank contact load

Greek characters

a	$[Pa^{-1}]$	Pressure – viscosity coefficient
η_0	$[Pa \cdot s]$	Ambient lubricant viscosity
η_e	$[Pa \cdot s]$	Effective lubricant viscosity
Θ_0	$[K]$	Bulk (inlet) lubricant film temperature
Θ_e	$[K]$	Current lubricant film temperature
δ	$[m]$	Relative gear displacement along the line of action
ΔU	$[m/s]$	Sliding velocity at the contact point

$\Delta\varphi_L$	$[rad]$	Loaded angular transmission error
μ	$[-]$	Friction coefficient
$\vec{\xi}$		Unit vector along the sliding direction
τ	$[N/m^2]$	Shear stress
υ	$[m/s]$	Vehicle cruising speed
ϕ_i	$[rad]$	Angular displacement of gear wheel due to elasticity
ϕ_∞	$[-]$	Lubricant film thermal correction factor
φ_i	$[rad]$	total angular displacement of gear wheel
ψ_i	$[rad]$	Angle between entraining velocity and contact ellipse semi axes
ω_i	$[rad/s]$	Mean angular velocity of each gear member

Chapter 1 - Introduction

1.1 - Background

Gear noise is a crucial issue when considering transmission systems. Sound emission can cause a great deal of inconvenience for passengers and perception of deteriorated vehicle quality when exceeding certain limits or lying within specific frequency ranges. Although a wide range of gear applications exists, the sources of gear noise remain fundamental. The fluctuations of tooth load associated with transmission error are considered as the primary source of such phenomena.

The sound generated from gear meshing is transmitted via forces and motions to the supporting shafts, bearings and housing, eventually reaching the surroundings of the transmission system. The basic cause for the gear mesh noise is the imperfect (non-conjugate) action of the teeth flanks. These imperfections create a set of dynamic forcing at the gear teeth, which in turn is transmitted to the shafts and bearings of the system and hence to the transmission casing. One may identify three main paths for the transmitted noise. The first path involves the airborne whereas the second is appointed to structure-borne noise, being transmitted through the casing walls. These can act as “loud speakers”, propagating the noise conceived by an external listener. One should also mention a third path of special importance, involving forces transmitted through the gearbox mounts to surrounding vehicle components, whose oscillations can generate noise. The vibration and noise generation mechanism is shown in Figure 1.1.

Axle gear whine is a high frequency noise appearing mostly in hypoid gear pairs of differentials. Unlike rattling which in encountered mostly in lightly loaded gear mechanisms, whining is associated to considerable external loading conditions. It covers a variety of operating conditions while its frequency content is related to the gear mesh orders. Gear manufacturing quality and inherent geometry are significant factors affecting axle whine. A strong correlation between noise and torsional vibrations of the differential has been established; their resonant behaviour has been matched in the frequency domain. Improper mesh generated by high amplitude

dynamic phenomena result into vibro-impacts and separation of the teeth flanks, affecting greatly the levels of perceived noise.

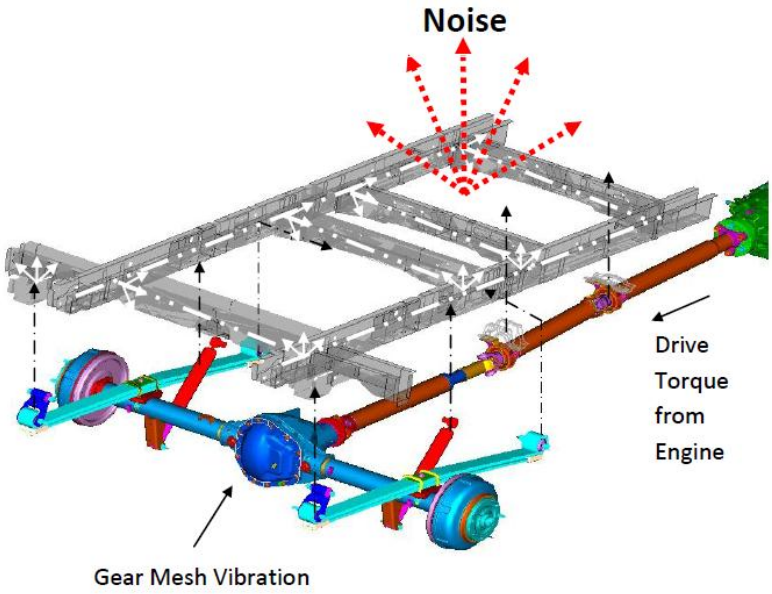

Figure 1.1- Differential Gear vibration and noise generation mechanism (after Saunders, 2005)

It is vital to control the generated sound even though an analysis for noise minimization presents considerable challenges. The reason is the geometric complexity; the manufacturing process is crucial for the surface geometry. Furthermore, it is not always possible to achieve perfect mesh, since conjugancy is usually feasible at one shaft mounting position. Also, one should not neglect the lack of analytical solutions for calculating the radii of curvature of the gear teeth and the difficulties in quantifying the tooth profiles and manufacturing complexities, including piece-to-piece variations. This fact creates significant complications in the modelling process.

In order to investigate the axle gear whine phenomenon, a dynamic model of gear pairs has been utilised in this thesis, simulating conditions that occur during meshing. The reported analysis is only confined to torsional vibrations, neglecting any other induced motions; nonetheless dynamic investigation is targeted towards realistic operating conditions. The aim is to investigate the pure interactions between the pinion and the crown gear during meshing without effects from other sources.

Special attention is paid to the introduction of geometric properties defining the contact and to the calculation of the factors affecting noise emission.

1.2 - Aims and Objectives

The overall **aim** of this thesis is to perform a thorough analysis of hypoid gear dynamics, identifying the root causes behind their behaviour.

The contact between two hypoid gears is considerably more complicated than in the case of other gearing systems, chiefly because of complex changing contact geometry through mesh. Each point in the contact area traces a curvilinear path in contrast to a nearly straight line pattern observed in spur or helical gears. Moreover, the surface curvatures are much more complex to determine, which affect contact footprint and meshing stiffness, as well as contact deformation and lubricant film thickness.

The complexity of the contact geometry explains the dearth of analytical solutions in the open literature with regard to the meshing parameters. Hence, semi-analytic expressions, based on numerical data will be proposed for the latter in this thesis.

The specific **objectives** of this thesis are:

- To create a detailed dynamic model, able to capture the complicated dynamic response of hypoid transmissions under a broad range of realistic operating conditions.
- To compute the family of periodic solutions and the stability of the various response branches followed by parametric studies.
- To expand the analysis to the more realistic lubricated elliptical point contact under elatohydrodynamic regime of lubrication; coupling the effect of dynamics to a tribological consideration.
- To relate the gear pair dynamic behaviour with conditions potentially leading to noise generation and study the effect of non-linear palliative attachments while acting as passive vibration absorbers.

Therefore, even if the general aim of the thesis is the study of hypoid gear dynamics, the specific objectives are oriented on the engineering Noise, Vibration and

Harshness (NVH) problem as posed by gear whine phenomenon. This fact is supported by the potential use of this study for noise evaluation purposes.

The approach implemented in this work is based on contact mechanics and elastohydrodynamics (EHL) theory. However, in accordance with the theory, Tooth Contact Analysis (TCA) numerical data will be imported into the dynamic model. The concept of Targeted Energy Transfer (TET) will be also discussed. This approach has not hitherto been applied to non-linear phenomena in powertrain systems.

1.3 - Hypoid Gears and applications

Hypoid gear sets transfer power and motion between crossed axes. They resemble spiral bevel gears which perform rotation about intersected axes. The other main difference is the asymmetrical teeth flanks; the pressure angle on each side of the tooth is different. Nevertheless, many of the machines used for manufacturing spiral bevel gears can be used to manufacture hypoids. A typical hypoid gear pair can be seen in Figure 1.2.

Figure 1.2- A hypoid gear pair

The primary domain of application for hypoid gear drives has been the automotive industry for almost 90 years now. The rotary motion of an engine, installed lengthwise in a vehicle, can only be transmitted to the crosswise positioned wheels by means of angular gearing. Although most of the first engine-driven vehicles in Europe used worm gears, spiral bevel and hypoid gearing were proved to be the best solution in USA by 1920. When the engine architecture was shifted towards cross-wise installations instead of lengthwise, a reduction in demand occurred. Yet,

designs requiring such gear sets (tractors, trucks, train engines, luxury car automobiles) still persist. Furthermore, there is a trend towards four wheel drive automobiles, requiring two to three bevel/ hypoid gear sets.

The history of hypoid gears is connected with the development of gear machine technology. There exist three major manufacturing companies; Gleason Works (USA), Oerlikon-Buhrle (Switzerland) and Klingelnberg-Sons (Germany). Both Gleason and Oerlikon have begun the manufacturing of cutting machines at the end of 19^{th} century. The production of bevel gears was affected by the fact that curved tooth traces demonstrated much better rolling behaviour, resulting in larger contact ratios and increased torque transmissibility. Thus, a combination of linear and circular motion was introduced in the manufacturing process. The first machines able to produce hypoid gears were built by Gleason in 1925. One year later Shell Oil Company began marketing the first hypoid oil pump and Ford Motor Company in USA started equipping vehicles with hypoid bevel gears. Ford was the first automotive company to do so.

High reduction and contact ratios are one of the main advantages of hypoid gearings. By applying positive axial offset, the face module can be increased substantially, resulting in doubling of the outside diameter. Therefore, there is an important increase in pinion strength without noticeably increasing the overall space requirements. In this case the number of teeth is not proportional to the pitch diameter. This fact enables the reduction of the smallest number of teeth on the pinion. Hence, it is possible to make large pinions, while minimizing the driven gear size. Furthermore, the contact ratio is affected due to a strong overlap ratio increase. If the introduction of helical or worm gears can achieve an increase of contact ratio from 1.5 up to 2.5, the hypoid offset can result in an increase up to 3.5. This fact reduces the meshing impact as well as the flank compression and the root stress. Therefore, while in operation, hypoid gears are usually quieter and smoother than spiral bevel gears. They possess greater tolerance to shock loading and can be used at much higher single stage ratios than the spiral bevel gears.

The development of longitudinal sliding is another important characteristic of hypoid gear systems. Similar to the case of spur gear pairs, spiral bevel gears demonstrate only relative sliding in the profile direction. On the pitch cone, this relative velocity

diminishes. This pure rolling condition affects the destruction of the hydrodynamic oil cushion resulting in fatigue related symptoms along the pitch line leading to pitting development (Stadtfelt, 1993). By applying an axial offset, one can ensure that relative sliding takes place in the entire flank region, preserving the continuity of the lubricant film and smoothing the transmission line between the engine and the road. However, the high level of sliding reduces the efficiency of hypoid gear sets compared with a similar set of spiral bevel gears.

To summarize, hypoid gears have significant advantages in comparison with the spiral bevel gears. They operate in a more stable manner, absorbing the shock excitations induced by other parts of the powertrain system. They are characterized by high contact and transmission ratios, as well as minimal wear due to longitudinal sliding. The important role they have in the automotive industry has attracted a great deal of attention related to various NVH phenomena. The thesis attempts to study the dynamics of a hypoid gear pair in relation to the axle gear whine noise.

1.4 - Structure of the Thesis

Chapter 1 provides an introduction to gear noise in hypoid gear systems. It also states the aim and specific objectives of the thesis.

Chapter 2 is focused on a review of the theoretical background supporting this study. A brief description of axle noise is given correlating its appearance to hypoid gear vibration issues. Various mechanical gearing models are presented, highlighting the special treatment of hypoid gear sets in terms of Tooth Contact Analysis (TCA). The application of elastohydrodynamic (EHL) lubrication in gear mechanisms is also discussed followed by a number of applied measures to alleviate unwanted vibration problems. In the end, the advantages underlying the implementation of the concept of Targeted Energy Transfer (TET) are discussed.

Chapter 3 involves dry contact between the mating flanks. The fundamental mechanical model is proposed and the basic contact parameters are calculated by introducing semi-analytical expressions. The implications of applying Tooth Contact Analysis (TCA) are also illustrated.

In Chapter 4 the fundamental mechanical model is expanded to simulate the effect of lubrication. The necessary contact parameters are again computed leading to the definition of friction in the contact zone by considering the operating conditions of hypoid transmissions. Eventually this leads to a non Newtonian treatment of the problem while accounting for the heat dissipation of the lubricant due to the shear effect.

Chapter 5 discusses the results obtained by the dynamic analysis over a range of system parameters for the case of dry contact. Current formulation is compared to previous dynamic models illustrating the system nonlinearities appearing in the dynamic response. An analysis of the various response regimes is conducted followed by a stability analysis of the periodic solutions combined to parametric studies of the various factors.

Chapter 6 depicts the effect of lubrication on the dynamic response and vice versa. Comparison of various treatments is given including thermal, non Newtonian and two dimensional analyses.

Chapter 7 attempts the application of Targeted Energy Transfer (TET) in geared systems. This concept is applied to a hypoid gear set in order to attempt reduction of undesired dynamic responses. A variety of response regimes is identified while the energy transactions are illustrated.

Chapter 8 derives overall conclusions for the work completed, evaluates the approaches followed and suggests aspects that should be studied in the future.

Chapter 2 - Literature Review

2.1 -Introduction

A major step towards the completion of a research project is an effective definition of the problem. A dynamic model of a transmission system can be of varying complexity, based on the specifications of the investigation. An extremely complicated model may prove to be computationally inefficient and beyond scope. On the contrary, a simple modelling approach might be insufficient to reveal elaborate characteristics of the investigated phenomena. Therefore, it is important to understand the aspects of the problem and subsequently set the specifications of the numerical model that is going to be developed. This procedure is assisted by a thorough review of the already published material.

In the beginning of this chapter, industrial concerns arising from drivertrain oscillations will be discussed, highlighting the importance of detailed modelling. Eventually, vibration control methods will be assessed while underlying all state of the art achievements.

Initially, an overview of the problems related to differential unit vibrations in automotive industry is presented, underlying the importance of this research subject. The significance of teeth contact parameters affecting gear mesh is identified; simulation and experimental methods for their prediction are discussed. Subsequently, various numerical models describing the dynamics of systems with gears are presented. A variety of simulation techniques is available, linked to the level of detail maintained by the investigation.

After examining the macro (global) scale of gear teeth dynamics, focus will be shifted on their micro scale, namely the contact of the mating gear flanks. Equally important is the study of the dual nature of transmission vibrations combining dynamics with tribological and friction effects. The tribological foundation is presented by reviewing the general Elastohydrodynamics (EHL) theory, comprising of analytical, numerical, thermal and non-Newtonian considerations. Gear lubrication is covered in a separate section, describing the formation of lubricant film and friction generation mechanism

in gear flanks. Dynamic modelling of friction is also reviewed, stating the main issues requiring an auxiliary formulation.

The last part of this chapter illustrates the applied measures for solving issues associated to hypoid gear vibrations followed by an analysis of the concept of Targeted Energy Transfer (TET). There seems to be significant potential in exploiting the latter in order to be used as an effective active solution. Finally, the observed gaps in existing knowledge are recognised, identifying the space for the investigation which is covered by this study.

2.2 - Problem Description

Axle whine noise has been addressed as one of the major Noise, Vibration and Harshness concerns that automotive industry is facing. The continuous trend for improved vehicle noise quality led to the gradual revealing of previously masked noise sources (Yoon et al, 2011). Due to the extended use of axle components in drivetrain technology, controlling differential noise has been associated to the overall vehicle sound quality (Lee et al, 2005).

Whining of the differential axle is characterised by a tonal nature (Curtis et al, 2005), meaning that it is perceived on a specific frequency region (or intervals). It occurs mainly in loaded hypoid gears and the gear mesh frequency plays a dominant role herein (Juang et al, 2006). It appears at a variety of operating conditions; during drive and coasting, high and low torque loading (Lee, 2007) whereas the frequency range covers a bandwidth from 200 to 1200Hz based on the individual characteristics of the vehicle (Hirasaka et al, 1991; Lee and Kocer, 2003; Steyer et al, 2005). The overall noise can be divided into two discrete transfer paths; an airborne and a structure borne. The first one corresponds to a vibration of the axle system focusing on the dynamic mesh force (Lee et al, 2005). However, the second one includes the interaction of the body and driveline structural components towards the amplification of the axle vibration level (Kim et al, 1999).

The main source of the axle whine lies in the gear mesh characteristics. Figure 2.1 shows the analysis of the perceived noise from a traditional source – path – receiver point of view (Chung et al, 1999). The meshing process of the hypoid gear pair entails all the crucial excitation factors affecting noise generation. Initial credit can be

attributed to the gear design characteristics affecting the mesh stiffness variation. It was shown (Hellinger et al, 1997) that the latter can influence significantly both the magnitude and the frequency content of the generated dynamic forces.

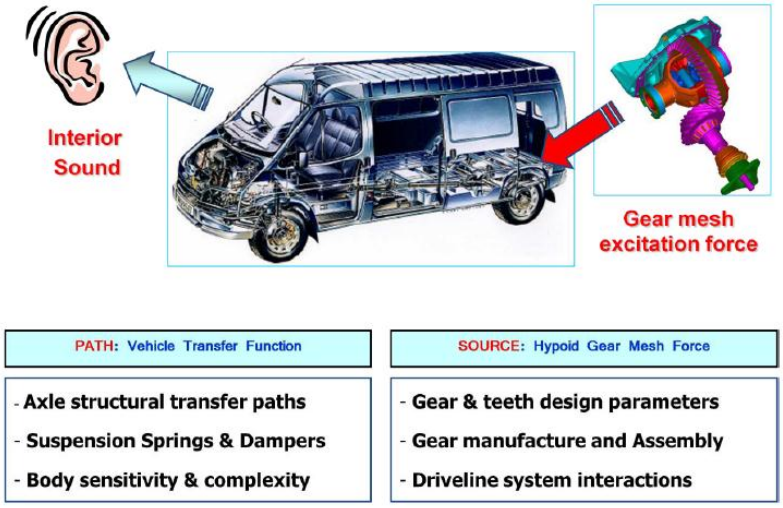

Figure 2.1- Axle whine noise source and transfer paths (source: FORD Motor Company UK Ltd)

Another significant contribution comes from the gear pair manufacturing quality, as well as potential assembly errors. It is widely acknowledged that transmission error is the most crucial factor when assessing gear quality. It can be regarded as “the deviation between the output gear and the position it would normally occupy if the gears were perfectly conjugate” (Dudley and Townsend, 1991). It can be expressed both in angular and translational form along the line of action. Its influence in noise excitation has been discussed in a number of research studies (Hirasaka et al, 1991; Lee, 2007; Yoon et al, 2011).

An equally important effect on the dynamic mesh force appears due to interactions with other driveline components. The effect of propshaft inertia and stiffness has been mentioned by Nakayashiki et al (1983), Chung et al (1999), as well as Lee (2007). Furthermore, it has been shown that both bending and torsional modes of the propshaft can significantly control the driveline noise (Steyer et al, 2005; Sun et al, 2011).

Besides the development of the teeth mesh force, the overall noise level is also affected by the structural transmissibility paths of the vehicle (Wani and Singh, 2005). Inside the axle assembly this is mainly due to the shafts, bearings and additional modes of lateral gear body oscillations. The latter have minimal impact on the tooth flank vibration level; however they effectuate large motions near the bearings. Therefore, if these modes coincide with mesh force resonances, the bearing support forces will get amplified (Miyauchi et al, 2001). The vibration energy also travels through structural components of the vehicle, such as the suspension springs and dampers. Additionally, body integrity is also critical, since it can result to amplification of the generated noise (Hagino et al, 1990; Chung et al, 1999).

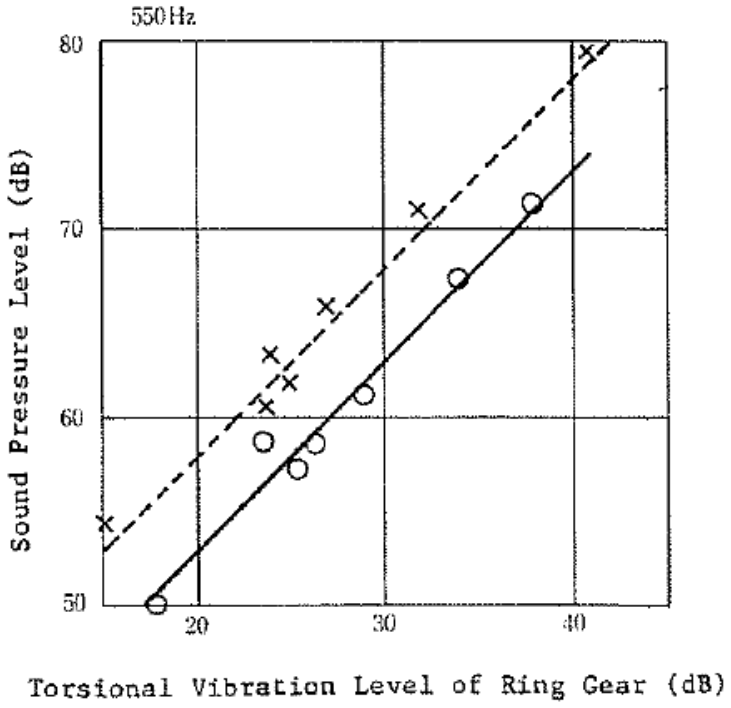

Figure 2.2:- Correlation of Sound Pressure Level and Torsional Vibration Level for 550Hz (after Nakayashiki et al, 1983)

Correlation between noise and vibration level has been provided in various studies, highlighting the importance for a rigorous dynamic analysis. Nakayashiki et al (1983) presented a strong correlation between the torsional vibration of the ring gear and the overall perceived axle whine noise for different frequencies. The correlation graph for the case of 550Hz is shown in Figure 2.2. They concluded that controlling

the torsional vibration level, would lead to axle whine alleviation. Additional experimental evidence was provided by a test rig (Hirasaka et al, 1991). The resonant frequencies of both noise and vibration amplitudes were found to correlate. This fact is depicted in Figure 2.3. The above findings are supported by the work of Lee et al (2005), where waterfall plots of the interior noise were compared to vibration amplitudes at certain locations of the differential axle. Therefore, it can be concluded that the axle whine noise as perceived in the vehicle cabin is strongly connected to the vibration level of the differential assembly.

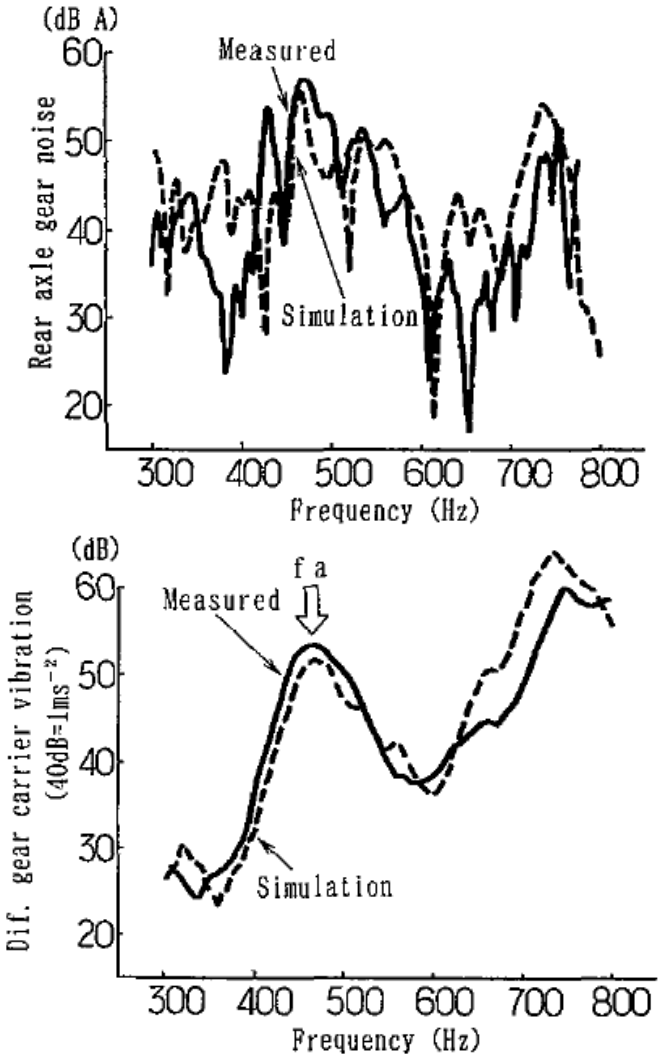

Figure 2.3- Correlation of resonant frequency of noise and vibration amplitudes (after Hirasaka et al, 1991)

The influence of differential unit vibrations on the radiated noise reveals the necessity for their study. Ideally, this task would require a multi-body dynamics

approach in order to account for the entire driveline system interactions. Nevertheless, such an analysis would demand a model of considerable complexity and a vast amount of computational time. Hence, the focus of this research study will be placed on the differential unit itself, where the dynamic mesh force is generated (Lee and Kocer, 2003; Sun et al, 2003). The total response at the differential casing is the product of the mesh force, amplified by the transmissibility function at the bearings (Miyauchi et al, 2001). Due to the lubricant effect at the bearings, a level of damping is introduced; hence the transmissibility curve is usually smooth without significant peaks. As a result, the bearing force curve retains the shape of the dynamic mesh force. It is therefore within reason to conclude that the dynamic mesh force can give a good representation of the vibration levels in the differential unit.

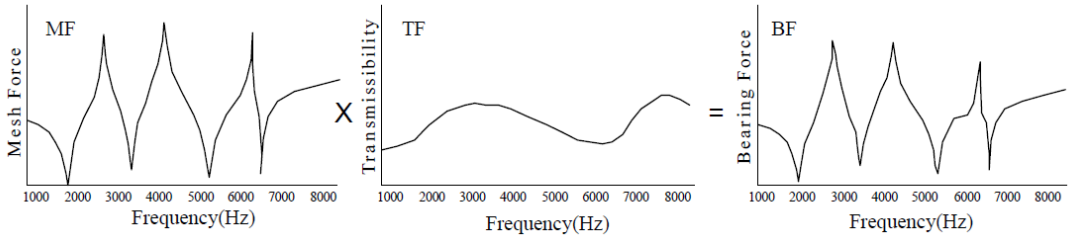

Figure 2.4- Bearing Forces as a product of Mesh force and Transmisibility function (after Miyauchi et al, 2001)

The dynamic mesh force is affected primarily by the gear train torsional dynamics (Sun et al, 2005). Therefore, a torsional gear pair model would effectively describe the dynamic responses associated to the noise generation. It would also be able to account for the various nonlinearities, such as contact loss and tooth flank impacts or estimate the magnitude of the frictional excitations due to the sliding motion of the mating surfaces. These factors have been linked to noise generation as well (Lee, 2007). Furthermore, although the effect of the propshafts was mentioned to be important, a hypothesis for its torsional rigidity would yield the worst case scenario. As shown by Hirasaka et al (1991), reducing the torsional rigidity of the propshaft leads to the decrease of the dynamic mesh force peak amplitude. Based on the above considerations, a simplified torsional model of the differential gear train would be effective in describing the general vibrational characteristics of the differential unit, while addressing the root causes of noise generation. Thus, any potential

method for reducing the amplitude of the induced vibrations could be applied on this fundamental model.

2.3 - Modelling / Simulation techniques

2.3.1 Dynamic modelling

The previous section stressed the importance of drivetrain vibrations as a major industrial concern; there is a strong correlation between unwanted oscillations and NVH issues. It was derived through the assumption that the dynamic response of the engaged gears can yield a representative picture of the overall system behaviour. Thus, it is a logical approach to focus on the various modelling techniques describing the dynamics of gear pairs.

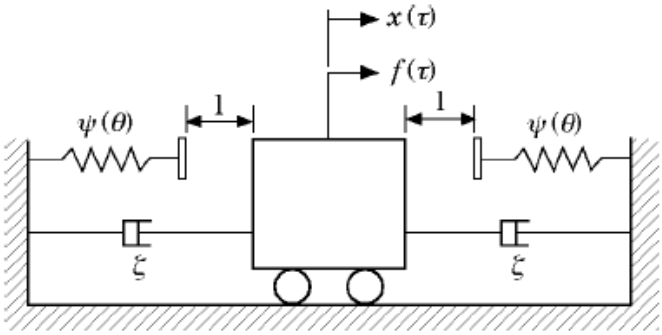

Figure 2.5- General form of a gear pair oscillator (after Blankenship and Kahraman, 1995)

There is a plethora of reasons underlying gear vibration; including backlash and errors in the form and finish of mating gear teeth pairs, defined as kinematic transmission error. These errors and misalignment of gear pairs and their supporting shafts are important causes of vibration and noise, as well as poor lubrication, friction and wear. Therefore, besides studying the effect of machine and cutter tool settings to reduce mal-form and finish, the dynamic response of gear sets when in situ, has also been extensively investigated. The latter area is due to the effect of various system nonlinearities. Consequently, an array of modelling techniques is used, depending on the conditions pertaining to a defined problem (Ozguven and Houser, 1988a).

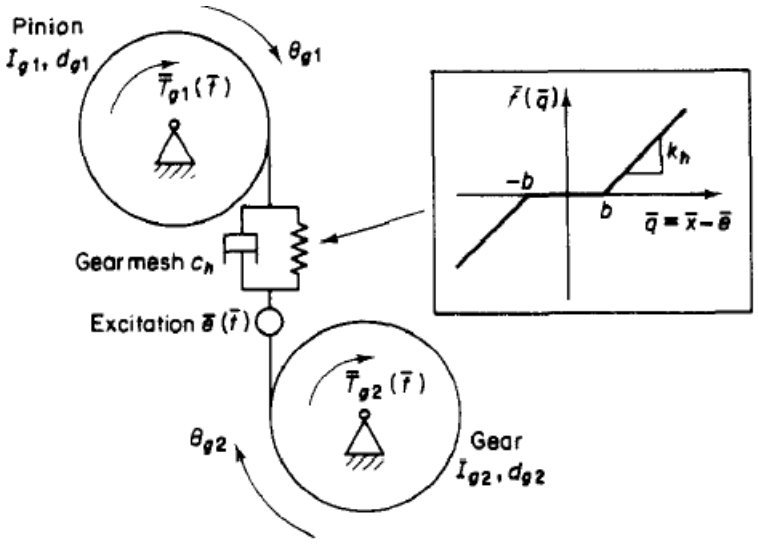

Figure 2.6- Mechanical Model of a spur gear pair (after Kahraman and Singh, 1990)

A number of numerical models have been proposed to obtain the dynamic response of gear pairs in order to ascertain the extent of system stability and capture the occurring periodic motions. Implementation of lumped parameter models is a common practice, followed by analytical expressions for time varying parameters, such as the teeth meshing stiffness. The main source of nonlinearity in these formulations is the presence of backlash, promoting impacts which can lead to impulsive actions and potential chaotic behaviour.

In certain cases, the general form of a geared system can be described by a simplified single degree of freedom mechanical oscillator (Blankenship and Singh, 1995), as depicted in Figure 2.5. The dynamic response is defined by the variable x denoting the relative deflection of the gear teeth. An external forcing function $f(\tau)$ is applied to the system; the stiffness factor $\psi(\theta)$ is periodic and is multiplied by a nonlinear restoring function $g[x(t)]$ due to the inherent backlash of the system. Eventually, the resulting equation of motion is given in the following expression:

$$\ddot{x} + 2\zeta\dot{x} + \psi[\theta(\tau)]g[x(\tau)] = f(\tau) \qquad \textbf{(2.1)}$$

In essence, this is the case of a Mathieu-Hill oscillator with piecewise linear restoring force.

Initial work on the dynamics of spur gear pair has been conducted by Ozguven and Houser (1988b), as well as Kahraman and Singh (1990). Both studies present a nonlinear modelling approach resulting in a torsional, single degree of freedom system. It was concluded that when the torsional mode is weakly coupled to the other vibration modes of the system, the gear pair dynamic behaviour can be efficiently described by the motion along the line of action. The mesh stiffness was assumed to be invariant with respect to time in both cases; hence only its mean value was included in the study. In the first case, the variable mesh stiffness effect was approximated by including the loaded transmission error as an internal excitation factor computed by a separate computational procedure. Experimental validation showed satisfactory correlation levels while the increase of the dynamic forces was attributed mainly to mesh stiffness variation.

The focus on the second study was on the nonlinear dynamic response inflicted by the combined effect of backlash and static transmission error. A combination of analytical and numerical techniques was applied to define the existence of multiple solutions based on the initial conditions. The mechanical model proposed by Kahraman and Singh (1990) can be viewed in Figure 2.6. Numerical integration revealed a multitude of coexisting solutions at certain conditions and parameter values. An analytical approach based on the Harmonic Balance Method (HBM) was able to yield the various response regimes without being affected by the initial conditions. Parametric studies confirmed the dependence of multiple response regimes on load and damping characteristics of the system. Experimental validation was in this case efficient in predicting the transition frequency between the different response regimes. Failure of exact qualitative correlation was due to the lack of knowledge for the properties of the experimental rigs and the adopted assumption of constant mesh stiffness.

Further work on the dynamics of spur gear pairs was targeted on the development of analytical methods in order to predict the various solutions exhibited by the system. Blankenship and Singh (1995) employed the Harmonic Balance Method, whereas Natsiavas et al (2000) introduced an alternative approximate method combining the treatment of piecewise linear systems with perturbation techniques applied at systems with time varying coefficients. Application of the first approach by

Blankenship and Kahraman (1995) (by taking into account a single harmonic term in the time varying parameters) was correlated with experimental data. Parametric studies showed the effect of various design variables such as the oscillating mesh stiffness component, damping ratio and applied preload. It was shown that the above parameters affect both the solutions' nature together with the bifurcation frequencies.

The second analytical method was investigated by Theodossiades and Natsiavas (2000). The analysis was concentrated on the fundamental parametric and external resonance. The system was found to undergo a complicated dynamic response, characterised by multiple coexisting solutions and jump phenomena. The gear pair parameters were proven to affect significantly the nature of the response and the generated dynamic amplitudes. It was also shown that their variation could lead into stability issues accompanied to period doublings, boundary crises and chaotic regimes. The obtained results from the analytical method were correlated efficiently to numerical integration.

The effect of mesh force transmissibility was also of importance so that the coupling between the lateral and torsional motion of the gear wheels could be investigated. A nonlinear, six-degree of freedom dynamic model was developed by Ozguven (1991); through a numerical integration procedure, the necessity of multiple degree of freedom model was investigated. It was derived that the coupling between torsional and lateral motions is highly dependent on the torsional compliance off the carrying shafts and the bearing stiffness. An additional model by Kahraman and Singh (1991) included the effect of periodic system coefficients expressed in Fourier series form. It was shown that the variation of mesh stiffness is related to the backlash induced nonlinearities rather than the ones attributed to the rolling bearing elements. The work of Blankenship and Singh (1995) addressed the same issue in helical gears while solving a linear time invariant system. The importance of lateral degrees of freedom was justified on the ground of structure borne noise prediction. Of great importance is the investigation conducted by Theodossiades and Natsiavas (2001a, 2001b). Two multiple degree of freedom dynamic models are presented, incorporating the effect of journal and rolling bearings in the dynamic response of geared systems. The significant part is the dependence of the resistive torque on the instantaneous angular velocity of the output shaft rather than being defined a priori.

The mesh stiffness and transmission error were now shown to behave in a strongly nonlinear manner. Complex dynamic behaviour was revealed by numerical integration of the equations of motion.

Similar analyses on crossed-axes gear sets have shown more complex responses. For example, hypoid gears used in a wide range of applications, present complex meshing geometry. Consequently, there is a lack of analytical expressions to quantify the effect of their underlying governing parameters. Prior to the development of Tooth Contact Analysis (TCA) tools, experimental and empirical formulations were common place (Kiyono et al, 1991; Donley et al, 1992). These early models precluded the exact meshing geometries. Instead, they were based on simplifications to the meshing force vector used in purely torsional dynamic analyses.

The first attempt to build a hypoid gear vibration model based on exact geometry, was made by Cheng and Lim (2001). The generation of gear pair surfaces and the discretisation of the elliptical contact area resulted in the development of a three-degree of freedom (DOF) model. The significance of this approach was in relating the meshing parameters to the actual gear geometric characteristics. Moreover, it allowed for the transmission of mesh load to the structural components of the differential unit. A further study (Cheng and Lim, 2004) included backlash non-linearity and time-dependent meshing parameters, enabling the identification of resonant modes and, therefore, the study of the effect of load torque on system dynamics. Wang et al (2007) focused on a hypoid gear pair, describing the dependence of meshing parameters' variation with the dynamic response of the system. An original two-DOF system was reduced to a single DOF and its dynamic response was computed using two different models. The first model only included the fundamental harmonics of the meshing parameters, whilst the second one imported their exact values. The generation of impacts was discussed, as well as the transition of system's response from a periodic motion to a chaotic state with the variation of load torque and introduction of damping.

2.3.2 Tooth Contact Analysis

As mentioned previously, gear whine noise is affected by certain design parameters as the static transmission error and variation of mesh stiffness. These factors, as will be shown in the following sections, affect significantly the dynamic response of the system, acting as internal and parametric excitations. Quantification of the above properties has been achieved in a number of studies, mainly by conducting a stress analysis together with experimental measurements. Spiral bevel and hypoid gear members will be the focus, since they are mostly exhibiting gear whine noise.

An overview of the principles of contact mechanics, describing the load distribution and the deflections of mating structures has been given by Johnson (1985). In his textbook, the Hetzian contact theory is discussed while cases that require numerical solutions are presented. Therefore, in gear mechanisms, global deformations due to bending and torsion need to be accounted for. Such complex three-dimensional contact problems were proven complicated to solve, on the grounds that the contact conditions could not be adequately introduced in a numerical formulation. An attempt to overcome this issue was done by Chaudhary and Bathe (1986) for both static and dynamic conditions, by applying the method of Lagrange multipliers.

All numerical stress analysis models rely on the knowledge of the contact bearing. The meshing area needs to be known a priori before applying the loading conditions. Indeed, as alleged by Litvin et al (2006), stress analysis is the final stage of an optimized gear design process. In the first place, an implementation of a local synthesis technique is necessary for the optimization of gear machine settings, followed by tooth contact analysis (TCA) in order to simulate the meshing action.

A method for the surface representation of spiral bevel/hypoid gear members is essential for the conduction of the aforementioned tasks. Such an approach was proposed by Litvin et al (1991) for the case of face hobbed hypoid gears. Equations in three dimensional space were provided, based on the kinematics of the gear generation process and on the geometry of the cutting tool. A similar work by Lin et al (1997) provided the surface characteristics of spiral bevel/hypoid gears manufactured using the modified roll method. Comparison of the theoretical

approximations with actual measured teeth surfaces showed satisfactory consistency.

Vijayakar (1991) employed the Simplex algorithm together with a linearization technique in order to solve complicated contact problems, applying this method in the case of gear pair contacts. The representation of the contacting bodies was found to be optimised by Chebyshev polynomials, while the analysis was able to yield load distribution and transmission error. This methodology was finally combined to a surface integral solution to overcome the problem of the continuous movement of the contact zone, appearing at hypoid transmissions. Published results for the case of a hypoid gear pair were provided, whereas the principles of this work were implemented for the formulation of Tooth Contact Analysis commercial software (Advanced Numerical Solutions, 1998).

A similar approach has been followed by Gosselin et al (1995, 2000). In the preceding study, the effect of spiral bevel geometry in load sharing capacity and loaded transmission error is investigated, showing that higher contact ratio is usually preferable. The subsequent experimental work validated the simulation technique adequately, while illustrating an increase in the measured transmission error values proportional to the value of the external torque.

Further experimental stress analysis of spiral bevel gears was conducted by Handschuh and Kircher (1999), comparing the extracted data with existing analytical models. The results obtained followed the trend predicted by analytical models; however, there was a certain deviation due to the position of the strain gauges. Furthermore, the dynamic effect was proved to be minimal when the gears were running in slow to moderate speeds.

An alternative numerical method using the Finite Element Method (FEM) was formulated by Simon (2007). He assumed that the contact is deployed along a “potential” contact line, yielded as the locus of points on the mating surfaces characterized by minimum separation. Tooth bending and shear effects are also considered herein, investigating the effect of certain design parameters on the contact properties.

The various steps involved in a computational stress analysis of spiral bevel gears were illustrated by Argyris et al (2002). Local synthesis and Tooth Contact Analysis are coupled in an iterative process in order to determine the optimal configuration. The consequences of previous formulation were implemented as a design tool by Litvin et al (2006) for noise reduction purposes. Gear sets with improved contact pattern, lower stress concentration and reduced transmission error were obtained. The effect of the latter in the generated noise and vibration issues was shown. Furthermore, advantages of parabolic cutting blades over straight ones were identified, leading to higher endurance of the gear teeth.

The major disadvantage of all FEA based models is the computational inefficiency. The requirement of a vast amount of computational time for yielding a contact representation results in restrictions on parametric studies. Kolinvand and Kahraman (2009) have suggested an alternative method based on ease off topography to determine the unloaded TCA. Teeth compliances were calculated though a semi analytical formulation based on Rayleigh-Reitz model, so that the computational efficiency was improved without distorting the accuracy of the results. An accurate TCA tool for simulating hypoid gear mesh is CALYX software (Advanced Numerical Solutions, 1998). It will be used to determine the mesh characteristics of the gear sets considered in this thesis.

2.4 - Tribological consideration

As already noted, friction generated in gearing systems is an important area of investigation, since it determines the efficiency of transmission and differential systems, as well as affecting their dynamic response. Confining oneself to some representative studies, it is important to note that gear teeth are often only partially lubricated, as many fore-running contributions have shown (Snidle et al, 1997; Gohar, 2001). This is known as mixed elastohydrodynamic regime of lubrication, where the mechanisms contributing to friction are viscous shear of a thin lubricant film and interaction of asperities of the contiguous surfaces with a film of insufficient thickness in between. This is referred to as boundary friction and is prevalent in gear teeth interactions (De la Cruz et al, 2010). Vaishya and Singh (2001a, 2003) developed a dynamic model with viscous friction on gear flanks. Neglecting the effect

of backlash and simplifying the derivation of coefficient of friction, they were able to perform a stability analysis for gear pairs using the Floquet theory (Floquet, 1883). Similar analyses were conducted for helical gears by Velex and Cahouet (2000), Velex and Sainsot (2002), as well as Kar and Mohanty (2007). The common approach in the above studies was the dependence of friction on the variation of the contact line length. A method based on TCA was introduced by He et al (2007) for calculating the effect of friction the bearing forces on a twelve-DOF helical transmission system.

For helical gear pairs, De la Cruz et al (2010) have reported models for a transaxle transmission system, where a combined tribological and dynamic analysis was carried out. In their work the unselected loose gear teeth pairs were modelled as lightly loaded thermo-hydrodynamic conjunctions with viscous friction, whilst the engaged gear pairs were subject to a mixed thermo-elastohydrodynamic regime of lubrication. They showed that thermal effects in the gear teeth pair contacts significantly reduce lubricant film thickness. An analytic solution to energy equation for the determination of lubricant temperature in the contact was used whilst Grubin's (1949) analytical solution was employed for the loaded elastohydrodynamic conjunctions of engaged gear teeth pairs. This provided a quasi-static solution, which does not take into account the enhanced load carrying capacity of the teeth pair contact conjunctions due to lubricant squeeze film effects. The approach, including the squeeze film effect was advocated by Rahnejat (1984, 1985) subject to various regimes of lubrication, including isothermal elastohydrodynamic conditions for contact vibration problems. It was shown that the lubricant film behaviour is frequency dependent. An extension of this work by Mehdigoli et al (1990), representing a pair of gears as wavy surfaced discs showed that fluid film lubrication possesses insignificant damping under elastohydrodynamic conditions, which verified the earlier experimental findings of Johnson and Gray (1975). However, these studies did not include the effects of viscous or boundary friction, nor shear thinning of the lubricant in a thermal contact. Another numerical quasi-steady mixed isothermal EHL solution, combined with torsional vibration of gear pairs was highlighted by Li and Kahraman (2009) for teeth line contact conditions, applicable to spur gears and as an approximation for helical gears.

A few tribo-dynamics studies have been reported for hypoid gears including the effects of viscous and boundary friction. Geometrical complexities of hypoid gears in mesh and the need to determine the instantaneous area of contact necessitates use of numerical methods, rather than the simpler analytical approaches. The sliding velocities of mating gear teeth pairs and the sense of application of friction cannot be calculated analytically due to the time varying nature of the mesh vector. As already noted, an approach to obtain the friction vector has been reported by Cheng and Lim (2003), based upon a simulated geometry, whereas the derivation of kinematic contact properties was described by Xu and Kahraman (2007). Authors validated the various empirical formulae for representation of coefficient of friction against an elastohydrodynamic lubrication model. Good agreement with experimental results was shown and a formula extrapolating the results was obtained.

A number of other researchers have also focused on transient EHL representation of the contact zone between the gear flanks. These include the works reported by Holmes et al (2003a, 2003b, 2005), who treated the contact zone of pairs of hypoid gear teeth as a point contact problem. Isothermal solution of gear lubrication problem has received more attention than those including thermal effects. An investigation of thermal effects was also reported by Handschuh and Kircher (1996), who calculated the temperature distribution in the contact zone due to heat generation.

In this thesis TCA is used to determine the kinematic and geometrical properties of the hypoid gears, necessary for the thermo-elastohydrodynamic analysis that follows. The rate of change of the teeth contact radii has been considered in the analysis. This is a main contribution of the current work compared to those previously published. It reveals more pronounced dynamics, characterised by teeth separation near 1:1 resonant conditions. Asperity contribution to friction is also included by characterisation of the tooth flank topography and use of the Greenwood and Tripp (1970, 1971) friction model. Therefore, the analysis in this paper is that of quasi-static mixed thermo-elastohydrodynamics of hypoid gear teeth pairs, and its effect upon the dynamics of a hypoid gear pair of a vehicle differential unit. Such an approach has not hitherto been reported in literature.

2.5 - Applied measures

Due to the severity and importance of axle vibrations, methods for alleviating the unwanted motions have been suggested. The nature of the problem was shown to be twofold; on one hand it is the transmission error acting as excitation, promoting vibrations of the gear teeth flanks; on the other hand it is the dynamic interactions of the various differential and driveline components. Thus, noise and vibration reduction can be achieved by combining two individual paths; either focusing on the micro-geometry and manufacturing methods of the gear members to ensure better surface quality and lower levels of transmission error or by applying dynamic tuning techniques so that the resonance issues between the mesh frequency and the natural frequencies of the system are attacked (Hagino et al, 1990).

The effect of altering the gear tooth profiles in a search of optimized contact geometry has been illustrated by Lee (2007), as well as Yoon et al (2011). In the former case, the ring gear was processed with different cutter settings, resulting to considerable reduction of the transmission error by almost 46%. Although the contact area remains unaltered, the profile modification retains the contact zone inside the tooth face even under fully loaded conditions. The result is an attenuation of previously reported high vibration levels at certain driveshaft speeds, despite the fact that the structural resonances remain. In the latter case, an enlargement of the contact zone was introduced in order to resolve noise issues under deceleration conditions. A decrease of the measured transmission error was confirmed to exist upon the modified gear set for the loading torques of interest. The overall interior noise was reduced considerably.

However, manufacturing interventions are not always effective. There are examples where although the gear manufacturing quality is the best possible, vibrations reach critical levels (Donley et al, 1992). In such cases the unwanted motions need to be studied using dynamic analysis. The essence lies into proper tuning and mapping of the system mode shapes in order to avoid resonance issues. Initially, concern should be given to the generated dynamic mesh force. The latter is analogous to the mesh stiffness, which in turn is affected by the dynamic compliances of the pinion and ring gear (Sun et al, 2003). The mesh force per unit transmission error can be

represented as the reciprocal of pinion motion (ϕ_p), ring gear motion (ϕ_g) and tooth compliance (ϕ_{th}) (Miyauchi et al, 2001):

$$MF_{unit} = \frac{1}{\phi_p + \phi_g + \phi_{th}} \qquad \textbf{(2.2)}$$

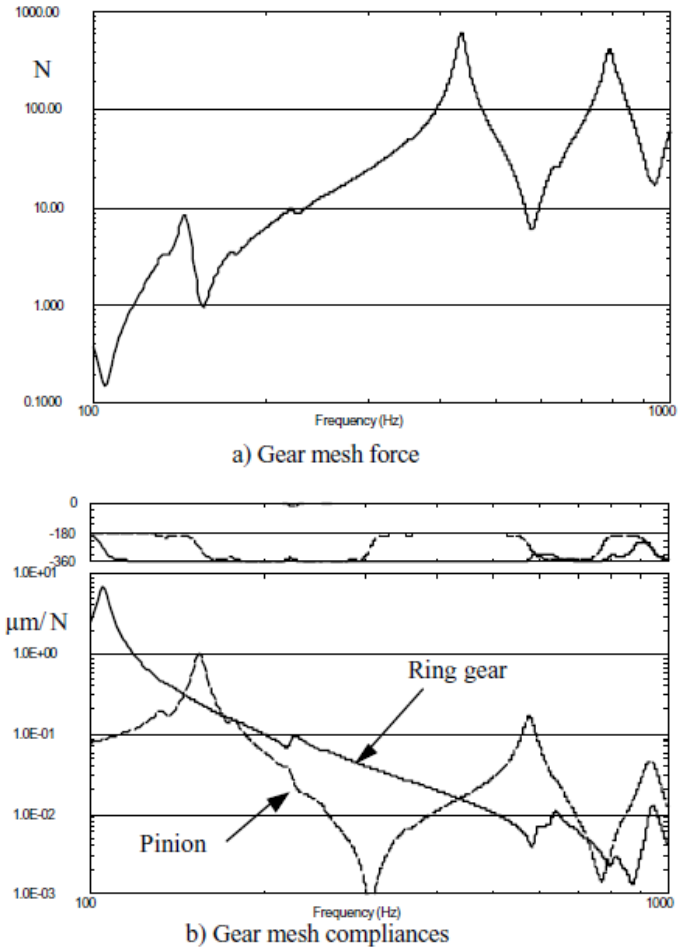

Figure 2.7- Dynamic mesh force and Gear pair compliances per unit transmission error (after Sun et al, 2003)

From the above expression, it can be observed that the mesh force is maximized at the frequencies defined by the intersection points of pinion and ring gear compliance. At these frequencies, the real parts of both compliances are opposite numbers; whereas the remaining imaginary parts are much smaller. Hence, the reciprocal of the summation of the compliances will reach its maxima as illustrated in the top

section of Figure 2.7. The principle of dynamic tuning involves various approaches. Lee and Kocer (2003) formulated an optimization method to reduce the peak amplitudes of mesh force. Their analysis relies on the identification of modal contributions at the resonant frequencies, followed by the determination of modal energy participation of each driveline component. The final step was a parametric analysis of the component design variables so that an improved configuration would

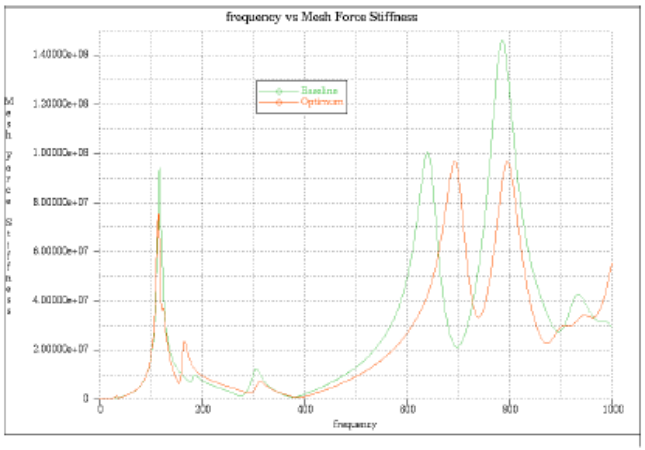

a) Formulation 1

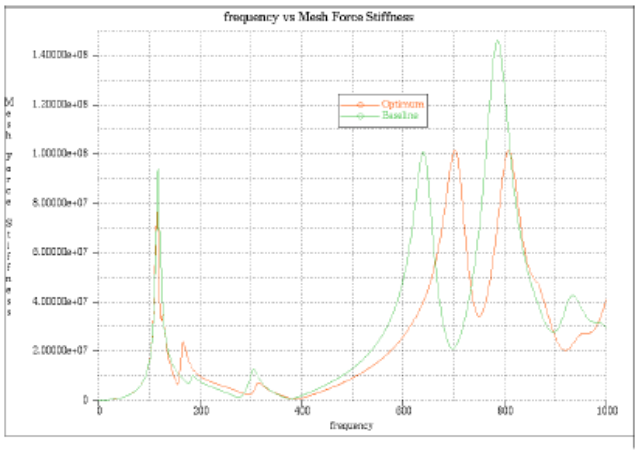

b) Formulation 2

Figure 2.8- Optimized designs towards dynamic mesh force reduction (after Lee and Kocer, (2003)

be created. Nevertheless, even though the dynamic mesh stiffness peaks were reduced, the new peaks were shifted towards a higher frequency range addressing potential new resonance issues. This fact is depicted in Figure 2.8 where the red

curves show the reduced levels of mesh stiffness compared to the green curves depicting the baseline case.

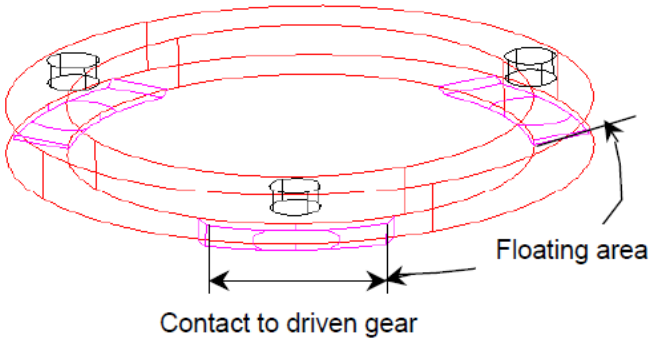

Figure 2.9- Noise reduction ring design (after Miyauchi et al, 2001)

An analysis towards achieving robust axle behaviour in terms of NVH issues was conducted by Sun et al (2003). The study is concentrated on optimizing the mesh force together with its transmissibility towards the rest of the structure. It was shown that a reduction of the ring gear inertia together with a decrease in the torsional stiffness of the pinion side could be favourable into downgrading the dynamic mesh force over certain frequency range intervals. In terms of the force transmissibility the main aim is to ensure that the resonant frequencies of the optimized mesh force do not coincide with bending and lateral resonances of additional driveline components. This is the essence of modal tuning which was presented by Steyer et al (2005). The main task is the avoidance of coalescent modes; sufficient frequency separation needs to be applied so that the response magnification will stay below acceptable levels.

Another method to enhance the above behaviour is by introducing an attachment to the gear member, as suggested by Miyauchi et al (2001). The component shown in Figure 2.9 was called “noise reduction ring” and was connected to the ring gear. Its effect on the generated vibrations was studied both numerically and experimentally. The tuning strategy of the ring local resonant frequency is focused towards the increase of the compliance magnitude at the intersection points. A parallel consequence of the “noise reduction ring” is the creation of high compliance around the region of three nodal modes due to a modal separation effect. This event results

into a further reduction of the mesh force. The combined effect can be observed in Figure 2.10.

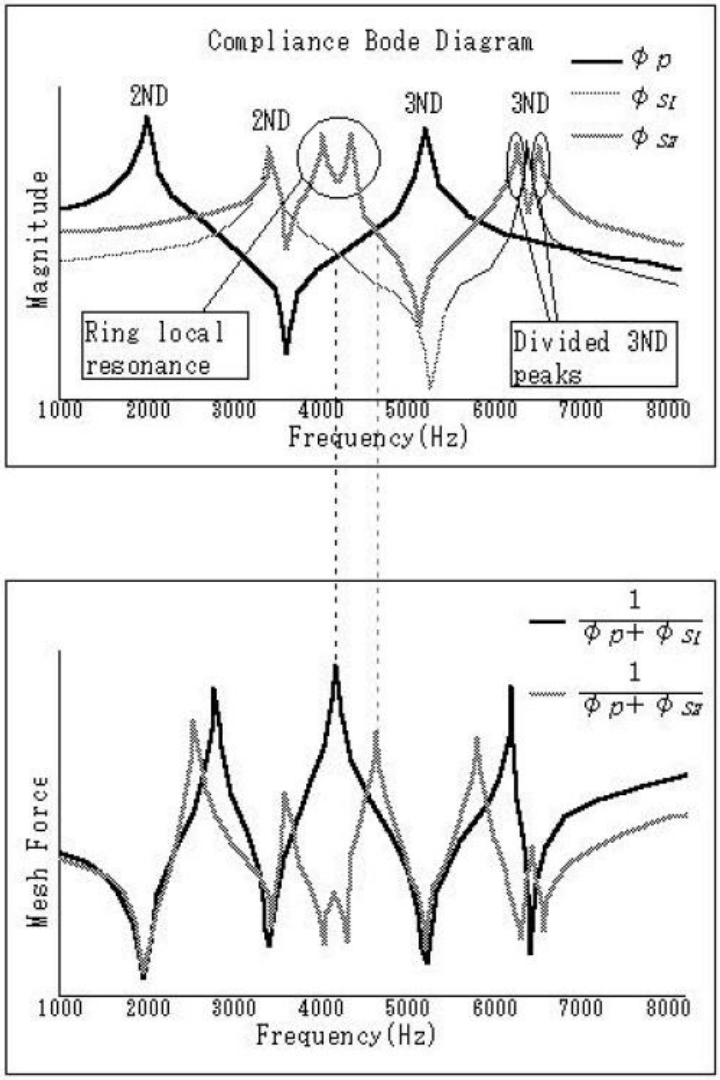

Figure 2.10- The effect of "noise reduction ring" on the compliance and mesh force magnitude (after Miyauchi et al, 2001)

Controlling axle vibrations is also achieved by exploiting the properties of the dynamic vibration absorber; whose principle can be found in vibration textbooks (Rao, 2004). In this case, the natural frequency of the absorber needs to coincide with the excitation frequency. Lee (2007) studied the possibility of attaching a torsional damper to the driveshaft in the form of a slip Yoke damper ring, shown in Figure 2.11. An effective tuning of the damper can split the major frequency peak into two, together with an almost 50% reduction of the maximum amplitude of the

mesh force. Similar effects have been observed by Wani and Singh (2005) when monitoring the pinion nose vibration level.

Figure 2.11- View of slip yoke damper ring (after Lee, 2007)

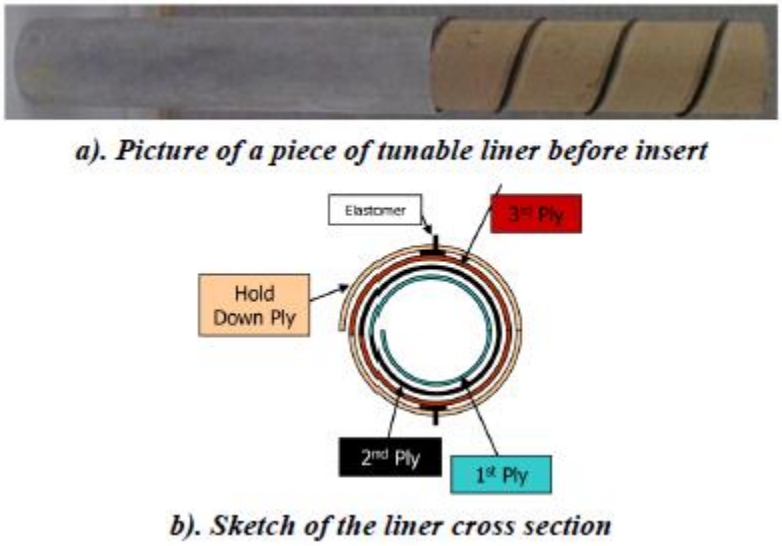

Figure 2.12- View of tunable cardboard liner (after Sun et al, 2011)

Attenuation of driveline vibrations can be accomplished by installing “tuned liners” inside the propshafts, as discussed by Sun et al (2011), shown in Figure 2.12. The latter has been proven to be the most compliant part in the driveline; hence its vibration behaviour is crucial for all NVH issues. The attached component is usually in the form of a cardboard tube and the dynamic tuning is accomplished through a spring element, connecting the absorber to the driveshaft. The desirable tuning frequency is in the range of 300 to 500Hz for axle whine alleviation. The feasibility of the design was examined by Finite Element modelling and testing. It was shown that the attachment increased the damping effect for the bending modes of the

propshafts. Validation at vehicle level confirmed the ability of the tuned liners to control both the driveshaft bending and the axle mesh torsional dynamics. Although tuned cardboard liners can effectively absorb unwanted motions, their efficiency is dependent on the ratio between their mass and the main structure. Applications of the concept in smaller diameter steel propshafts could prove to be problematic.

To summarize, the applied measures towards the reduction of axle noise and vibration can be divided into two major groups; the first involves the improvement of the gear pair manufacturing quality so that the effect of the internal excitation is substantially reduced. The second is related to the dynamic tuning of the system; special care should be taken in the achievement of mode separation in order to reduce the dynamic mesh force, as well as its transmissibility to the rest of the structure. However, if dynamic absorbers are used, the tuning frequency of the attachment must coincide with the resonant frequency. All the presented methods suffer from considerable disadvantages; for instance, manufacturing quality is often optimized and the transmission error is essential as a design variable. Furthermore, mode separation is not always possible due to design limitations whereas the tuned absorbers require the addition of considerable mass to the system (the cost is moderately estimated at £9 per kg of added mass), while their efficiency is only at a narrowband frequency range. Consequently, the efficiency of an additional method is going to be examined in this study; namely the exploitation of the concept of Targeted Energy Transfer (TET).

2.6 - The concept of Targeted Energy Transfer

The concept of Targeted Energy Transfer (TET) is a relatively contemporary aspect in the field of nonlinear dynamics. Theoretical and experimental studies have been published highlighting the importance of this phenomenon in capturing portions of unwanted vibrational energy, hence acting as a passive vibration absorber.

The first studies were focused on impulsively excited systems. An initial theoretical and numerical study of this concept was accomplished by Gendelman et al (2001). Systems comprising of linear and essentially nonlinear parts were considered and it was shown that the vibration energy can be transferred from the linear towards the nonlinear part of the system in an irreversible manner. The latter is termed a

Nonlinear Energy Sink (NES). The necessary condition was a certain energy threshold, able to trigger a 1:1 stable subharmonic orbit of the underlying Hamiltonian system. A following study by Vakakis et al (2003) showed the effect of coupling a non-linear attachment to a linear system of multiple degrees of freedom. It was proven that energy pumping can still be achieved through resonance of the attachment with all the existing modal oscillators. Important conditions are an adequate level of excitation energy and the presence of damping; undamped systems could generate beat phenomena and energy exchange but not in an irreversible form.

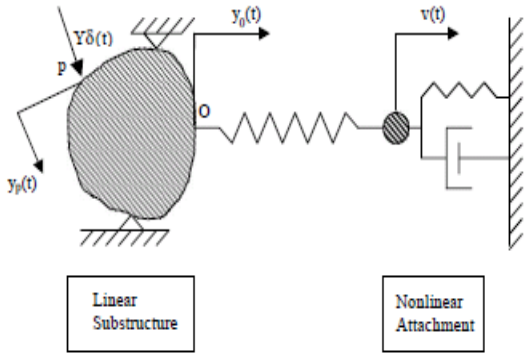

Figure 2.13- Linear substructure and Nonlinear attachment (after Vakakis et al, 2003)

A combined theoretical and experimental work was conducted by Jiag et al (2003). It was demonstrated that an NES can absorb energy from a linear oscillator under steady state conditions. Such an application presents certain advantages, such as the ability of energy absorption over a broadband frequency range rather than the narrow band of a tuned absorber. Further experimental evidence was provided by McFarland et al (2005). In this study the governing mechanisms were identified and correlation with analytical and numerical results was achieved. Effective energy pumping was taking place even with smaller mass ratios and the capability of an NES to resonate and subsequently extract energy from multiple modes of a structure was confirmed.

A practical application of TET was investigated by Lee et al (2007a). In this work a Nonlinear Energy Sink was attached to a two degree of freedom wing model so that aeroelastic instabilities were supressed. Numerically conducted parametric studies

yielded the mechanism behind efficient suppression. The NES initial design characteristics were set based on a rigorous theoretical analysis. Experimental validation was provided by a subsequent study (Lee et al, 2007b).

Based on the above findings, it seems feasible to exploit the benefits of an NES as a vibration absorber in a torsional geared system. The dependence of the natural frequency of the system on the loading conditions (Cheng and Lim, 2004) would require a broadband energy absorbing mechanism.

2.7 -Synopsis

This Chapter gives the background of the aspects that will be covered in the rest of the thesis. In the beginning, vibration issues of the differential unit are bridged to driveline noise. With the assistance of certain assumptions, it is explained how the dynamic analysis of the differential gear pair can reflect the overall behaviour of the driveline. Focus is therefore shifted towards the generation of the mesh force and the source of the excitation, the gear pair itself.

Even though a number of analytical and numerical studies have been reported in literature, there is a tendency to overlook certain important aspects of the dynamic problem. The dynamic transmission error is essentially a non holonomic constraint when a variation of contact radii occurs as a result of the geometric complexity. Current formulations tend to overlook this fact through a set of assumptions, neglecting the contact radii variation inside this constraint. The validity of this approximation was nevertheless not properly documented. There is no reported work retaining the non integrable form of the dynamic transmission error in the dynamic analysis. Such a case needs to be investigated. It is also challenging to study the effect on the perceived periodic solutions and conduct subsequent parametric studies. Furthermore, the operating conditions need to be adjusted accordingly by relating the resisting torque to the angular velocity of the differential unit.

An inclustion of the frictional effects in the dynamic formulation of hypoid gears was also never attempted. Models with constant kinematic and loading conditions exist yielding the magnitude of the friction coefficient. An addition of the friction excitation in the dynamic model would add more depth to the overall analysis, determining the

interdependence between the dynamics and tribology. The above tasks are associated with the novelty of the current study.

The following section covers the dynamic modelling of gear systems. The transition from simple models of spur gears with approximated mesh parameters to the more complicated hypoid transmissions is described. A discussion of the derivation method of the mesh parameters follows. The importance of a tribological consideration is included before moving to the applied measures for alleviating the unwanted vibrational motions. Eventually the concept of TET is discussed as an alternative of the existing measures.

Chapter 3 - Global Dynamics

3.1 - Introduction

The objective of this chapter is to present the theoretical foundation for simulating the torsional dynamics of hypoid transmissions. The fundamental mathematical model is based on a system of coupled harmonic oscillators with stiffness and damping characteristics. Analysis is confined to torsional motions of the gear pairs, neglecting any lateral forces generated from shafts and bearings. The investigation of steady state oscillations requires the inclusion of aspects from drivetrain and vehicle dynamics.

The variables appearing in the equations of motion are explained; they are kinematic, geometric and forcing functions, characterised by periodicity because of the nature of gear teeth contacts. This leads the discussion to the Loaded Tooth Contact Analysis (LTCA). Unlike spur and helical transmissions, mesh sequence and contact properties cannot be derived analytically; hence a numerical simulation of the gear teeth engagement is necessary.

3.2 - Dynamic Modelling

3.2.1 Gear Pair Dynamics

A wide number of studies on the dynamics of parallel axis gears are available in literature. For the case of spur gears, torsional vibrations can be uncoupled from the other modes of the system resulting to a single equation of motion (Kahraman and Singh, 1990). A similar approach was followed by Wang et al. (2007), (with certain simplifications) when proposing a model for hypoid transmissions. However, this approximation will be proven to lead into false conclusions; hence its adoption will be avoided in this study.

The mechanical model of the hypoid gear pair studied in the current work is shown in **Error! Reference source not found.**, where only the torsional vibrations are being considered. It is a common practice to model the teeth contact as if it is concentrated on a single point (Ozguven and Houser, 1988). Thus, the gear mesh is represented

by two elements of negligible mass; a spring of stiffness (k_m) and a damper (c_m) deployed along the line of action. The same approach has been realised in most torsional gearing models (Blankenship and Singh, 1995; Theodossiades and Natsiavas, 2000; Wang et al., 2007). The gear set members are considered as a couple of rigid rotating disks.

For the case of spur gears, due to the involute profile, the contact force in every flank has the same direction; along the line of action defined by the base radii (Dudley and Townsend, 1991). The mesh point moves on this line regardless of the external factors. However, the geometric complication of hypoid transmissions, forbids the definition of a base radius. The contact pattern is elliptical and the contact load is distributed on a finite area rather than a line (Kolivand and Kahraman, 2009). Therefore, a theoretical mesh point needs to be defined to account for the effect of all the load distribution across the gear flanks. This point is not essentially lying on a line, implying that the line of action will be constantly changing, defining a couple of hypothetical base radii which will be referred as contact radii Figure 3.1. The pinion angular displacement (φ_p) is used as a reference variable to define the modulation of all the contact properties.

The contribution of various misalignments and geometrical errors are considered by an input displacement function ($e(\varphi_p)$) exerted in the direction of mesh, namely the kinematic transmission error.

The free body diagram can be seen in Figure 3.2. The two bodies are assumed to be rigid solids. The centres of rotation are not allowed to move laterally, since the shafts and the bearings supporting the wheels are assumed to be rigid. The motion of each gear is described by its rotation; the latter can be regarded as a composition of the rigid body angular displacement plus a perturbation component expressing the torsional vibration motion. In other words:

$$\varphi_i = \omega_i t + \phi_i(t) \quad , i = p, g$$

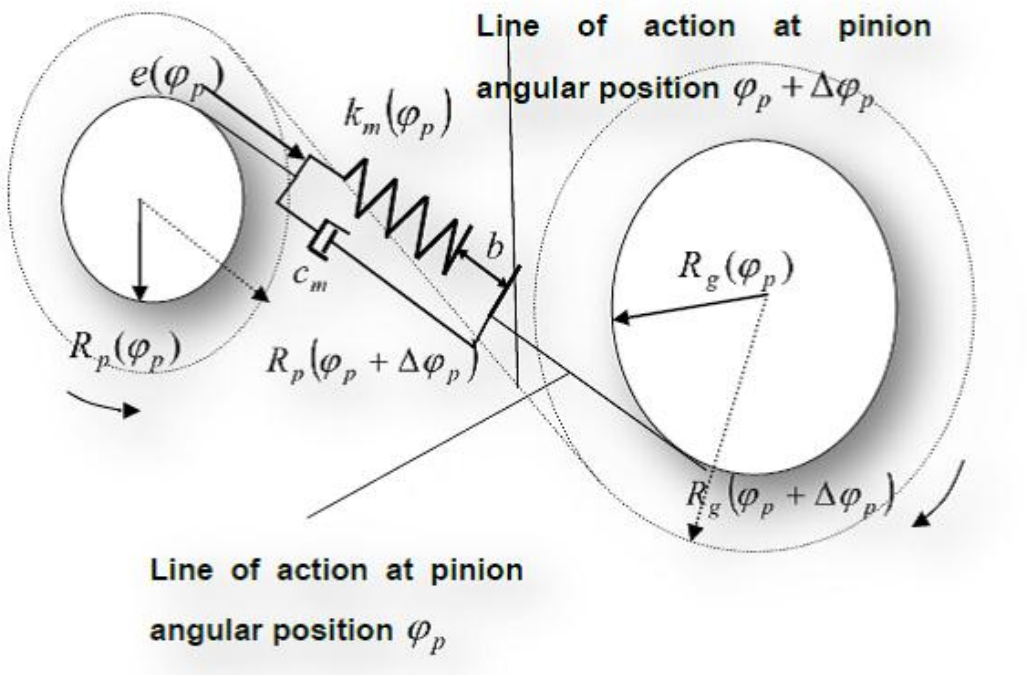

Figure 3.1- General hypoid gear pair mesh model

where ω_p and ω_g are the constant angular velocities of the rigid bodies. Subscripts *p* and *g* will be appointed to the pinion and gear, respectively, from now on.

The meshing stiffness accounts for the internal reaction force generated in the system. It depends on the number and position of the mating flanks and is a periodic function of the relative angular position of the gears. The same applies to the kinematic (manufactured) transmission error which describes the profile inaccuracies.

Taking into account that the mean angular velocities of the gears remain constant, the previous parameters may also be expressed as periodic functions of the pinion angle. By neglecting the tooth variations, the fundamental frequency of both quantities is equal to the gear meshing frequency:

$$\omega_{mesh} = N_p \omega_p = N_g \omega_g$$

where N_p and N_g represent the number of teeth of the pinion and gear, respectively. The above consideration allows the expression of mesh stiffness and static transmission error in a Fourier series (angular) form:

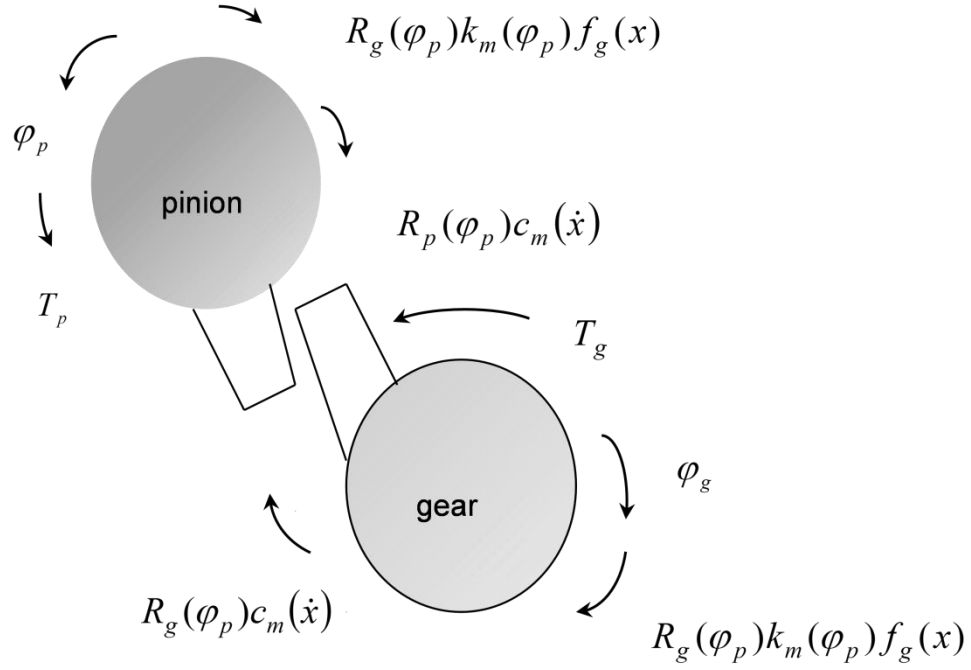

Figure 3.2- Free body diagram of the hypoid gear pair

$$k_m(\varphi_p) = k_0 + \sum_{i=1}^{n}[k_{ci}\cos(iN\varphi_p) + k_{si}\sin(iN\varphi_p)] \qquad \textbf{(3.1)}$$

$$e(\varphi_p) = e_0 + \sum_{i=1}^{n}[e_{ci}\cos(iN\varphi_p) + e_{si}\sin(iN\varphi_p)] \qquad \textbf{(3.2)}$$

The harmonic nature of both quantities introduces harmonic excitations in the system, triggering resonance issues.

The equations of motion with respect to the angular rotations (φ_p) and (φ_g) can be written in the following form:

$$I_p\ddot{\varphi}_p + R_p(\varphi_p)c_m(\dot{x}) + R_p(\varphi_p)k_m(\varphi_p)f_g(x) = T_p \qquad \textbf{(3.3)}$$

$$I_g\ddot{\varphi}_g + R_g(\varphi_p)c_m(\dot{x}) + R_g(\varphi_p)k_m(\varphi_p)f_g(x) = -T_g \qquad \textbf{(3.4)}$$

where terms ($c_m(\dot{x})$) and ($k_m(t)\,f_g(x)$) express the damping and elastic forces developed during gear meshing. The mesh stiffness is represented by the term ($k_m(\varphi_p)$), whereas (c_m) is the structural damping coefficient. Variable x is a function of the rotational angles ($\varphi_p(t)$), ($\varphi_g(t)$), the contact radii (R_p, R_g) and the static transmission error input ($e(\varphi_p)$):

$$x(t) = \int_{t_0}^{t} R_p(\varphi_p)d\varphi_p - \int_{t_0}^{t} R_g(\varphi_p)d\varphi_g - e(\varphi_p) \qquad \textbf{(3.5)}$$

Parameters (T_p) and (T_g) represent the externally applied torques at the pinion and gear respectively, whereas (I_p, I_g) are the mass moments of inertia of the two sides of the differential gear pair. Function ($f_g(x)$) defines the effect of backlash nonlinearity in the deflection between the mating teeth. If the quantity ($2b$) represents the total gear normal backlash, then:

$$f_g(x) = \begin{cases} x-b, & x \geq b \\ 0, & -b < x < b \\ x+b, & x \leq -b \end{cases} \qquad \textbf{(3.6)}$$

Therefore, gear backlash introduces strong nonlinearities to the dynamic response. This may lead to regions of multiple solutions and chaotic attractors, depending on the system characteristics (Theodossiades and Natsiavas, 2001a).

3.2.2 Vehicle and Drivetrain Dynamics

In the previous section, the equations of motion of the mathematical model were presented. However, no particular discussion was made over the external torque

excitations applied to the system and their relation. In order to understand their dependence and extend the mathematical model to realistic conditions, some elements of vehicle and drivetrain dynamics need to be taken into account.

One of the objectives of the present study is the numerical identification and evaluation of axle whine. This form of drivetrain noise has been shown to occur during driving (Lee et al., 2005) or coasting conditions (Choi et al., 2011), namely when the axle dynamic response deviates from an equilibrium. Therefore, it is of great importance to define the necessary conditions leading to all possible equilibrium positions which the system is able to reach.

An equilibrium point implies a condition when the external excitations balance each other so that the system settles to steady state response. In any other case the system will be accelerated infinitely, resulting to unbounded solutions. When considering the previous gear mesh models in literature, some comments can be made. At spur gear models, the transmission ratio is always constant, hence input and output torque are related with the ratio of the base radii:

$$T_p = \frac{R_{bp}}{R_{bg}} T_g \qquad \textbf{(3.7)}$$

Nonetheless, in hypoid transmissions the mesh vector is shifting, hence the transmission ratio follows the variation of contact radii (R_p) and (R_g) (equations (3.3), (3.4)). As a result, by using a similar expression to equation (3.7), input and output torque values cannot balance each other, causing the system to settle to a solution far away from an initial input condition. A numerical solution shows that the system decelerates far from its initial velocity, implying that such a relationship is incompatible with the physics of the system. Therefore, an alternative expression needs to be sought by incorporating the dynamics of the drivetrain, as well as the vehicle itself.

The equation governing the equilibrium between drive and resistance forces at the drivetrain system is derived from the energy conservation principle. In specific, the

input force supplied by the engine must be equal to the total resistance requirement at the wheels of the vehicle (Bosch, 2004):

$$T_e \frac{i_{tot}}{r} \eta_{tot} = mgf\cos a + mg\sin a + ema + c_w A \frac{\rho}{2} \upsilon^2 \qquad \textbf{(3.8)}$$

The left hand side term of the above equation denotes the input force at the rear axle. The right hand side is separated into four types of resistance; rolling, ascent, acceleration and aerodynamic. The various terms appearing inside the equation are related to the vehicle properties and traction conditions. They are presented in Table 3.1.

Table 3.1- Vehicle properties and operating conditions

Variable	Physical Meaning
T_e	engine torque
i_{tot}	total conversion ratio
r	dynamic radius of the tyre
η_{tot}	total mechanical efficiency
m	vehicle mass
g	gravitational acceleration
f	coefficient of rolling resistance
a	ascent angle
a	acceleration of the vehicle
c_w	aerodynamic drag coefficient
A	frontal area of the vehicle
ρ	air density
υ	vehicle speed

Parameter e is the rotational inertial coefficient given by the following expression (Bosch, 2004):

$$e = 1 + \frac{J_R + {i_h}^2 J_A + {i_h}^2 {i_G}^2 J_m}{m r^2} \qquad \textbf{(3.9)}$$

The mass moment of inertia of the wheels is denoted by (J_R), whereas the drivetrain and engine by (J_A) and (J_m), respectively. Conversion ratios (i_h) and (i_G) refer to the final drive and transmission.

When the mean vehicle speed is constant, the acceleration term in equation (3.8) can be dropped and the latter yields the necessary condition for achieving a stable equilibrium condition. The mean engine torque requirement is defined if the mean vehicle speed of the specific equilibrium point is substituted therein. Therefore, due to the aerodynamic drag, a certain value of the vehicle velocity υ_0 defines a unique equilibrium point. For a dynamic analysis, the input engine torque consists of a constant term (T_{e0}) yielded by equation (3.8) and an engine order perturbation term. The resistance torque is also time variant due to the kinematic relationship relating the angular velocity of the differential to the vehicle speed: $\upsilon = r\dot{\varphi}_g$. Looking back at equations (3.3) and (3.4), the properties of the engine and the differential unit need to be substituted for the ones of the gear pair.

This is in accordance to the physical concept of the system. At a specific throttle position, the mean engine delivered torque is constant. At the same time, the vehicle moves with a constant mean velocity and the differential rotates with the corresponding angular speed, which are unique for every equilibrium point. Nevertheless, the resistive torque follows the angular velocity fluctuation while its mean value remains fixed based on the equilibrium requirements.

Alternatively, the equilibrium can be violated after a certain time step (t_c), for instance under the occurrence of coasting conditions. In this case, the numerical investigation should be split into two periods; the first for $t < t_c$ and the second for $t > t_c$. During steady state, the mean input torque will be equal to (T_{e0}) whereas in

the transient case its value will depend on whether the system is accelerating or decelerating. Figure 3.3 shows an indication of the input torque variation with respect to time, depending on the driving conditions, where the input torque is assumed to alter linearly outside the equilibrium. The transient phase needs to be analysed by applying the complete form of equation (3.8), including the acceleration term. In the same manner, the angular acceleration of the drivetrain will be connected to the vehicle acceleration with the expression: $\mathrm{a} = r\ddot{\varphi}_g$.

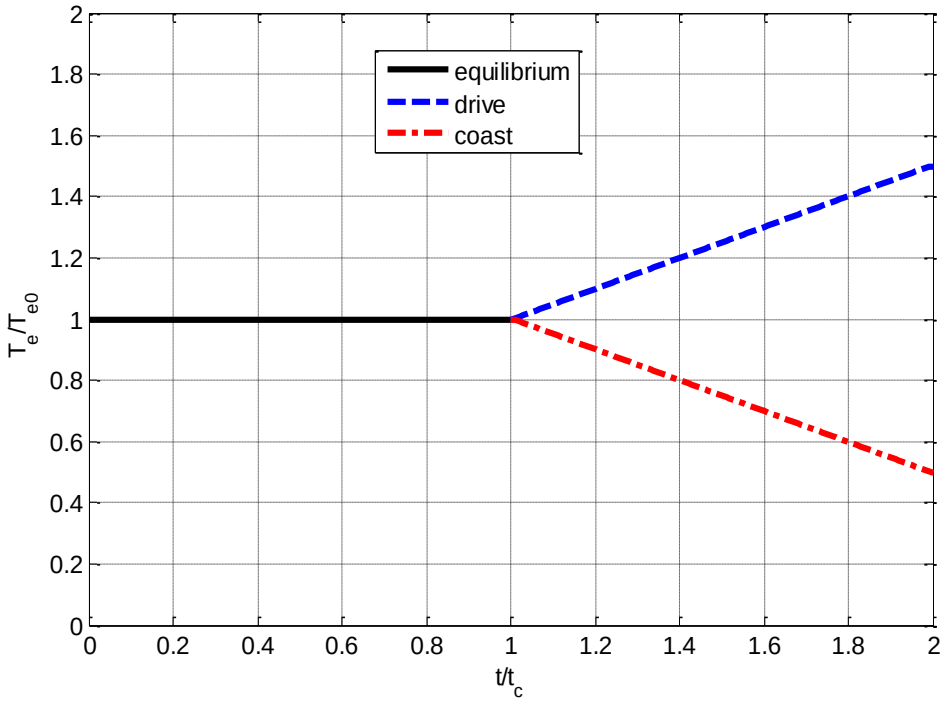

Figure 3.3- Torque variation for Equilibrium, Drive and Coasting conditions

The inclusion of vehicle and drivetrain dynamics in the equations of motion is crucial for the accurate representation of the system, since the mathematical formulation now reflects the operating conditions of the vehicle.

3.3 - Formulation of Gear Mesh

Equations (3.1) to (3.9) describe the dynamics of the drivetrain system. As already mentioned, moments of inertia and the applied torques appearing at equations (3.3), (3.4) need to be replaced with the ones of the whole powertrain

system. This is due to the fact that the main point of concern is the dynamic response of the gear pair which generates the noise emission mechanism.

In reality, gear mesh is deployed on a contact area of multiple flanks. However, the dynamic model presented in the previous sections assumes the gear mesh to be concentrated on a single point. This means that the correspondence between the real contact zone and the mesh parameters present in the dynamic model needs to be established. Hence, from the gear pair design characteristics and through a mesh simulation, contact radii, mesh stiffness and kinematic transmission error need to be defined.

Before analysing the gear mesh, it is necessary to define a set of coordinate systems. Their formation is illustrated in Figure 3.4. Each coordinate system denoted by (S_i) is represented by a set of axes (x_i, y_i and z_i). The global coordinate system (S_f) is identical to (S_g), which is attached to the crown gear wheel. The third one (S_p) is connected to the pinion body. Similar notation has been followed by other researchers (Kiyono et al, 1981; Cheng and Lim, 2003; Wang et al, 2007).

3.3.1 Kinematic Analysis

Contact radii (R_p) and (R_g) affect crucially the dynamics of the system. They represent the moment arm of the meshing force (equations (3.3), (3.4)) and simultaneously define the relative displacement of the gears (equation (3.5)). Before attempting their calculation, it is important to explain their relation to the geometry of the gear configuration. A kinematic analysis will reveal this.

The modelling approach discussed in the previous section (Figure 3.1) involves a continuous variation in the orientation of the line of action. At an arbitrary time snapshot t_i, the linear velocity of the pinion along the line of action will be:

$$v_p = \vec{n} \cdot \left(\vec{\omega}_p \times \vec{r}_M \right) \qquad \textbf{(3.10)}$$

with $\vec{n} = [n_x \quad n_y \quad n_z]^T$ being the instantaneous unit vector in the direction of the contact force, $\vec{\omega}_p = \begin{bmatrix} 0 & \omega_p & 0 \end{bmatrix}^T$ the angular velocity of the pinion and $\vec{r}_M = [x_M \quad y_M \quad z_M]^T$ the position vector of the theoretical mesh point M (Figure 3.5). All vectors are defined with respect to the pinion coordinate system. If all vectors are substituted in equation (3.10), the following expression can be derived:

$$v_p = \omega_p \vec{n}^{(S_p)} \left(\vec{j}_p \times \vec{r}_M{}^{(S_p)} \right) = \omega_p R_p = \dot{\theta}_p R_p \qquad \textbf{(3.11)}$$

with ($\vec{j}_p$) being the unit vector along the rotational direction (y_p) of the pinion. Therefore:

$$R_p = \vec{n}^{(S_p)} \left(\vec{j}_p \times \vec{r}_M{}^{(S_p)} \right) = n_x{}^{(S_p)} z_M{}^{(S_p)} - n_z{}^{(S_p)} x_M{}^{(S_p)} \qquad \textbf{(3.12)}$$

Similar expressions can be derived for the gear, assuming that the corresponding quantities are expressed with respect to coordinate system, S_g:

$$v_g = \omega_g \vec{n}^{(S_g)} \left(\vec{j}_g \times \vec{r}_M{}^{(S_g)} \right) = \omega_g R_g = \dot{\theta}_g R_g \qquad \textbf{(3.13)}$$

$$R_g = \vec{n}^{(S_g)} \left(\vec{j}_g \times \vec{r}_M{}^{(S_g)} \right) = n_x{}^{(S_g)} z_M{}^{(S_g)} - n_z{}^{(S_g)} x_M{}^{(S_g)} \qquad \textbf{(3.14)}$$

The kinematic analogy of the hypoid contact radius with spur or helical gear base radius is profound. It yields the approaching velocity of the wheels along the line of action if multiplied to their angular speed. The main difference is its variation; it follows the evolution of mesh position vector $\vec{r}_M$ and mesh force vector $\vec{n}$. Gear mesh will engage into a curvilinear path instead of a straight line.

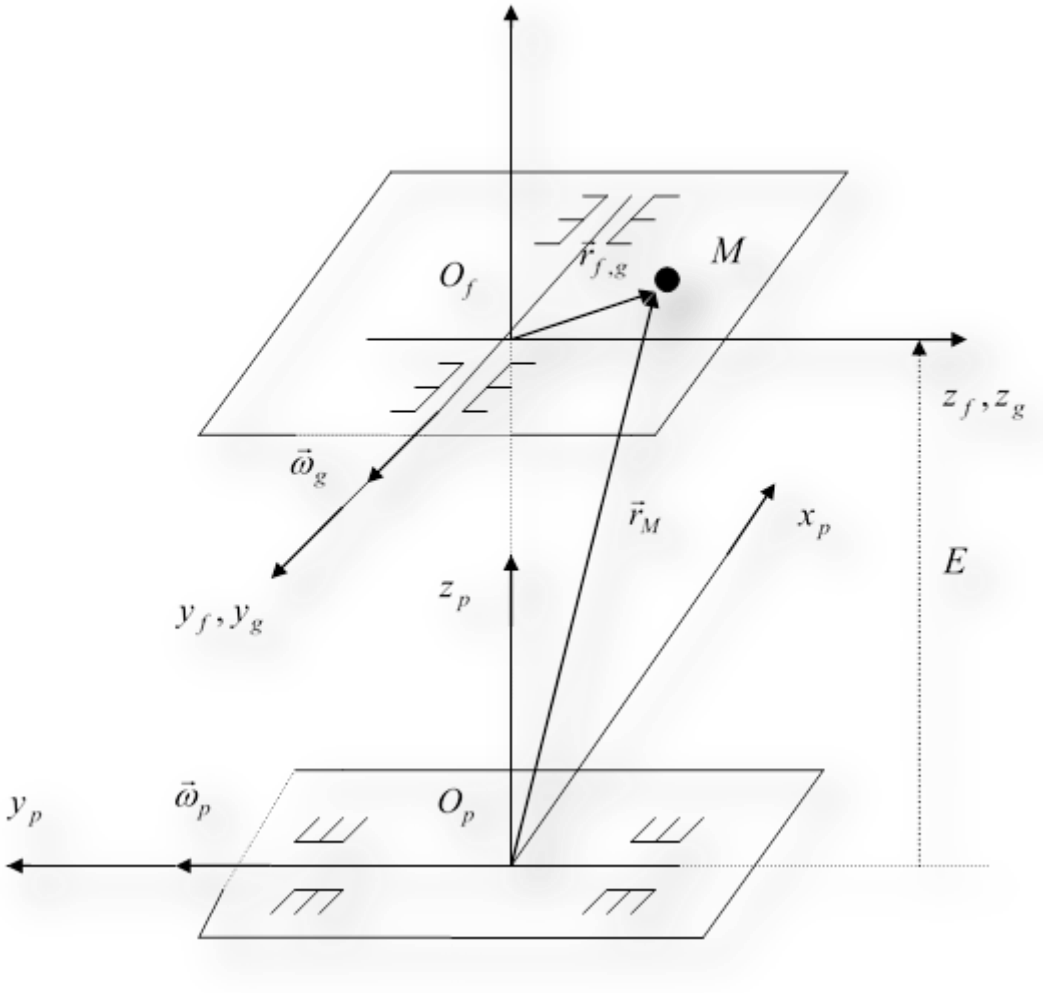

Figure 3.4- Global and Local Coordinate Systems

Looking back to the teeth mesh model of Figure 3.1, the infinitesimal displacement $d\delta$ between the two bodies during a time interval dt in the mesh direction will be:

$$d\delta = v_p dt - v_g dt = R_p \dot{\theta}_p dt - R_g \dot{\theta}_g dt \qquad \textbf{(3.15)}$$

The overall total displacement at a time instant (t) can be derived by integrating equation $d\delta = v_p dt - v_g dt = R_p \dot{\theta}_p dt - R_g \dot{\theta}_g dt$ (3.15) with respect to time:

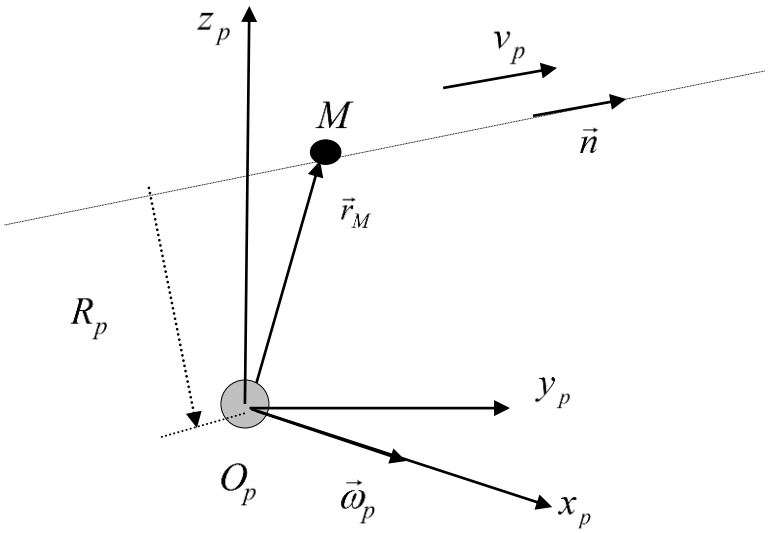

Figure 3.5- Derivation of linear velocity along the line of action

$$\delta(t) = \int_{t_0}^{t} R_p \dot{\theta}_p dt - \int_{t_0}^{t} R_g \dot{\theta}_g dt \qquad \textbf{(3.16)}$$

where (t_0) is the initial time of reference. This function is the expression of the dynamic transmission error for hypoid gear pairs. It can be used for spur gears as well, however in that case the radii R_p and R_g are independent of time. In this case:

$$\delta(t) = R_p \theta_p - R_g \theta_g \qquad \textbf{(3.17)}$$

This expression describes the dynamic transmission error in parallel axis systems. It leads to the reduction of the order of the system to a single degree of freedom by decoupling the rigid body rotations and revealing only the relative torsion.

The same formula was applied by Wang et al. (2007), followed by a reduction of the rank of the system to one degree of freedom, on the basis that the derivatives of the

contact radii with respect to time are trivial ($\dot{R}_p = \ddot{R}_p \cong 0$, $\dot{R}_g = \ddot{R}_g \cong 0$). Nevertheless, this approximation is not realistic; even though their variation with respect to pinion angle may be small, the corresponding time derivatives become significant at higher angular velocities. This approach is, therefore, insufficient to reveal the real dynamic behaviour of the system. Moreover, if the aforementioned approximation is adopted, the definition of the dynamic transmission error by equation (3.17) will yield unbounded solutions. Because of the above, in this study the dynamic transmission error is defined by equation (3.16); in a form of a time integral, in contrast to previous studies. This method results essentially into a two degree of freedom system which will be the foundation for conducting a tribological analysis. Numerical evidence on the above claims will be given in the following chapters.

In essence, contact radii in hypoid gear mesh are varying quantities and their calculation is associated with the determination of mesh point (M) and mesh force direction vector $\vec{n}$ as suggested by equations (3.12) and (3.14). The same equations have been introduced by Cheng and Lim (2003) and were also adopted by Wang et al (2007). From Figure 3.5, it can be seen that any point on the instantaneous line of action of the mesh force will produce the same result for the contact radii. The important value is the distance between the line of action and the axis of rotation, which is confirmed by the cross product present in equations (3.12) and (3.14). Hence, determination of the line of action is sufficient for the calculation of the contact radii. The geometric complexity necessitates the implementation of numerical techniques for the derivation of the necessary mesh quantities.

3.3.2 Load distribution and contact geometry

It was shown that the calculation of the contact radii is associated to the contact geometry; the orientation of the contact force (unit vector $\vec{n}$), as well as its line of action (locus of mesh points M) need to be defined. Additionally the equivalent stiffness of the meshing teeth as well as the kinematic transmission error is required for predicting the dynamic response.

A rigid body representation of the pinion under quasi-static equilibrium is depicted in

Figure 3.6, where the gear is assumed to be fixed and only the pinion is free to rotate. The pinion gear reaches an equilibrium position through the balance of the externally applied torque (T_p) and elastic reaction forces ($F_{c,i}$) exerted by the crown gear due to the contact of the mating flanks. The determination of the total reaction force is the first step required for the solution of the dynamic model. The line of action and the direction of the contact force yield the contact radii (eq. (3.12) and (3.14)). Furthermore, its magnitude combined with the angular deflection of the rigid body will lead to the calculation of the mesh stiffness.

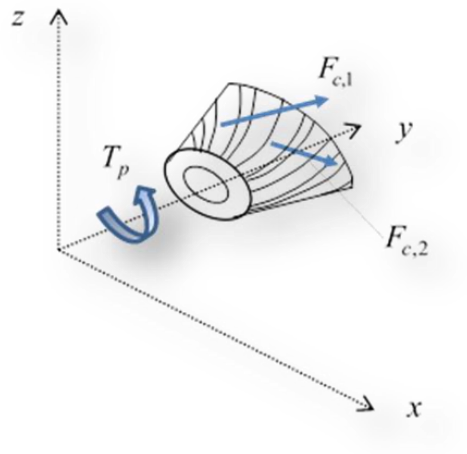

Figure 3.6- The pinion under quasi-static equilibrium

Although methods for generating the contact zone (Litvin and Fuentes, 2004) and FEA models predicting the loaded deflection (Gosselin et al, 1995; Simon, 2000) are present in literature, sometimes the arising equations are too complex to be solved analytically. Therefore, it is necessary to employ a fully numerical simulation of the gear mesh known as Loaded Tooth Contact Analysis (LTCA).

An efficient numerical tool in analysing hypoid gear mesh is CALYX (Vijayakar, 1998), a commercial software conducting three dimensional LTCA. If the gear pair design data is imported in the program, CALYX is able to provide an accurate representation of the mesh sequence quasi-statically. Calculations are made by a

combination of a surface integral method together with Finite Element Analysis; in this way the derivation of the actual compliances accounting for Hertzian contact, as well as bending and torsion of the tooth is possible (Vijayakar, 1991). The gear pair characteristics on which the analysis is based are shown in Table 3.1. The output of LTCA renders the contact zone properties between the mating flanks. For instance, Figure 3.7 shows the distribution of the contact pressure on the meshing teeth.

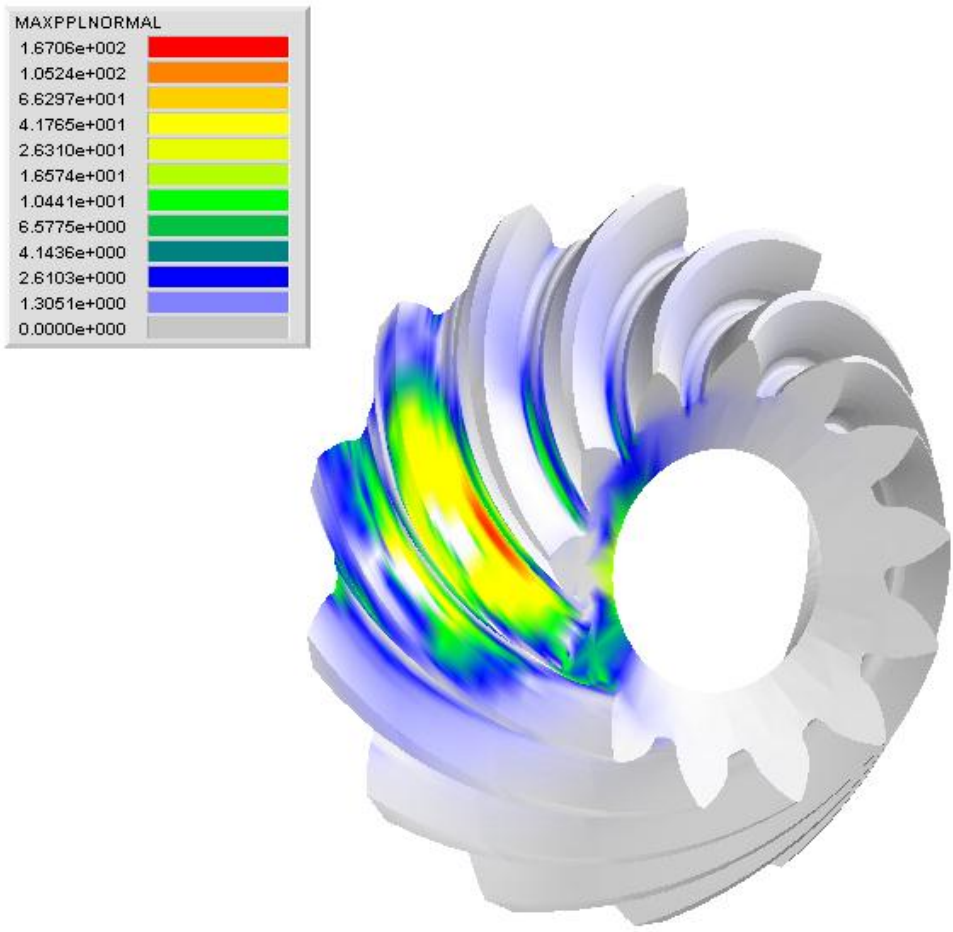

Figure 3.7- Distribution of contact pressure (N/mm^2) on the pinion flanks (LTCA by CALYX)

The objective of LTCA, as already mentioned, is to calculate the total mesh force. Numerical output is attributed to the individual segments of the contact zone; a number of cells are forming the computational grid. The important data pieces entail their position vector ($\vec{r}_i$) and surface normal vector ($\vec{n}_i$), as well as the applied load w_i. The force applied on a contact cell can be expressed as $\vec{f}_i = w_i \vec{n}_i$. Hence, a

system of forces $\vec{f}_1, \vec{f}_2, \vec{f}_3 \ldots, \vec{f}_N$ applied at discrete points $\vec{r}_1, \vec{r}_2, \vec{r}_3, \ldots, \vec{r}_N$ is obtained. This is in general a system of non-concurrent, non-coplanar forces acting on a rigid body. Definition of the resultant force will yield the equivalent mesh point.

In Statics (Riley, Sturges and Morris, 1995), two different force systems are considered equivalent if they produce the same external effect when applied to a rigid body. In this way, a general force system consisting of various forces acting on different positions can be resolved into a resultant force ($\vec{F}$) and a couple, ($\vec{C}$). The resultant $(\vec{F}, \vec{C})$ of the system $\vec{f}_1, \vec{f}_2, \vec{f}_3 \ldots, \vec{f}_N$ can be determined if each force of the system is resolved into an equal parallel force through an arbitrary chosen point (for simplicity at the origin of the fixed coordinate system) and a couple, ($\vec{c}_i$) (Figure 3.8). Thus the original system will be replaced by two systems:

a) a system of non-coplanar, concurrent forces through the origin O with the same magnitude and direction as the forces of the initial system

b) a system of non-coplanar couples

The resultant of the concurrent force system is a force through the origin O:

$$\vec{F} = \vec{F}_x + \vec{F}_y + \vec{F}_z = F_x \vec{i} + F_y \vec{j} + F_z \vec{k} = F \cdot \vec{n} \qquad \textbf{(3.18)}$$

With:

$$F_x = \sum f_{ix},\ F_y = \sum f_{iy},\ F_z = \sum f_{iz} \quad \textbf{(3.19)}$$

$$F = \left|\vec{F}\right| = \sqrt{\left(\sum f_{ix}\right)^2 + \left(\sum f_{iy}\right)^2 + \left(\sum f_{iz}\right)^2} \quad \textbf{(3.20)}$$

$$\vec{n} = \cos\theta_x \vec{i} + \cos\theta_y \vec{j} + \cos\theta_z \vec{k} \quad \textbf{(3.21)}$$

$$\cos\theta_x = \frac{\sum f_{ix}}{\left|\vec{F}\right|}, \cos\theta_y = \frac{\sum f_{iy}}{\left|\vec{F}\right|}, \cos\theta_z = \frac{\sum f_{iz}}{\left|\vec{F}\right|} \quad \textbf{(3.22)}$$

Each force ($\vec{f}_i$) applied at a contact cell i will introduce a couple ($\vec{c}_i$) at the origin O of the global coordinate system when transferred at that point. This couple will have the same moment as the moment of the original force about point O (Figure 3.8). This is expressed by:

$$\vec{c}_i = \vec{r}_i \times \vec{f}_i \quad \textbf{(3.23)}$$

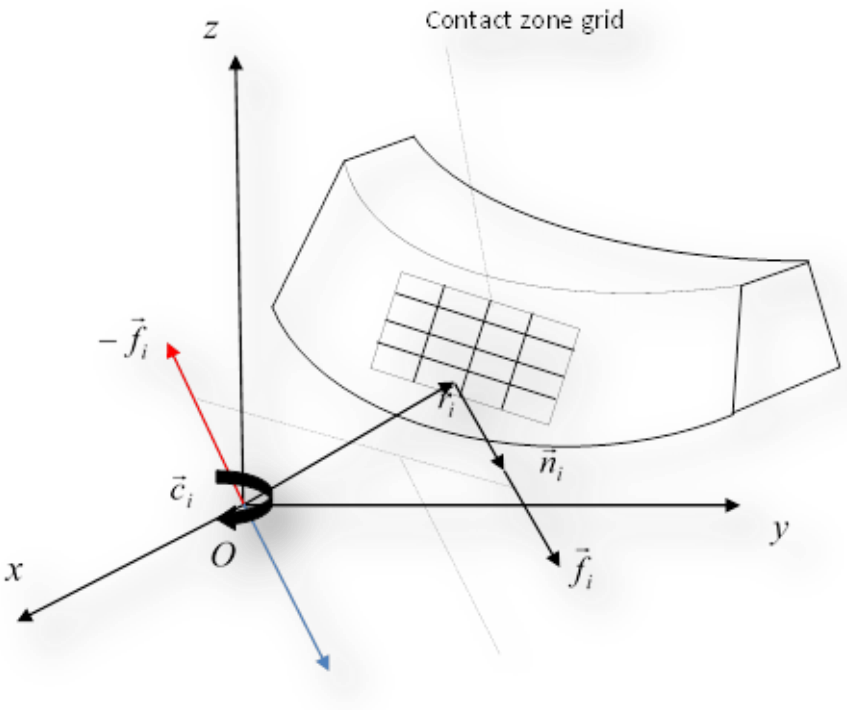

Figure 3.8- Determination of the equipollent forcing system. Each force is equivalent to a parallel force and a couple with respect to a reference point

The total moment induced by all the couples will be:

$$\vec{C} = \vec{C}_x + \vec{C}_y + \vec{C}_z = C_x\vec{i} + C_y\vec{j} + C_z\vec{k} = C \cdot \vec{e} \quad \textbf{(3.24)}$$

With:

$$C_x = \sum c_{ix} = \sum (f_{iz}r_{iy} - f_{iy}r_{iz}) \quad \textbf{(3.25)}$$

$$C_y = \sum c_{iy} = \sum (-f_{iz}r_{ix} + f_{ix}r_{iz}) \quad \textbf{(3.26)}$$

$$C_z = \sum c_{iz} = \sum (f_{iy}r_{ix} - f_{ix}r_{iy}) \quad \textbf{(3.27)}$$

$$C = \left|\vec{C}\right| = \sqrt{\left(\sum c_{ix}\right)^2 + \left(\sum c_{iy}\right)^2 + \left(\sum c_{iz}\right)^2} \quad \textbf{(3.28)}$$

$$\vec{e} = \cos\psi_x\vec{i} + \cos\psi_y\vec{j} + \cos\psi_z\vec{k} \quad \textbf{(3.29)}$$

$$\cos\psi_x = \frac{\sum c_{ix}}{\left|\vec{C}\right|}, \cos\psi_y = \frac{\sum c_{iy}}{\left|\vec{C}\right|}, \cos\psi_z = \frac{\sum c_{iz}}{\left|\vec{C}\right|} \quad \textbf{(3.30)}$$

Table 3.2- Gear pair parameters and machine/cutter settings (Gleason face hobbed gear set)

Pinion parameters:	
Number of pinion teeth	13
Pinion face width (mm)	33.851
Pinion face angle (deg)	29.056
Pinion pitch angle (deg)	29.056
Pinion root angle (deg)	29.056
Pinion spiral angle (deg)	45.989
Pinion pitch apex (mm)	-9.085

Pinion face apex (mm)	1.368
Pinion Outer cone distance (mm)	83.084
Pinion offset (mm)	24.000
Pinion hand	Right

Gear parameters:	
Number of gear teeth	36
Gear face width (mm)	29.999
Gear face angle (deg)	59.653
Gear pitch angle (deg)	59.653
Gear root angle (deg)	59.653
Gear spiral angle (deg)	27.601
Gear pitch apex (mm)	8.987
Gear face apex (mm)	10.948
Gear Outer cone distance (mm)	95.598
Gear offset (mm)	24

Pinion machine and cutter parameters:	
Inside cutter blade angle (IB) (deg)	21.529
Outside cutter blade angle (OB) (deg)	16.743
Machine center to back (mm)	-0.288

Basic swivel angle (deg)	-32.865
Basic cradle angle (deg)	64.433
Tilt angle	31.736
Sliding base (mm)	20.647
Ratio of roll	2.762
Blank offset (mm)	23.908
Machine root angle (deg)	0.202
Cutter point radius (mm)	63.743
Radial setting (mm)	86.983

Gear machine and cutter parameters:	
Machine root angle (deg)	59.653
Machine center to back (mm)	7.026
Horizontal setting (mm)	66.650
Vertical setting (mm)	62.642
Inside cutter blade angle (deg)	22.436
Outside cutter blade angle (deg)	15.815
Cutter point radius (mm)	64.185

By implementing the above methodology, the initial system $\vec{f}_1, \vec{f}_2, \vec{f}_3 \ldots, \vec{f}_n$ coincides with a resultant force and a couple $(\vec{F}, \vec{C})$ drawn at the origin O of the

global coordinate system. According to the theory of equipollent systems, when the couple ($\vec{C}$) is perpendicular to the resultant force ($\vec{F}$), the two can be combined to form a single force ($\vec{F}$) whose line of action is at a distance $d = C/F$ from point O in a direction that makes the moment of ($\vec{F}$) the same as that of ($\vec{C}$). Indeed, one can prove that in the studied case, at every angular position of a meshing cycle $\vec{n} \cdot \vec{e} = 0$. If the resultant force is applied at a point $M(x_m, y_m, z_m)$, then the cross product of theoretical mesh point with the resultant force must be equal to the total moment applied at the body. Hence:

$$\vec{r}_{M/O} \times \vec{F} = \vec{C}$$

or,

$$\begin{vmatrix} \vec{i} & \vec{j} & \vec{k} \\ x_m & y_m & z_m \\ F_x & F_y & F_z \end{vmatrix} = \begin{Bmatrix} C_x \\ C_y \\ C_z \end{Bmatrix}$$

which finally leads to the following system of linear equations:

$$\left.\begin{aligned} F_z y_m - F_y z_m &= C_x \\ -F_z x_m + F_x z_m &= C_y \\ F_y x_m - F_x y_m &= C_z \end{aligned}\right\} \qquad \textbf{(3.31)}$$

The above system is in the form $A \cdot X = B$ with:

$$A=\begin{bmatrix} 0 & F_z & -F_y \\ -F_z & 0 & F_x \\ F_y & -F_x & 0 \end{bmatrix}, X=\begin{Bmatrix} x_m \\ y_m \\ z_m \end{Bmatrix}, B=\begin{Bmatrix} C_x \\ C_y \\ C_z \end{Bmatrix}$$

It can be seen that $|A|=0$, hence the system might have infinite or no solutions at all. To define this fact, we find the reduced matrices A_R and $[A\vdots B]_R$ (O'Neil, 2011):

$$A_R=\begin{bmatrix} 1 & 0 & -F_x/F_z \\ 0 & 1 & -F_y/F_z \\ 0 & 0 & 0 \end{bmatrix}$$

$$[A\vdots B]_R=\begin{bmatrix} 1 & 0 & -F_x/F_z & -C_y/F_z \\ 0 & 1 & -F_y/F_z & C_x/F_z \\ 0 & 0 & 0 & C_z+(F_yC_y/F_z)+(F_xC_x/F_z) \end{bmatrix}$$

Since $\vec{n}\cdot\vec{e}=0$:

$$C_z+(F_yC_y/F_z)+(F_xC_x/F_z)=(F_zC_z+F_yC_y+F_xC_x)/F_z=\frac{1}{F_z}\vec{n}\cdot\vec{e}=0$$

Thus, $rank(A_R)=rank([A\vdots B])_R=2$, so the system has infinite number of solutions. The solution of system by selecting $z_m=t$ as independent unknown is given by:

$$\begin{cases} x_m = -\dfrac{C_y}{F_z} + \dfrac{F_x}{F_z} t \\ y_m = \dfrac{C_x}{F_z} + \dfrac{F_y}{F_z} t \\ z_m = t \end{cases} \quad \textbf{(3.32)}$$

By arbitrarily selecting a value for (z_m) the locus of points $M(x_m, y_m, z_m)$ is found, described by the following vector equation:

$$\vec{r}_{OM} = \vec{a} + t\vec{b} \quad \textbf{(3.33)}$$

With

$$\vec{a} = \begin{bmatrix} -C_y / F_z & C_x / F_z & 0 \end{bmatrix}^T, \quad \vec{b} = \begin{bmatrix} F_x / F_z & F_y / F_z & 1 \end{bmatrix}^T$$

As it can be seen, the calculation of radial distances is independent of the point of application of the force. Hence, any point $M(x_m, y_m, z_m)$ of line (3.33) verifies the properties of the mesh point. At this stage, the mesh force unit vector $\vec{n}$ has been calculated by equation (3.21), whereas the position of the mesh point $\vec{r}_M$ has been defined by the set of equations (3.32). Thus, by importing those values in equations (3.12) and (3.14), the contact radii of the gear pair can be derived, with respect to pinion rotational angle. Figure 3.9 depicts the normalized contact radii (with respect to their mean value) for various values of the input torque, during one mesh cycle. It can be noticed that the exhibited fluctuation over the mean value seems to fade when the input torque increases.

The mesh factor (k_m) represents the overall meshing stiffness of the gears during contact. It includes the contribution of elastic contact of the meshing teeth (Hertzian deformation), the bending and shearing effect of the flanks, as well as the tooth base rotation.

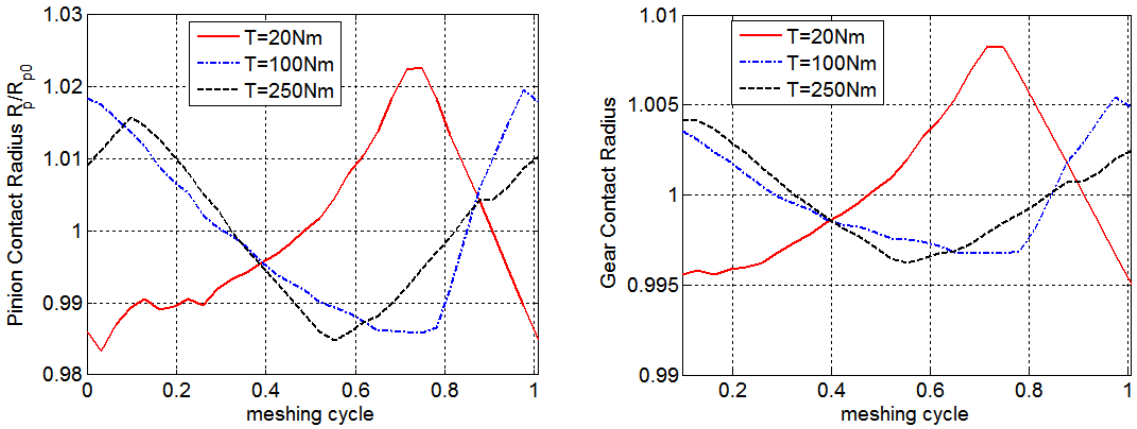

(a) **(b)**

Figure 3.9- Dimensionless contact radii with respect to pinion angular rotation for a complete mesh cycle: (a) Pinion contact radius $\hat{R}_p$, (b) Gear contact radius $\hat{R}_g$.

An expression for the derivation of mesh stiffness for hypoid transmissions has been proposed by Cheng and Lim (2003). This is similar to previous equations used by Ozguven and Houser (1988) for spur gears and by Blankenship and Singh (1995) for helical gears. This equation is applicable to quasi-static conditions, realised usually in Loaded Tooth Contact Analysis. The mesh stiffness is given by:

$$k_m = \frac{F}{R_p \Delta\varphi_L - \varepsilon_0} \qquad \textbf{(3.34)}$$

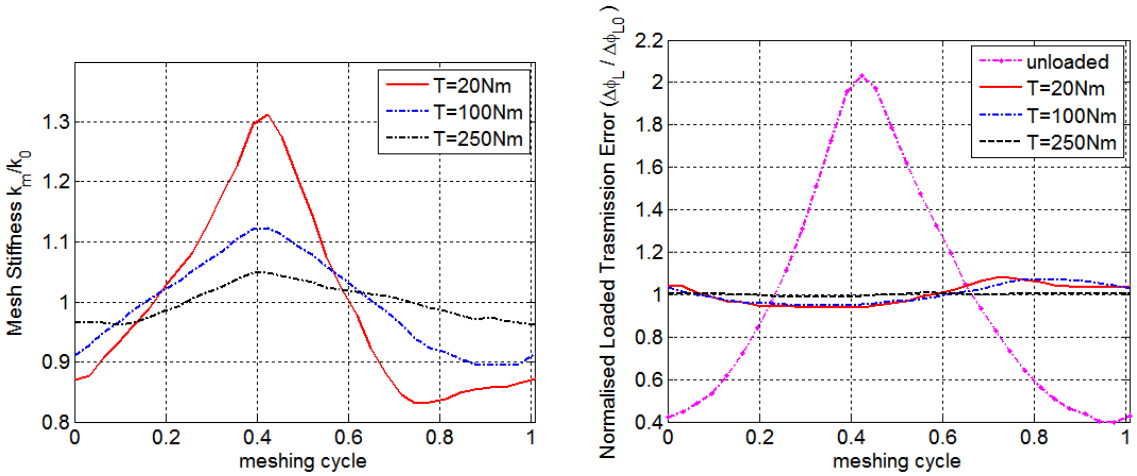

(a) **(b)**

Figure 3.10- Dimensionless mesh parameters with respect to pinion angular rotation for a complete mesh cycle: (a) Mesh Stiffness $\hat{k}_m$, (b) kinematic transmission error $\hat{\Delta}\varphi_L$

Current modelling approach simulates the gear contact by neglecting the effect of lubrication. This approximation is valid for relatively high levels of contact load. In this case, it can be assumed that the dry contact stiffness is much lower than the stiffness of the lubricant fluid; the latter can be regarded as almost incompressible. Hence the equivalent stiffness is assumed to be independent of the lubricant film with no loss of generality. In the above equation, (F) is the resultant load acting on the meshing teeth, ($\Delta\varphi_L$) is the loaded angular transmission error and (ε_0) is the unloaded transmission error in translational form. As implied by equation (3.34), mesh stiffness is a function of load distribution, contact and geometric imperfections, flank modifications and is also dependent on the angular position of the gears. Therefore, it is obvious that the calculation of the total deflection between the mating bodies under loaded and unloaded conditions is a prerequisite. This procedure should be repeated for a number of angular positions during the meshing cycle to ensure sufficient data is collected.

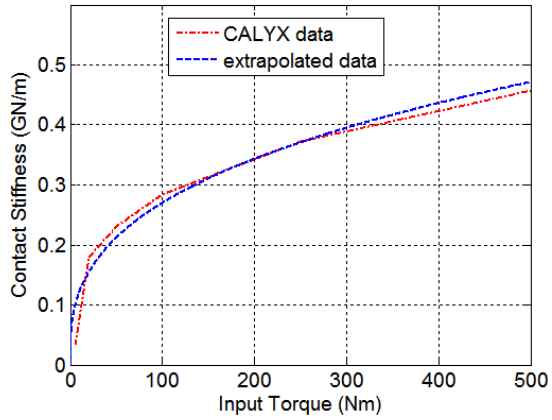

Figure 3.11- Dependence of mean contact stiffness with input torque

Loaded and unloaded body deflections are calculated by CALYX. For the pure geometric (unloaded) contribution, a quasi-static analysis with (almost) zero applied input torque is performed. The transmission error results can be seen in Figure

3.10b, whereas the stiffness is depicted in Figure 3.10a. The fluctuations over the mean value seem to dissipate as well while the torque level increases. The mean stiffness value with respect to input torque is illustrated in Figure 3.11. There seems to be a significant growth rate at low to medium torque levels, before gradually dropping until reaching high loading conditions. The mean stiffness values derived by CALYX can be extrapolated to an expression in the form of:

$$k_0(T_p) = C_1 \cdot T_p^{\,C_2} \qquad \textbf{(3.35)}$$

where (C_i) are constants. Similar results have been obtained by Cheng and Lim (2003).

Throughout this section, it was shown how the geometric complexity of hypoid transmissions perplexes the derivation of mesh parameters. The whole process is not straightforward at all, since a complete LTCA is required. The value of each contact parameter is inserted in the equations of motion and the dynamic problem can be numerically solved. As expected, the contact properties are periodic functions of the pinion angle. Hence, to increase the computational efficiency and resolve discontinuity issues, the above quantities are expressed into Fourier series. Neglecting any tooth-to-tooth variations, the fundamental period is $\theta_T = 2\pi/N$ (in angular form), where N_p is the number of teeth for the pinion. For instance, the pinion contact radius R_p can be expressed in a Fourier series with respect to the pinion angular position φ_p as:

$$R_p(\varphi_p) = R_{p0} + \sum_{i=1}^{n}[R_{pci}\cos(iN\varphi_p) + R_{psi}\sin(iN\varphi_p)] \qquad \textbf{(3.36)}$$

It can be shown that a Fourier expansion with three harmonic terms describes the contact parameters adequately. The original output is compared with the Fourier expansion in Figure 3.12.

The procedure for calculating the mesh properties can be summarized in the following steps:

(a) For pinion angular position (φ_p), calculate the resultant force and moment from LTCA data using equations (3.18), (3.22) and (3.24) - (3.30).

(b) For an arbitrary selected value of (t), determine the coordinates of the equivalent mesh point using equations (3.32).

(c) From equations (3.12) and (3.14) calculate the contact radii ($R_p(\varphi_p)$ and $R_g(\varphi_p)$).

(d) From equation (3.34) derive the mesh stiffness $k_m(\varphi_p)$ along the line of action.

To conclude, a list of the main assumptions involved in the formulation of the dynamic model and the derivation of the contact properties are presented.

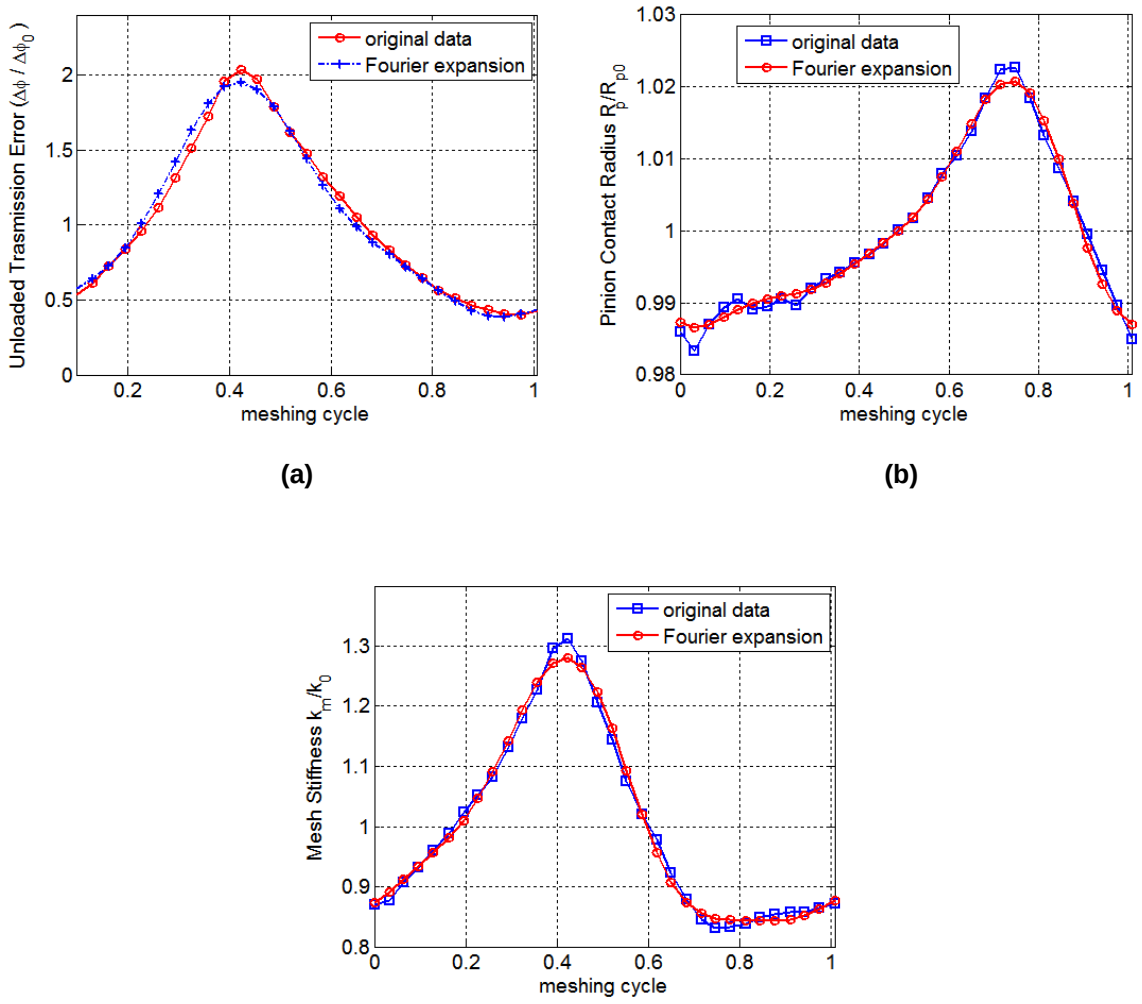

Figure 3.12- Comparison of derived mesh properties and the corresponding Fourier expansion for input torque 20Nm: (a) kinematic (unloaded) transmission error (b) pinion contact radius (c) mesh stiffness

Table 3.3- List of main assumptions

(1) The gear mesh is concentrated into a single point.
(2) The equations of motion are formulated in the form of coupled mechanical oscillators comprising of mass, stiffness and damping elements.
(3) Mesh stiffness (k_m) is the effect of the elastic reaction contact force between the two gears; it is assumed to be identical under quasi-static and dynamic

conditions.

(4) The lateral motion of the gear wheels, as well as the bearing interactions are ignored; only the torsional motions are accounted for.

(5) The torsional rigidity of the powertrain and differential unit is assumed so that their inertias can be introduced in the gear pair model.

(6) The resisting torque is a function of the vehicle speed and, therefore, the angular velocity of the differential unit.

3.4 - Synopsis

In this chapter the concepts of global dynamics of hypoid gears were presented. Initially, the fundamental mechanical model was introduced in a similar manner to previous studies for spur and helical gear sets. The main difference is focused on a time variant line of action resulting in an alternative expression for the dynamic transmission error. Hence, reduction of the order of the system is not possible, resulting essentially in a three degree of freedom system.

The determination of the contact parameters is crucial for the solution of the system. Their physics was discussed and analytical expressions for their derivation were presented. However, the complex geometrical issues encountered in hypoid gear sets enforce the use of numerical simulation tools. Therefore, the basic aspects of Loaded Tooth Contact Analysis were introduced stressing on the numerical simulation of the contact and eventually the calculation of load distribution and rigid body deflection.

The data provided by such a quasi-static analysis was used to derive the contact parameters. By this means, it is possible to switch from a multiple contact cell representation into a model focused on a single mesh point. The results obtained were compared and successfully validated with previously published research studies. The periodicity observed in their fluctuation allowed expansion in Fourier series. The fitment was proved satisfactory. The discrete set of values was thus

transformed into analytical expressions which can be inserted in the dynamic model, improving computational efficiency.

Through all the preceding steps, the equations of motion can be solved and the system response can be determined for teeth dry contacts. The significance of the dry contact model is important; it is the backbone for the upcoming numerical models, covering the aspects of lubrication and Targeted Energy Transfer.

Chapter 4 - Tribological Consideration

4.1 - Introduction

The previous chapter discussed the formulation of a global dynamic model for the differential gear pair. An “integrated” approach was maintained, meaning that the derivation of the external and internal forcing elements was achieved on a macro-scale; the system components were practically treated as rigid bodies. The current chapter is focused on the micro-scale of the problem, investigating the dependence between the global dynamics and the sliding motion of the mating flanks. Interesting conclusions can be drawn about the properties of the lubrication regime, friction generation and mechanical efficiency of the transmission.

Various modelling approaches are presented based on an increased level of complexity; the operating conditions of hypoid transmissions necessitate the consideration of non-Newtonian fluid analysis. The tribological investigation will be restricted on analytic solutions. It is true that a numerical solution would be more accurate; however, it would require a significant amount of computational time. Therefore, the lubricant film will be estimated by an analytical expression derived by Grubin (1949). Thermal effects will also be considered (heat dissipation conducted by the lubricant due to the sliding motion of the gear flanks). Tooth Contact Analysis will be implemented once again since a number of contact parameters characterizing the mating surfaces need to be specified.

4.2 - Dynamic Modelling of Lubricated Contact

During the meshing process, the gears in contact exhibit a combined motion of rolling and sliding. Velex and Cahouet (2000) have concluded that sliding friction is mainly responsible for power losses in helical gears for low to medium rotational speeds. When considering hypoid gear sets, due to the axial offset, an intensive longitudinal sliding occurs (Stadfelt, 1993). For the above reasons, it can be implied that the sliding effect overwhelms the rolling; hence rolling friction can be regarded as insignificant. This notion is maintained by Gohar (2001) in the analysis of frictional effects in EHL contact problems.

The available gear dynamics models in literature tend to include friction as an external excitation caused by the relative sliding motion of the working teeth. However as shown by Vaishya and Singh (2001b), friction can interact with the dynamics of the system in a complex manner by:

- acting as a parametric excitation,
- inducing nonlinearities due to its dependence to the instantaneous sliding velocity,
- enhancing the damping capability of the system

In an accurate dynamic model all the above factors need to be addressed.

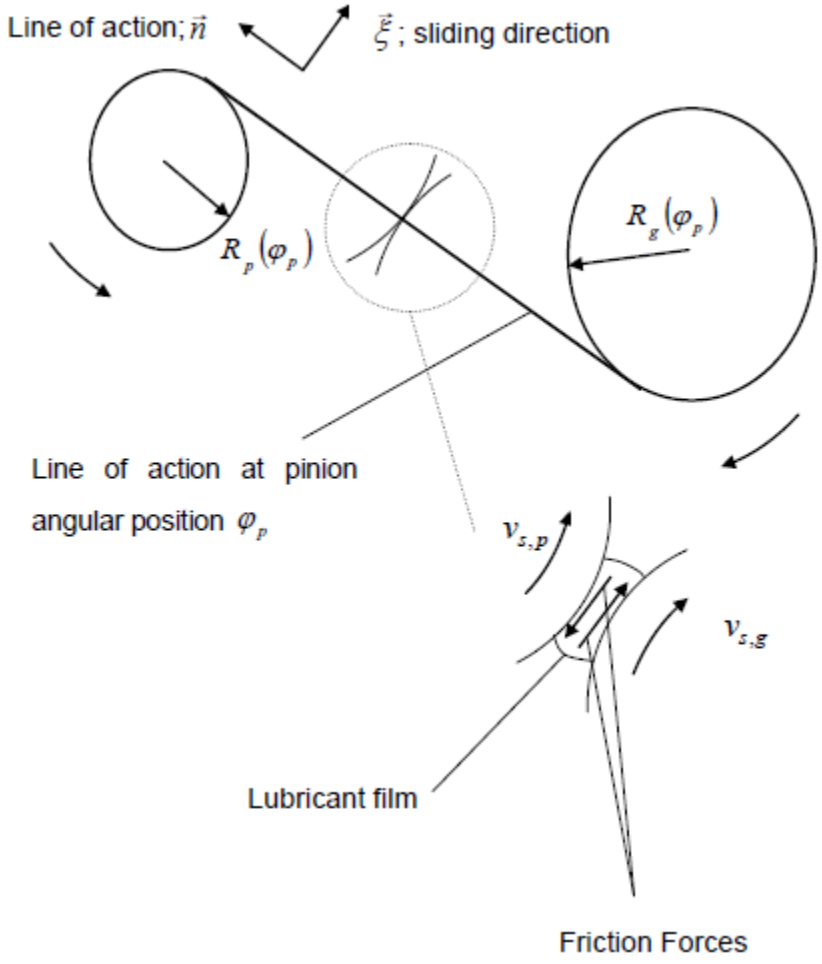

Figure 4.1- Frictional model of a gearing system

The mechanical model used to account for the friction generation mechanism is presented in Figure 4.1. A frictional force is exerted on a direction perpendicular to

the line of action of the gear mesh. The latter, defined by unit vector $(\vec{n})$, is dependent on the angular position of the system as already mentioned in Chapter 3. Friction is the result of the relative sliding of the mating flanks, which takes place in the direction denoted by unit vector $(\vec{\xi})$. An analogous approach has been implemented by Vaishya and Singh (2001a) for parallel axis gears; in a hypoid transmission, however, the variation of the sliding direction during a mesh cycle should be considered.

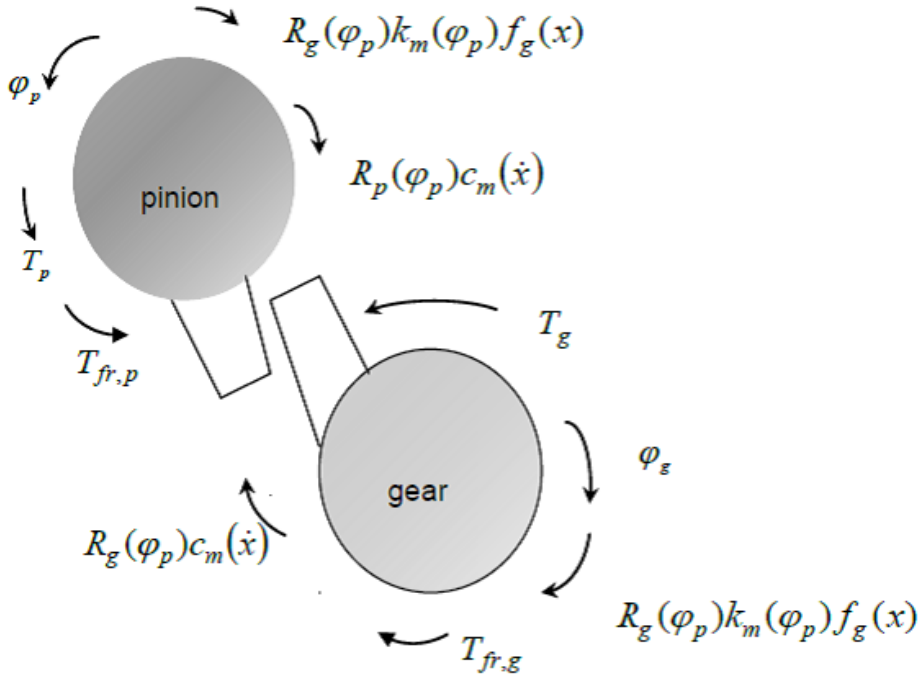

Figure 4.2- Free body diagram of lubricated model

The corresponding free body diagram, shown in Figure 4.2, is an expansion of the one presented in the dynamic analysis of the previous chapter. The main suppositions of section 3.2.1 are still in effect; the mesh force along the line of action is represented by stiffness and damping elements. The dynamic effect of lubrication is summarized in the appearance of a pair of frictional torques generated by the relative sliding. Hence, such a formulation only involves the torsional motion,

neglecting the effect of friction on the lateral motion of the system, especially along the sliding direction.

The equations of motion are similar to equations (3.3) and (3.4) with the only addition being the inclusion of the corresponding frictional torque $(T_{fr,p})$ and $(T_{fr,g})$:

$$I_p\ddot{\varphi}_p + R_p(\varphi_p)c_m(\dot{x}) + R_p(\varphi_p)k_m(\varphi_p)f_g(x) = T_p + T_{fr,p} \quad \textbf{(4.1)}$$

$$I_g\ddot{\varphi}_g + R_g(\varphi_p)c_m(\dot{x}) + R_g(\varphi_p)k_m(\varphi_p)f_g(x) = -T_g + T_{fr,g} \quad \textbf{(4.2)}$$

All the other parameters are yielded by the formulation presented in Chapter 3. By convention, it is always assumed that the friction assists the motion of each gear member. This fact is also reflected in the above equations. Nevertheless, both terms $(T_{fr,p})$ and $(T_{fr,g})$ will be treated as algebraic quantities; whether their effect is assistive or resistive is revealed by the sign of the friction force itself. This is in accordance with prior considerations by Vaishya and Singh (2003), Kar and Mohanty (2007) as well as Liu and Parker (2008).

4.3 - Thermal Elastohydrodynamic Analysis

The previous chapter illustrated the process for the derivation of the mesh properties. The main hypothesis required the application of the gear contact force on a single equivalent mesh point instead of a finite area over a number of flanks; this resulted eventually to a macro-scale analysis. However, when considering the updated model described by equations (4.1) and (4.2), a different approach needs to be introduced.

A tribological analysis needs to be conducted on each of the mating teeth pairs in contact. The individual frictional contributions need to be added together so that the total frictional torque is formed. Such a formulation involves essentially two basic steps; the first one refers to the definition of the direction of friction which always opposes the relative sliding velocity. The second step involves understanding the underlying mechanism of friction; in the case of viscous shear this is inversely proportional to the lubricant film thickness (Gohar and Rahnejat, 2009). There would be also a significant boundary friction contribution due to asperity interactions on the

contiguous surfaces when the lubricant film thickness is insufficient to guard against their direct interaction (Vaishya and Singh, 2003). Therefore, friction is investigated on the micro-scale of the gear pair system, where the kinematic, forcing and lubricant properties are vastly pronounced.

The lubrication regime of gearing mechanisms has been proven to lie in the mixed Elastohydrodynamic (EHD) region (Snidle and Evans (1997); Gohar (2001)). The thinning of lubricant film results into coexistence of viscous shear and asperity interactions between the mating teeth surfaces. Athough a numerical transient analysis of the lubricated conjunction would include the squeeze film effect (thus, the continuity of film history); it would be computationally very intensive. This is because a number of meshing teeth pairs (typically 2 to 3) are in simultaneous mesh in each step of the dynamic simulation. The influence of additional salient factors for a realistic solution such as asperity interactions and thermal shear thinning of a lubricant film would make the problem almost computationally intractable. To ensure that steady state condition is achieved, a vast number of time steps needs to elapse; hence numerical efficiency is decreased further. Therefore, an analytic treatment should be preferred, along the same lines as that of De la Cruz et al (2010), while applying an EHL analytical approach of Grubin (1949) for the elliptical conjunction of hypoid gears.

An outline of the EHL generic formulation is depicted in Figure 4.3. Due to the relative sliding of the gear flanks, a lubricant film is formed between the two surfaces. The contact load is applied in a direction normal to the sliding motion. This raises the operating temperature of the lubricant. The main parameters of Figure 4.3 are explained below:

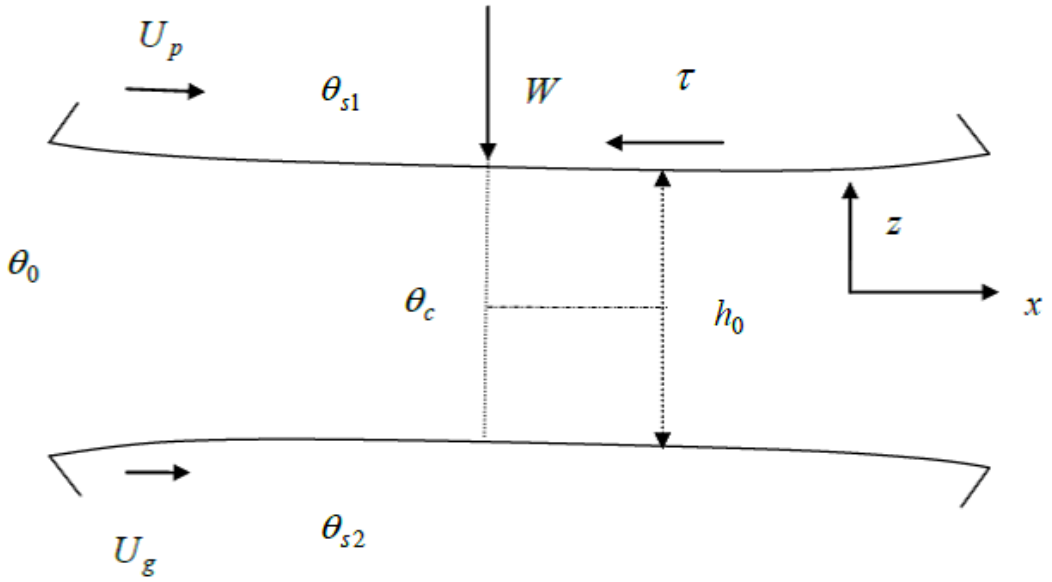

Figure 4.3- The Elastohydrodynamic Conjunction

Table 4.1- Basic parameters in EHL formulation

Variable	Physical Meaning
U_p	pinion surface velocity on the tangential plane of the contact
U_g	gear surface velocity on the tangential plane of the contact
$\theta_{s,p}$	pinion surface temperature
$\theta_{s,g}$	gear surface temperature
θ_0	bulk (inlet) temperature
θ_c	temperature at the center of lubricant film
h_0	parallel region film thickness
W	contact load
τ	shear stress

When considering involute profile gear mechanisms, the relative motion always occurs in a direction normal to the contact line (Velex and Maatar, 1996; Wang et al,

2004; Theodossiades et al, 2007). However, in hypoid transmissions, geometric complexity results in a continuous rotation of the contact zone (Litvin et al, 2006). This results in the implementation of TCA tools for deriving the kinematic and geometric properties of the distributed contact area. Such a technique was employed by Xu and Kahraman (2007), by discretising the mesh zone into a set of finite line increments; subsequently a quasi-static tribological analysis was conducted.

In this work, a tribological analysis will be enforced on the contact ellipse based on the properties of its central location point. By this means, it will be assumed that the latter characterizes the entire conjunction. This formulation enables the analytical treatment of the lubrication problem (Grubin, 1949; Mostofi and Gohar, 1982; Chittenden et al, 1985), hence avoiding time consuming numerical techniques.

As mentioned previously, the direction of friction coincides with the direction of the sliding velocity. Therefore, a kinematic analysis for the identification of the relative sliding direction is the first necessary step.

4.3.1 Contact Kinematics

The kinematics of the contact are crucial for the ensuing tribological analysis. The various kinematic and geometric attributes are presented in Figure 4.4. The corresponding notation is explained in Table 4.2. In general, the velocity of the contact point will be synthesis of two individual components. The first (not depicted in the figure) which lies along the direction normal to the contact zone has been already defined in equations (3.11) and (3.13). The second is set on the tangential plane of the contact area (Kolivand et al, 2010).

The tangential component influences the frictional properties; equally important is its orientation with respect to the contact ellipse, so that analytical estimations for the film thickness can be applied (Gohar and Rahnejat, 2008). As seen in Figure 4.4, the entraining and sliding velocities are forming angles ψ_1 and ψ_2 with respect to the minor axis of the contact ellipse. The semi-axes of the latter are defined by unit vectors $\hat{x}$ and $\hat{y}$ .The corresponding velocity projections of the pinion at the contact point are obtained as:

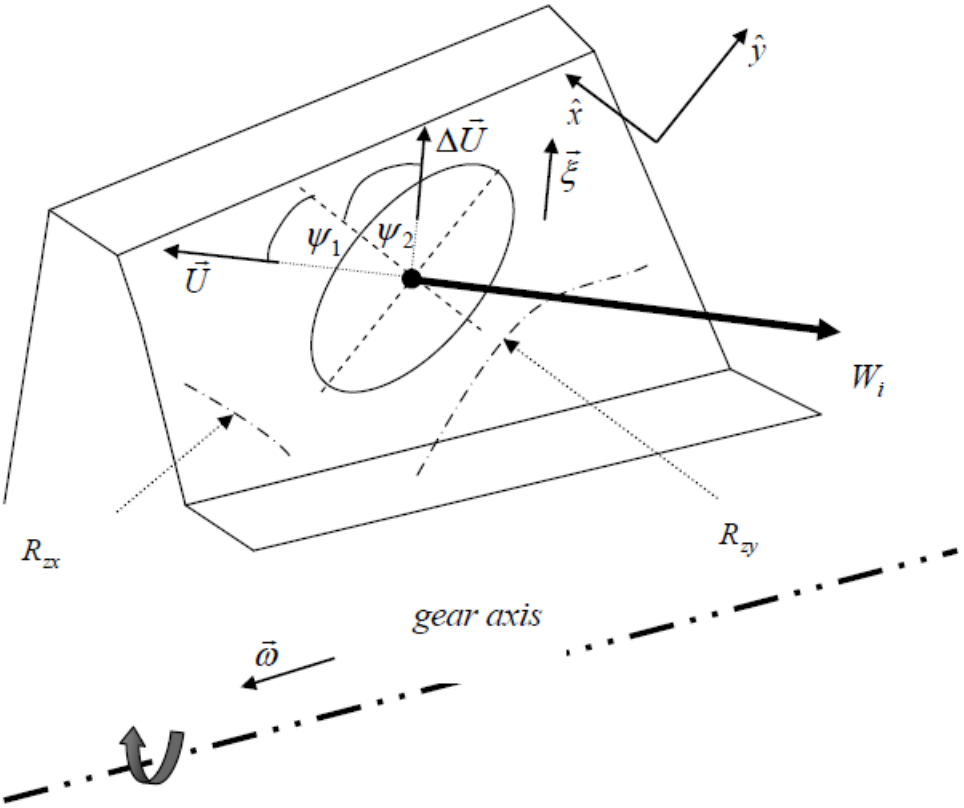

Figure 4.4- Geometric and kinematic properties at the contact footprint

$$u^{(p)} = \hat{x}\cdot\left(\vec{\omega}_p \times \vec{r}\right) = \omega_p \hat{x}\cdot\left(\vec{j}_p \times \vec{r}\right) \quad \textbf{(4.3)}$$

$$\upsilon^{(p)} = \hat{y}\cdot\left(\vec{\omega}_p \times \vec{r}\right) = \omega_p \hat{y}\cdot\left(\vec{j}_p \times \vec{r}\right) \quad \textbf{(4.4)}$$

Table 4.2- Notation of contact footprint variables

Variable	Physical Meaning
$\vec{U}$	Entraining velocity of the lubricant at the contact point
$\hat{x}$	Unit vector along the minor axis of the contact ellipse
R_{zx}	Radius of curvature along the minor axis of the contact ellipse
$\hat{y}$	Unit vector along the major axis of the contact ellipse

R_{zy}	Radius of curvature along the major axis of the contact ellipse
$\Delta\vec{U}$	Sliding velocity at the contact point
ψ_1	Angle between entraining velocity and minor axis of contact ellipse
ψ_2	Angle between sliding velocity and minor axis of contact ellipse
$\hat{\xi}$	Unit vector along the direction of relative sliding

The notation used in the previous equations is consistent with section 3.3.1, where $(\vec{\omega}_p)$ is the pinion angular velocity and $(\vec{j}_p)$ is the unit vector along the rotational direction of the pinion. In this case the position vector $(\vec{r})$ represents the contact point on the individual flank under consideration and not the equivalent mesh point derived in section 3.3.2. All vectors are defined with respect to a coordinate system $S_p(x_p, y_p, z_p)$ fixed at the centre of the pinion (Figure 3.4). By definition:

$$r_{fr,p,x} = \hat{x} \cdot \left(\vec{j}_p \times \vec{r}\right) \quad \textbf{(4.5)}$$

$$r_{fr,p,y} = \hat{y} \cdot \left(\vec{j}_p \times \vec{r}\right) \quad \textbf{(4.6)}$$

A set of similar expressions also exists for the gear wheel, if all vectors are expressed relatively to the coordinate system $S_g(x_g, y_g, z_g)$, fixed at the centre of the gear wheel (Figure 3.4):

$$u^{(g)} = \hat{x} \cdot \left(\vec{\omega}_g \times \vec{r}\right) = \omega_g \hat{x} \cdot \left(\vec{j}_g \times \vec{r}\right) \quad \textbf{(4.7)}$$

$$\upsilon^{(g)} = \hat{y} \cdot \left(\vec{\omega}_g \times \vec{r}\right) = \omega_g \hat{y} \cdot \left(\vec{j}_g \times \vec{r}\right) \quad \textbf{(4.8)}$$

$$r_{fr,g,x} = \hat{x} \cdot \left(\vec{j}_g \times \vec{r}\right) \quad \textbf{(4.9)}$$

$$r_{fr,g,y} = \hat{y} \cdot \left(\vec{j}_g \times \vec{r}\right) \quad \textbf{(4.10)}$$

Equations (4.6), (4.7), (4.9)-(4.10) are equivalent to the contact radii which were calculated in section 3.3.1. If they are multiplied by the angular speed of the gear member, they yield the instantaneous velocity component with respect to the contact ellipse. Thus, in this thesis, they will be called surface velocity radii as well. Therefore, their importance is associated with the inclusion of the dynamic effect in the kinematics of the mating flanks. This fact will be proved numerically in the following section by comparing the velocities obtained directly from CALYX and the ones derived by the above analytic expressions. The sliding velocity is yielded by (Theodossiades et al, 2007):

$$\Delta\vec{U} = \Delta U \hat{\xi} \quad \textbf{(4.11)}$$

$$\Delta U = \sqrt{\left(u^{(p)} - u^{(g)}\right)^2 + \left(\upsilon^{(p)} - \upsilon^{(g)}\right)^2} \quad \textbf{(4.12)}$$

$$\hat{\xi} = \frac{1}{\Delta U}\left[\left(u^{(p)} - u^{(g)}\right) \cdot \hat{x} + \left(\upsilon^{(p)} - \upsilon^{(g)}\right) \cdot \hat{y}\right] \quad \textbf{(4.13)}$$

The friction force essentially lies in the direction of the sliding velocity ($\hat{\xi}$). The moment arm of the frictional torques can be calculated in the same sense to contact radii - see equations (3.12), (3.14):

$$r_{fr,p} = \hat{\xi}^{(S_p)} \cdot \left(\vec{j}_p{}^{(S_p)} \times \vec{r}^{(S_p)} \right) \quad \textbf{(4.14)}$$

$$r_{fr,g} = \hat{\xi}^{(S_g)} \cdot \left(\vec{j}_p{}^{(S_g)} \times \vec{r}^{(S_g)} \right) \quad \textbf{(4.15)}$$

Radii $r_{fr,p}$ and $r_{fr,g}$ represent the moment arms for friction torque applied to the pinion and gear wheel, respectively. As shown by Cheng and Lim (2003), they are related to the tangential friction component at the contact point in the sliding direction $(\vec{\xi})$. They depend on the position of the contact point and the orientation of the contact ellipse. This information is derived from CALYX, based on a numerical representation of the gear pair geometry.

4.3.2 Contact properties

4.3.2.1 Contact ellipse imposition

From the preceding analysis, it can be seen that the contact point definition is essential for calculating the oil entrainment conditions. Additionally, the location of the contact zone on the gear flank is associated to the equivalent radii of curvature, affecting both the elastostatic distortion and the formation of the lubricant film. Therefore, the imposition of a contact zone is a crucial task.

For the case of spur and helical gears, the involute profile yields a representation of the contact zone in a form of finite line; hence the mobility and surface characteristics of the contact can be analytically defined (Dudley and Townsend, 1991; Theodossiades et al, 2007). Yet the geometric complexity of hypoid gears, as already discussed in the previous chapter, enforces the use of TCA for the derivation of the contact conditions. The formulation presented in section 3.3.2 illustrated the prediction of an average mesh point by balancing the overall load and moment distribution. However, the tribological analysis is conducted on each flank; thus the results of TCA obtained by CALYX need to be applied on each individual pair of mating surfaces rather than the whole gear member.

As already seen, CALYX provides a representation of the contact zone in the shape of a grid of points. The points of particular interest are termed ‘principal’; they can approximate the centreline of the contact ellipse. A quasi-static numerical model

predicting the friction coefficient has been proposed by Xu and Kahraman (2007), focusing the tribological consideration on the line joining the principal points. The current study employs an analytical approach of the lubrication problem; thus an alternative characterisation of the contact zone will be sought. Such a simplified approximation of the contact grid has been introduced by Park and Kahraman (2009) as part of surface wear model for hypoid gears. This technique which matches the finite grid to a contact ellipse by using an interpolation algorithm is illustrated in Figure 4.5.

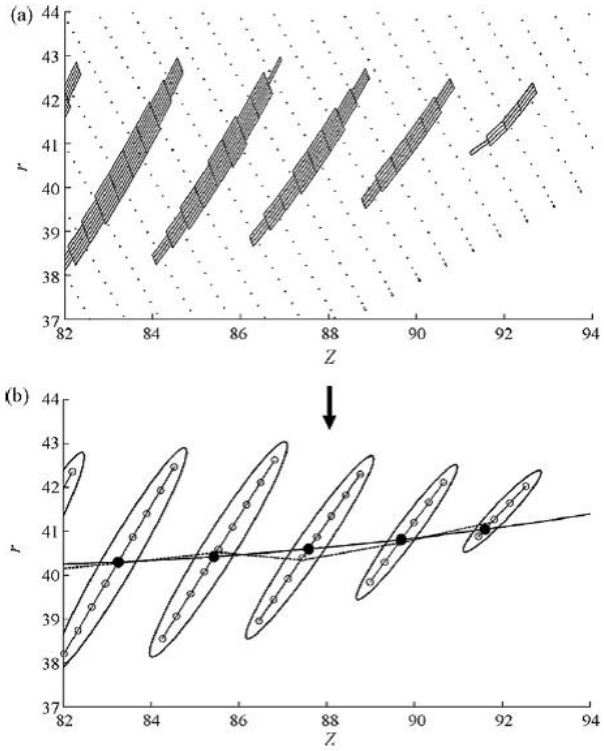

Figure 4.5- Evaluation of contact zone from TCA (after Park and Kahraman, 2009)

The method implemented in this thesis is even simpler; the instantaneous contact ellipse is represented by the central principal point. Hence, all the properties of the latter are attributed to the contact zone itself permitting the use of closed form solutions for the tribological aspect of the problem.

4.3.2.2 Meshing and engagement cycle

Before presenting the contact properties derived from TCA, it is useful to provide the definition of the meshing and engagement cycles. These quantities may be

expressed in angular form, for instance with respect to the pinion roll angle (φ_p). Their physical meaning is illustrated in Figure 4.6.

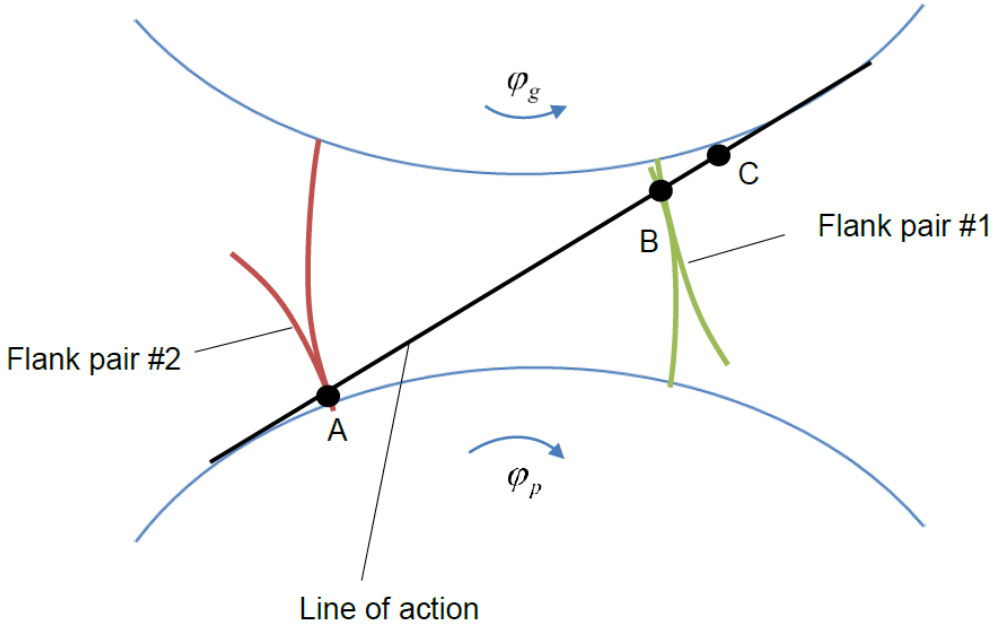

Figure 4.6- Mesh and engagement cycle

In the above diagram, the line of action is bounded by points A and C. At the initial point of observation $(t=0)$, it is assumed that the flank pair #2 is engaging into contact by entering the line of action at point A; at the same time the preceding flank pair #1 is at position B. The meshing cycle is defined as the elapsed time needed for flank pair #2 to reach position B (He et al, 2007). It is related to the base pitch for the case of spur and helical gears; nevertheless for the hypoid transmissions an equivalent expression can be used by using the angular pitch instead due to the absence of a base radius as a physical quantity. Hence:

$$t_{mesh} = \frac{2\pi}{\omega_p N} \qquad \textbf{(4.16)}$$

By comparing the previous equation with the definition of meshing frequency in section 3.2.1, it is obvious that the meshing cycle is in essence the meshing period; furthermore it expresses the phase difference between two successive mating

flanks. If the number of pinion teeth is denoted by N, equation (4.16) can be also expressed in angular form, thus:

$$\varphi_{mesh}^{(p)} = \frac{2\pi}{N} \qquad \textbf{(4.17)}$$

The next step is the determination of the engagement cycle, identified as the elapsed time during the engagement process of gear pair. From Figure 4.6, this corresponds to the distance between positions A and C. The quotient of engagement to meshing cycle yields the overall contact ratio (m_t):

$$m_t = \frac{t_{eng}}{t_{mesh}} = \frac{\varphi_{eng}^{p}}{\varphi_{mesh}^{p}} \qquad \textbf{(4.18)}$$

The meshing cycle can be calculated numerically from TCA, by computing the time or the angular hysteresis between the engagements of 2 successive pairs. Indeed a value of 0.4712 rad is derived for the hypoid gear pair under investigation. The theoretical value is equal to $2\pi/13$ (Equation 4.17) yielding a relative error of almost 2.5% which is an acceptable value.

Likewise, the overall contact ratio can be computed from two individual methods to test the validity of Equation 4.18; either by dividing the numerically obtained cycles or by finding the mean value of the mating flanks in contact for a meshing cycle. Both approaches rely on TCA results aiming to compare Eq. (4.18) to the theoretical definition of the contact ratio (Dudley and Townsend, 1991). From Eq. (4.18) a value 2.8611 is maintained while from the definition the result is 2.8378. Comparison of the two quantities conveys an error of 0.82%. The error magnitude is also relevant to the time/angular increment used by TCA; therefore a reduction in the step of the quasi-static analysis would diminish the observed error.

4.3.2.3 Surface velocities and radii

As mentioned previously, the contact ellipse is characterized by the centre point of the numerically predicted contact grid. As a result, the contact properties of the overall elliptical contact coincide with those of that principal point. If the position vector $(\vec{r})$ is identified, the corresponding surface velocities and radii can be derived from equations (4.3) - (4.10). The results displayed in Figure 4.7 are attributed to the 12th pinion and 3rd gear flank. It should be mentioned that the depicted quantities are dimensionless, as typical length is chosen the mean value of equivalent radius of curvature along the x-direction $R_{zx0} = 0.0181m$ and as typical angular velocity the pinion angular velocity of the quasi-static analysis $\omega_{p0} = 104.6 rad/\sec$.

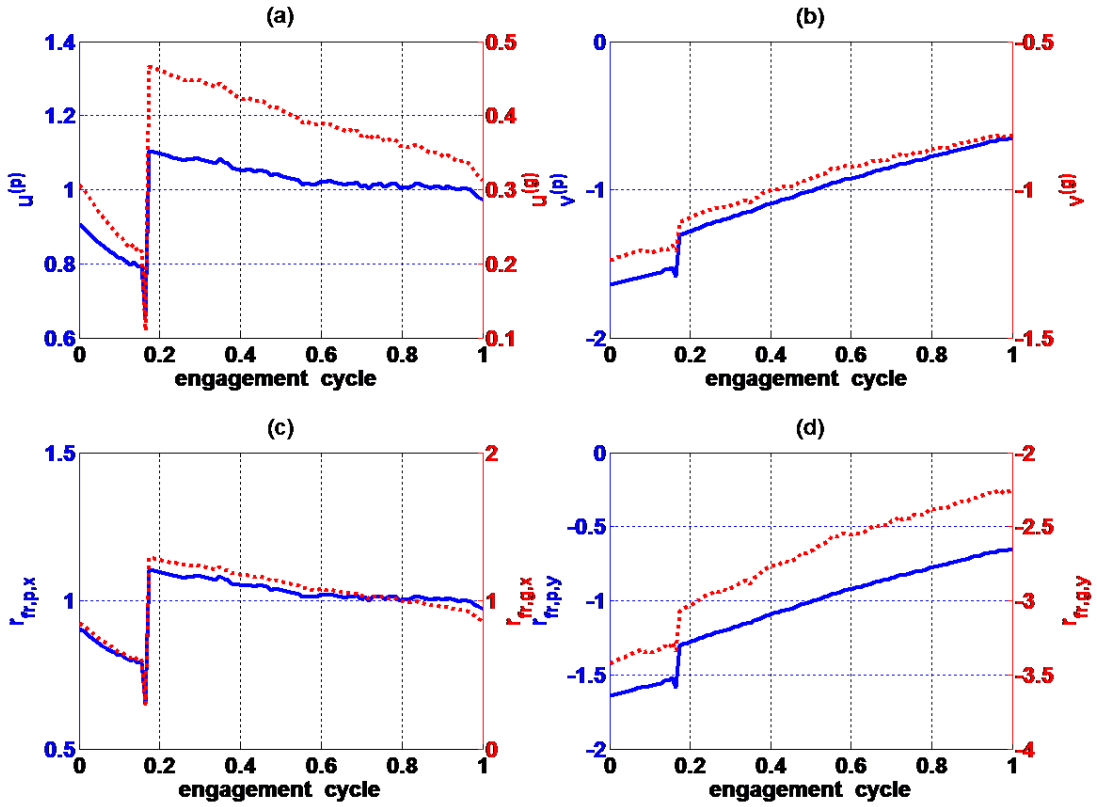

Figure 4.7- Velocities and surface velocity radii; (a) velocity across x-direction, (b) velocity across y-direction, (c) surface velocity radius $r_{fr,x}/R_{zx0}$ and (d) surface velocity radius $r_{fr,y}/R_{zx0}$. ——pinion , ... gear. The pinion torque is equal to 50Nm.

The validity of expressions (4.3) - (4.10) can be confirmed if the velocities derived directly from CALYX are compared to those predicted by the analytic expressions (4.3) - (4.4) and (4.7) - (4.8). The comparison charts in dimensionless form shown in Figure 4.8 prove that the analytical expressions are valid; hence the surface velocity can be yielded as the product of the instantaneous angular velocity and the surface velocity radius. By this means the fluctuations appointed to the dynamic effects will be incorporated in the tribological analysis, similarly to the methodology followed by Vaishya and Singh (2001a) for a spur gear pair.

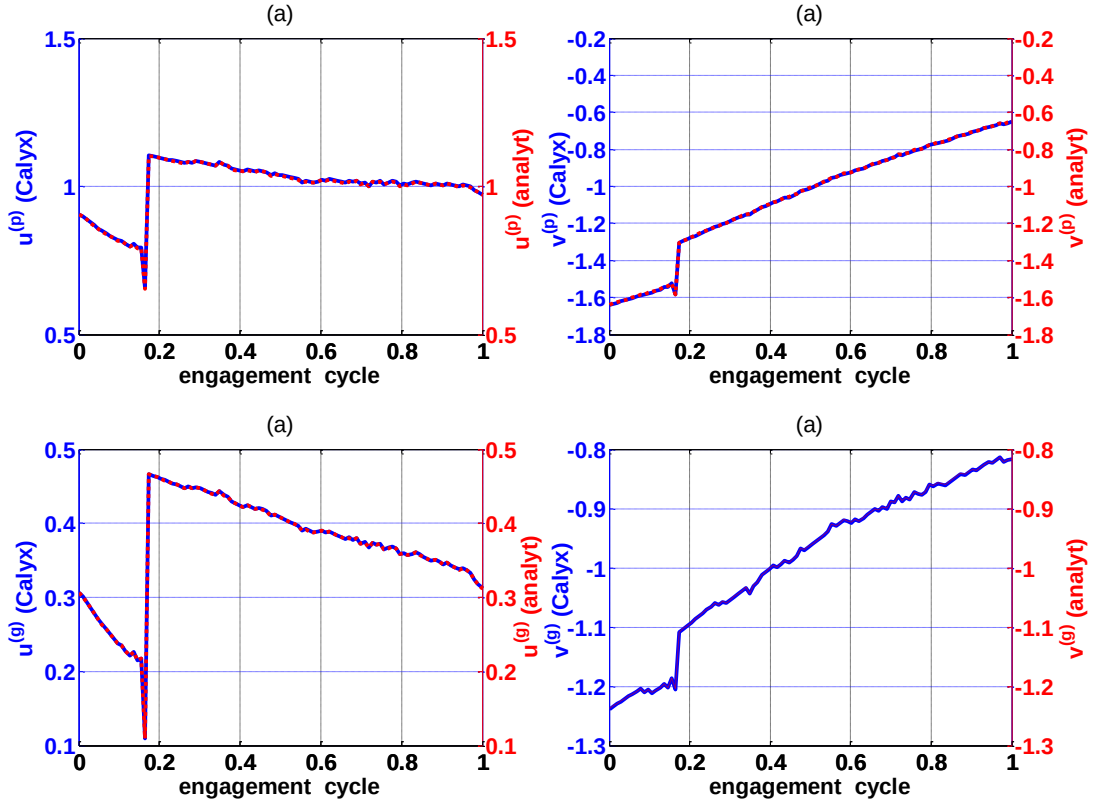

Figure 4.8: Comparison between analytical and CALYX predicted velocities; (a) pinion direction –x, (b) pinion direction –y (c) gear direction –x, (d) gear direction –y _____CALYX , ... analytical. The pinion torque is equal to 50Nm.

4.3.2.4 Contact geometry and load distribution

The approximation of the contact zone into an elliptical footprint requires the knowledge of the equivalent radius of curvature, as well as the magnitude of the

contact load. The equivalent radii of curvature R_{zx}, R_{zy} along the $-x$ and $-y$ axis of the contact ellipse are given by the following set of expressions (Gohar, 2001):

$$\left(\frac{1}{2R_{zx}}+\frac{1}{2R_{zy}}\right)=\frac{1}{2}\left(\frac{1}{R_{11}}+\frac{1}{R_{12}}+\frac{1}{R_{21}}+\frac{1}{R_{22}}\right) \qquad \textbf{(4.19)}$$

$$\left(\frac{1}{2R_{zx}}-\frac{1}{2R_{zy}}\right)=\frac{1}{2}\left[\begin{array}{l}\left(\frac{1}{R_{11}}-\frac{1}{R_{12}}\right)^2+\left(\frac{1}{R_{21}}-\frac{1}{R_{22}}\right)^2+\\ 2\left(\frac{1}{R_{11}}-\frac{1}{R_{12}}\right)\left(\frac{1}{R_{21}}-\frac{1}{R_{22}}\right)\cos 2\vartheta\end{array}\right]^{1/2} \qquad \textbf{(4.20)}$$

The values R_{11} and R_{12} denote the principal minimum and maximum radii of curvature of the pinion, whereas R_{21} and R_{22} denote the corresponding values for the gear. The angle ϑ is formed between the planes containing R_{11} and R_{21}. The principal curvatures are obtained from TCA for the current contact position; hence from the above equations the relative (equivalent) curvature values can be computed. The dimensions of the contact ellipse are determined by its semi-axes. Considering that the parameter $\cos\theta=\dfrac{1/2R_{zx}-1/2R_{zy}}{1/2R_{zx}+1/2R_{zy}}$ determines the gap shape of mating flanks, the contact ellipse semi axes are given by (Gohar, 2001):

$$b_{axis} = \alpha \left[\frac{3\pi W}{4E_r \left(1/2R_{zx} + 1/2R_{zy} \right)} \right]^{1/3} \qquad \textbf{(4.21)}$$

$$a_{axis} = \beta \left[\frac{3\pi W}{4E_r \left(1/2R_{zx} + 1/2R_{zy} \right)} \right]^{1/3} \qquad \textbf{(4.22)}$$

The parameters α and β are provided in tabulated form with respect to $\cos\theta$ (Gohar, 2001); a polynomial fit of 7th power is proved to yield satisfactory accuracy. Comparisons are shown in Figure 4.9.

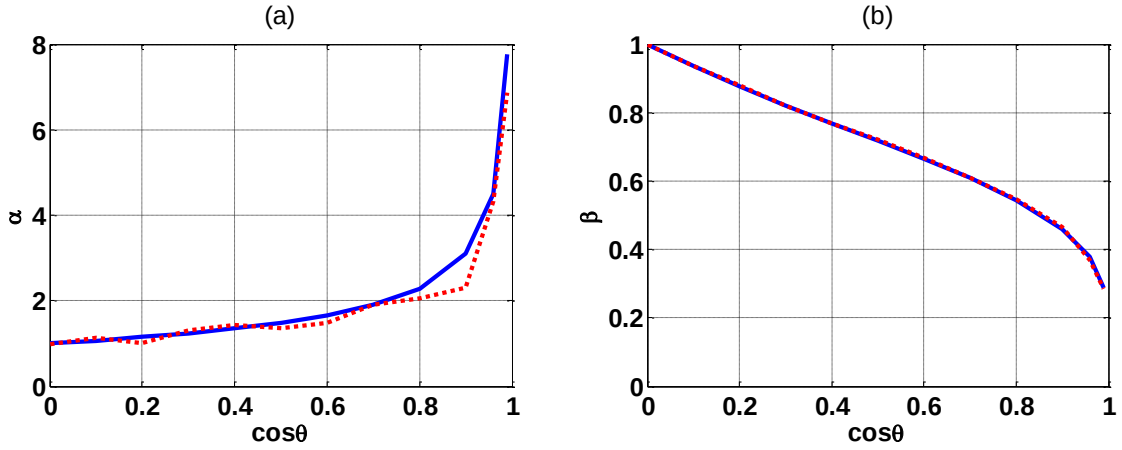

Figure 4.9- Parameters α and β; ——— tabulated data , ... polynomial fit

The contact load magnitude is calculated in accordance to the analysis presented in section 3.3.2; however in this case only the resultant force across the flank into consideration will be computed. The mean contact pressure will be derived by dividing the flank load W to the elliptical contact area (Gohar and Rahnejat, 2008):

$$p_{mean} = \frac{W}{\pi a b} \tag{4.23}$$

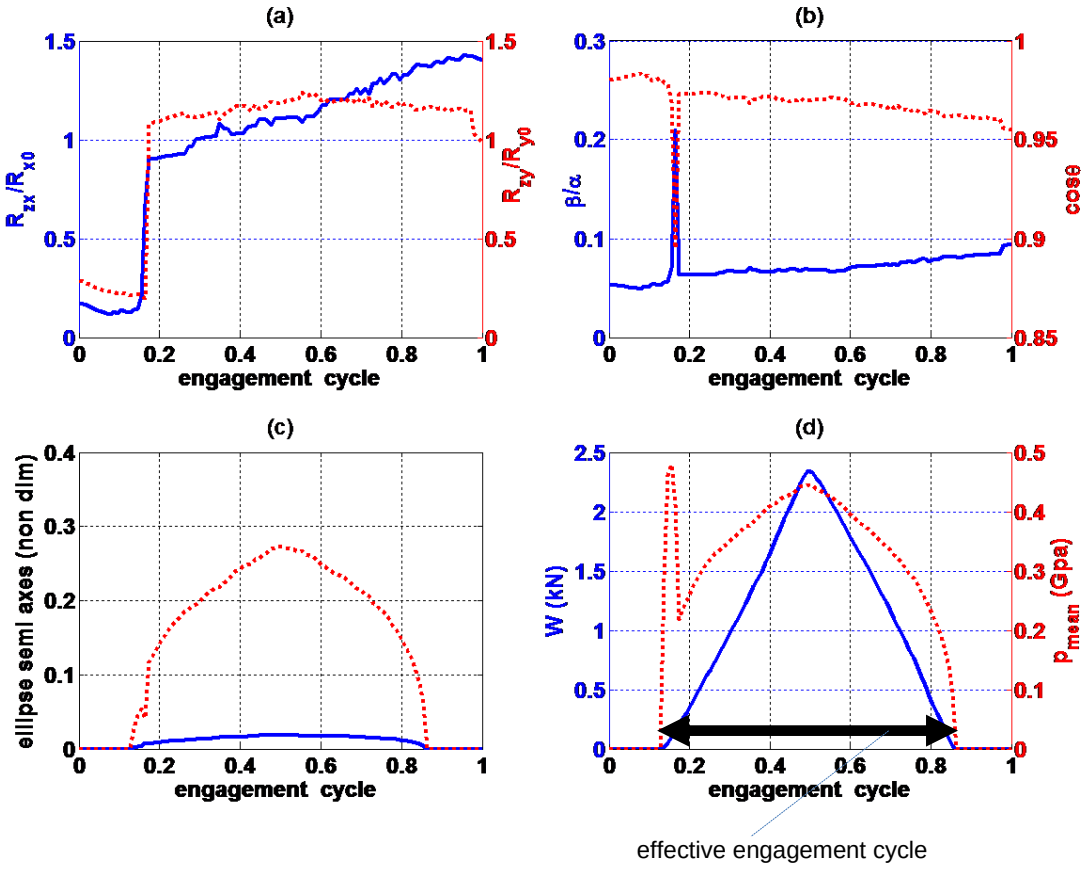

Figure 4.10- Geometric and load factors; (a) Radii of curvature, ——— $\hat{R}_{zx}$, ... $\hat{R}_{zy}$, **(b)** ——— β/α, ... $\cos\theta$, **(c)** ——— a_{axis}, ... b_{axis}, **(d)** ——— W, ... p_{mean} **. The pinion torque is equal to 50Nm.**

The basic geometric and loading factors are presented in Figure 4.10. The radii of curvature are depicted in dimensional form with respect to their mean value whereas the semi axes of the contact ellipse are divided by the mean value of R_{zx}. The radii of curvature at the first instances of the contact take relatively low values (Figure 4.10a); hence from equations (4.21) and (4.22), the contact ellipse covers a limited area on the gear flank resulting in the observed pressure spikes of Figure 4.10d. Another important observation from the last figure is that there is no load transmission for a considerable portion of the engagement cycle; even though TCA

predicts that the flank is under contact. Therefore, a contradiction exists between the effective and the calculated value of the engagement cycle from equations (4.17) and (4.18). An explanation will be given by examining the effect of input torque to the teeth contact properties.

4.3.2.5 The input torque effect

To determine the role of pinion external loading, additional TCA will be conducted for different input torque values; subsequently the contact parameters will be compared.

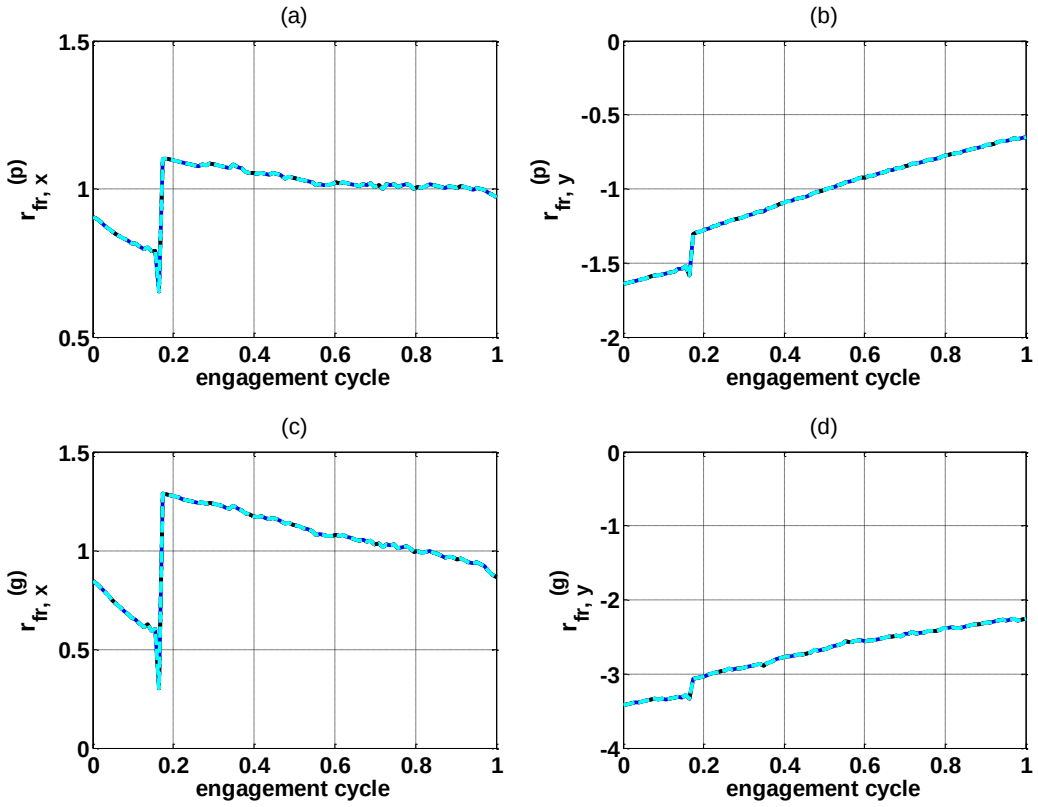

Figure 4.11- Surface velocity radii with respect to input torque; (a) $r_{fr,x}^{(p)} / R_{zx0}$ **, (b)** $r_{fr,y}^{(p)} / R_{zx0}$ **, (c)** $r_{fr,x}^{(g)} / R_{zx0}$ **, (d)** $r_{fr,y}^{(g)} / R_{zx0}$ **50Nm, 100Nm, 200Nm, 300Nm)**

Figure 4.11 shows the effect of input torque on the surface velocity radii. It can be seen that the latter are independent of the torque magnitude implying that the orientation of the contact ellipse remains unaffected. The same conclusions can be drawn from Figure 4.12 where the equivalent radii of curvature are depicted. As a

result, the contact position remains fixed regardless of the applied loading conditions.

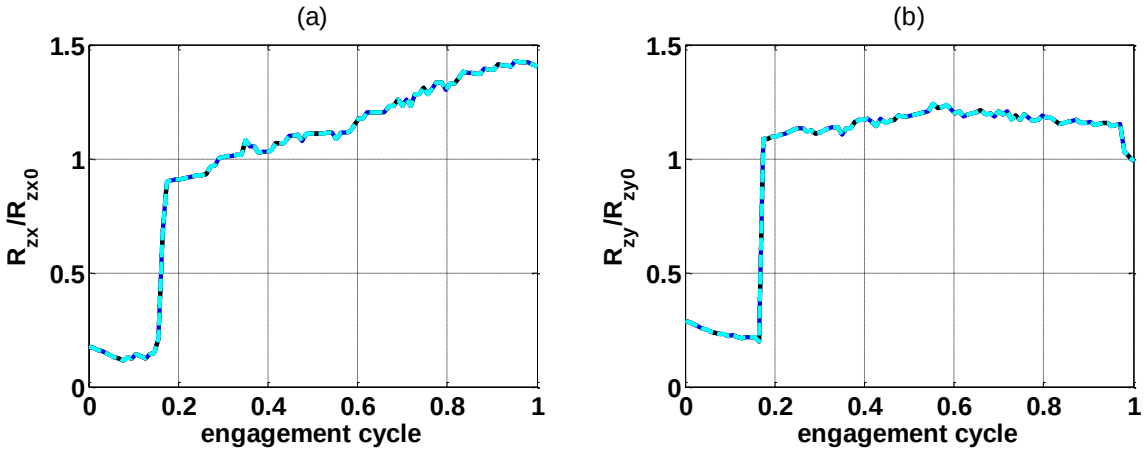

Figure 4.12- Radii of curvature with respect to input torque; 50Nm, 100Nm, 200Nm, 300Nm

The effect of input torque on the applied load, mean pressure and size of the contact zone is illustrated in Figure 4.13. In this case, the input torque affects all the above quantities. Increased torque results in greater applied load, which in turn causes an enlarged contact area. The combined effect is also reflected in the mean pressure which also rises with load. A second crucial remark is the extension of the effective engagement cycle with the ascent of external loading.

The previous fact becomes more obvious if the effective contact ratio is recalculated with an alternative version of equation (4.17) by using the effective engagement cycle instead. The ratio of the effective to the nominal contact ratio is plotted with respect to the input torque in Figure 4.14. It can be seen that the effective contact ratio approaches the nominal one as the input torque increases.

The overall conclusion from LTCA is that the geometric properties (curvature and surface velocity radii) remain unaffected by the torque fluctuation. Nonetheless, the loading conditions, the dimensions of the contact zone and the effective duration of the contact are significantly altered. Since the dynamic model needs to be established for a wide input torque range (eq.3.18), then the contact load distribution on the engagement cycle needs to be adjusted for the torque. This is due to the fact

that the dimensions of the contact zone and the mean pressure are dependent on the load itself as seen in equations (4.21) - (4.23).

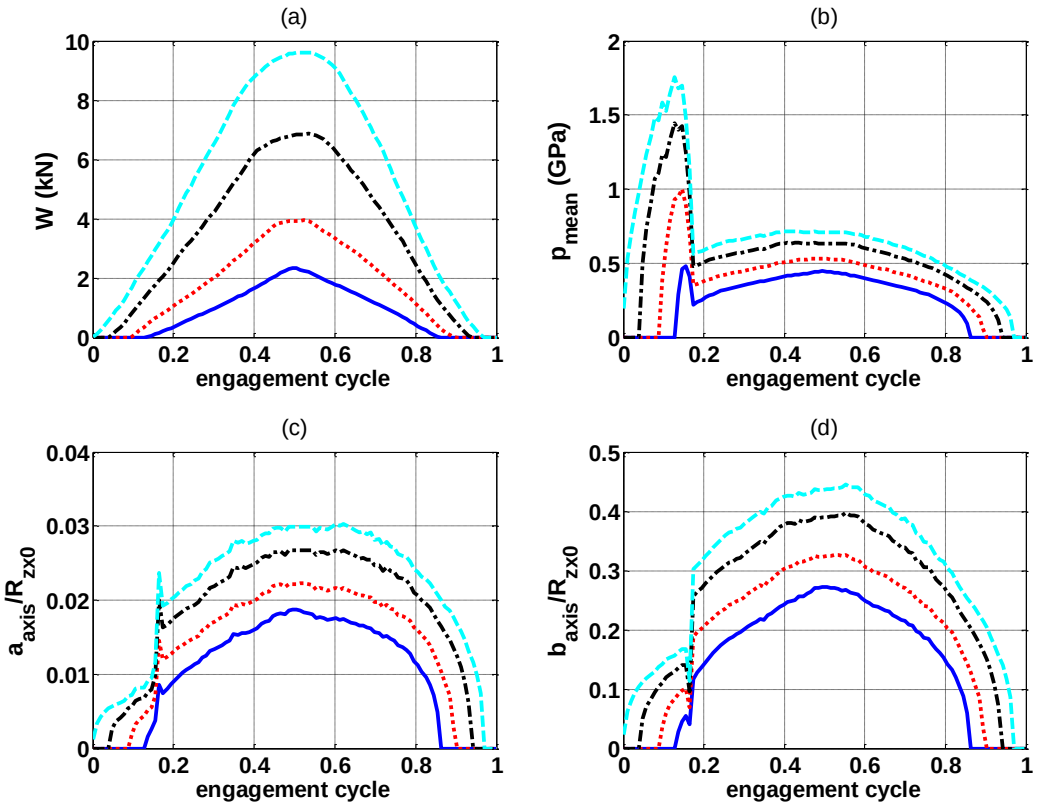

Figure 4.13- Effect of input torque on the applied load, mean pressure and dimensions of contact ellipse; (a) contact ellipse minor semi axis a_{axis}/R_{zx0}, (b) contact ellipse major semi axis b_{axis}/R_{zx0}, (c) contact load W and (d) mean contact pressure p_{mean} ; 50Nm, 100Nm, 200Nm, 300Nm

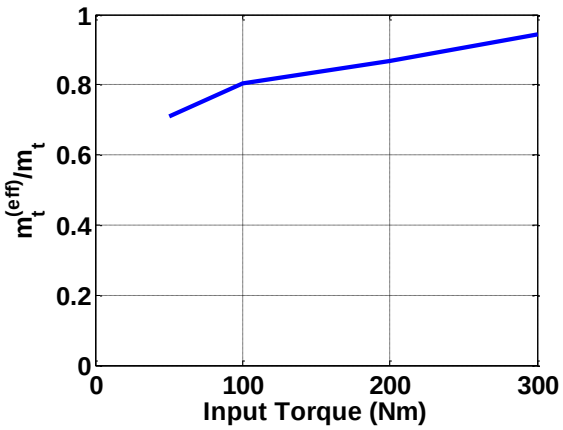

Figure 4.14- Ratio of effective contact ratio to the nominal one

4.3.2.6 Coupling of contact properties with the dynamic model

All the previously presented teeth contact parameters refer to quasi-static TCA. The coupling with the dynamic model is implemented in two ways; initially by using equations (4.3) - (4.4) and (4.7) - (4.8). The mean angular velocities ω_p and ω_g are substituted with the instantaneous values of $\dot{\varphi}_p$ and $\dot{\varphi}_g$ that arise from the dynamic analysis. By this means, the nonlinearities caused by the fluctuation of the angular velocities will be taken into account, similarly to the modelling approach of Vaishya and Singh (2003).

The second link between dynamics and tribology is identified in the influence of the dynamic load. Due to parametric resonances seen frequently in gear systems, the dynamic load can escalate considerably at certain operating conditions. Such an event will cause increased values of the contact load. The latter is influencing explicitly the formation of the lubricant film. Nevertheless, this dependence is usually weak under EHL conditions as shown analytically by Grubin (1949). Yet, another indirect influence exists due to the change of lubricant properties under piezo-viscous conditions. The extremely high levels of contact pressure cause the shear stress to exceed the Eyring limit value so that a non-Newtonian treatment is necessary.

For the above reasons, while taking into account the effect of contact load in the formation of the contact zone, a loading sharing function needs to be defined. Hence

the overall dynamic load can be shared into the individual flanks in contact based on the quasi-static TCA. The load sharing factor can be easily calculated by division of the contact load on the flank under consideration to the overall transmitted load on the gear member. A similar technique was followed for spur and helical gears (Vaishya and Singh, 2001; He et al., 2007). Therefore:

$$lf = \frac{W_i}{W_{total}} \qquad \textbf{(4.24)}$$

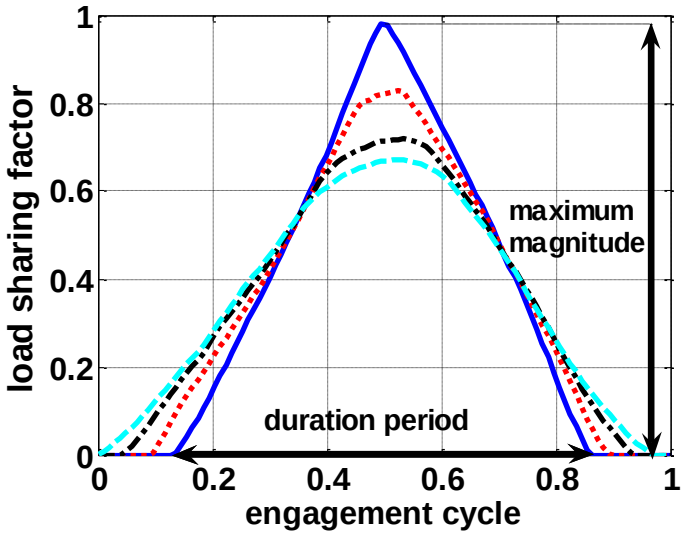

Figure 4.15- Load sharing factor for different values of input torque ——50Nm, ……100Nm, – . –200Nm, – – –300Nm

The shape of load sharing factor with respect to different torque levels during the engagement cycle is seen in Figure 4.15. Its significance is dual for the purposes of the dynamic analysis; in the first place it yields the percentage of dynamic load applied on each mating flank and at the same time it defines the idle period of the engagement cycle. It is characterized by two quantities; its maximum magnitude and its duration, which is naturally equal to the effective engagement cycle. It is obvious that as the external input torque rises, the maximum value of the load sharing factor drops and the duration period increases. This is due to the increase on the effective

engagement cycle causing the effective contact ratio to reach the nominal value of one, showing consistency with the findings of Figure 4.14.

To summarize the remarks of TCA, there are two types of parameters required for the link between the tribological and dynamic analysis. The first type is independent of the external loading conditions and depends only on the instantaneous contact position, as defined within the engagement cycle. These set of parameters involve the surface velocity and curvature radii. On the other hand, the second type of contact properties is associated with the specific operating conditions. This type involves mainly the load carrying capacity of the gear pair which is defined by the load sharing coefficient. If the contact load is defined, a set of additional properties affecting the lubricant rheology can be determined; for instance the mean contact pressure.

The contact parameters are inserted into the numerical model through an interpolation technique. By this manner, the combined effect of numerical integration of equations of motion and quasi-static contact analysis is obtained. This an efficient way to account for the geometrical complexities posed by hypoid gear transmissions.

4.3.3 Film thickness calculation

The film thickness determination is a crucial part of the tribological analysis. A plethora of factors need to be considered concurrently; the pressure distribution along the conjunction is combined with elastostatic deformation and lubricant fluid properties.

As stated earlier, a numerical solution of the problem would require a significant amount of computation (Xu et al, 2007; Holmes et al, 2005). Therefore, in this work, the estimation of the lubricant film thickness will be based on analytical (Grubin, 1949) or extrapolated formulae (Mostofi and Gohar, 1982; Chittenden et al, 1985). The above expressions convey the lubricant film magnitude along the parallel flanks' region; hence they can be employed for the approximation of the frictional excitation which is the ultimate objective of the tribological analysis.

4.3.3.1 One dimensional analysis

The first approach maintains the assumption that the lubricant entrainment takes place along the minor axis of contact ellipse (Figure 4.4). A similar assumption has been adopted by Xu and Kahraman (2007). By this means the velocity components of both gear surfaces along y - direction will be neglected and only the x - components will be taken into account.

The implemented method is purely analytical and is attributed to Grubin and Ertel (1949). The main concept is the introduction of a reduced pressure:

$$q = \frac{1}{\alpha}\left(1 - e^{-\alpha p}\right) \qquad \textbf{(4.25)}$$

Thus the problem can be treated in a pseudo-isoviscous manner in the following form of Reynolds equation:

$$\frac{dq}{dx} = 6U\eta_0\left(\frac{h - h_c}{h^3}\right) \qquad \textbf{(4.26)}$$

The high load carrying capacity was attributed to the shape deformation of the mating surfaces. The pressure is therefore maximised on a wide region of the contact area around the centre of the footprint, forcing the reduced pressure gradient dq/dx to be equal to zero according to equation (4.25). Consequently, from equation (4.26) the film thickness will be equal to h_c, forming a nearly parallel profile (denoted by h_0) as evidenced by experimental observations (Gohar, 2001). The oil film in the inlet region is defined by a superposition of the parallel and the elastic deformation:

$$h(x) = h_0 + h_s(x) \qquad \textbf{(4.27)}$$

The second term in the above equation can be approximated by an expression derived from elasto-statics; substitution in equation (4.26) and integration while assuming fully flooded inlet conditions leads to the following estimation of the parallel film thickness (Gohar, 2001):

$$\frac{h_0}{R_{zx}} = 1.212\left(\frac{\alpha\eta_0 U}{R_{zx}}\right)^{3/4}\left(\frac{W}{E_r {R_{zx}}^2}\right)^{-1/12}\psi^{2/3} \qquad \textbf{(4.28)}$$

The reduced elastic modulus E_r is:

$$\frac{1}{E_r} = \frac{1}{\pi}\left(\frac{1-{\nu_1}^2}{E_1} + \frac{1-{\nu_2}^2}{E_2}\right)$$

Where: E_1, E_2 are the Young's moduli of the contacting bodies and ν_1, ν_2 are the corresponding Poisson's ratios.

The effect of gear geometry is described by the equivalent radius of curvature R_{zx} along the sliding direction. The parameter ψ is a correction factor appended to the original Grubin's formula by Gohar (2001) to take into account the side leakage from an elliptical conjunction:

$$\psi = \left(1 + \frac{2}{3}\frac{R_{zx}}{R_{zy}}\right)^{-1} \qquad \textbf{(4.29)}$$

Some important assumptions need to be discussed. The lubricant film evaluation described by eq.(4.28) is derived by a form of Reynolds equation by considering Newtonian fluid behaviour. However, this expression can also approximate non Newtonian flow (Gohar, 2001); yet the difference in lubricant behaviour will be introduced by the calculation of the frictional force. Additionally, the considered

simplified form of Reynolds equation does not include the effect of surface texture; this effect will be introduced again in the calculation of boundary friction by implementing the formulation of Greenwood and Tripp (1970). It is also important to mention that the analytical solution attributed to Grubin implies fully flooded inlet conditions, meaning that the pressure inlet lies far enough from the centre of the contact (Gohar and Rahnejat, 2008).

The one-dimensional lubricant entrainment cancels the kinematic effect of the y-velocity component. As a result, the entraining velocity present in the film thickness estimation formula will be calculated as follows (Vaishya and Singh, 2001b):

$$U = \frac{1}{2}\left(r_{fr,p,x}\dot{\varphi}_p + r_{fr,g,x}\dot{\varphi}_g\right) \qquad \textbf{(4.30)}$$

4.3.3.2 Two dimensional analysis

The analysis previously described implies that the lubricant entrainment is taking place along the minor axis of the contact ellipse. Nonetheless, this approximation is not valid for hypoid transmissions. The orientation of the contact ellipse with respect to the lubricant entrainment can be determined from TCA.

A typical representation of the contact zone size and its orientation can be seen in Figure 4.16. The graphs are drawn for three different torque values with respect to the engagement cycle for 50Nm of input torque. The axes are non-dimensional with respect to the maximum value of the major axis for $T_p = 50Nm$. The lubricant entrainment motion is in the X- direction. It is clear that only the size of the contact area is sensitive to input torque whereas its orientation remains unaffected. Furthermore the assumption that lubricant entrainment takes place along the X-axis is questionable; therefore a two dimensional formulation is required for determining the oil film magnitude.

Yet, no analytical expressions similar to equation (4.28) can be found for the two dimensional problem; alternatively extrapolated expressions will be used. These formulae are derived from numerical solutions assuming isothermal fully flooded inlet conditions. During regression analysis, a variety of ellipticity ratios and entraining

angles have been investigated but just a few values of rolling speeds. The variables used herein are in the form of non-dimensional groups associated with load, velocity, lubricant and material properties.

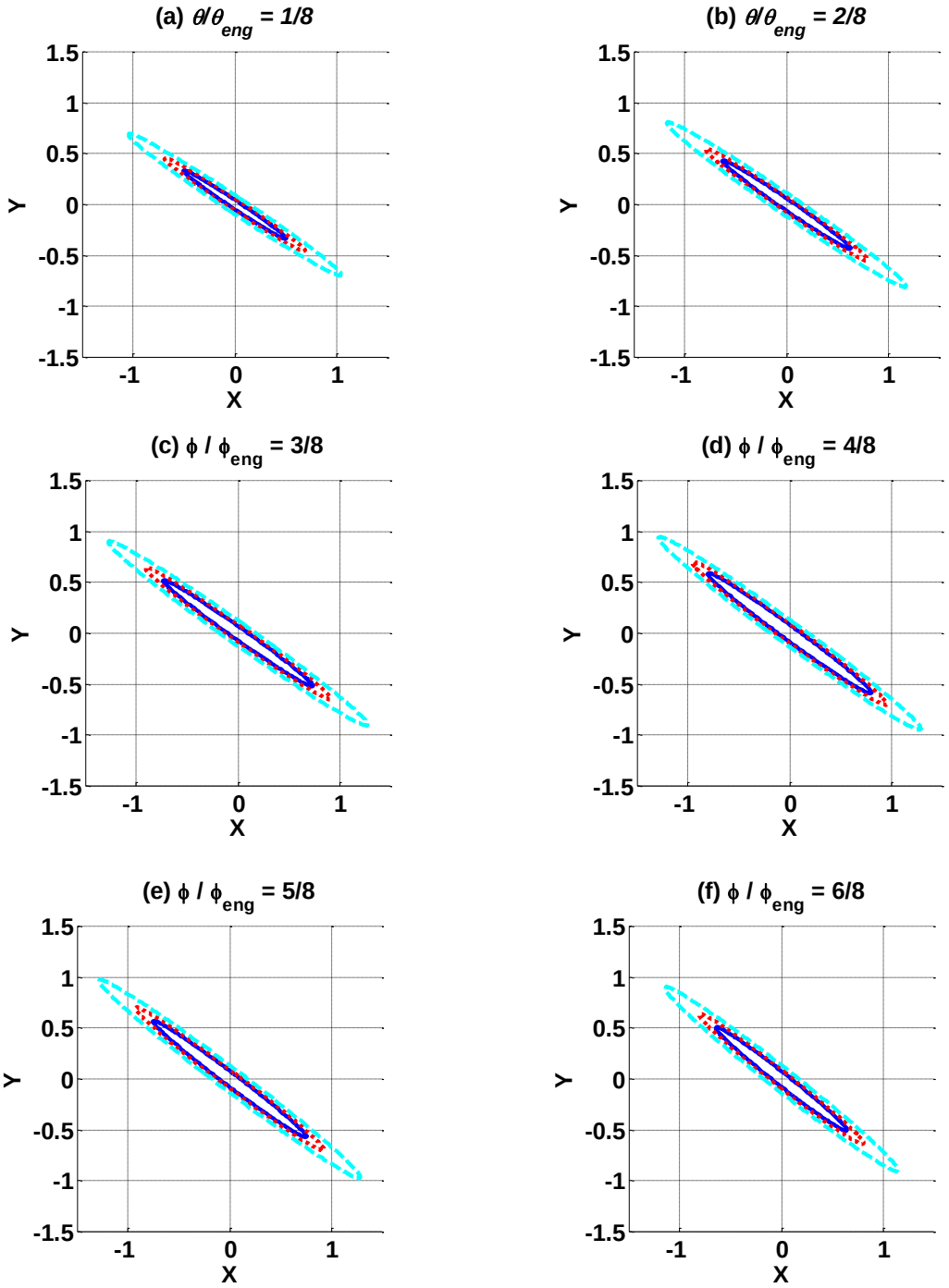

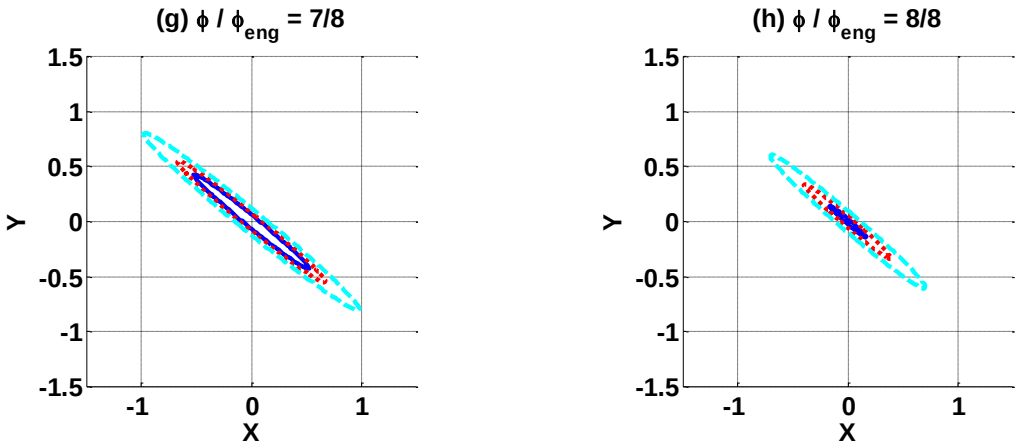

Figure 4.16- Orientation of the contact ellipse during the engagement cycle; (a) $\varphi = 1/8\varphi_{eng}$**, (b)** $\varphi = 2/8\varphi_{eng}$**, (c)** $\varphi = 3/8\varphi_{eng}$**, (d)** $\varphi = 4/8\varphi_{eng}$**, (e)** $\varphi = 4/8\varphi_{eng}$**, (e)** $\varphi = 5/8\varphi_{eng}$**, (f)** $\varphi = 6/8\varphi_{eng}$**, (g)** $\varphi = 7/8\varphi_{eng}$**, (h)** $\varphi = 8/8\varphi_{eng}$**. Lubricant entrainment is taking place on X-direction. 50Nm, 100Nm, , 300Nm**

An approximation of the central film thickness under two dimensional flow conditions has been proposed by Chittenden et al (1985):

$$H_{cen} = 4.31\left(U_e^*\right)^{0.68}\left(G_e^*\right)^{0.49}\left(W_e^*\right)^{-0.073}\left\{1-\exp\left[-1.23\left(\frac{R_s}{R_e}\right)^{2/3}\right]\right\} \quad \textbf{(4.31)}$$

In the above equation, R_e and R_s are the orthogonal radii of curvature of the bodies in parallel and vertical directions with respect to entraining velocity $U = \sqrt{\left(u^{(p)}+u^{(g)}\right)^2+\left(\upsilon^{(p)}+\upsilon^{(g)}\right)^2}$:

$$\frac{1}{R_e} = \frac{\cos^2\psi_1}{R_x} + \frac{\sin^2\psi_1}{R_y} \quad \textbf{(4.32)}$$

$$\frac{1}{R_s} = \frac{\cos^2\psi_1}{R_y} + \frac{\sin^2\psi_1}{R_x} \quad \textbf{(4.33)}$$

The dimensionless groups are defined as follows:

$$U_e = \frac{\pi\eta_0 U}{4E_r R_e},\ W_e = \frac{\pi W}{2E_r R_e^2},\ G_e = \frac{2}{\pi}(E_r\alpha),\ H_{cen} = \frac{h_0}{R_e}$$

The lubricant entraining motion takes place at an angle ψ_1 to the minor axis of the contact ellipse (Figure 4.4); hence:

$$\psi_1 = \arccos\left(\frac{u^{(p)} + u^{(g)}}{U}\right) \qquad \textbf{(4.34)}$$

The following formula yields the minimum value of the lubricant film at the point where the contact pressure spike occurs (Mostofi and Gohar, 1982):

$$G^{*2}h_m^* = 3.51\left(U^*G^{*4}\right)^n\left(W^*G^{*3}\right)^m\left(1-0.683e^{-0.669e_p*}\right)\left(1-0.559\cos^3\psi_1'\right) \qquad \textbf{(4.35)}$$

The dimensionless groups are defined with the following set of equations:

$$U^* = \frac{U\eta_0 K'}{R_x},\ W^* = \frac{WK'}{R_x{}^2},\ G^* = \frac{\alpha}{K'},\ h_m^* = \frac{h_m}{R_x} \qquad \textbf{(4.36)}$$

Despite the fact that the previous expression derives the minimum value of film thickness, it can be used for the purposes of this study; for current operating conditions, minimum and central film magnitudes are very close. In this case the lubricant flow is at an angle ψ_1' relative to the y –axis (major axis of the contact ellipse); therefore:

$$\psi_1' = \arcsin\left(\frac{u^{(p)} + u^{(g)}}{\sqrt{\left(u^{(p)} + u^{(g)}\right)^2 + \left(\upsilon^{(p)} + \upsilon^{(g)}\right)^2}}\right) \qquad \textbf{(4.37)}$$

The entraining velocity in this case is defined as the mean value of the individual surface velocities:

$$U = \frac{1}{2}\sqrt{\left(u^{(p)} + u^{(g)}\right)^2 + \left(\upsilon^{(p)} + \upsilon^{(g)}\right)^2}$$

The main parameters taking part in the calculation of the film thickness are presented in Table 4.3.

Table 4.3- Variables used in film thickness expressions

Variable	Physical Meaning
q	reduced pressure
p	pressure
h_c or h_m	Film thickness at maximum pressure
h_0	Film thickness in the parallel region
α	Pressure viscosity coefficient
E_r	Reduced elastic modulus
η_0	lubricant viscosity at inlet
ψ	Side leakage factor
R_e	Radius of curvature parallel to the entraining velocity
R_s	Radius of curvature normal to the entraining velocity
ψ_1'	Entraining angle with respect to y-axis
$U_e, W_e, G_e\ H_{cen}$	Dimensionless Groups (Chittenden et al, 1985)
U^*, W^*, G^*, h_m^*	Dimensionless Groups (Mostofi and Gohar, 1982)
$K' = \left(1 - \nu_1^2\right)/\pi E_1$	Parameter (Chittenden et al, 1985)
$m = \left(0.0865\cos^2\psi_1' - 0.045\right)$	Parameter (Mostofi and Gohar, 1982)

$n = \left(0.649 - 0.0875\cos^2 \psi_1'\right)$	Parameter (Mostofi and Gohar, 1982)
$e_p^* = \frac{b_{axis}}{a_{axis}}$	Ellipticity ratio

The above extrapolated equations rely on regression analysis of numerical results; hence their accuracy is optimized at certain range of the dimensional groups. Nonetheless, they represent a useful tool for modelling the effect of two dimensional flow without adding excessive complexity to the mathematical formulation. A combination of pure analytical treatment (Grubin, 1949) and extrapolated formulae (Mostofi and Gohar, 1982; Chittenden et al, 1985) can yield useful conclusions on the boundaries of film thickness during an engagement cycle. It should also be noted that all the film thickness predictions assume isothermal conditions. As a result, the predicted film has been proved to be overestimated compared to experimental investigations due to the reduction in the inlet lubricant viscosity appointed to shear heating. Thus a thermal correction factor (ϕ_∞) is applied to the isothermally predicted lubricant film (Gohar, 2001):

$$h_{0T} = h_0 \cdot \phi_\infty$$

$$\phi_\infty = \frac{1}{1 + 0.182 \cdot L^{*0.548}}$$

In the above expression (L^*) is a constant depending on entraining velocity, a constant derived by Houpert (1985), lubricant inlet viscosity and thermal conductivity.

4.3.4 Effect of Temperature and Pressure

Besides the effect of heat generation in the lubricant film thickness due to the change of inlet viscosity, equally important is the effective viscosity inside the conjuction leading to the calculation of friction. The dependence of effective lubricant viscosity on the combined influence of temperature and pressure can be estimated by using the equation proposed by Houpert (1985):

$$\eta_e = \eta_0 \exp(a^* p) \qquad \textbf{(4.38)}$$

$$a^* p = \left[\ln(\eta_0) + 9.67\right]\left\{\left(\frac{\Theta_e - 138}{\Theta_0 - 138}\right)^{-S_0}\left(1 + 5.1\cdot 10^{-9} p\right)^Z - 1\right\}$$

The above expression conveys the value of the effective viscosity η_e due to temperature rise from a reference temperature Θ_0 (usually at inlet) to a current temperature Θ_e . Constants Z and S_0 are independent of temperature and pressure:

$$Z = \frac{\alpha}{5.1\cdot 10^9\left(\ln(\eta_0) + 9.67\right)},\ S_0 = \frac{\beta\left(\Theta_0 - 138\right)}{\left(\ln(\eta_0) + 9.67\right)}$$

The prediction of temperature rise in an EHD contact is based on the energy conservation principle. In a two dimensional form, it can be expressed as follows (Gohar, 2001):

$$\nu u\theta\frac{\partial p}{\partial x} + \eta\left(\frac{\partial u}{\partial z}\right)^2 = \rho u C_p\frac{\partial\theta}{\partial z} - k\frac{\partial^2\theta}{\partial z^2} \qquad \textbf{(4.39)}$$

On the left hand side of the above equation, the first term expresses the compressive heating caused by the pressure gradient while the second term represents the viscous heating. The remaining terms appearing at the right hand side are associated to the convection cooling, expressing the heat carried away along the x-direction of the lubricant and conduction cooling along the film thickness.

The validity of neglecting the convection term can be checked by considering the contribution of each of the above terms separately. This approach (Gohar and Rahnejat, 2008) leads to the definition of Peclet number, expressing the quotient of convected to conducted heat:

$$Pe = \frac{Uh_0^2 \rho C_p}{2ka_{axis}} \qquad \textbf{(4.40)}$$

The effect of convection can be overlooked if Peclet number is proven to be low $(Pe << 1)$. In this case:

$$\nu u\theta \frac{\partial p}{\partial x} + \eta\left(\frac{\partial u}{\partial z}\right)^2 = -k\frac{\partial^2 \theta}{\partial z^2} \qquad \textbf{(4.41)}$$

The parameters used in lubricant rheological properties and energy balance equations are shown in Table 4.4.

Table 4.4- Parameters in lubricant rheology-energy balance equation

Variable	Physical Meaning
η_e	Effective viscosity at temperature Θ_e
$\Theta_e(K)$	Current lubricant temperature
$\Theta_0(K)$	Reference (inlet) temperature
Z , S_0	Constants
β	Thermo-viscous coefficient
ν	Coefficient of thermal expansion
ρ	Lubricant density
C_p	Specific heat
k	Thermal conductivity
Pe	Peclet number

4.3.4.1 Newtonian treatment

The individual terms appearing in the simplified energy equation (4.41) can be integrated separately and eventually yield an analytical expression for the temperature rise inside the conjunction. The formulation presented in this section is based on an individual consideration of the various contributions while implying isoviscous conditions across the film thickness (Figure 4.3).

Initially, the conductive cooling is considered for a lubricant column of width dx and height h. The temperature gradient at a certain position x is assumed to vary linearly (Gohar and Rahnejat, 2008) with a rate of $\frac{\delta\theta}{h}$. Integration of the conduction quantity with respect to z yields the corresponding heat flow:

$$(dx)k\int_0^h\left(\frac{\partial^2\theta}{\partial z^2}\right)dz=(dx)k\frac{\delta\theta}{h} \qquad \textbf{(4.42)}$$

Furthermore, if a linear temperature rise is imposed along the conjunction (x direction), $\delta\theta=x\frac{\Delta\theta}{a_{axis}}$; $\Delta\theta$ being the maximum temperature rise. If eq.(4.42) is integrated with respect to x:

$$conductive\,cooling=\frac{k\Delta\theta}{a_{axis}h}\int_0^{a_{axis}}xdx=\frac{k(\Delta\theta)a_{axis}}{2h} \qquad \textbf{(4.43)}$$

Likewise, if a linear pressure gradient is assumed along $x-$direction, $\frac{\partial p}{\partial x}=\frac{p_{\max}}{a_{axis}}$, double integration of the compressive heating term with respect to x and z:

$$compressive\ heating = \int_0^{a_{axis}} \int_0^h \nu u \theta_e \left(\frac{\partial p}{\partial x} \right) dxdz = \nu u \theta_e p_{\max} h \qquad \textbf{(4.44)}$$

Moreover, under Newtonian conditions: $\eta \left(\frac{\partial u}{\partial z} \right)^2 = \eta \left(\frac{\Delta U}{h} \right)^2$, hence by integrating the viscous heating term with respect to x and z:

$$viscous\ heating = \int_0^{a_{axis}} \int_0^h \eta \left(\frac{\partial u}{\partial z} \right)^2 dxdz = \frac{\eta (\Delta U)^2 a_{axis}}{h} \qquad \textbf{(4.45)}$$

All individual integrations resulting into equations (4.43) - (4.45) can be combined with equation (4.41) to derive an approximate analytical expression of the maximum temperature rise inside the conduction:

$$\nu u \theta_e p_{\max} h + \frac{\eta (\Delta U)^2 a_{axis}}{h} = \frac{k(\Delta \theta) a_{axis}}{2h} \qquad \textbf{(4.46)}$$

Since $\theta_e = \theta_i + \Delta \theta$,

$$\Delta \theta = \frac{\nu u \theta_i p_{\max} h + \frac{\eta (\Delta U)^2 a_{axis}}{h}}{\frac{k a_{axis}}{2h} - \nu u p_{\max} h} \qquad \textbf{(4.47)}$$

The above expression defines the rise in the lubricant temperature with respect to inlet conditions. It is clear that the temperature rise is a function of the film thickness and effective viscosity in the parallel region. As a result, an iterative process needs to be established by imposing initially a temperature rise guess. The lubricant effective viscosity needs to be adjusted based on current temperature and pressure conditions with a simultaneous calculation of film thickness. For the last calculation, effective viscosity is only adjusted towards temperature. This is due to the fact that the film thickness formulae include implicitly the pressure-viscosity adjustment in the

form of reduced pressure gradient, $\frac{dq}{dx}$. The next step involves the comparison of the imposed temperature rise to the one predicted by equation (4.47). The process will be repeated until convergence of the two temperature values is achieved.

It should also be noted that equation (4.47) is an approximate formula. It is based on individual integrations of all the heat transfer contributions; furthermore it relies on an isoviscous hypothesis across the lubricant film (z-direction). These assumptions lack accuracy; however an analytical estimation of the lubricant temperature can be derived. The same expression has been used by De la Cruz et al (2012) for accessing the thermal effects of lightly loaded EHL conjunctions in manual automotive transmission systems.

4.3.4.2 Non Newtonian rheological model

Under piezovicous EHL conditions, Newtonian treatment results often in unrealistic estimation of friction. This is due to the high values of encountered pressure under high contact loads, pushing the lubricant effective viscosity into high orders of magnitude (Gohar and Rahnejat, 2008). For this reason, an alternative rheological model needs to be established, to address this behaviour.

Thin films formed in gear teeth pair conjunctions are often subject to thermal non-Newtonian shear. This behaviour is determined by a limiting shear stress, first defined by Eyring (1936). Johnson and Greenwood (1980) showed that in the flat parallel region of a thin elasto-hydrodynamic film the dominant mechanism giving rise to contact temperature is viscous shear at the effective viscosity of the lubricant:

$$\eta_e \frac{\partial u}{\partial z} = \eta\dot{\gamma} = \tau_0 \sinh\left(\frac{\tau}{\tau_0}\right) = \tau^* \qquad \textbf{(4.48)}$$

Because of the thin dimension of the film, any variation in the Eyring shear stress τ_0 across the film may be neglected. The heat generated through shear is conducted away through the bounding surfaces in contact (Gohar and Rahnejat, 2008; Johnson and Greenwood, 1980), thus the energy equation becomes:

$$\tau \frac{\partial u}{\partial z} = \frac{\tau \tau^*}{\eta_e} = -K \frac{\partial^2 \theta}{\partial z^2} \qquad \textbf{(4.49)}$$

To simplify the problem, some assumptions are adopted. Both bounding surfaces are assumed to act as *perfect* conductors of heat; thus, emitting away from the conjunction the same amount of energy. This implies that they will remain on the temperature of the bulk oil inlet. Indeed Crook (1961) has shown that only a trivial error is introduced by this approximation. Additionally, all the properties inside the conjunction $(\eta, \tau_0, \beta^*, K, a^*)$ are characterized by their mean values along the $x-$ direction. Using these assumptions, the original set of equations derived by Johnson and Greenwood (1980), are given in the following form (Gohar, 2001):

$$\sinh\left(\frac{4A^2 X^* X}{\Delta U^*}\right) = \Delta U^* \frac{X^*}{X} \qquad \textbf{(4.50)}$$

The various parameter groups appearing in the above expression are yielded by:

$$X = \left\{\exp\left[\beta^*\left(\Delta\bar{\theta}\right) - 1\right]\right\}^{1/2} \qquad \textbf{(4.51)}$$

$$X^* = \frac{\sinh^{-1} X}{\left(1 + X^2\right)^{1/2}} \qquad \textbf{(4.52)}$$

$$\Delta U^* = \frac{(\Delta U)\bar{\eta}_s}{\bar{\tau}_0 h_0} \qquad \textbf{(4.53)}$$

$$\eta_s = \eta_0 \exp\left(a^* p_{mean}\right) \qquad \textbf{(4.54)}$$

The sliding velocity ΔU is obtained from equation $\Delta U = \sqrt{\left(u^{(p)} - u^{(g)}\right)^2 + \left(\upsilon^{(p)} - \upsilon^{(g)}\right)^2}$ (4.12) whereas the surface lubricant viscosity $\bar{\eta}_s$ is defined at inlet temperature and mean pressure. The

governing equation (4.50) can be solved in an iterative manner, using an initial guess value of temperature rise $\Delta\bar{\theta} = \bar{\theta}_e - \theta_0$. This yields the effective temperature and viscosity based on equations (4.38) and (4.41). Note that the viscosity term in film thickness formulae is adjusted for temperature only, similar to the discussion of the Newtonian case.

4.3.5 Calculation of viscous and boundary friction

The surfaces of gear flanks are rough and the thickness of lubricant film may be insufficient to guard against asperity pair interactions. Typical values of composite root mean square roughness (R_q) vary from $0.4\mu m$ to $2.3\mu m$, depending on the method of finishing (Gohar, 2001). Then, the Stribeck oil film parameter $\lambda = \dfrac{h}{R_q}$ can be obtained at any instant for each pair of interacting gear teeth flanks. The surface roughness of gear flanks is assumed to be represented by a Gaussian distribution according to the roughness parameter $\zeta\kappa\sigma$. Then, the asperity area of contact is obtained as (Teodorescu et al, 2003):

$$A_a = \pi^2 (\zeta\kappa\sigma)^2 A F_2(\lambda) \qquad \textbf{(4.55)}$$

The statistical function $F_2(\lambda)$ is defined according to the formula:

$$F_2(\lambda) = \frac{1}{\sqrt{2\pi}} \int_{\lambda}^{\infty} (s-\lambda)^2 e^{-s^2/2} ds \qquad \textbf{(4.56)}$$

Figure 4.17 shows a polynomial fit of the above function with respect to the Stribeck oil film parameter λ.

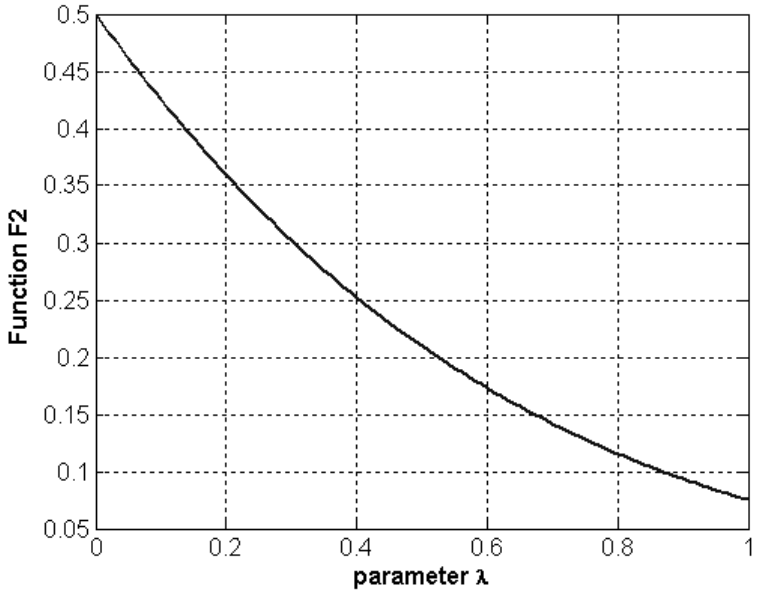

Figure 4.17- Function representing statistical asperity distribution

The contribution due to viscous friction is obtained as:

$$F_v = \tau(A - A_a) \qquad \textbf{(4.57)}$$

For Newtonian treatment, the shear stress in the parallel region is mainly due to shear effect rather than the pressure gradient (Gohar, 2001). Therefore, the shear stress is yielded by:

$$\tau = \eta \frac{\partial u}{\partial z} \cong \eta_e \frac{\Delta U}{h_0} \qquad \textbf{(4.58)}$$

Alternatively, for an Eyring fluid, equation (4.48) will be used. The boundary friction is obtained as in (Greenwood and Tripp, 1970):

$$F_b = \tau_0 A_a + m P_a \qquad \textbf{(4.59)}$$

In the above equation, m is the pressure coefficient of the boundary shear strength (0.17 for steel on steel contact) (Theodorescu et al). The overall friction force is the sum of these two individual components of friction:

$$F_{fr} = F_v + F_b \tag{4.60}$$

Finally, the coefficient of friction μ is defined as the quotient of the total friction force at each flank to the corresponding dynamic mesh force:

$$\mu = \frac{F_v + F_b}{W} \tag{4.61}$$

It should be stressed that any temperature rise in the contact due to localised flash temperature of asperity pair interactions is assumed to have a negligible effect on the bulk lubricant effective viscosity.

A comment should be made with regard to the sense of friction force. The sign of friction force (and corresponding torque) is governed by the sign of the relative sliding velocity (Vaishya and Singh, 2003; Kar and Mohanty, 2007). If the latter is negative, friction opposes the pinion motion and assists the motion of the gear. The situation is reversed for the case of positive sliding velocity. Nevertheless, even though the friction torque on a pinion flank during an instant of the meshing cycle might be positive, the total friction torque exerted by all teeth pairs in contact, is always negative. The opposite applies for the gear member. The energy deficit induced by the generation of friction can be calculated from the algebraic sum of the power incurred from the frictional moments:

$$P_{deficit} = \dot{\theta}_p \cdot \sum_i \vec{r}_{fr,pi} \times \vec{F}_{fr,pi} + \dot{\theta}_g \cdot \sum_i \vec{r}_{fr,gi} \times \vec{F}_{fr,gi} \tag{4.62}$$

4.4 - Synopsis

This Chapter discussed the theory behind the inclusion of lubrication in the dynamic model. The modelling approach treated friction as an additional torsional excitation inducing further nonlinearities to the gear pair formulation.

Definition of friction guided the analysis through a series of elaborate steps; understanding the kinematics, deriving the necessary contact properties, determining the magnitude of the lubricant film, coupling with energy balance and temperature

rise and establishing more reliable rheological models. Throughout this process a necessary amount of simplifications was introduced so that analytical expressions can be implemented and efficiency in the computational power can be maintained.

Chapter 5 - Dynamic Response Analysis

5.1 - Introduction

The theoretical background describing the dynamics of a hypoid gear pair will be applied throughout this chapter, aiming at simulating numerically the power transmission behaviour under sets of typical vehicle operating conditions.

Dry conditions will be maintained and the derived results will be compared to the output of existing dynamic models. Observations will be made regarding the nonlinear nature of the system by identifying the regions of multiple solutions associated with contact loss and noise generation. After assessing the dynamic response over steady state cruising, the dynamic model will be expanded to coasting conditions.

The dynamic model investigated in this chapter is in accordance to the assumptions adopted previously in this thesis (Chapter 3). The current study is restricted to a torsional double–DOF model in order to capture the basic characteristics of the dynamic teeth mesh force.

5.2 - Solution methodology

The general problem is characterized by second order differential equations with nonlinearities (effect of backlash), varying coefficients (change of contact properties in hypoid transmissions) and complex forcing (static transmission error and angular velocity related external torques).

A multitude of solutions has been proposed for the treatment of simpler cases. Comparin and Singh (1989) solved the nonlinear problem with constant coefficients and the inclusion of only external forcing by using the Harmonic Balance Method (HBM) and numerical integration. Kahraman and Singh (1989) addressed the case of internal excitation in the form of kinematic transmission error and commented on the importance of initial conditions in successfully producing frequency response spectra. The mutual effect of backlash nonlinearity and time varying parameters was investigated by Padmanabhan and Singh (1995), by a combination of harmonic balance and shooting methods. Natsiavas et al (2000) matched perturbation

schemes to piecewise linear treatment techniques; hence restricting the problem to the solution of algebraic expressions. The Finite Element Method has also been used by Parker et al (2000) to define the gear pair dynamic response.

The nonlinearities associated to expressing the mesh stiffness and internal forcing in terms of pinion angle as well as the dependence of the resisting torque on the gear angular velocity have been examined by Theodossiades and Natsiavas (2001a, 2001b). Derivation of the periodic solutions in the traditional form of frequency response spectra was accomplished by numerical continuation techniques through the implementation of the solution continuation method (Doedel, 1981).

The inclusion of friction inside the gear dynamics induces additional complexities. Additional time varying parameters are introduced inside the equations of motion (Kar and Mohanty, 2006); the frictional torque nonlinearities have been discussed in the previous chapter. If the effect of oscillations in the angular velocities is neglected, the dynamic response and stability of the system can be studied through a combination of state transition matrix and Floquet theory (Vaishya and Singh, 2001a). However, if the sliding velocity perturbation is considered, an alternative methodology needs to be sought. Due the multiple harmonic terms involved, the potential application of harmonic balance method is proven to be inefficient (Vaishya and Singh, 2001b). Analytical treatment has been possible for the case of Coulomb friction models (Velex and Sainsot, 2002; Liu and Parker, 2009). Nevertheless, numerical integration has been favoured, with the 4^{th}-5^{th} order Runge-Kutta algorithm being one of the implemented methodologies (He et al, 2007).

When considering mechanical models of hypoid transmissions, the level of difficulty escalates. The number of time (angle) dependent parameters increase as the variation of the contact point inflicts a fluctuation of the equivalent contact radii (Eq. 3.36). Wang et al (2007) applied a numerical solution methodology to the problem, by using the Runge-Kutta (Strogatz, 2001) technique. Their analysis was based on hypothesis of a slow variation of the contact radii, enabling the reduction of the order of the system to a single DOF. This results in a positive definite system which can always achieve dynamic balance if the external forcing ratio is proportional to the gear ratio.

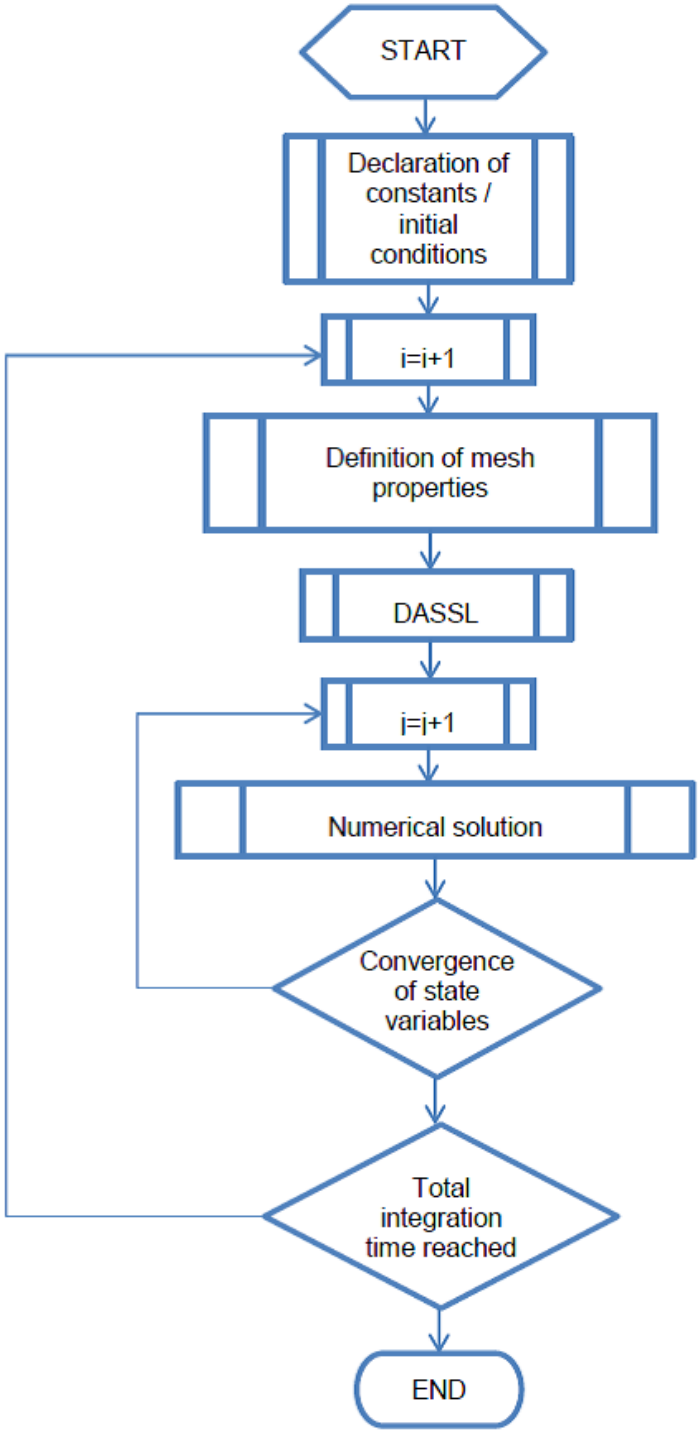

Figure 5.1- Flowchart of the fundamental mechanical model

Nevertheless, the reduction of the order of the system is an approximation which can yield significant deviations in the simulation process (Peng, 2010). This fact will be proven by comparing the simplified model (Wang et al, 2007) and the model proposed by this thesis. It will be shown that a change of variables can indeed be

implemented so that the response of the system can be expressed by a single quantity. However, the order of the system will be increased yielding a third order differential equation while the previous state variables are given as implicit functions of the new variable. This technique will be applied for determining the periodic solutions of the system with the solution continuation method by employing software AUTO (Doedel, 1981).

Furthermore, in order to overcome dynamic balance issues, the resisting torque needs to be related to the instantaneous angular velocity of the axle (Eq. 3.8) based on the formulation of Theodossiades and Natsiavas (2001a; 2001b). Considering the effect of friction as an additional source of nonlinearity, the analytical treatment of the problem becomes a challenge.

The simulation data presented hereby address the pair of dynamic models presented in Chapters 3 and 4. Their relation has been well identified in the preceding discussion. The fundamental mechanical model which can be short-termed as “dry” due to lack of tribological effects employs the DASSL subroutine integration scheme (Petzold, 1983). The source code is written in FORTRAN programming language and is preferred due to its high computational efficiency. The lubricated model which in fact is an extension of the “dry” case is solved by using the Runge-Kutta method implemented by MATLAB ode45 in-built solver. Despite being less efficient than a FORTRAN code, MATLAB has the advantage of matrix manipulation and availability of additional library functions able to solve systems of nonlinear algebraic equations inherent in the tribological consideration (Eq. 4.50).

5.3 - Fundamental Dynamic Model

The importance of the fundamental dynamic model lies on its definition; it presents the structure on which the tribological analysis is deployed. Inarguably, excluding the frictional excitation, the modelling principle is the same. Furthermore, the “dry” case is the platform for importing the new features of the current modelling approach; definition of dynamic transmission error as a time integral and dependence of the resistive torque on the angular velocity of the axle. Hence, the fundamental model can also be acknowledged as a means of validation and comparison to the existing formulations.

The computational algorithm is illustrated in Figure 5.1. It involves two internal loops; the first one (i-counter) is related to the integration time, whereas the second (j-counter) to the computational time, measuring the number of iterations needed to achieve convergence of the state variables. Both the absolute and relative convergence tolerances are set equal to $1*10^{-08}$ so as to ensure the accuracy and computational efficiency of the time integration. Convergence criteria might seem tight, nevertheless unavoidable given the strong nonlinearities inherent in the problem.

The mesh properties include the variant mesh stiffness, the contact radii and the internal excitation induced by the kinematic transmission error. The derivation procedure has been explained in Chapter 3 where analytical expressions have been derived to represent the numerical output. A Fourier series approximation in the form of (Eq. 2.36) has been proven to be adequate (Figure 3.12). The aforementioned quantities are defined with respect to the state variable of pinion angle rather that the integration time. This is favourable since the TCA is conducted quasi-statically hence the concept of time has a different meaning. Furthermore, using the pinion angle as independent variable permits the embracement of nonlinearities associated with its oscillatory nature (Theodossiades and Natsiavas, 2001a).

The numerical algorithm is launched by a set of initial conditions based on the driving conditions. When considering steady state cruising, the angular velocity of the axle can be addressed explicitly to the nominal vehicle speed. The later in turn defines the nominal input torque (Eq. 3.8). Due to the inherent connection of axle (crown gear) angular velocity and external forcing, it is reasonable to anticipate that the system will settle into the same state, regardless of the initially imposed angular velocity. The extent of this claim needs to be proven by the upcoming computational analysis. The system is also expected to exhibit parametric resonances and multiple solutions as a consequence of intrinsic parameter variation and nonlinear characteristics. The construction of frequency–response diagrams will be numerically achieved by conducting speed sweeps; numerical integration results at a certain vehicle speed will be used as the initial conditions for the next vehicle speed point. Therefore, an additional loop will be added to the flowchart presented in Figure 5.1 overlapping the iteration of the integration time.

5.3.1 Initial Results – model capabilities under steady state cruising

The main objective of the fundamental dynamic model is to simulate the motion of the differential gear pair under realistic operating conditions. The importance of such an analysis is associated to the correlation of the system dynamics with unwanted resonance phenomena. The latter can induce significant amplification of the dynamic mesh force leading to noise emission, classified as structure borne axle gear whine (Lee, 2007). This behaviour is encountered under a variety of vehicle running conditions; steady state cruising is the first to be examined.

Based on experimental work, axle noise has been reported under highway cruising for certain vehicle speed range (Yoon et al, 2011). Therefore, it is reasonable to select a low transmission ratio for the purposes of the current investigation. Indeed, this work is focused on a light truck (FORD Transit Connect Van); by assuming cruising conditions with the third gear engaged, transmission ratio is set to 1:1. Furthermore, by imposing a cruising velocity, the magnitude of the nominal resistance torque can be defined through equation (3.8). The main system parameters are defined in Table 5.1.

Figure 5.2 shows the dynamic response time histories of the gear pair under the equilibrium conditions discussed in section 3.2.2. The initial conditions are chosen in a way that the relative distance of the two gear members is equal to half backlash. Additionally, initial angular velocities are defined by the kinematic expression relating the vehicle speed and the axle angular velocity:

$$\upsilon = r\dot{\varphi}_g \qquad \textbf{(5.1)}$$

Numerical integration takes place on a time window equal to 20000 meshing periods. Choosing such a significant integration window may seem unusual; however this selection is necessary for comparison purposes as will be seen in section 5.3.3. Steady state is usually achieved for less than 200 mesh periods. The dynamic response is recorded for the last 100 meshing periods, on a time increment equal to 1/250 of the meshing period. Both angular velocities oscillate about their mean value which represents the rigid body rotation. The dynamic mesh force is always positive

indicating that the gear flanks stay always in contact. This is also illustrated by the dynamic transmission error which typically represents the dynamic response of geared systems. Its magnitude stays always above the boundary level of $75\mu m$, namely the half backlash value defining contact loss conditions.

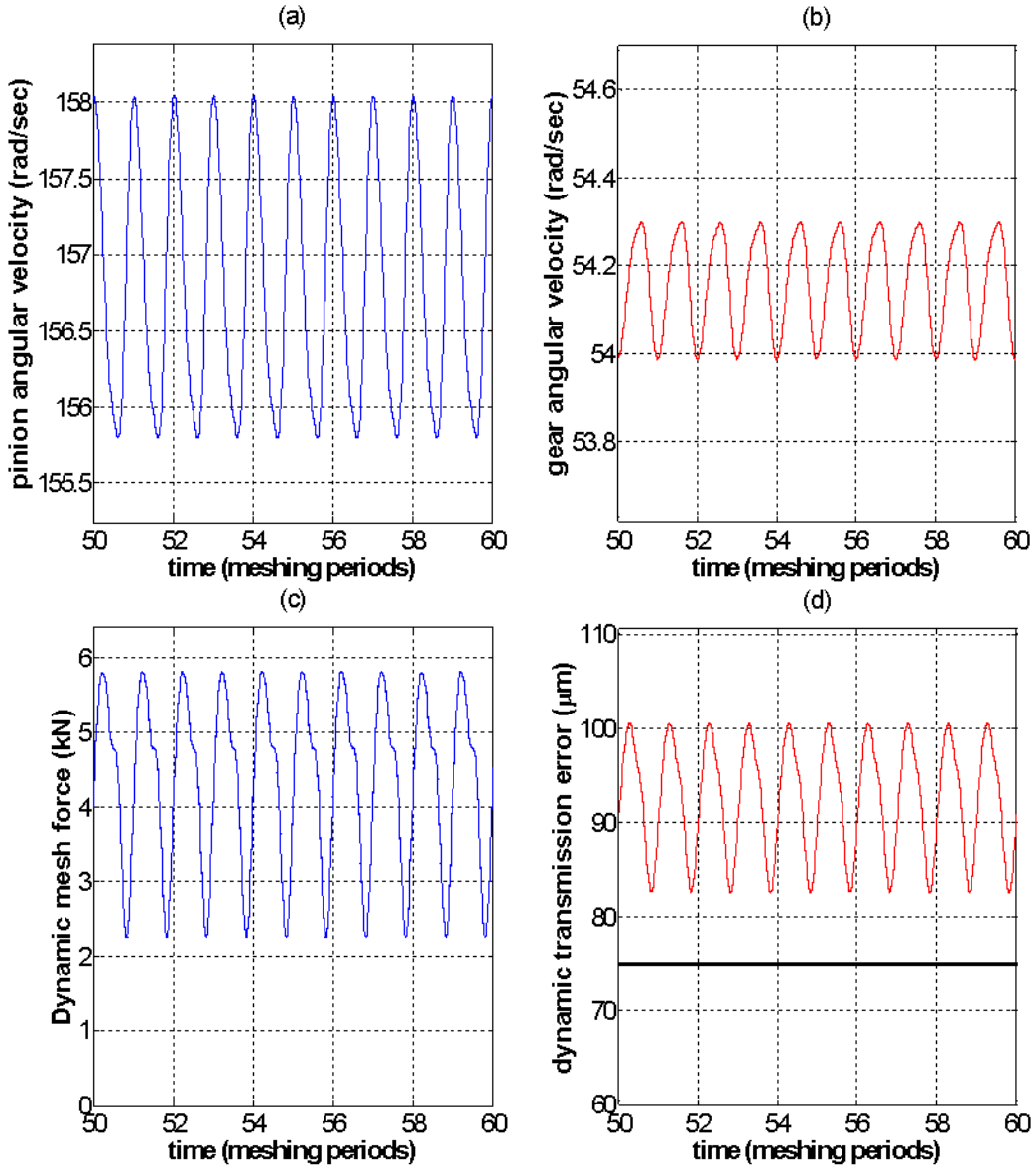

Figure 5.2- Response Characteristics of the gear pair: (a) pinion angular ; (b) gear angular velocity; (c) dynamic mesh force; (d) dynamic transmission error

The response charactertics imply that steady state conditions have been reached. This is supported by the phase plots shown in Figure 5.3(a); only a single stable periodic orbit is visible in the phase space. Validation evidence for the numerical formulation can be derived from the energy balance equation. The instantaneous

total energy of the system is expressed as a sum of the instantaneous kinetic and mesh energy of the gear pair. The latter is equal to the work done by the dynamic mesh force which is essentially an non conservative term due to the variation in the mesh stiffness:

Table 5.1- Definition of system parameters

Variable	Numerical value
I_p; moment of inertia-pinion	13892.6e-06 $kg \cdot m^2$
I_g; moment of inertia-gear	288735.4e-06 $kg \cdot m^2$
c; mesh damping coefficient	5.839e+03 Ns/m
r; tyre dynamic radius	$0.320m$
m; vehicle mass	$3000kg$
g; gravitational acceleration	$9.810m/s^2$
f; coefficient of rolling resistance	0.008
a; ascent angle	0^0
c_w; aerodynamic drag coefficient	1.15
A; vehicle frontal area	$2.662m^2$
ρ; air density	$1.2kg/m^3$
υ; vehicle speed	$62.4kph$

$$E_{total}(\tau)=\left[\frac{1}{2}I_p\dot{\varphi}_p{}^2+\frac{1}{2}I_g\dot{\varphi}_g{}^2\right]_{Kinetic}+\left[\int_0^{\tau}k_m(\varphi_p)f_g(x)\dot{x}ds\right]_{Non\ Conservative\ Work} \quad \textbf{(5.2)}$$

The energy dissipated by the mesh damping element is given by:

$$E_d(\tau)=c_m\int_0^{\tau}\dot{x}^2ds \quad \textbf{(5.3)}$$

The input energy is the sum of the initial energy supplied by the initial conditions and the non conservative work done by the external torque loading:

$$E_{input}(\tau)=E_{total}(0)+\int_0^{\tau}\left(T_p\dot{\varphi}_p-T_g\dot{\varphi}_g\right)ds \quad \textbf{(5.4)}$$

Eventually, the instantaneous energy balance will be:

$$E_{total}(\tau)=E_{input}(\tau)-E_d(\tau) \quad \textbf{(5.5)}$$

The ratio between the two sides of equation (5.5) is presented in Figure 5.3b. It follows that the energy balance is satisfied for every time increment; hence the numerical algorithm seems to be functioning properly. The non conservative nature of the mesh force is depicted in Figure 5.3c, showing a constant increase of the work done. Figure 5.3d shows the mesh force – deflection diagram forming a closed area expressing the work done over a meshing cycle.

The spectral content of the dynamic response is of great importance since noise emission is associated to the frequency characteristics of the mesh force (Hirasaka et al; Lee, 2007). The various frequency contributions in the dynamic response will be identified by applying the Fast Fourier Transform (FFT). Figure 5.4 shows the FFT analysis of the dynamic mesh force. The mesh frequency has the most prevalent contribution inside the time history, followed by its 2nd and 3rd harmonic. All the above plots are derived by imposing a vehicle speed of 62.4 kph . This

corresponds to an input torque of 87 Nm, a pinion rotational velocity of 1497 RPM and a fundamental mesh frequency of 324 Hz.

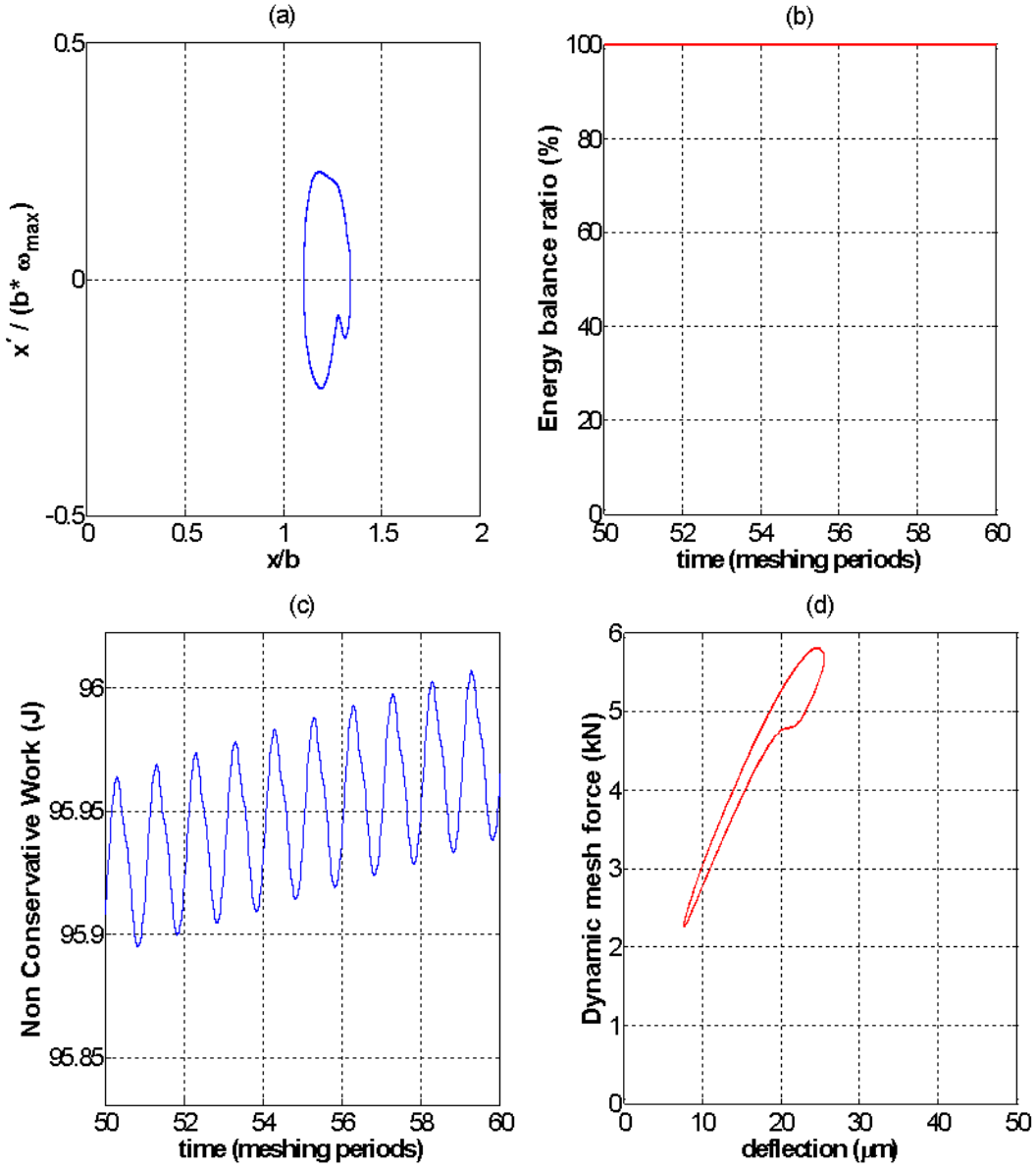

Figure 5.3- (a) Phase plots; (b) Energy ratio; (c) Non conservative work; (d) Mesh force over deflection

The basic principle of the Fourier Transform is the correlation of a given signal with a set of harmonic functions over a certain frequency range; the MATLAB function *fft* is used for this purpose. The algorithm leads to a series of Complex terms whose amplitude is depicted in Figure 5.4. Practically, this amplitude expresses the amount of the energy corresponding to each frequency.

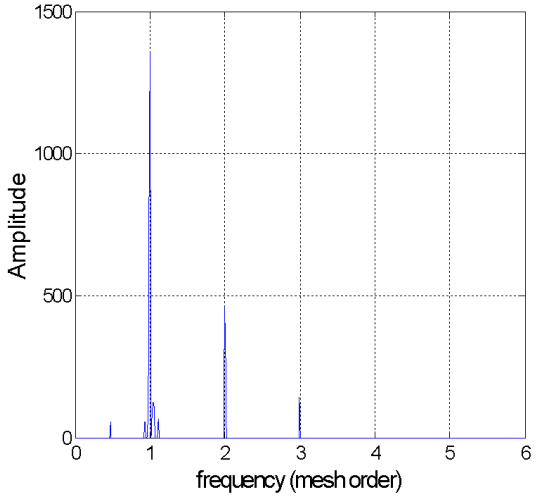

Figure 5.4- FFT of dynamic mesh force time history

5.3.2 Dynamic transmission error in integral form

After presenting the characteristics of the dynamic response of the gear pair and providing validation evidence, the discussion will be shifted toward the crucial factors introduced by the fundamental mechanical model.

The first novel property is a direct consequence of equation (3.5); the dynamic transmission error representing the relative displacement of the gear pair is given by an integral equation instead of the typical expression of (3.17). This definition is due to the variation of contact radii over a meshing cycle; the latter are functions of the instantaneous pinion angle based on TCA (Eq. (3.36)). This feature is a distinct peculiarity of hypoid transmissions, affecting considerably the dynamic behaviour. This effect will be addressed subsequently. The primary concern of this section are the arising stability issues. The operating conditions remain similar to the ones discussed in the previous section.

The expression (3.5) if differentiated yields:

$$\dot{x} = R_p(\varphi_p)\dot{\varphi}_p - R_g(\varphi_p)\dot{\varphi}_g - \dot{e}(\varphi_p) \quad \textbf{(5.6)}$$

In fact, a non-holonomic constraint is introduced in the dynamic system, requiring an additional numerical integration. In hypoid gear models introduced before, the

simplified equation of (3.17) was employed. By neglecting partially the variation of the contact radii (Wang et al, 2007), the constraint was transformed in an integretable form. This approach was followed by a system reduction to a single degree of freedom mechanical oscillator by achieving positive definiteness. However, if the simplified expression is used in the generic double degree of freedom system, stability problems are caused.

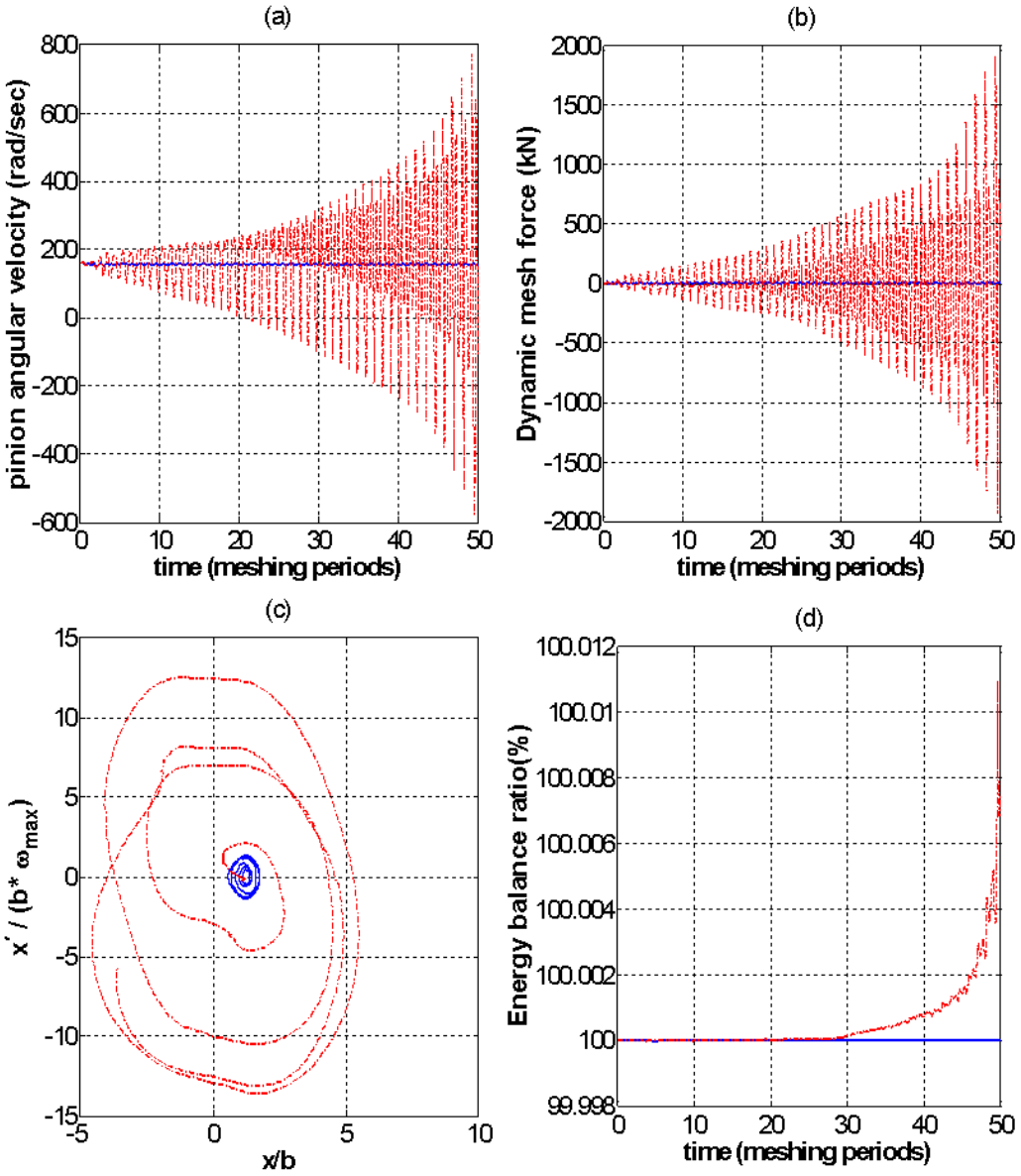

Figure 5.5- Illustration of stability issues: (a) pinion angular velocity, (b) dynamic mesh force, (c) phase plots, (d) energy balance; integral form , simplified form

Figure 5.5 illustrates the appearance of unbounded solutions associated to the improper definition of dynamic transmission error. The simplified equation (3.17) inflicts an exponential growth in the dynamic response, even from the initial stages of integration; the dynamic flow deviates rapidly from the initial conditions. On the contrary, application of equation (3.5) yields smooth steady state response characteristics while the dynamics are attracted by a single periodic orbit. The energy balance ratio shows a steep increase in the energy level of the system violating the energy conservation principle. This implies that equation (3.17) is not compatible with the mathematical formulation of the system. Therefore, equation (3.7) or (5.6) in differentiated form, are the ones which properly account for the system behaviour.

5.3.3 The dependence of external torque to the axle angular velocity

After observing the mathematical consistency of the proposed definition of dynamic transmission error, another aspect of the fundamental mechanical model is going to be stressed. This involves the dependence of the resistive torque on the axle angular velocity, leading to an expression of the following form:

$$T_g = C_0 + C_1 \dot{\varphi}_g^{\,2} \qquad \textbf{(5.7)}$$

In the above equation, constant $C_0 = 75.341$ is related to the rolling resistance whereas $C_1 = 6.019 * 10^{-3}$ to the aerodynamic drag. The importance lies in the establishment of dynamic equilibrium.

Figure 5.6 shows a time history comparison of the angular velocities using two different expressions for the resistive torque. Operating conditions remain identical to the previous sections. The first case employs equation (5.7) letting the torque applied at the gear to follow the instantaneous variation of its angular velocity. The second case uses a constant torque value related to the mean value of the angular velocity. The results correspond to an integration time from 1100 to 1120 meshing

periods. Angular velocities seem to diverge in terms of magnitude and phase, the ones corresponding to constant resisting torque experience a slow reduction of their mean value. However in Figure 5.7, the dynamic mesh force is almost identical and the phase plots coincide almost into the same periodic orbit.

Figure 5.8 shows the gear angular velocities when the integration time is increased above 100000 periods. This is done to indicate the differences in the observed system output. When the resistive torque is a function of angular velocity, dynamic response is independent of the integration time, hence supporting the claim of established steady state conditions. On the other hand, a constant resistive torque inflicts a drop in the angular velocities magnitude by almost 35% in terms of their mean value indicating a lack of dynamic equilibrium.

The dynamic mesh force and the phase plot shown in Figure 5.9 are consistent with the above findings. A constant resistive torque causes a reduction both in magnitude and in the oscillating part of the contact load. For a meshing period, the trajectories on the phase space deviate from the picture of Figure 5.7; the absence of a closed curve suggests a change in the frequency characteristics of the response. On the contrary, for variable resistive torque the phase portrait is unchangeable.

The difference in the spectral content of the two cases is presented in Figure 5.10. For variant torque, the amplitude and harmonics of the mesh force are unaffected by the integration time if the comparison with Figure 5.4 is made. Nonetheless, the picture is totally contradictory if the resistive torque is kept constant. An overall drop in the energy level of the signal is observed, along with the appearance of irregular frequencies. This phenomenon is attributed to a deceleration of the rigid body rotation seen in Figure 5.8 when the resistive torque is independent of the angular velocity. As a result the meshing frequency is shifted to lower values, deviating from the nominal mesh orders. The non periodic nature of the dynamic response under constant resitive torque is visualized in Figure 5.11 showing the corresponding Poincare maps.

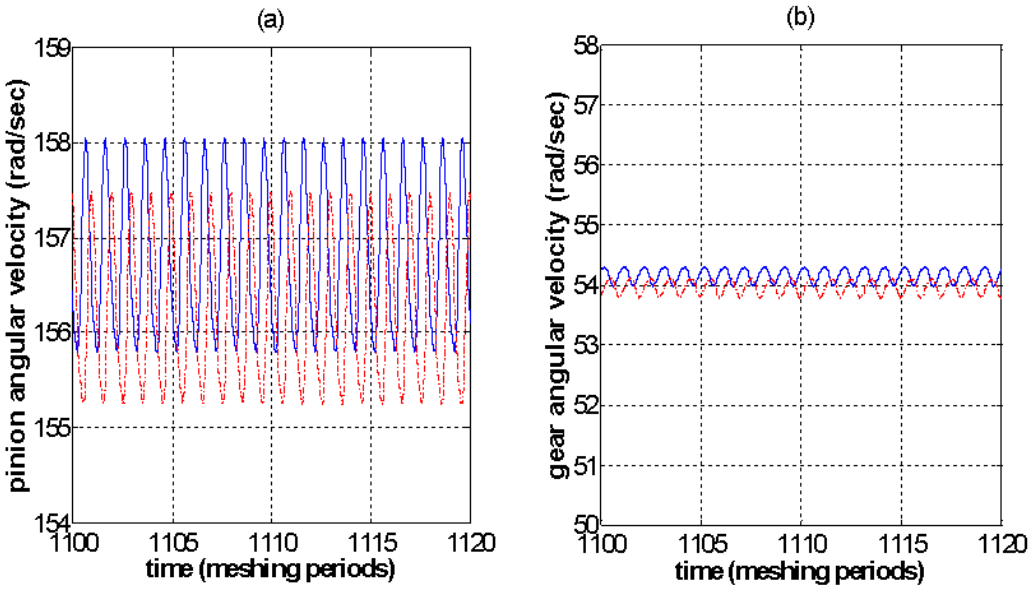

Figure 5.6- Angular velocities of gear members at 1100-1120 meshing periods: (a) pinion, (b) gear; ——velocity dependent torque , — . — velocity independent torque

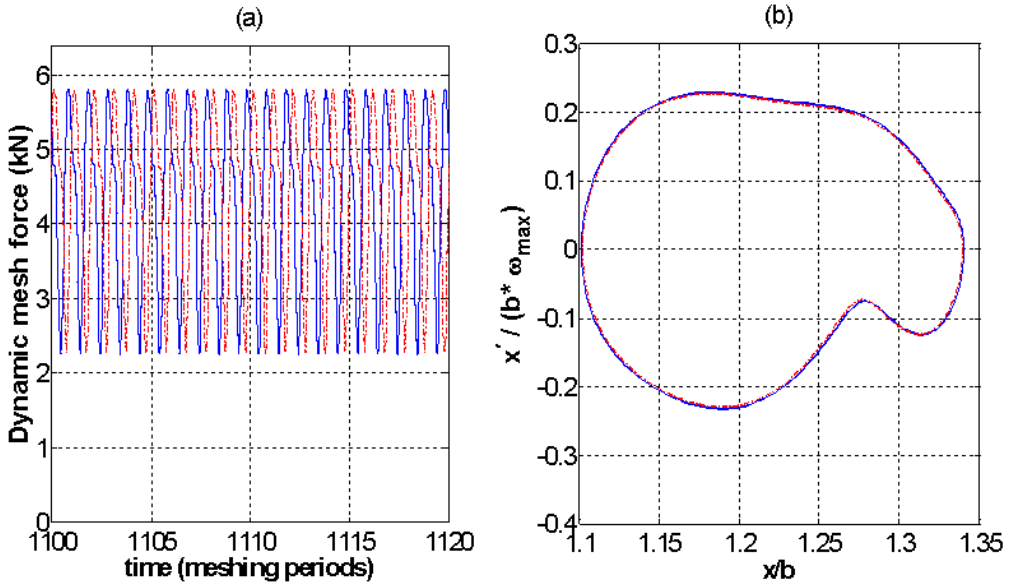

Figure 5.7- (a) Dynamic mesh force and (b) phase plots at 1100-1120 meshing periods; —— velocity dependent torque, — . — velocity independent torque

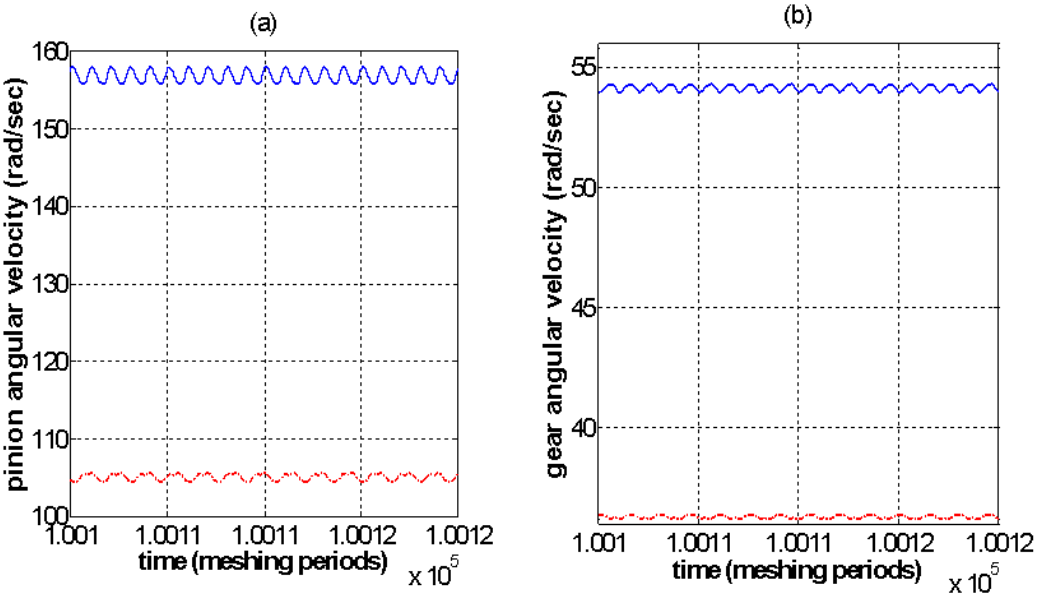

Figure 5.8- Angular velocities of gear members at 100100-100120 meshing periods: (a) pinion, (b) gear; _____velocity dependent torque , _ . _ velocity independent torque

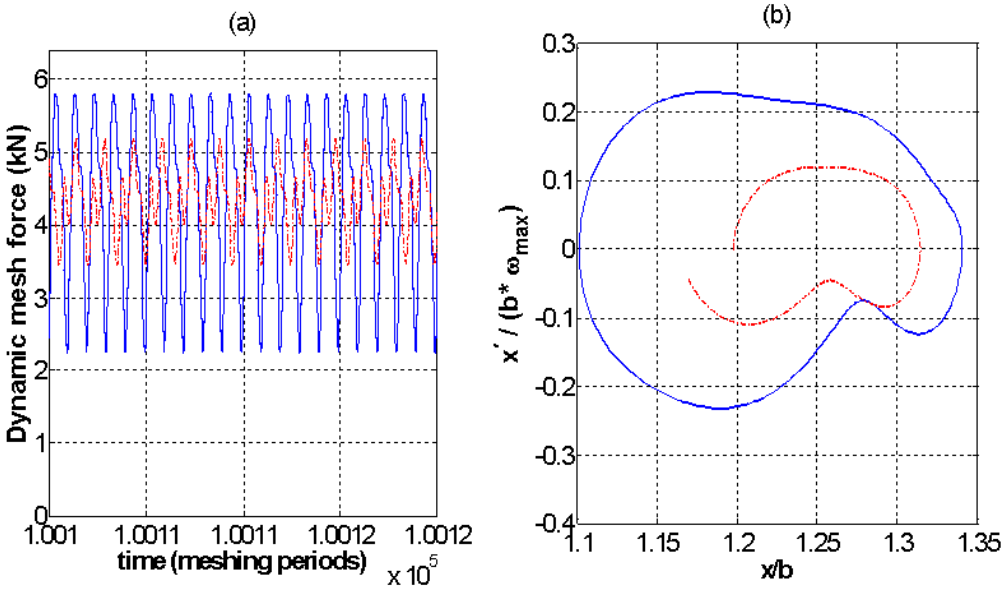

Figure 5.9- (a) Dynamic mesh force and (b) phase plots at 100100-100120 meshing periods; _____velocity dependent torque, _ . _ velocity independent torque

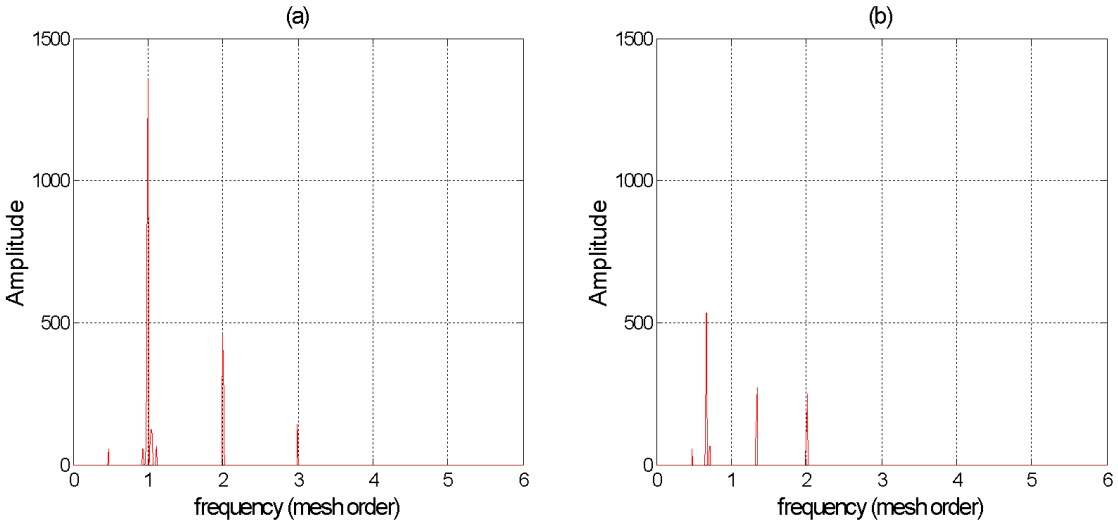

Figure 5.10- FFT of the dynamic mesh force at 100100-100120 periods: (a) variant (b) constant resistive torque

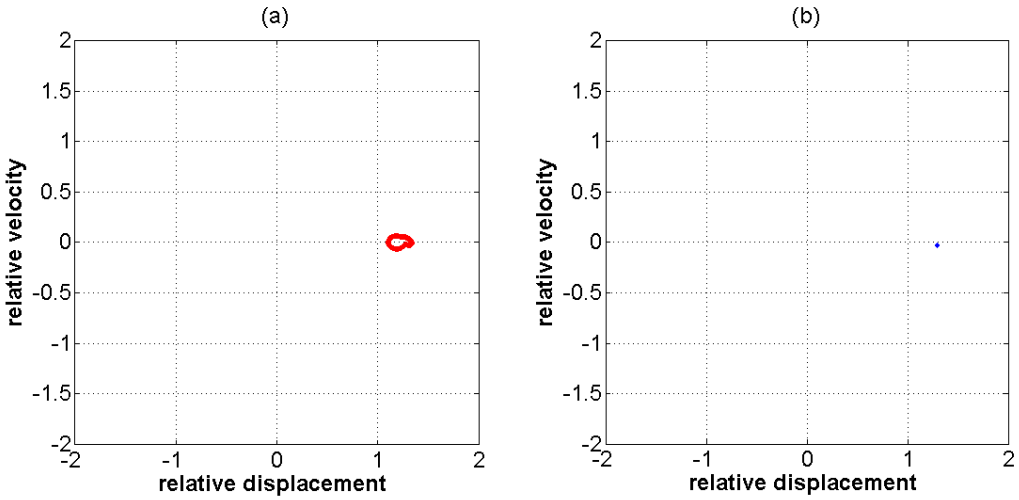

Figure 5.11- Poincare maps: (a) variant (b) constant resistive torque

It is obvious that equation $T_g = C_0 + C_1 \dot{\varphi}_g^{\,2}$ (5.7) is crucial for achieving dynamic balance. Due to the classification of the system as semi-definite (Rao, 2004) and the simultaneous variation of the contact radii, a dynamic equilibrium cannot be reached with constant applied torques. Therefore, a dependence of the resistive torque on the instantaneous angular velocity of the axle solves this problem and also matches the physical requirements of the problem (Theodossiades and Natsiavas, 2001a).

5.3.4 The effect of initial velocities

It was proved that the proposed methodology eliminates the appearance of unbounded solutions and concurrently brings the system to a dynamic equilibrium. However, the effect of the initial velocities has been defined yet. For this reason, investigation on whether the system settles to the same steady state will be conducted.

As already mentioned in section 5.3.1, there is a direct relation between vehicle speed, axle angular velocity and resistive torque based on current operation conditions. The arising question is whether the dynamic response is affected if the above relation is violated. An inquiry into this matter will be accomplished by setting the input loading based on the imposed vehicle cruising speed and on the same time exciting the system from different angular velocities. Initial rotations are taken again equal to zero while assuming that the relative displacement is at the mid-backlash position. If the above statements are quantified:

$$\varphi_p = 0; \dot{\varphi}_p = n\omega_{p0}; \varphi_g = 0; \dot{\varphi}_g = \frac{R_p(0)}{R_g(0)}\dot{\varphi}_p; x = -\dot{e}(0) \qquad \textbf{(5.8)}$$

In the above expression, n is the ratio between the initial and nominal pinion angular velocity ω_{p0}. The latter is connected to the imposed vehicle cruising speed in terms of:

$$\omega_{p0} = \frac{R_{g0}}{R_{p0}}\frac{\upsilon}{r} \qquad \textbf{(5.9)}$$

Eventually, two competing factors coexist; the operating conditions defining the input loading and the initial velocities setting the primal state of the system.

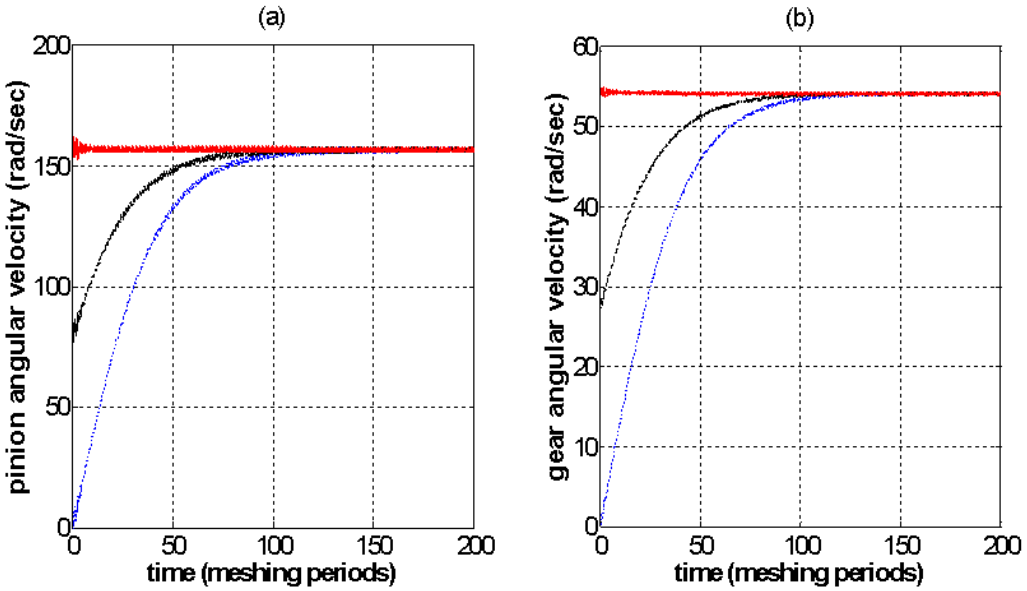

Figure 5.12- (a) Pinion (b) Gear angular velocity for initial angular velocities below the nominal; ..... $n=0$, _____ $n=0.5$ _ . _ $n=1$

Figure 5.12 shows the angular velocities time histories for the initial 200 meshing periods, when their initial values are below the nominal. It is clear that regardless of the starting point, all the time histories converge after an elapsed time of 120 meshing periods. After this transient interval, the dominant steady state corresponds to the one defined by the nominal initial conditions. This fact is also clear in Figure 5.14a depicting the analogous dynamic transmission error. Again the resulting relative gear displacement is concurrent for the three initial cases examined, apart from a phase difference due to the difference in the variation of contact properties.

Different principles apply to initial velocities greater than the nominal one, as illustrated in Figure 5.13. In this instance, the different transients converge on the same steady state again; however the latter is different to the nominal steady state. The fluctuation around the mean angular velocity is much greater resulting to a proportional effect in the dynamic transmission error seen in Figure 5.14b. There is a considerable deviation in the extreme amplitude values; in excess, the minimum drops under the backlash threshold, leading to contact loss between the mating flanks.

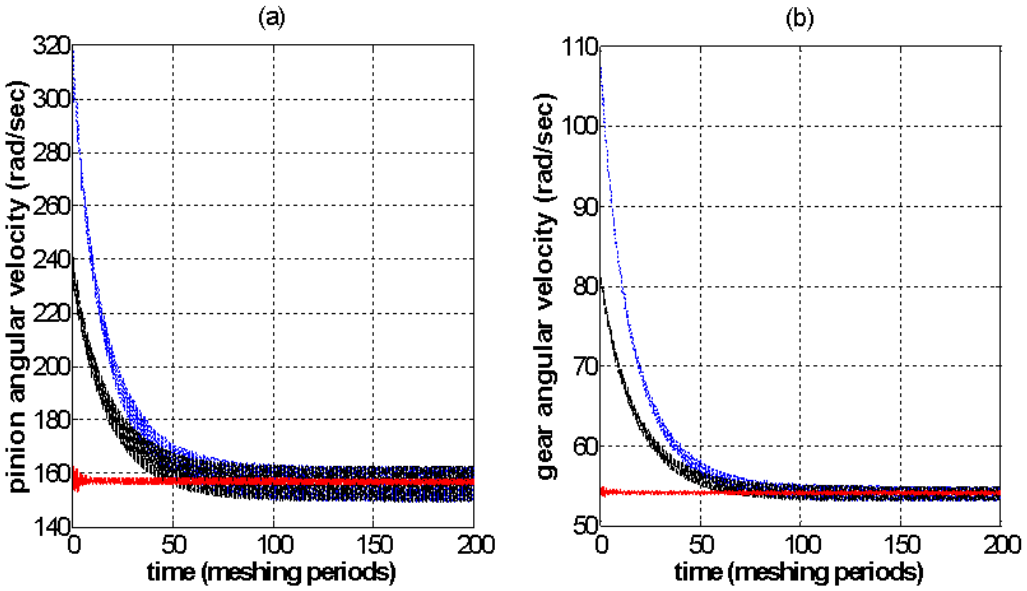

Figure 5.13- (a) Pinion (b) Gear angular velocity for initial angular velocities above the nominal; ..... $n=2$, _____ $n=1.5$, _ . _ $n=1$

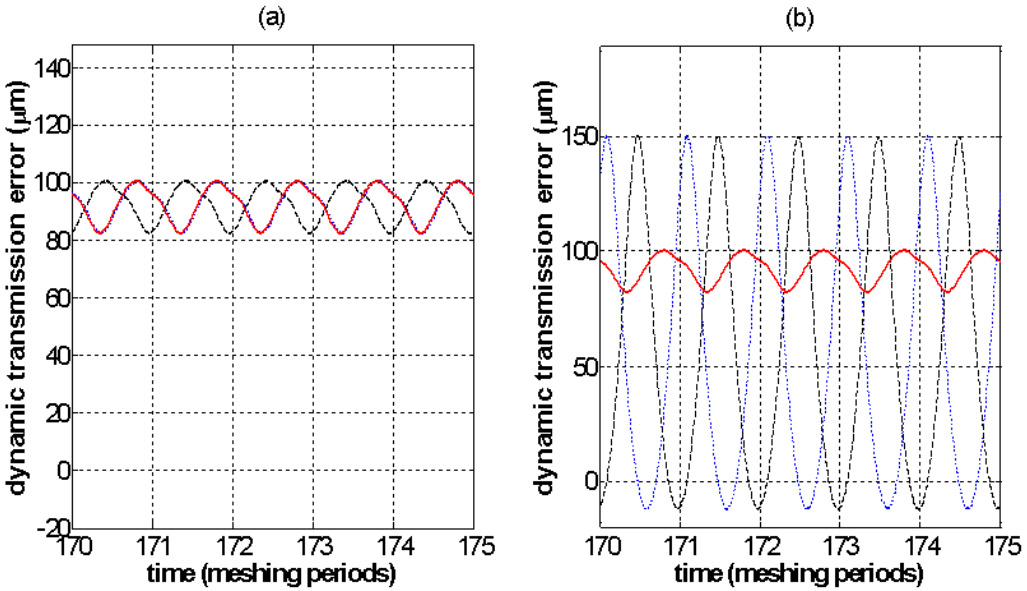

Figure 5.14- Dynamic transmission error for initial angular velocities (a) below the nominal; ..... $n=0$, _____ $n=0.5$, _ . _ $n=1$, **(b) above the nominal;** ..... $n=2$, _____ $n=1.5$, _ . _ $n=1$

An important conclusion can be drawn from the above consideration. In essence, there seem to be two dominant steady state conditions depending on the level of the

input angular velocities. The nominal one seems to attract the dynamics of all the initial conditions below or equal to its angular velocity level. Additionally, if this level is exceeded, another steady state of higher vibration amplitude is likely to prevail. This behaviour necessitates a more thorough insight into the effect of the complete vector of initial conditions. In either case, the important aspect is yielded by the influence of the operating conditions in the dynamic response. The two converging solutions are a consequence of the defined external loading, highlighting the importance of equation (3.8).

5.3.5 Detection of gear teeth separation (vibro-impacts)

It was indicated that the gear pair dynamics are governed by regimes of multiple solutions, depending of the value of input angular velocities. This is in accordance to previous works where multiple responses were realised on the grounds of backlash nonlinearity.

In section 5.3.2, definition of the dynamic transmission through an integral equation due to varying contact radii resulted into the introduction of the additional differential equation $\dot{x} = R_p(\varphi_p)\dot{\varphi}_p - R_g(\varphi_p)\dot{\varphi}_g - \dot{e}(\varphi_p)$ (5.6). Thus, the number of necessary initial conditions for proper definition of the problem needs to entail this new variable. By this means, the construction of frequency – response diagrams is possible via the implementation of speed sweeps. This procedure involves varying the mesh frequency, beginning from low values and gradually increasing covering the whole operational range. Current numerical integration should export its solution as initial condition for the one to follow. This process is reversed, starting from the higher boundary and incrementally reducing the meshing frequency level. Furthermore, by exploiting the direct connection between operating conditions (given by the vehicle speed), the gear pair nominal angular velocities and the meshing frequency defined explicitly in section 3.2.1, a different x-abscissa can be chosen. Namely, the vehicle speed can be used instead of the meshing frequency, yielding a more illustrative perception of the vehicle state.

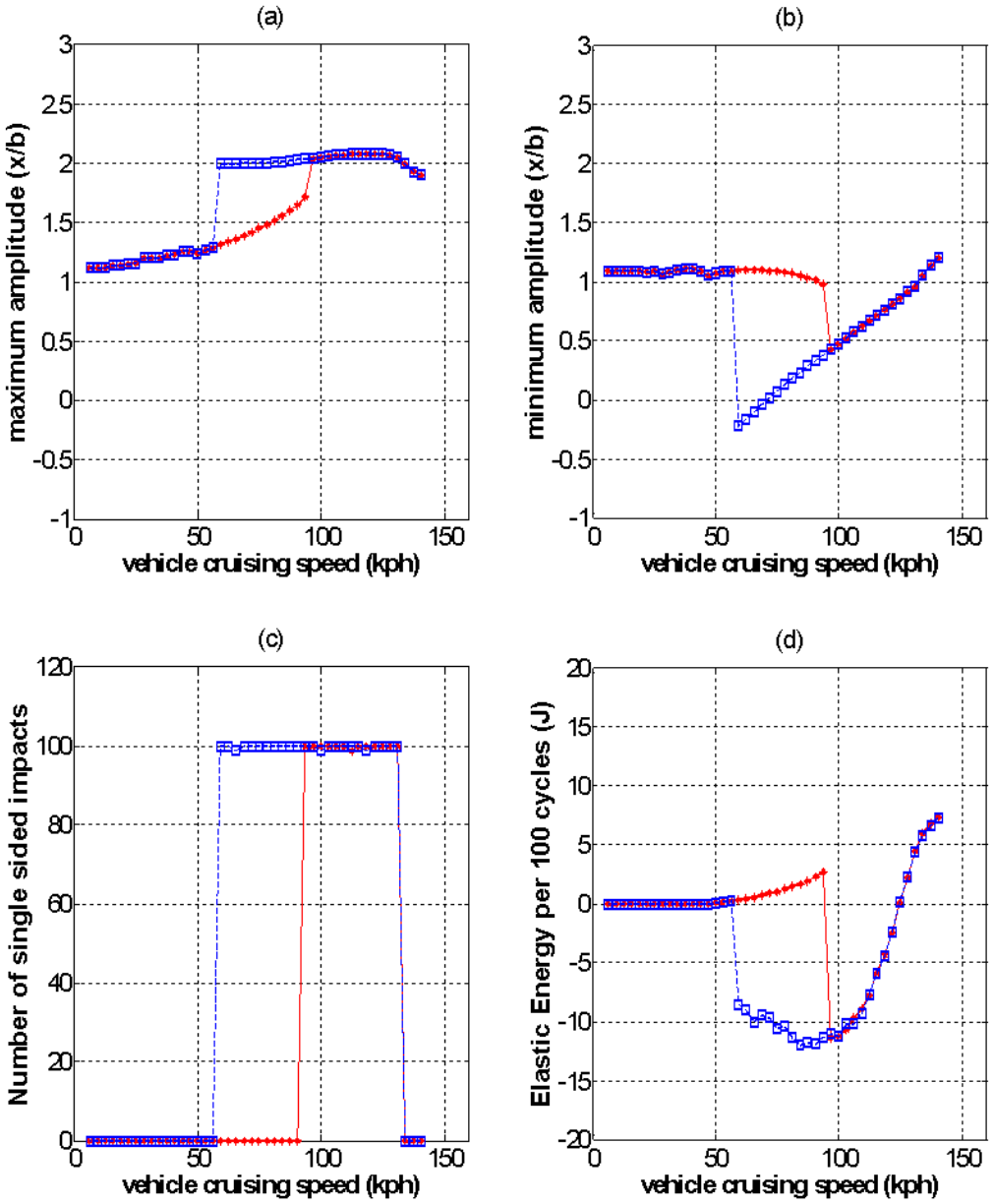

Figure 5.15- Response Spectra: (a) Maximum, (b) Minimum Amplitude, (c) Number of single sided impacts, (d) Elastic Energy per 100 cycles; speed * increasing, ■ decreasing

The speed sweeps are depicted in the graphs of Figure 5.15. All quantities are characterized by jump phenomena, inflicted by the occurrence of multiple solution regimes for a vehicle speed region from 59 to 94kph. Dimensionless dynamic transmission error shown in Figure 5.15(a)-(b), suggests the existence of two distinct response branches. The first one is derived when the system is accelerated from low initial angular velocities. Mesh between the gears is constant since the minimum amplitude never drops below the half backlash threshold. When the vehicle cruising

speed approaches the vicinity of 94kph, the jump to the higher amplitude branch is realized. From this point and onwards, the system response is governed by contact loss and a resonant behavior seen by the extreme values of maximum amplitude. The second branch, generated if the integration sequence is commenced from the upper boundary of operating conditions, is projected leftwards until the second jump at a cruising speed of 59kph.

Therefore, the nonlinear nature of the system is contributing to the parametric resonances instigated by the variation of contact parameters in order to yield a complex dynamic response. Similar conclusions have been yielded by previous studies on hypoid gear pairs (Wang et al, 2007). Nonetheless, in those systems, multiple solutions and contact loss was only realized under lightly loaded conditions. Additionally, the resonance was due to a match between the meshing and natural torsional frequency of the system. In this case, impact phenomena between the mating flanks are developed under high loading conditions as well ($81-295Nm$). Furthermore, the dependence of meshing stiffness on input torque (Figure 3.11) results into a variation of the natural torsional frequency.

The overall region of single sided impacts and aggravated dynamic response is extended from 59 to 131kph, covering a vast proportion of the operating range. In Chapter 2, the correlation of the above factors to gear whine noise has been discussed. From vehicle testing results related to commercial vans similar to the case study presented here, it was shown that gear whine noise is critical in speed ranges from 130 to 80kph during deceleration (Yoon et al, 2011) and 60 to 120kph during acceleration (Lee, 2005). Moreover, the noise frequency range stated by previous investigations (Hirasaka et al, 1991; Lee and Kocer, 2007; Lee, 2005) varies from 200-1200Hz depending on the case. Current model predicts tooth separation and resonant behavior for a meshing frequency range from 308 to 681Hz lying within the values presented in literature.

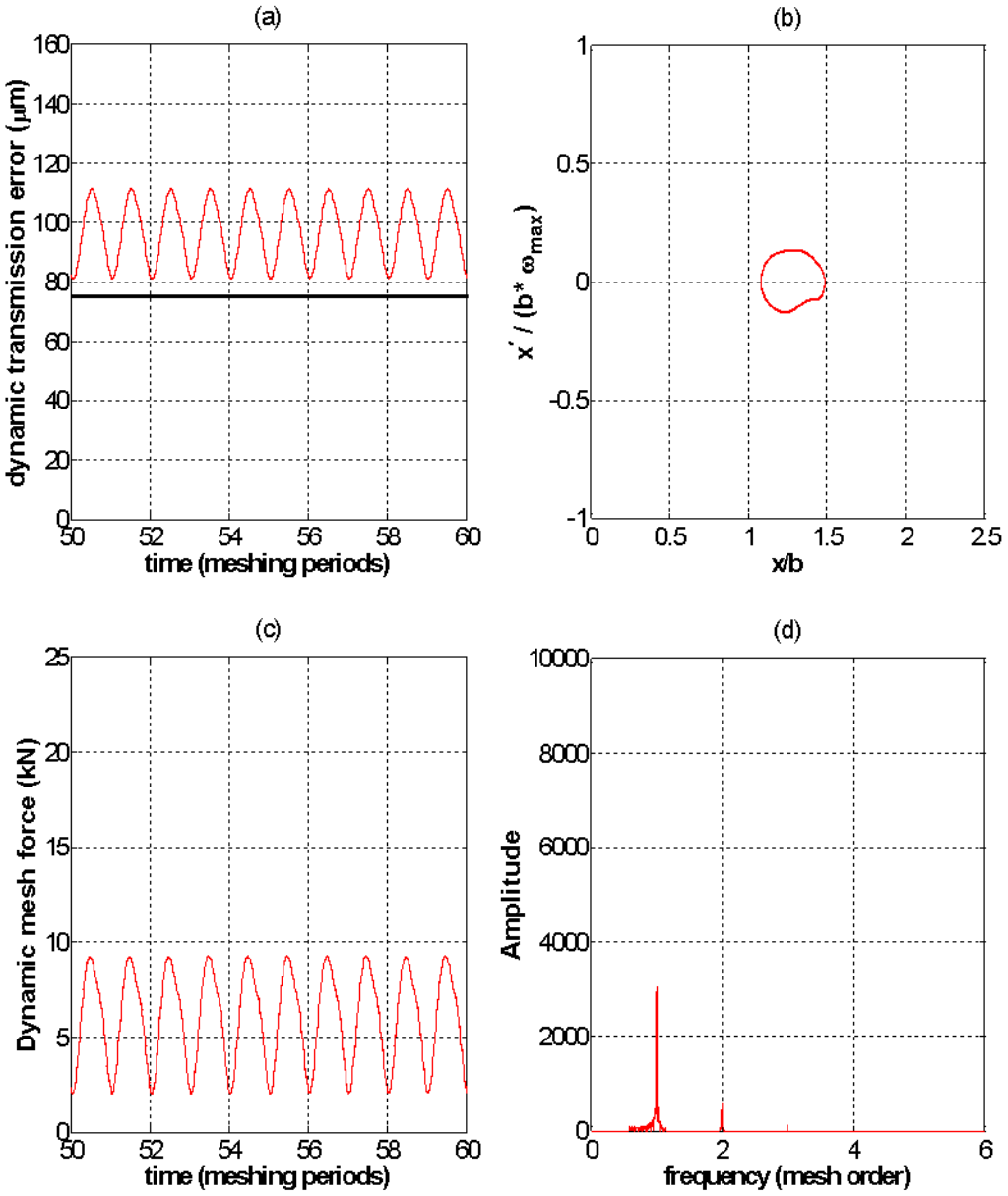

Figure 5.16- Response at 78kph, constant mesh conditions; (a) Dynamic transmission error, (b) Phase portrait, (c) Dynamic mesh force, (d) FFT of dynamic mesh force

Figure 5.15c shows the number of single sided impacts taking place within 100 meshing periods. It is clear that once the contact loss is ignited, the number of impacts remains constant for the whole response range, implying a periodical repetition following the mesh frequency. This fact is in accordance with the experimental data found in literature correlating noise with the mesh frequency. Another interesting aspect of the obtained speed sweeps is the change of sign in the elastic energy plot in Figure 5.15d. The jump points are defined by a change in the

nature of elastic energy; branch switching is related to lower energy levels in the system since the elastic energy is now contributing towards overall energy loss.

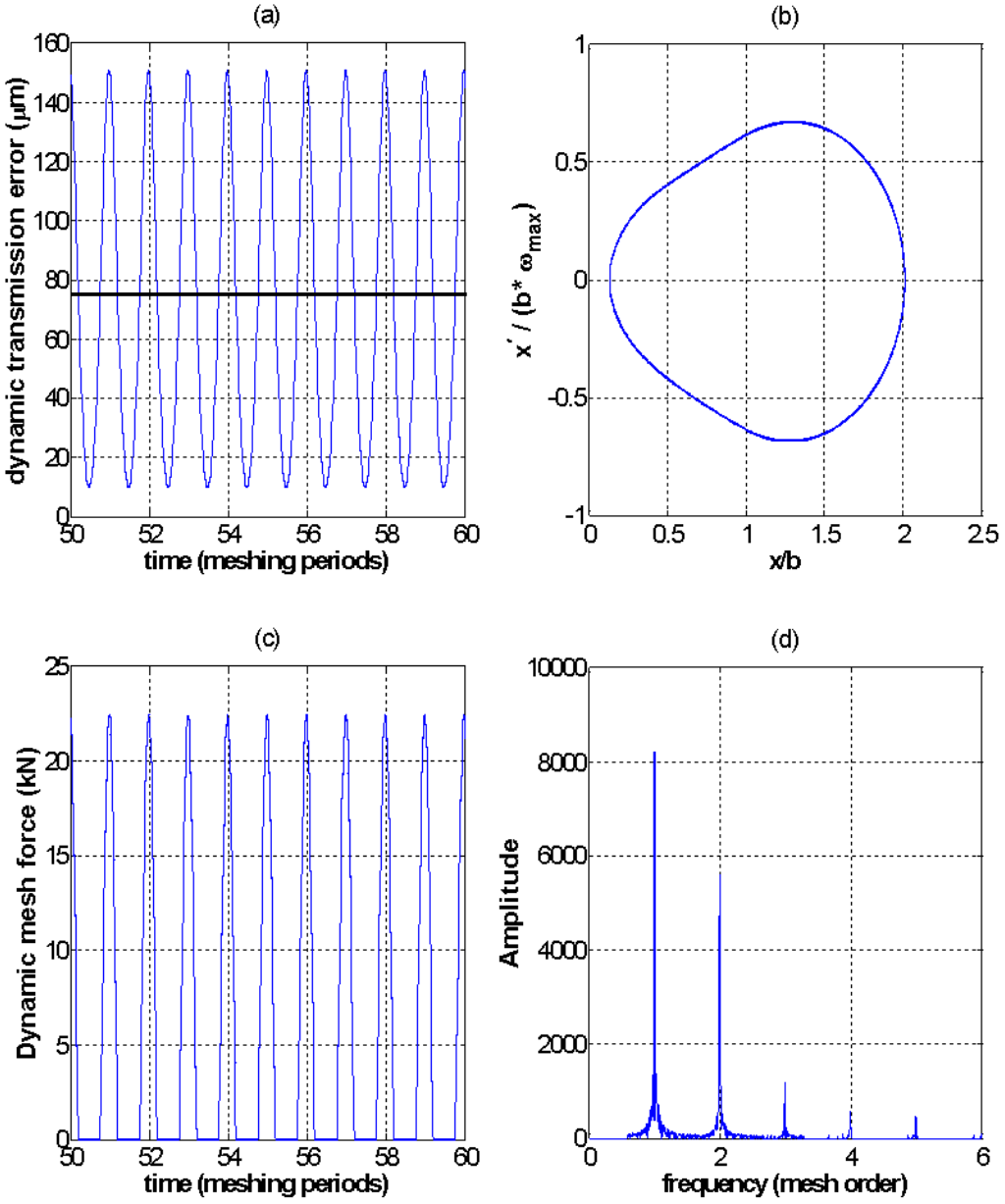

Figure 5.17- Response at 78kph, contact loss conditions; (a) Dynamic transmission error, (b) Phase portrait, (c) Dynamic mesh force, (d) FFT of dynamic mesh force

An overview of the dynamic response exhibited by the system under constant mesh is illustrated in Figure 5.16. Vehicle cruising speed is at 78kph corresponding to an input torque of 121.3Nm. The time history of dynamic transmission error confirms the findings of the spectra shown in Figure 5.15. The mesh between the flanks is

maintained throughout the steady state condition. In the phase portrait a single stable periodic orbit exists while the mesh force is always positive validating the lack of separation instances. Its spectral content seen in Figure 5.16d shows the dominant presence of fundamental mesh harmonic, whereas the contribution of higher harmonics is trivial.

Figure 5.17 shows the dynamic response of the corresponding operational point lying on the upper branch. The differences are clear in every aspect. The maximum amplitude of the dynamic transmission error is increased by almost 36% compared to the previous case while the minimum is reduced by almost 87.5%. The half backlash line is crossed periodically twice at every meshing period, yielding a single sided impact during this time increment. The phase portrait is described by a single periodic orbit as well; however the extreme values of both state variables are considerably increased. The mesh force time history shows the anticipated discontinuities under contact loss conditions together with a highly resonant behaviour revealed by the tripling of its maximum amplitude compared to the previous case. It is now in the form of a series of finite pulses, resembling a repetition of a Dirac function. The effect of the altered nature of the dynamic mesh force can be considerable if transferred by the gear bearing assembly to the other structural components of the vehicle. The chance of exciting high frequency modes is realistic as seen by the spectral content of Figure 5.17d. In this case, the first mesh order seems to share its dominant role together with the second harmonic, showing that the elastic energy is now shifted to higher frequency contents.

5.3.6 Comparison to previous hypoid gear pair models

The advantages for the proposed modelling formulation have been discussed, focusing on the elimination of unbounded solutions, achievement of dynamic balance and robustness on the alteration of the initial conditions. In this section, a comparison to a previously presented methodology (Wang et al, 2007) will be made. This is based on the assumption that the variation of contact radii is adequately slow so that their time derivatives can be neglected. Therefore by differentiating twice the expression yielding the dynamic transmission error (Eq. (3.17)), it follows that:

$$\ddot{x} = R_p(\varphi_p)\ddot{\varphi}_p - R_g(\varphi_p)\ddot{\varphi}_g - \ddot{e}(\varphi_p) \quad \textbf{(5.10)}$$

The above expression allows the reduction to a single DOF system. In the current modelling approach, two degrees of freedom need to be sustained due to the dependence of the resistive torque on the gear angular velocity. By employing a change of variables through setting $u_p = R_p\varphi_p$ and $u_g = R_g\varphi_g$ while utilizing the approximation of Wang et al (2007) yields:

$$\ddot{u}_p = R_p\ddot{\varphi}_p \quad \textbf{(5.11)}$$

$$\ddot{u}_g = R_g\ddot{\varphi}_g \quad \textbf{(5.12)}$$

$$\ddot{x} = \ddot{u}_p - \ddot{u}_g - \ddot{e}(\varphi_p) \quad \textbf{(5.13)}$$

If the above expressions are used in compliance with the initial equations of motion (3.1), (3.2) and (3.6), the formulation of Wang et al (2007) can be expanded to a two-DOF system.

The dynamic response after Wang et al (2007) is shown in Figure 5.18. The results of the original single DOF system corroborate to the expanded two-DOF system. Thus the latter can be regarded equivalent to the formulation of Wang et al (2007), enabling an effective comparison to the methodology proposed in this thesis, so that potential differences are conveyed.

The response spectra comparison shown in Figure 5.19 indicates a significant difference between the simplified approach relying on equations (5.11)-(5.13) and the methodology introduced in this thesis. The aforementioned simplifications result in the elimination of the nonlinear properties of the system while the upper and lower boundaries of the dynamic response are equally affected. Regions of multiple solutions no longer exist; hence, the realization of jumps of the dynamic flow is now impossible. The contact between the gear flanks is steadily maintained throughout the whole operational range without the existence of single sided impacts (Figure 5.19(b)-(c)).

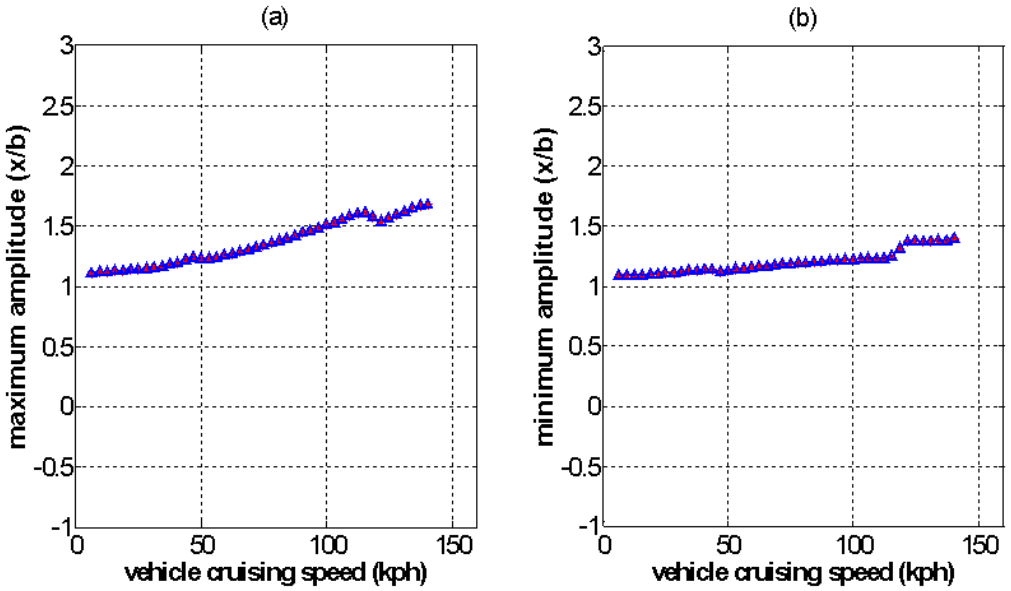

Figure 5.18- Dynamic transmission error after Wang et al (2007): (a) maximum (b) minimum amplitude; * single DOF, ▲ double DOF

The resonant behaviour is less pronounced and it only concerns a small peak around the vehicle speed of 110kph compared to the broadband resonance predicted by the current model (59-131kph). The only region of relative compliance between the two cases seems to be at low cruising speeds, up to 50kph. This is justified as the corresponding gear angular velocities and mesh frequency (Eq.(5.9)) will result into a slow variation of the contact radii granting the feasibility of the approximations involved in the simplified model. Nevertheless, for higher vehicle speeds the derivatives of the contact radii will be considerable quantities, weakening the implementation of equations (5.11), (5.13). Apparently there is a limit for adopting this level of simplification.

Time histories and phase portraits are depicted in Figure 5.20. The graphs correspond to the operating point discussed in the previous section, namely a cruising speed of 78kph and a pinion input torque of 121.3Nm. The duality of solutions representing the current methodology is in contrast with a single steady state solution yielded by the approximation of Wang et al (2007). The difference to the lower branch solution is notable in the phase space as well; a totally different dynamic response is derived.

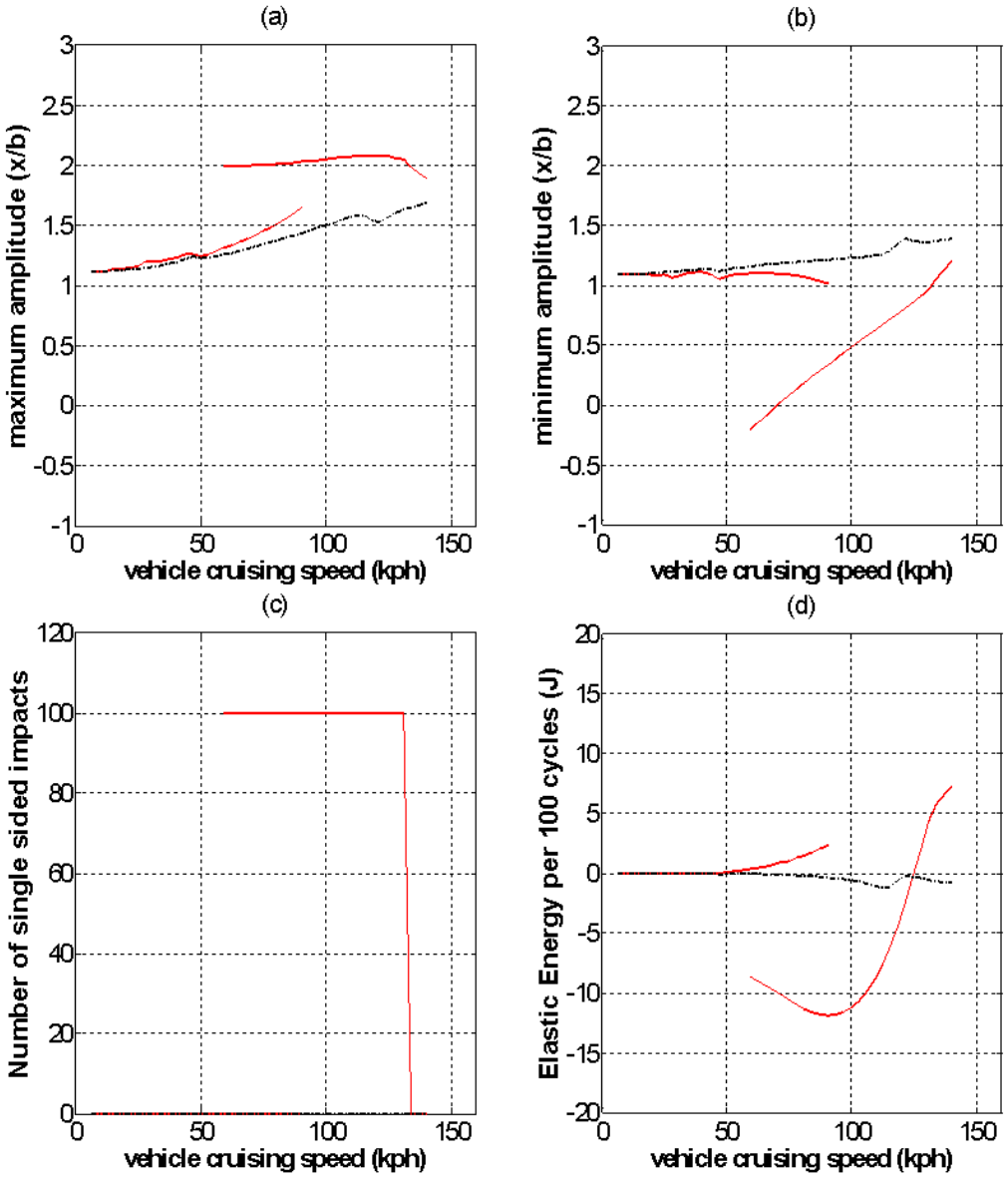

Figure 5.19- Comparison of response characteristics: : (a) Maximum, (b) Minimum Amplitude, (c) Number of single sided impacts, (d) Elastic Energy per 100 cycles; _____ current methodology, _ . _ . . Wang et al (2007)

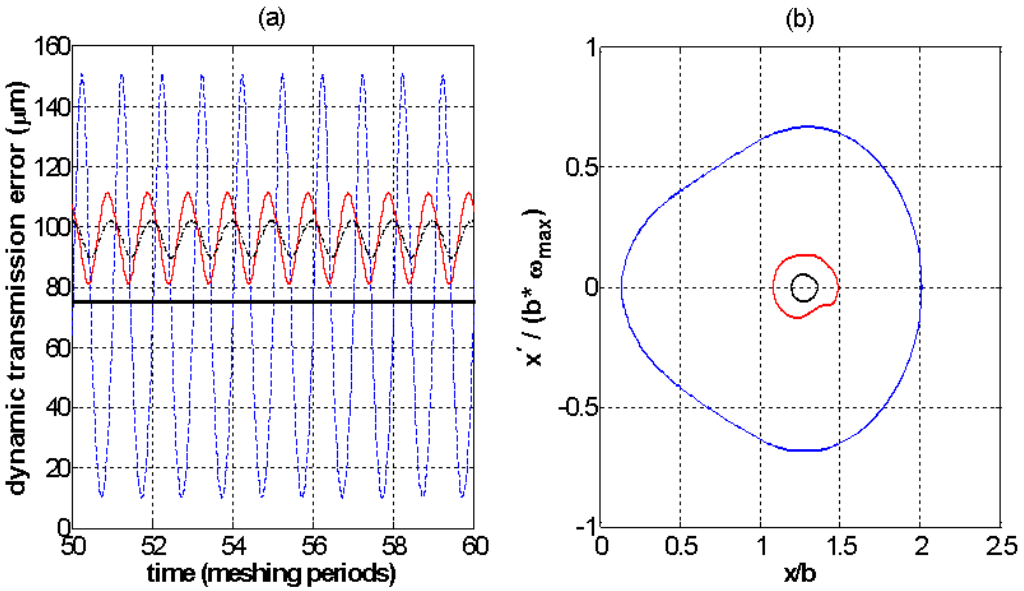

Figure 5.20- (a) Time history of dynamic transmission error and (b) phase portrait at cruising speed of 78kph, input torque of 121.3Nm; current methodology upper branch, lower branch, Wang et al (2007)

In general, the current methodology is expected to promote a more realistic representation of the physical system, since it preserves its nonlinear properties in a broadband range of operating conditions. This behaviour is in accordance to the reported literature (Chapter 2) where noise issues related to improper mesh were reported for broadband frequency regions. On the contrary, the simplifications stated by Wang et al (2007) do not predict any separation effects, neither any significant resonance behaviour. The significance of the variation of the contact radii is thus stressed as the main dissimilarity between the two approaches. Their variation while related to the intrinsic characteristics of hypoid transmissions, introduces a substantial dynamic effect which is impossible to be captured by the previous gear pair models. In essence, as illustrated in Figure 5.21, the assumptions of Wang et al (2007) are similar to regarding the contact radii as constant as if the gear pairs were on a parallel axis configuration. The compared response spectra show significant matching hence providing additional evidence on the potential of the current modelling formulation over the previous simplified models, to capture a detailed dynamic behaviour.

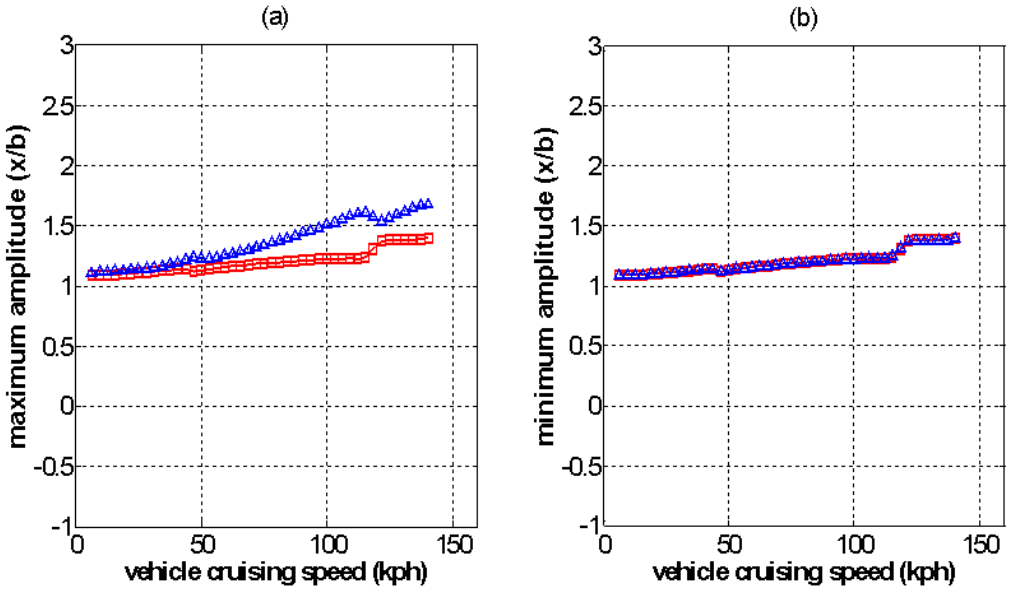

Figure 5.21- Comparison of response spectra: (a) maximum, (b) minimum amplitude; ▲Wang et al (2007), ■constant contact radii

5.3.7 Family of periodic solutions – stability and parametric studies

The numerical integration of the equations of motion revealed the existence of two main response branches governed by different solution types and jump phenomena. Nonetheless, as shown by Kahraman and Singh (1990), the numerical simulations are incapable of yielding the complete picture of such dynamical systems. The initial conditions are a crucial factor settling the system to different domains of attraction and response regimes; therefore there is always the possibility of failing to identify a solution branch when following the speed sweep technique described previously. The entire branches of periodic motions along with the stability characteristics will be obtained by employing a numerical continuation methodology (Doedel, 1981).

The application of the above methodology requires the representation of the system by a single variable through the disappearance of the rigid body rotations. Only the principles of this transformation will be mentioned in this section. The complete derivation will be provided in the Appendix. The aim of this process is the substitution of rotations φ_p, φ_g with the dynamic transmission error x. Initially, from equations (3.3) and (3.4):

$$\ddot{\varphi}_p = h_p\left(x, \dot{x}\right) \quad \textbf{(5.14)}$$

$$\ddot{\varphi}_g = h_g\left(x, \dot{x}\right) \quad \textbf{(5.15)}$$

By differentiating equation (5.6):

$$\ddot{x} = \dot{R}_p(\varphi_p)\dot{\varphi}_p + R_p(\varphi_p)\ddot{\varphi}_p - \dot{R}_g(\varphi_p)\dot{\varphi}_g + R_g(\varphi_p)\ddot{\varphi}_g - \ddot{e}(\varphi_p) \quad \textbf{(5.16)}$$

Equations (5.6) and (5.16) combined with equations (5.14), (5.15) can be solved simultaneously to yield angular velocities $\dot{\varphi}_p$, $\dot{\varphi}_g$ as functions of x, $\dot{x}$. Hence all the derivatives of the gear rotations can be expressed with respect to the transmission error and its derivatives.

The solution of the original dynamic system requires the differentiation of equation (5.16) and subsequent substitution of the rotation derivatives to the new variable x. Thus, the transformation results into a third order differential equation of a single variable related to the relative motion of the gear pair. Since the angular rotations of the gear wheels are now absent from the system description, the mesh properties need to be given in terms of time and mesh frequency rather than the pinion angle. This change introduces only a marginal difference on the steady state dynamic response.

Numerical continuation is enforced in order to define the family of periodic solutions. The results are presented in the form of frequency response diagrams; however the vehicle speed is used again as the independent variable in accordance with the analysis of the previous sections. The branches of stable/unstable solutions are illustrated by solid/dashed curves respectively.

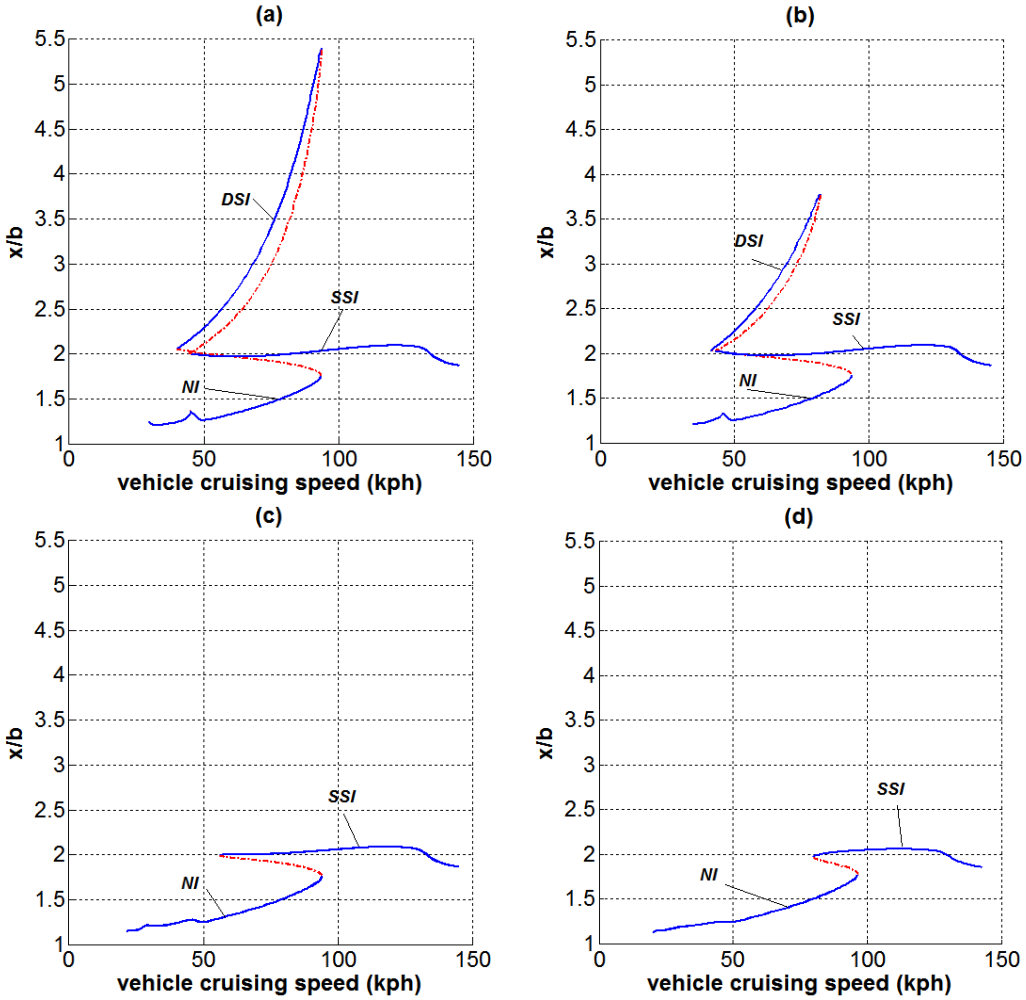

Figure 5.22- Effect of mesh damping coefficient on periodic motions, maximum amplitude: (a) c= 1.9130e+003 Ns/m (b) c= 2.8695e+003 Ns/m (c) 5.7390e+003 Ns/m (d) 1.1478e+004 Ns/m;

stable branch, unstable branch

The first set of response diagrams (Figure 5.22-Figure 5.23) depict the effect of mesh damping on the periodic motions under nominal system parameters. Case (c) is the closest to the numerical results analysed in the previous sections. The form of the response curve confirms previous numerical integration findings. A no-impact (NI) solution branch ($x > b$) evolves at the left hand side of the graph whose amplitude is maximized around 94kph. In the same range of vehicle speeds a single sided impact (SSI) ($x > -b$) branch co-exists, exhibiting a near softening behaviour. Likewise, stability is lost under deceleration at 57kph.The decrease of the damping coefficient has a multiple effect on the response characteristics. Primarily, the

minimum amplitude increases significantly together with the length of the SSI branch, shifting its stability loss at a lower velocity. At the same time, a third solution branch appears characterised by double sided impact (DSI) phenomena ($x<-b$), followed by a hardening behaviour. Multiple response regimes coexist on a broad range of cruising speeds, enabling the potential of jump phenomena between all three solution types. These results are consistent to previous studies of parallel axis gear pairs (Theodossiades and Natsiavas, 2000).

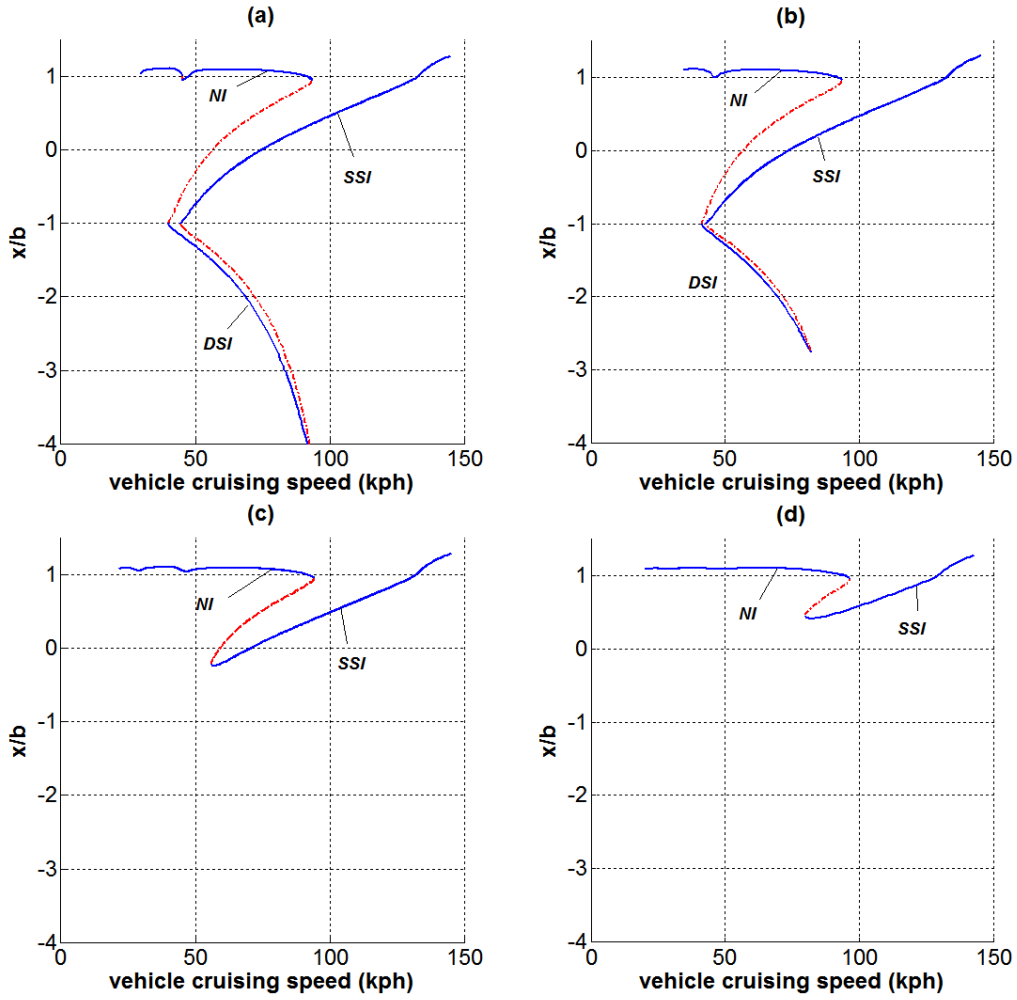

Figure 5.23- Effect of mesh damping coefficient on periodic motions, minimum amplitude: (a) c= 1.9130e+003 Ns/m (b) c= 2.8695e+003 Ns/m (c) 5.7390e+003 Ns/m (d) 1.1478e+004 Ns/m; _____ stable branch, _ _ _ _branch with unstable solutions

The contribution of an out of phase mesh stiffness variation with respect to the static transmission error is shown in Figure 5.24. The mesh damping coefficient is selected equal to that of case of Figure 5.22(b) while the other system properties remain

unaltered. Additionally, a harmonic fluctuation of the mesh stiffness is imposed with respect to its mean value. A single sinusoidal term is being used; the variation parameter k_{s1}^{*} present in the graphs expresses the normalised amplitude of this fundamental mesh harmonic with respect to the mean contact stiffness. A simple calculation yields the phase of the fundamental harmonic of static transmission error equal to 0.9639π . Therefore, positive k_{s1}^{*} values will cause an out of phase variation of the mesh stiffness with respect to the static transmission error. For the given conditions, an increase in the value of k_{s1}^{*} inflicts a rise in the reached extreme amplitudes while triggering DSI solution branches.

Opposite conclusions are drawn from Figure 5.25, displaying the in phase stiffness – transmission error variation. In this case, negative k_{s1}^{*} values cause the disappearance of the DSI branch. Furthermore, the amplitude of the in phase stiffness harmonic is counter proportional to the magnitude of the minimum amplitude reached by the system. The region of coexisting solution branches declines considerably and both bifurcation points move to the right side of the graph; hence suppressing the regions of SSI. Similar observations have been reported in previous parametric studies on gear pairs (Theodossiades and Natsiavas, 2000) and piecewise nonlinear time varying oscillators (Ma and Kahraman, 2005).

The response spectra of Figure 5.26 demonstrate the influence of contact radii variation. The mesh stiffness is again represented by the fundamental mesh harmonic, setting $k_{s1}^{*}=0.1$, while the remaining system parameters correspond to the nominal case. The normalized contact radii variation $R_{p,g,s1}^{*}$ is supposed to follow a sinusoidal form while being equal for both gear wheels. By this configuration, positive $R_{p,g,s1}^{*}$ values imply that contact radii and mesh stiffness are in phase. At the same time both quantities are in opposite phase with the static transmission error. An increase in the variation amplitude of the contact radii induces an aggravated dynamic response, enhancing the effect of stiffness variation. Regions of multiple solutions expand significantly, whereas the bifurcation points are displaced to lower vehicle speed levels. Superharmonic resonances are also activated and

loss of stability is observed on those branches for increased levels of contact radii variation.

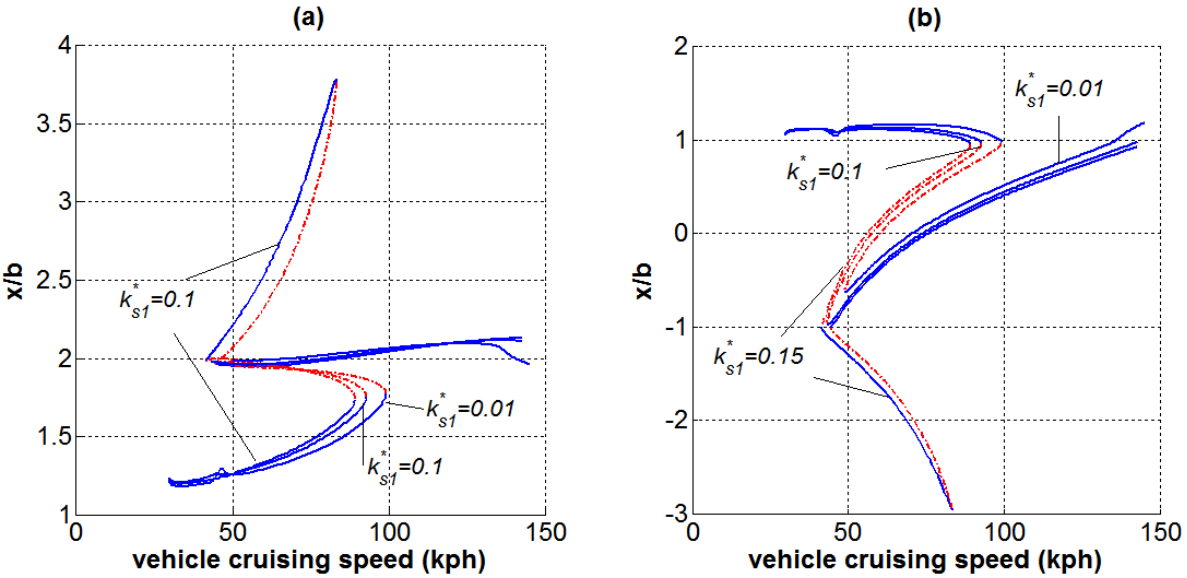

Figure 5.24- Effect of out of phase stiffness variation: (a) maximum (b) minimum amplitude;

_____stable branch, _ _ _ _ branch with unstable solutions

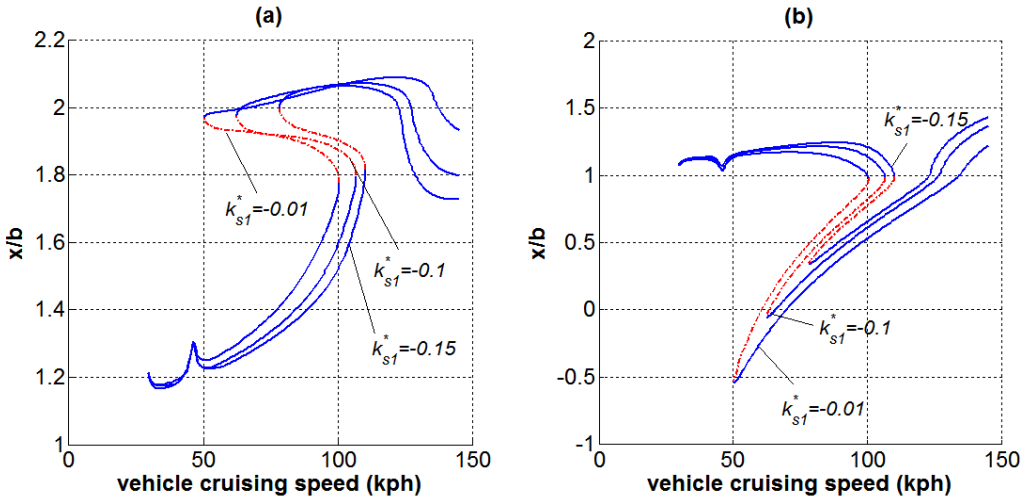

Figure 5.25- Effect of in phase stiffness variation: (a) maximum (b) minimum amplitude;

_____stable branch, _ _ _ _ branch with unstable solutions

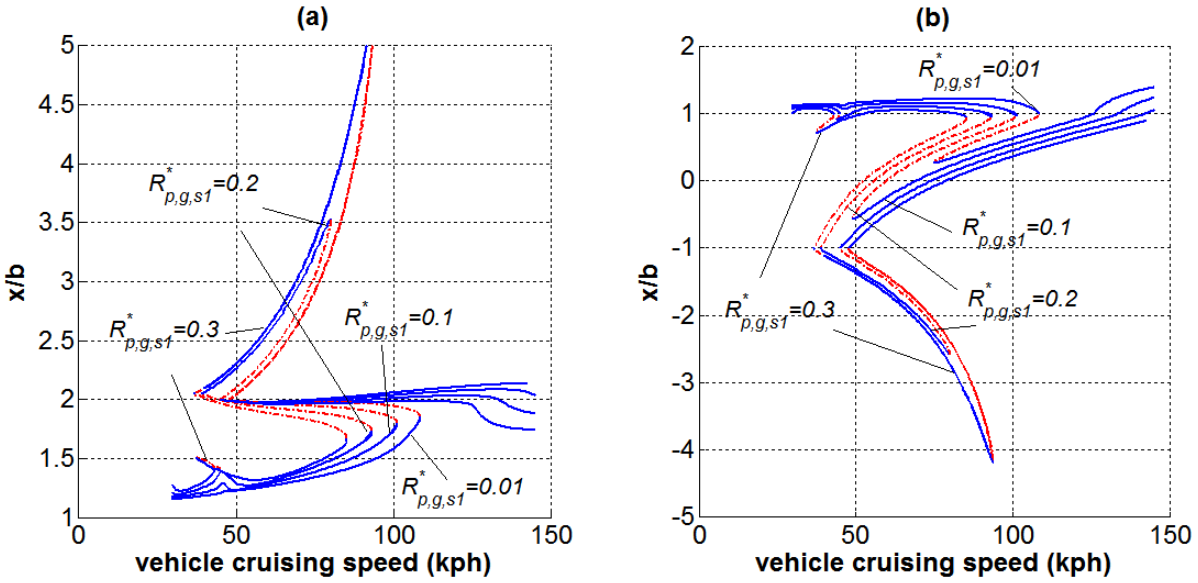

Figure 5.26- Effect of contact radii variation: (a) maximum (b) minimum amplitude

stable branch, branch with unstable solutions

Another time varying parameter which tends to affect the dynamic response is the kinematic transmission error. In the nominal case, it is given as a periodic function in the form of Fourier series. It was already shown that the phase of the mesh order harmonic is crucial when interacting with the mesh stiffness. Figure 5.27 has been produced for different amplitude values e^*_{s1} of the sinusoidal fundamental harmonic. The other Fourier coefficients are set to zero, whereas constant meshing stiffness is assumed, since the aim is to investigate the interaction between the variations of contact radii and static transmission error. The fundamental harmonic term of contact radii $(R^*_{p,g,s1})$ is set equal to 0.1, whereas the higher harmonics ($R^*_{p,g,si}; i \neq 1$) equal to zero. The rest of system parameters maintain their nominal values.

The previous consideration implies that both varying mesh properties (contact radii and static transmission error) are in phase with each other. The thick curve indicates the case where no variation of the transmission error is accounted, namely $e^*_{cj} = e^*_{sj} = 0$, for every $j-$ term of the Fourier series. Increase of the static transmission error variation magnitude causes a gradual annihilation of the nonlinear characteristics. Maximum amplitudes experience a significant drop; bifurcation points

approach each other shrinking the region of multiple solutions. For an extreme value of e_{s1}^{*} the system response becomes practically linear and maximum amplitude is reduced by almost 20%. Therefore, it can be claimed that the two varying quantities tend to cancel each other when applied in phase.

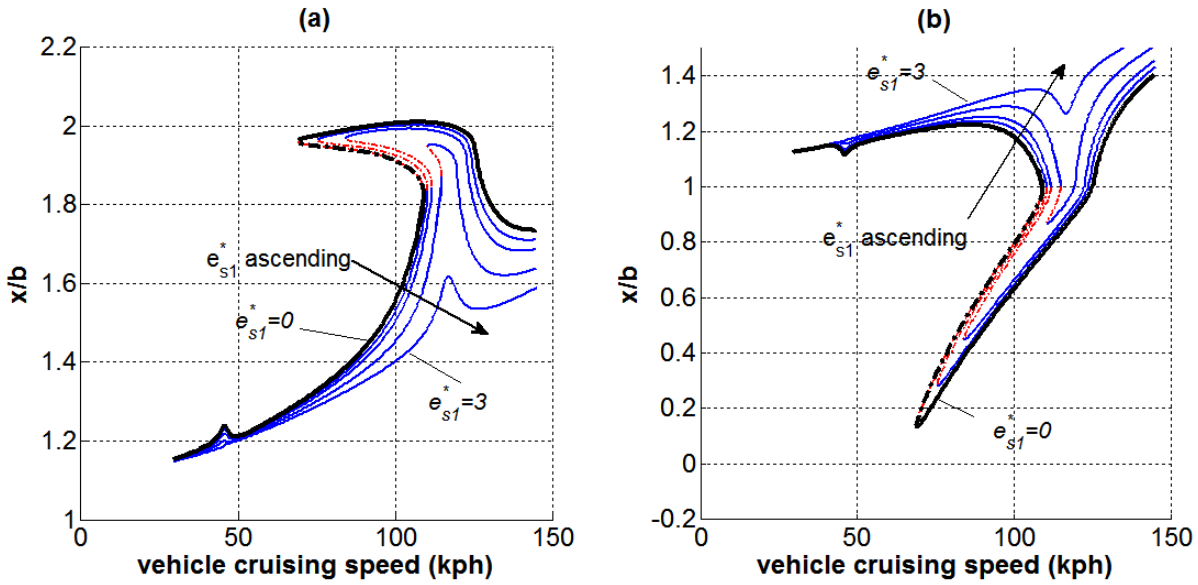

Figure 5.27- Effect of the kinematic transmission error, in phase case: (a) maximum (b) minimum amplitude; _____ stable branch, _ _ _ _ unstable branch

The case of a phase discrepancy is presented in Figure 5.28. In this instance, a phase difference of $\pi/2$ (compared to the previous case) is imposed on the static transmission error by keeping only the first cosine term e_{c1}^{*}. The thick curve depicts again the case of no variation. A rise in its magnitude seems to aid the system in retaining its nonlinear characteristics. The overall difference in the observed amplitudes can be treated as trivial; so is the expansion of the SSI region from the relocation of the bifurcation points. Nonetheless, the opposing mechanism encountered during in phase conditions is gradually eliminated and the contact radii variation is the dominant factor in the response diagrams.

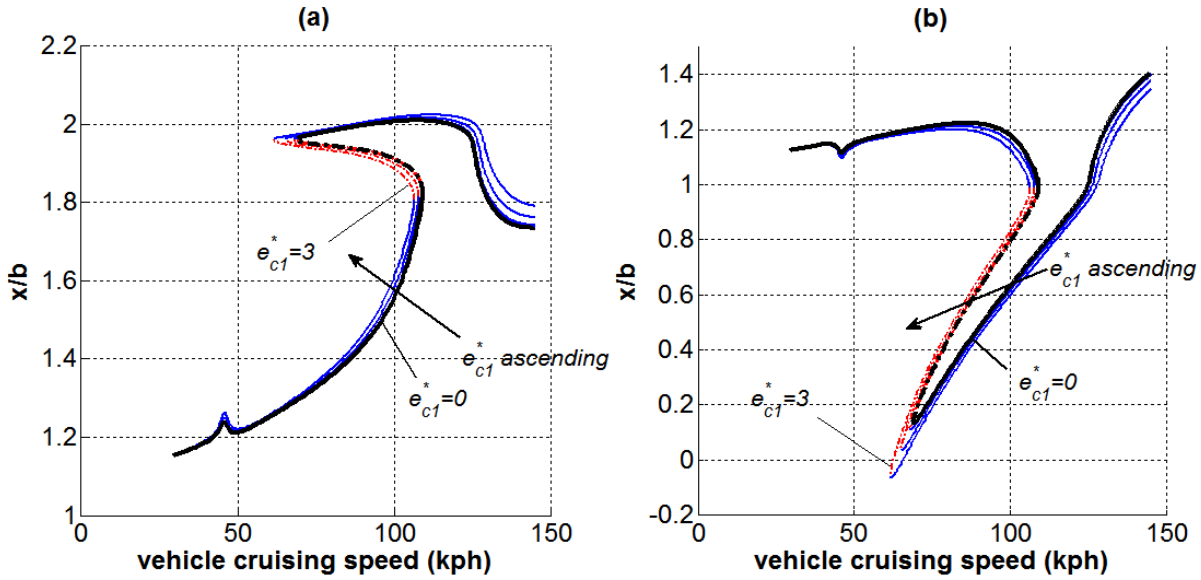

Figure 5.28- Effect of kinematic transmission error, $\pi/2$ phase difference: (a) maximum (b) minimum amplitude; _____ stable branch, _ _ _ _ unstable branch

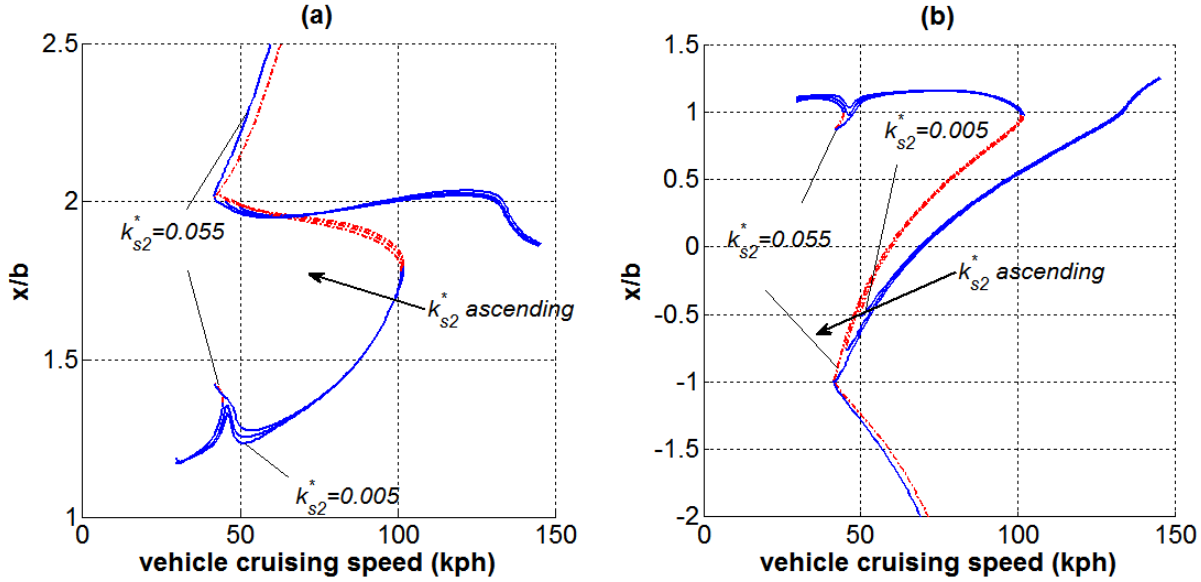

Figure 5.29- Effect of second mesh stiffness harmonic: (a) maximum (b) minimum amplitude;

_____ stable branch, _ _ _ _ unstable branch

Figure 5.29 represents the response spectra under the influence of the second stiffness harmonic. The time varying parameters are in phase, with $k^*_{s1}=0.1$, $R^*_{p,g,s1}=0.1$, $e^*_{s1}=0.5$. The remaining properties are in accordance to the previous

set of parametric investigations while no other higher order harmonics are considered. For low levels of the second mesh stiffness harmonic, the major contribution is concentrated on the superharmonic resonance (42~49kph). However, while $k_{s2}^{*} < 0.055$ no SSI impacts are realized in this region. A gradual rise of k_{s2}^{*} ignites a parametric resonance at $2\omega_{mesh} = \omega_n$, illustrated by the generation of the DSI branch and the amplification of the response magnitude in this vicinity. This parametric resonance enhances the effect of the primary resonance induced by the first mesh harmonics. For $k_{s2}^{*} \geq 0.055$ SSI solutions appear at the superharmonic region aggravating the overall response characteristics.

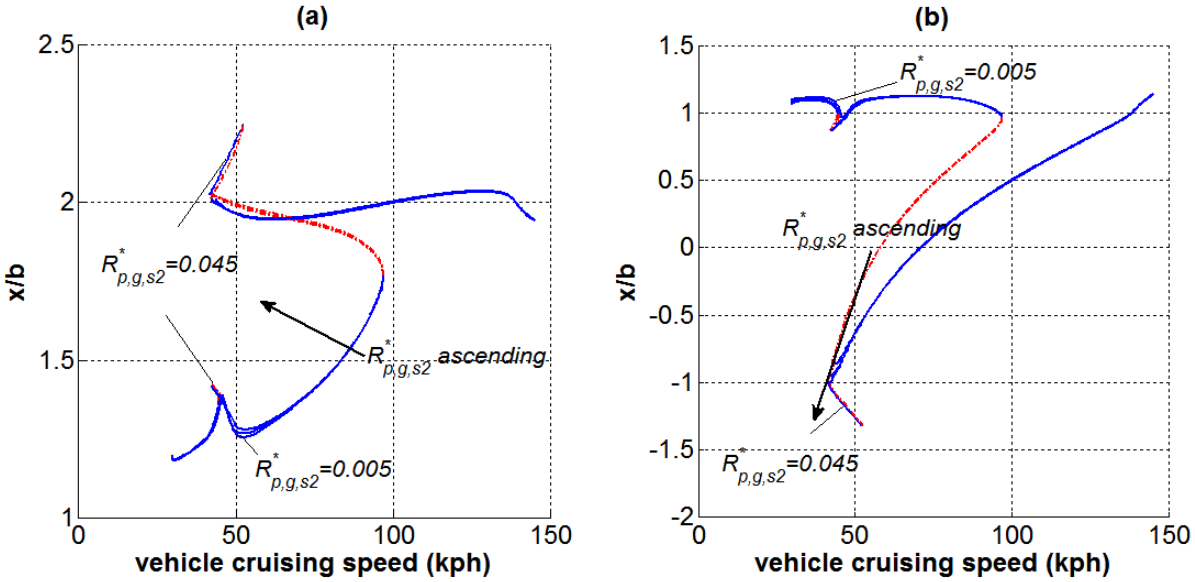

Figure 5.30- Effect of second radii variation harmonic: (a) maximum (b) minimum amplitude; ——— stable branch, _ _ _ _ unstable branch

The second harmonic term of the contact radii variation introduces analogous consequences as shown in Figure 5.30. In this instance: $k_{s1}^{*} = 0.15$, $R_{p,g,s1}^{*} = 0.1$, $e_{s1}^{*} = 0.5$, whereas the higher harmonic terms are neglected except for $R_{p,g,s2}^{*}$. An increase in its amplitude has a dual effect on primary and superharmonic resonances triggering DSI and SSI type solutions respectively. Nevertheless, this high order harmonic term is less influential compared to the one appointed in the fluctuation of mesh stiffness.

In the final stage of the parametric studies, the effect of the second harmonic term e_{s2}^* of the static transmission error is investigated. Only the fundamental mesh harmonics of all the contact parameters are considered as obtained by TCA; with the exception of k_{s1}^* which is set equal to 0.1.The above consideration is depicted in Figure 5.31, with the view concentrated at the region of superharmonic resonances. Indeed, the influence of e_{s2}^* on the primary resonance is marginal. A rise in its amplitude instigates SSI motion types in the vicinity of $2\omega_{mesh} = \omega_n$.

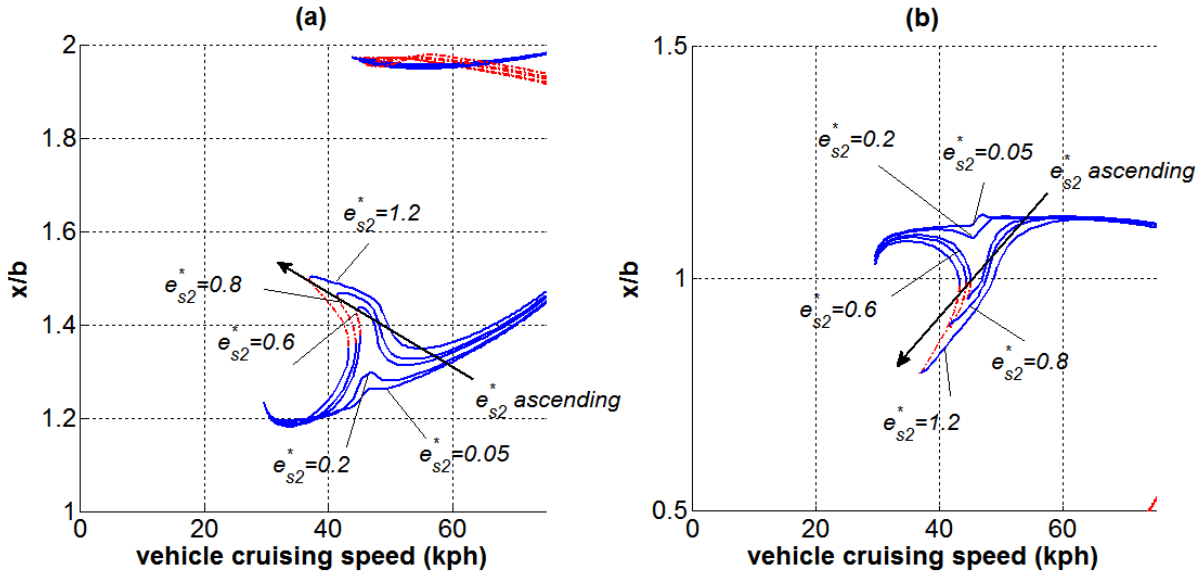

Figure 5.31- Effect of second static transmission error harmonic: (a) maximum (b) minimum amplitude; _____ stable branch, _ _ _ _ unstable branch

As a synopsis, the overall bifurcation analysis revealed a series of valuable conclusions. A complex behaviour is realised, affected by the various parameters inherent in the system. Initially, for low mesh damping values, double sided impact solution branches become possible. All the fluctuating system parameters contribute to the qualitative characteristics of the dynamic response. Mesh stiffness and contact radii when in phase tend to aggravate the system dynamics, promoting higher response amplitudes and DSI motions over a wide range of operational vehicle speeds and potentially raising considerable noise radiation issues. The reverse effect is observed when a simultaneous in-phase static transmission error mechanism is introduced, which smoothens the nonlinear behaviour and alleviates

the maximum response amplitudes. A phase shift yields contradictory consequences. Higher order harmonics of mesh stiffness and contact radii influence both the primary and the superharmonic resonance, whereas the effect of static transmission error is restricted at low vehicle speeds. All the above observations should be taken into account when designing a hypoid transmission. In contemporary mechanisms, the static transmission error is introduced as a design parameter. The contact geometry arising from the cutting tools affects the contact radii variation. The mesh stiffness variation is a consequence of the total contact ratio. Therefore, from a design perspective, it could be practically possible to introduce the above mechanisms to the design of such a system.

5.3.8 Transient conditions

The final part of the dynamic analysis concerns the transient problem. Until now, all the discussion was on the basis of dynamic balance; in this section the investigation will be expanded to cover the case when the resisting torque is greater than the input one (the vehicle is coasting). The various reports of gear whine noise under coasting conditions highlight the importance of this analysis.

The occurrence of coasting is connected to the violation of the dynamic equilibrium; the external loadings on each side of the differential do not cancel, therefore the acceleration term in equation (3.8) cannot be dropped. Input torque reduces to 15~20% of the maximum possible engine supply following a throttle release. The system is hence decelerated since the resisting torque overcomes the input. In order to simulate these conditions, the system is initially brought to steady state cruising conditions. After a certain time has elapsed (200 mesh periods), the input torque is dropped at 20% of the maximum engine supply. The resistive torque is yielded by the complete form of equation (3.8), including the inertial term expressing the resistance due to vehicle acceleration. These conditions are maintained for 200 mesh periods until the external loading takes its nominal value, leading the system again to dynamic equilibrium (Figure 5.32(a)).

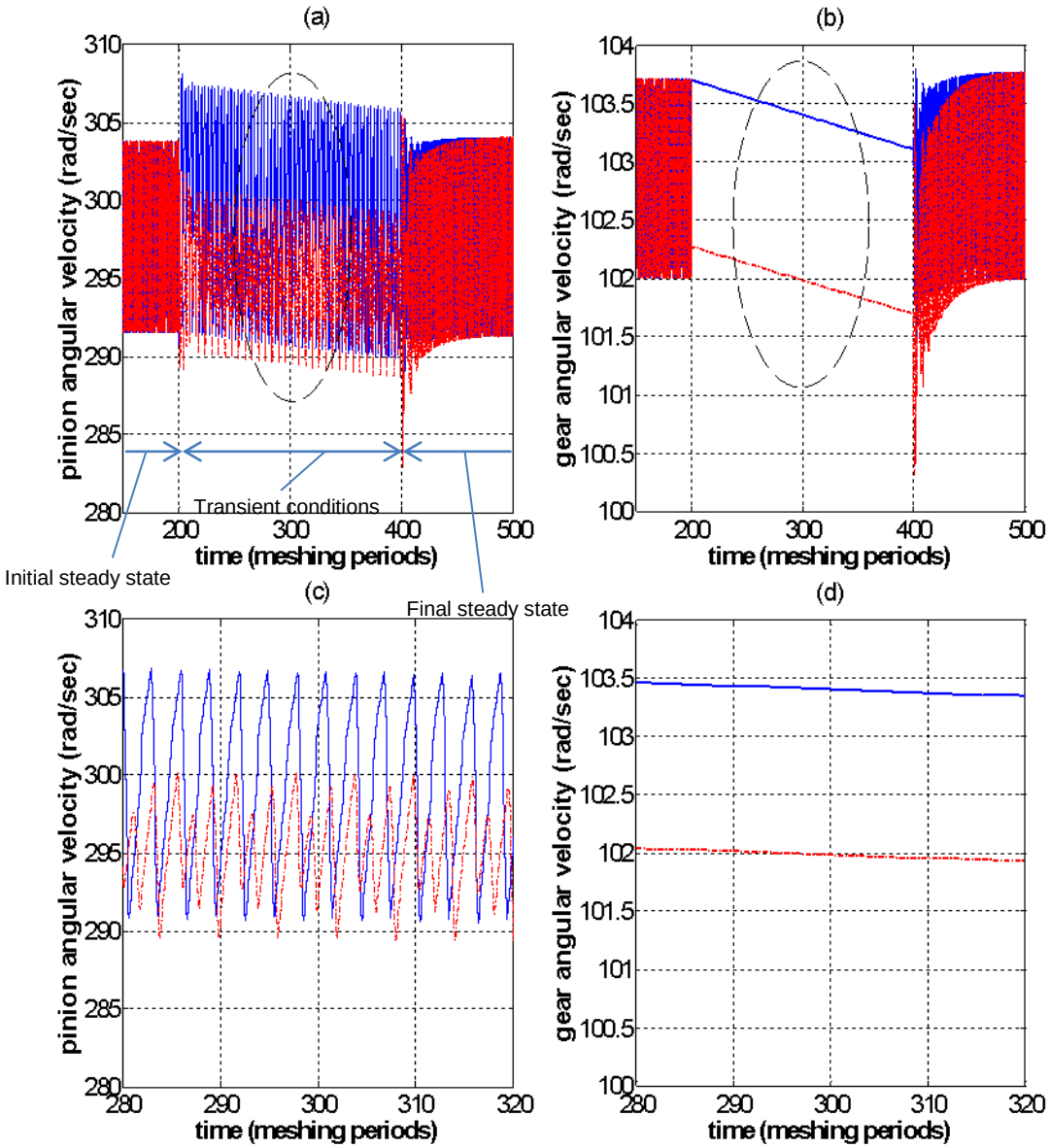

Figure 5.32- Angular velocities under coasting conditions: normal view, (a) pinion; (b) gear, detailed view, (c) pinion; (d) gear, _ _ _ _SSI , _____DSI

Time histories of the angular velocities are shown in Figure 5.32, corresponding to different sets of initial conditions. The latter are selected so as to indicate the existence of different solution types. After allowing the system to settle on steady state cruising (input torque of 246 Nm , vehicle cruising speed of 118.56kph), coasting conditions are imposed revealed by the response discontinuities at $t = 200$. The instance defining the breach of dynamic equilibrium is crucial for the system dynamics, defining the initial state used as input for the transient. Therefore, the problem is regarded as an initial value, as multiple transient solutions can be derived

from a global steady state motion. Another rupture is observed at the point where the equilibrium is re-established; both transients gradually reach the initial steady state condition.

A more detailed view of the response time histories in Figure 5.32(c) depicts a significant difference between the two transients. The divergence is both in terms of amplitude and frequency; the aggravated case seems two oscillate slower with a frequency ratio of almost 2:3. Another important notice is the deceleration of both gear components. Finally, by observing Figure 5.32(d), it is implied that the crown gear motion is dominated only by the rigid body rotation whereas the oscillating component is not visible.

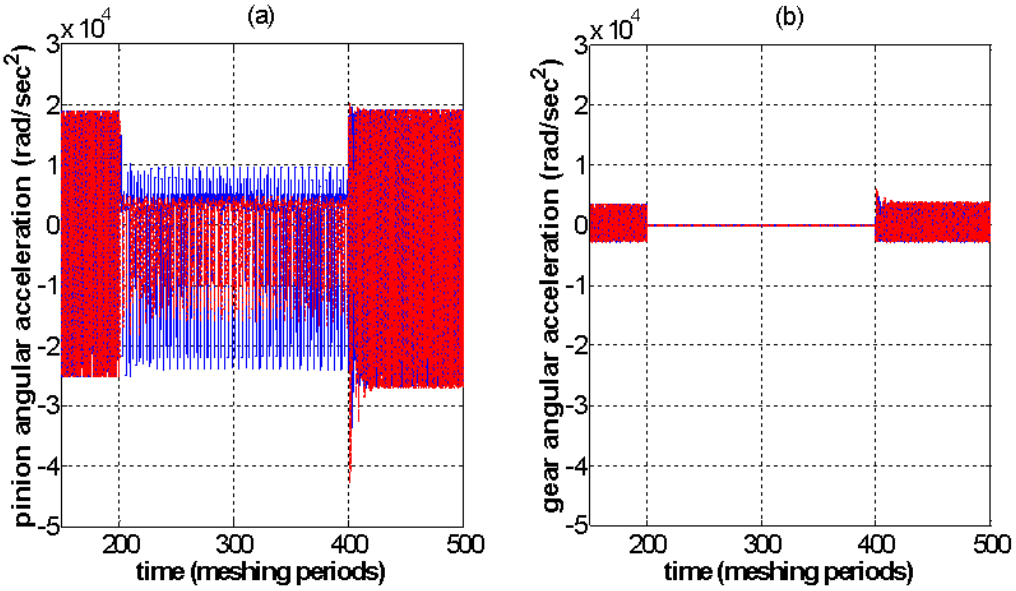

Figure 5.33- Angular accelerations under coasting conditions: (a) pinion; (b) gear, _ _ _ _ SSI , _____DSI

Figure 5.33 depicts the corresponding angular accelerations. For the pinion, the acceleration level during steady state and transient conditions is within the same order of magnitude. On the other hand, for the crown gear the difference is within orders of magnitude. This is due to the acceleration term present in equation (3.8), defining the overall resisting torque. This quantity can be expanded with the aid of equation (3.9), thus yielding an equivalent inertia term I_a, which should be added to the differential unit inertia I_g (eq. (3.4)). Hence, I_a can be defined as follows:

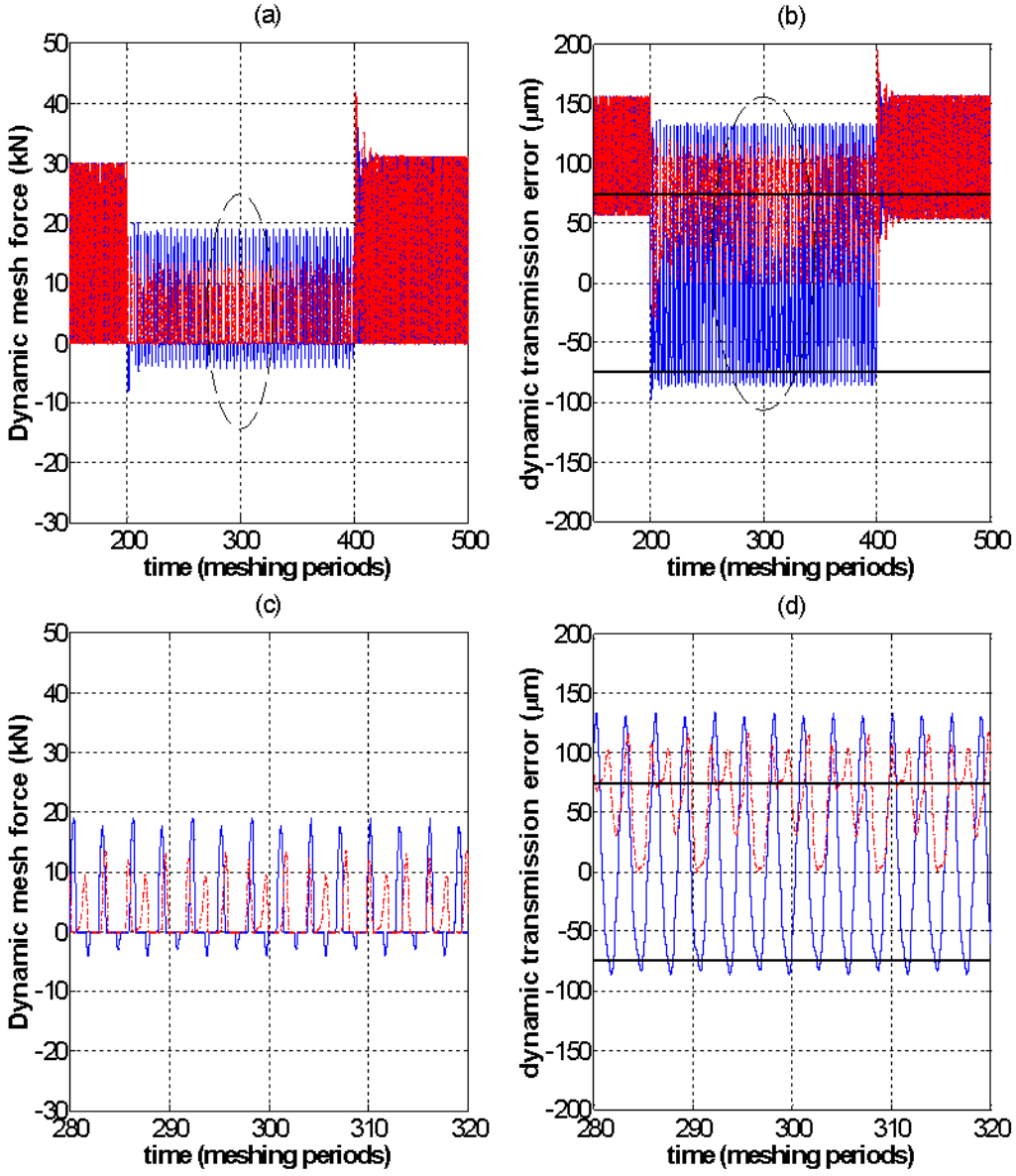

Figure 5.34- Dynamic response time histories under coasting conditions: normal view, (a) mesh force; (b) dynamic transmission error, detailed view, (c) mesh force; (d) dynamic transmission error, _ _ _ _ SSI, _____ DSI

$$I_a = mr^2 + J_R \qquad \textbf{(5.17)}$$

It should be noted that m represents the vehicle mass and J_R corresponds to the road wheels inertia. Acknowledging that I_a is almost three orders of magnitude

greater than I_g, the excessive difference in the crown gear acceleration between steady state and transient motions is justified.

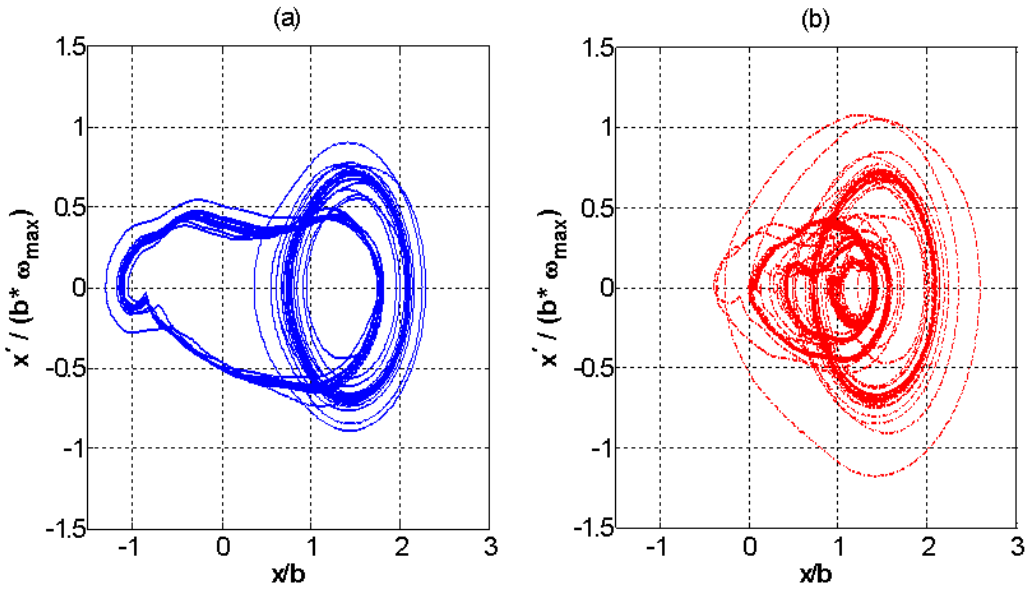

Figure 5.35- Phase plots: (a) Double Sided Impact (b) Single Sided Impact motion

The time histories of mesh force and dynamic transmission error are illustrated in Figure 5.34. Both quantities are naturally related to the relative displacement of the gear teeth. Clearly, under coasting, the relative motion is characterized by a shift in the extreme oscillating positions. This change, depending on the initial conditions, can switch the sign of the mesh force and induce double-sided impacts between the mating flanks. The phase plots of Figure 5.35 show how the initial steady state can generate two completely different motions by starting from different initial conditions; these are defined by the dynamic balance break point.

The spectral content of the dynamic mesh force (Figure 5.34(c)) is shown in Figure 5.36. Apart from the mesh order contribution present in both signals, a clear influence of the subharmonic frequencies can be identified. However, different frequency components are present in each case. It is also important to examine the time-frequency characteristics of the two motions. This is accomplished by employing the wavelet transform (WT), a windowing technique capable of analysing not stationary signals. WT conducts a multi-resolution analysis with respect to both time and frequency, revealing more information than the FFT spectra. The MATLAB

subroutine *cwtft* is utilised for the purposes of the analysis, yielding the temporal evolution of the frequency content of each signal.

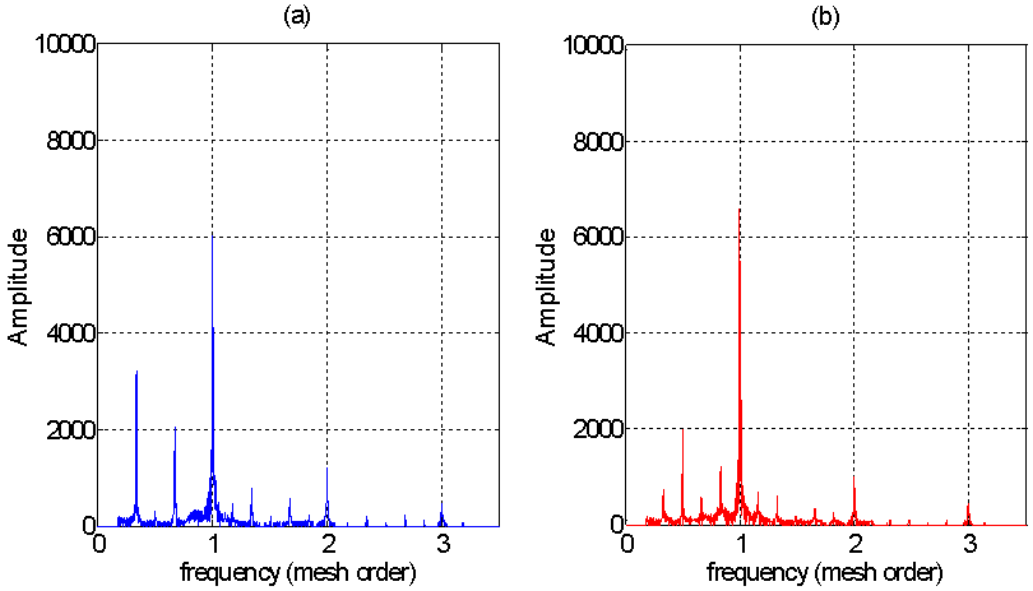

Figure 5.36- FFT of the dynamic mesh force: (a) Double Sided Impact (b) Single Sided Impact motion

The wavelet transform results applied to the angular acceleration of the pinion are seen in Figure 5.37 - Figure 5.38. The graphs depict the amplitude of the WT with respect to frequency (y-axis) and time (x-axis). High amplitude intensity is denoted by red contours, whereas the blue ones correspond to low amplitude regions. Purple lines are indicating the frequency level of certain mesh orders. The examination of the instantaneous frequency components implies that in both cases the mesh order is dominating during conditions of dynamic equilibrium, while a small contribution of the super harmonics is also evident. Under the occurrence of coasting, the frequency undergoes a transition to mesh order sub harmonics, followed by disappearance of the mesh order. The new governing frequency is highly dependent on the type of solution; the 1:3 and 2:3 mesh order sub harmonics are dominant under DSI motions whereas the 1:2 governs the dynamic response when SSI are realised.

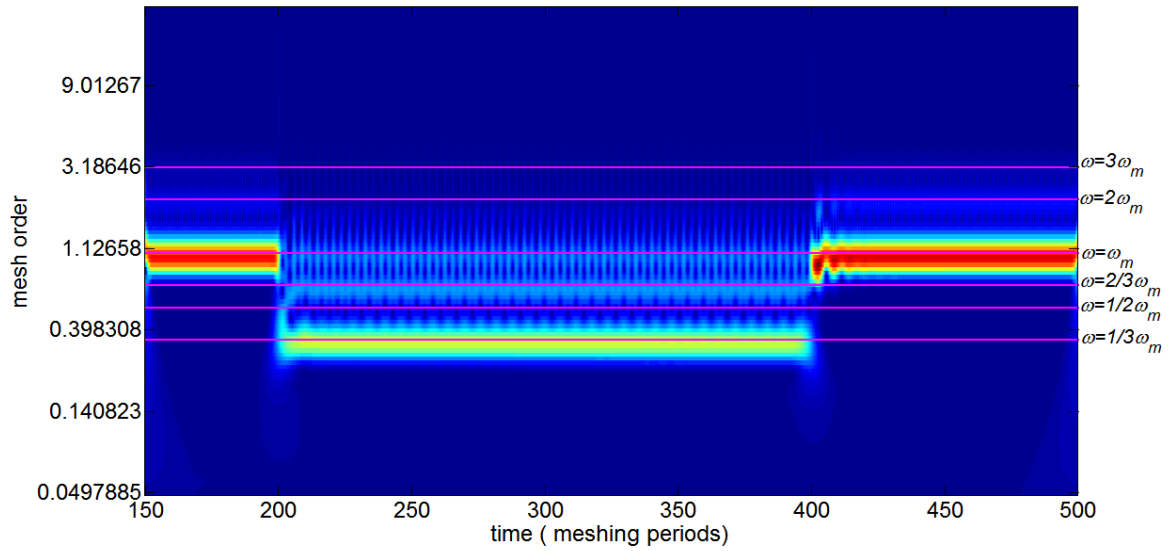

Figure 5.37- Wavelet analysis of pinion acceleration, DSI case

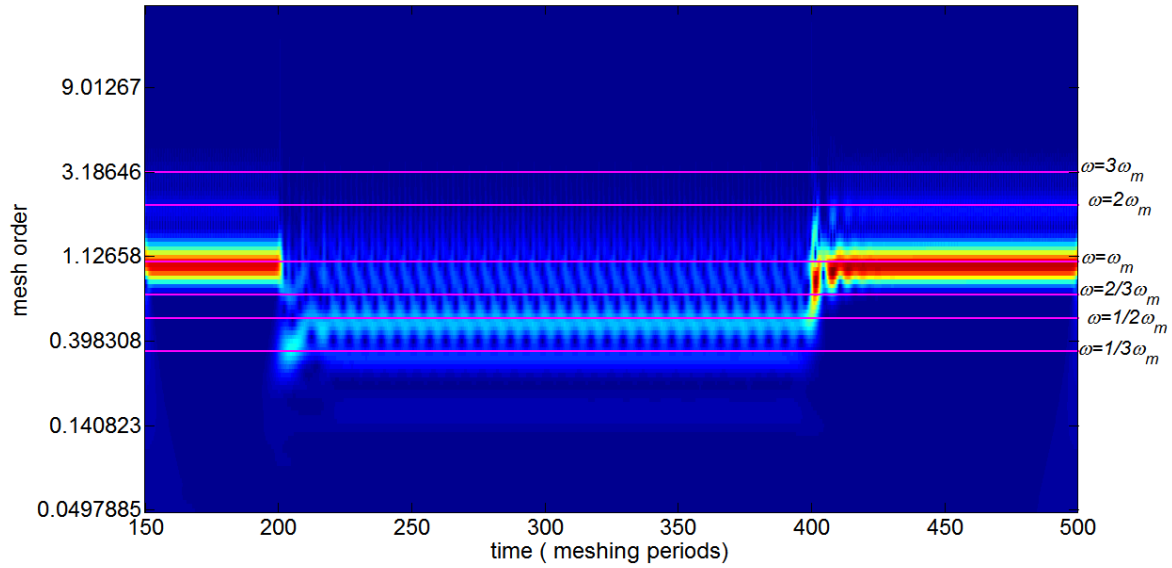

Figure 5.38- Wavelet analysis of pinion acceleration, SSI case

The possibility of DSI motions is a crucial factor for the generation of gear noise (Lee, 2007). Hence, the preceding analysis needs to be expanded to the whole operational range of the vehicle speed, in order to address the severity of this phenomenon. Vehicle speed - response diagrams are constructed by performing speed sweeps. Coasting conditions are applied at different stages of a meshing period within the initial steady state motion. The need of accounting all the possible

initial states of the transient response requires the trial of 100 different initial conditions arising from the steady state motion. The individual dynamic responses generated by these initial conditions are recorded and compared in terms of maximum double-sided impact events. The results corresponding to the worst case scenario at each vehicle speed are presented in Figure 5.39.

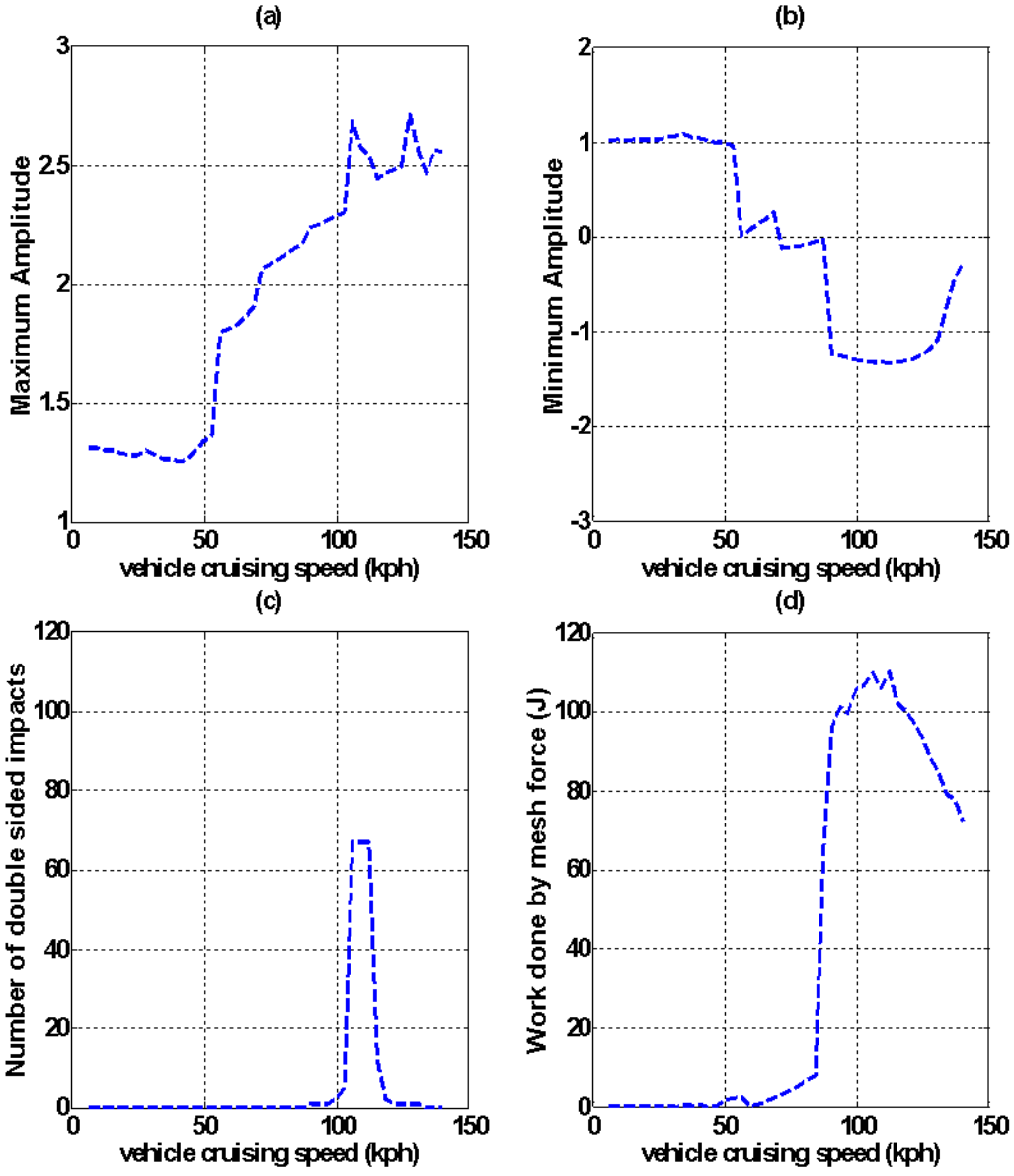

Figure 5.39- Response Spectra for coasting conditions: (a) Maximum, (b) Minimum Amplitude, (c) Number of double sided (d) Elastic Energy per 100 cycles

Only the acceleration case is illustrated, since in this case the difference between ascending and descending velocities is only marginal. A vehicle speed region

extending from 90 to 131kph presents double-sided impact phenomena, as seen in Figure 5.39(b). Nonetheless, the number of the double sided impacts becomes significant around a vehicle speed of 120kph (Figure 5.38(c)). From this point and onwards, DSI appear at a considerable rate, as already shown in the response time histories of Figure 5.34 and was also witnessed by the frequency content of the motion. In this vehicle speed range, maximum and minimum amplitudes reach their extreme values, indicating that the mating flanks suffer from severe separation.

To summarize, it was shown that besides the DSI solution branches encountered under steady state cruising, similar solutions are possible when the dynamic balance is violated. Under these circumstances, the resisting torque is now driving the system, causing a deceleration of both gears. The dynamic response observed during coasting is highly sensitive to the initial conditions, namely the time instance of the throttle release. Under certain conditions, the dynamics of the relative motion will settle to a double-sided impact motion which can induce considerable noise issues. Realization of such a motion is accompanied to a frequency shifting to 1:3 and 2:3 of the mesh order sub harmonics. These phenomena appear on a broad region of vehicle speeds, yet they are more pronounced on higher velocity scales.

5.4 -Synopsis

In this chapter, the dynamics of the gear pair were presented on the basis of the theoretical background developed in Chapter 3. The contribution of friction was neglected, focusing on identifying the capabilities of the proposed mechanical model. The inherent considerations were explained and their effect on the dynamic response was illustrated. Beginning from steady state cruising, the importance of multiple solutions and jump phenomena was highlighted. The study of periodic solutions proved the possibility of more aggravated dynamic response, induced by double-sided impacts. A thorough parametric investigation was conducted to verify the importance of the system parameters when such behaviour is realised. Similar phenomena were encountered under coasting conditions. Therefore the system possesses a tendency of exhibiting violent behaviour on a significant part of its operating range, hence promoting NVH issues.

Chapter 6 - Tribodynamic Analysis

6.1 - Introduction

In the previous chapter, the numerical results were yielded by assuming frictionless contact conditions. The lubrication characteristics were neglected focusing on the prediction of the various types of motions arising from the dynamic problem. Indeed, such an approximation is valid since the effect of friction on the torsional dynamics has been shown to be marginal.

Nonetheless, friction can affect the off line of action dynamics if lateral degrees of freedom are considered, whereas it is the main element associated with the transmission efficiency. Furthermore, a tribological analysis can yield an insight into the film thickness magnitude and the temperature rise inside the transmission; important factors for the design of a differential unit.

In this chapter, simulation of the multi-scale physics of the problem will be attempted by coupling dynamics and tribology. Correlation with respect to published material will be presented for validation purposes.

6.2 - Computational Algorithm

The computational algorithm solving the dynamics was presented in section 5.3, whereas the corresponding flowchart in Figure 5.1. Evaluation of the lubrication properties requires the inclusion of an additional subroutine addressing the EHL regime of lubrication. By this means, coupling of the different scales of the problem on a multi-physics level is achieved.

Properties obtained from the dynamic analysis such as the mesh force and the angular velocity are affecting the formation of the film thickness as seen in section 4.3.3. It was also observed in the preceding chapter that these variables exhibit a considerable change in their magnitude following the acceleration or deceleration of the vehicle due to resonance. At the same time, the relative sliding of the mating flanks induces friction caused by both surface asperities and viscous shear. Friction affects the system dynamics by introducing an additional excitation, setting a further link between dynamics and tribology.

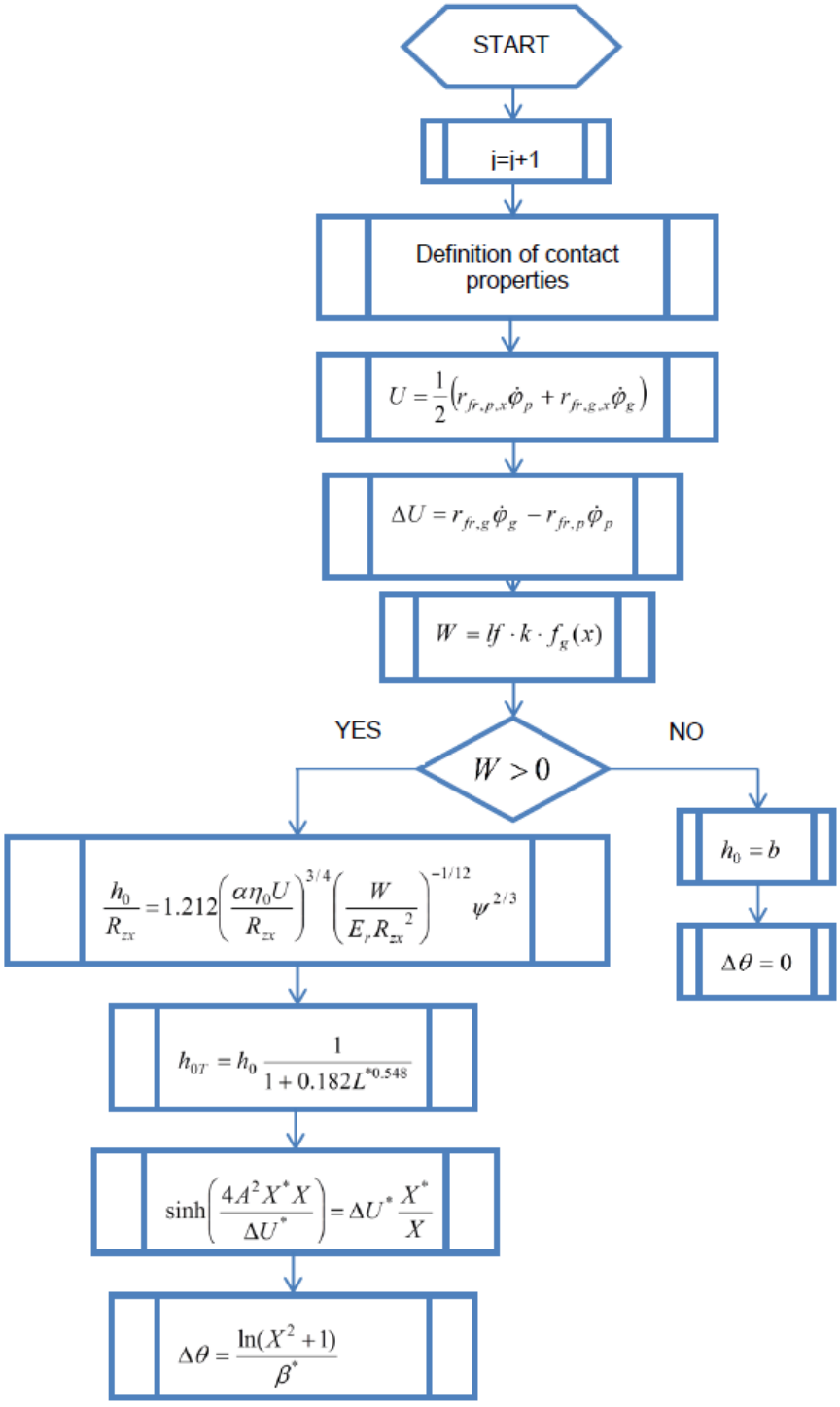

Figure 6.1- EHL subroutine for Grubin type solution

The maximum temperature rise inside the differential is also of great importance for designers. The film thickness is affected by inlet viscosity, which is a function of the corresponding temperature rise; hence a thermal correction factor is applied to

accommodate this change in the lubricant properties. The viscous shear rate results into heat generation which is transferred to the mating surfaces mainly though conduction, since the thin film size under EHL conditions (typically below $2\mu m$) renders the convective terms insignificant. The corresponding temperature rise needs to be calculated, since it will influence the effective lubricant viscosity and thus the magnitude of friction.

The computational procedure employed in the tribological analysis is presented in Figure 6.1. It involves the engagement process of an individual gear pair under non Newtonian regime of lubrication by employing Grubin's equation to compute the lubricant film thickness. The same formulation is implemented under two dimensional flows, by using the appropriate expressions for kinematics and film thickness. Eventually the output of the EHL subroutine is inserted in the equations of motion in the form of the overall frictional torque, providing the second link in this tribo-dynamic approach.

It should be noted that the EHL routine is not iterative; it just requires the solution of the nonlinear equation (4.50). In this case, the dynamics of the problem are addressed by the Runge-Kutta algorithm, inherent in ode45 MATLAB solver. The latter is preferred as a programming interface due to its built in subroutines which can be used to solve nonlinear algebraic equations. Nevertheless, this comes at the expense of the numerical efficiency, increasing considerably the necessary computational time.

6.3 - Load and film thickness variation under non Newtonian isothermal conditions

The consideration of isothermal conditions is the first step of the tribological analysis. During this stage, the lubrication conditions governing the hypoid gear mesh will be identified. At the same time, the variation of the fundamental lubrication properties along a complete meshing cycle will be illustrated. The latter will form the basis of comparison when assessing the heat generation effect. The simulation results presented in this section correspond to the set of system parameters presented in the previous chapter (Table 5.1). The only difference is observed in the vehicle

cruising speed, which is equal to 59.28kph, resulting to an input torque of 81.07 Nm and a pinion rotational velocity of 1423 RPM. This nominal case will be used frequently for a set of simulations throughout this chapter. The graphs, unless specified differently will address the aforementioned conditions. The main lubricant properties are seen in Table 6.1, whereas the roughness of each individual gear surface is given by the root mean square (RMS) value which is taken equal ton $0.5\mu m$.

Table 6.1- Lubricant fluid properties

Property	Numerical value
Kinematic viscosity at $100^0 C$ (cSt)	16.7
Kinematic viscosity at $40^0 C$ (cSt)	109.1
η_0; Dynamic viscosity at $100^0 C$ (Pa s)	0.0145
η_0; Dynamic viscosity at $40^0 C$ (Pa s)	0.09483
Density (kg/m^3)	870
Thermal conductivity at $100^0 C$ (W/mK)	0.1077
Thermal conductivity at $40^0 C$ (W/mK)	0.1121
α_0; pressure viscosity coefficient (Pa^{-1})	$14.4*10^{-9}$
β; temperature viscosity coefficient (K^{-1})	0.0217
τ_0; Eyring stress (MPa)	5

The tribological status of the gear contact is characterised by the dual effect of lubrication and traction regimes. The former defines the severity of the local deformations in the formation of the lubricant film whereas the latter influences the rheological properties of the fluid demonstrating potential deviation from the traditional Newtonian treatment.

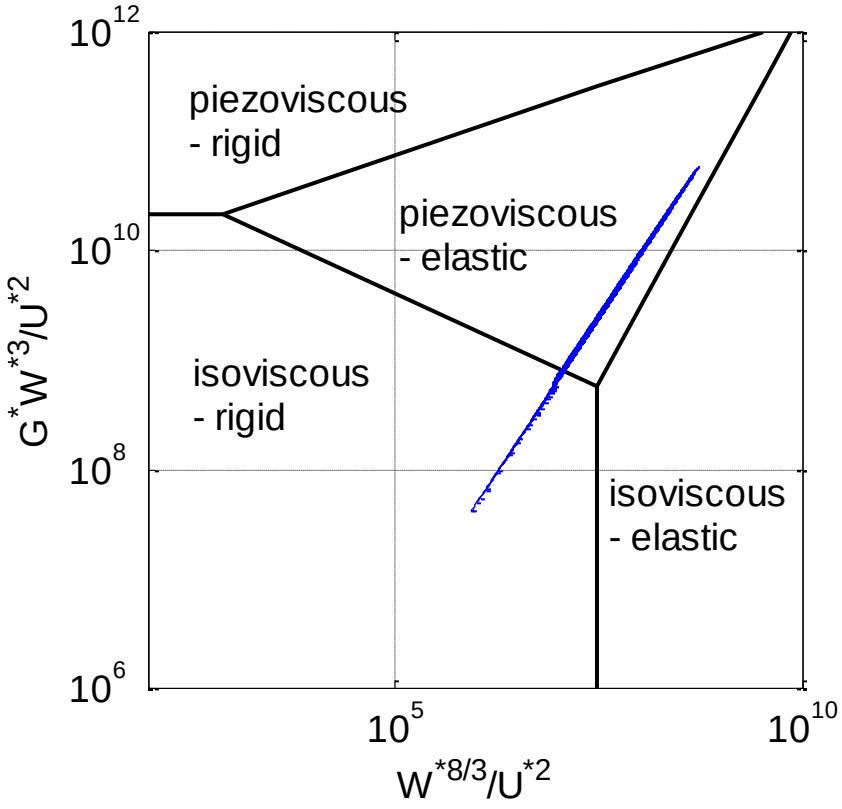

Figure 6.2- Lubrication regime chart; boundaries (black lines) and meshing cycle (blue line)

The boundaries separating the different lubrication regimes are illustrated in the form of two dimensional charts, expressed with respect to dimensional groups related to load, speed and material properties. An algorithm for constructing such diagrams is provided by Gohar (2001), by employing extrapolated formulae (Chittenden et al, 1985) for the film thickness estimation under point contact conditions. A typical lubrication regime chart is shown in Figure 6.2. The dimensionless quantities acting as ordinate and abscissa are defined in Table 6.2.

If the elastic deformation of the solid surfaces is significant (trivial) the lubrication region is termed elastic (rigid). Furthermore, if the lubricant fluid viscosity is affected

(unaffected) by pressure, then the area is classified as piezoviscous (isoviscous). The blue curve in figure 6.2 represents a complete meshing cycle under isothermal conditions when the inlet lubricant temperature is equal to $40^0 C$. It is clear that the lubrication regime falls mainly into the piezoviscous elastic (EHL) region whereas another fragment lies inside the isoviscous rigid (hydrodynamic).

Table 6.2- Dimensionless Group definition

Dimensionless Group	Definition
U^*	$\frac{\eta_0 U}{E_r R_{zx}}$
G^*	$E_r \alpha$
W^*	$\frac{W}{E_r R_{zx}^2}$

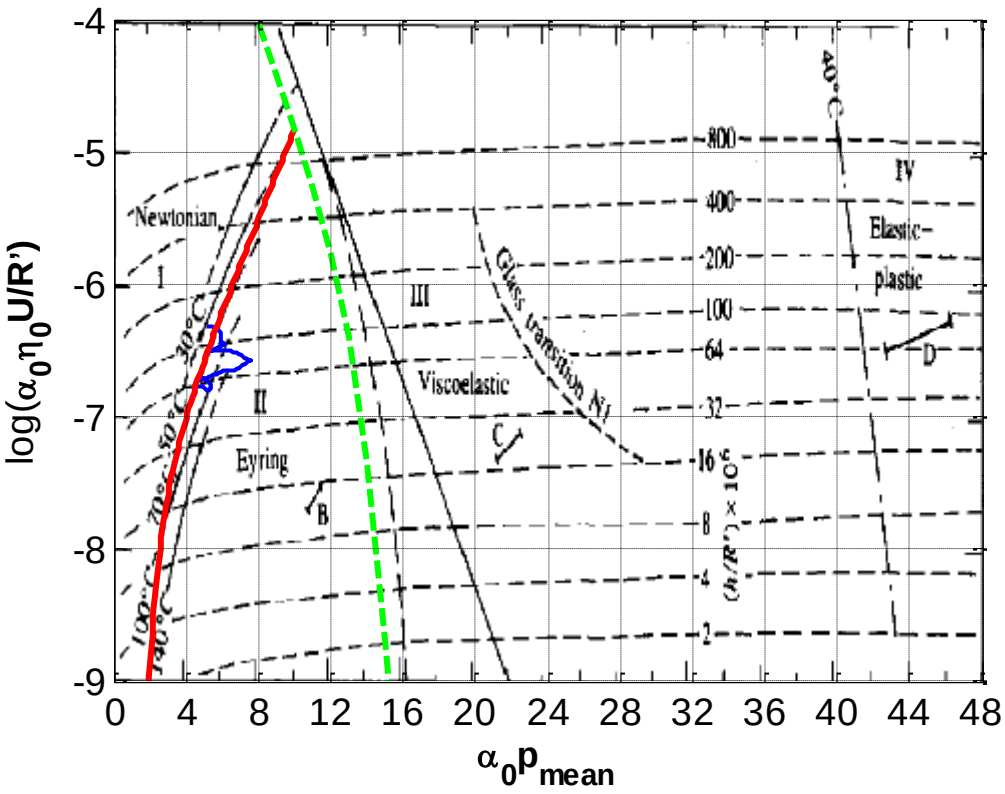

Figure 6.3- Traction map for high viscosity mineral oil (after Evans and Johnson, 1986); non Newtonian boundary (red curve _____), viscoelastic boundary (green curve _ _ _ _) and meshing cycle (blue curve _____).

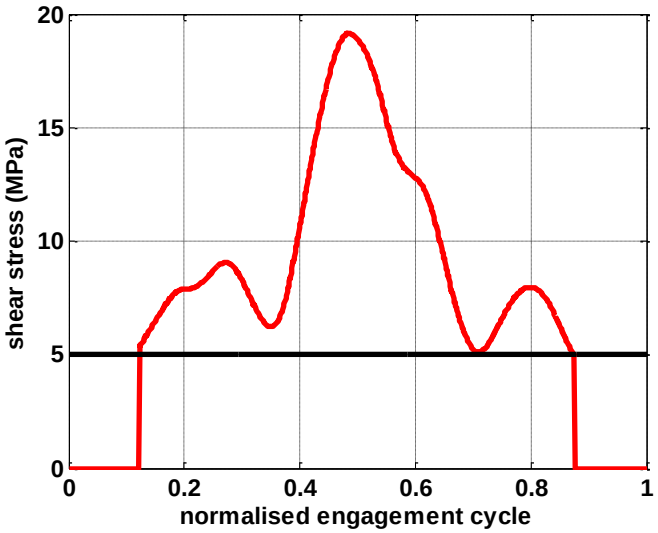

Figure 6.4- Shear stress under Newtonian consideration

The traction map is demonstrated in Figure 6.3. The background is attributed to Evans and Johnson (1986), corresponding to the case of a high viscosity mineral oil. It is obvious that the boundary curves governing the transition towards Eyring and viscoelastic regions are close to the ones predicted for the hypoid transmission oil. The latter are represented by the red and green curve respectively, derived from the analytical expressions of Evans and Johnson (1986). A set of points describing a complete meshing cycle is again placed on the graph forming the blue curve; it can be noted that it lies almost entirely in the Eyring region. Additional evidence on the traction regime is presented in Figure 6.4. The shear stress under Newtonian conditions is depicted for the same conditions as previously. It is noted that the Eyring stress limit is exceeded throughout the engagement cycle. Therefore, a nonlinear model needs to be applied to address modified lubricant rheology, based on the analysis of Johnson and Greenwood (1980).

The load and film thickness variations along a meshing cycle are shown in Figure 6.5(a) for a two dimensional lubricant flow (Chittenden et al, 1986). The flank load is obviously influenced by the dynamic effects during the cycle. At the same time the film thickness remains almost constant in the first half of the cycle, insensitive to the contact load variation which is a typical characteristic of the EHL regime. The size of the lubricant film is mainly attributed to the entraining velocity and the radius of curvature along this direction as suggested in equation (4.31). These quantities,

illustrated in Figure 6.5(b), exhibit an almost linear variation within the engagement cycle; their gradient being opposite in sign. It seems that these two competing factors “cancel out”, resulting in an almost constant value for the lubricant film.

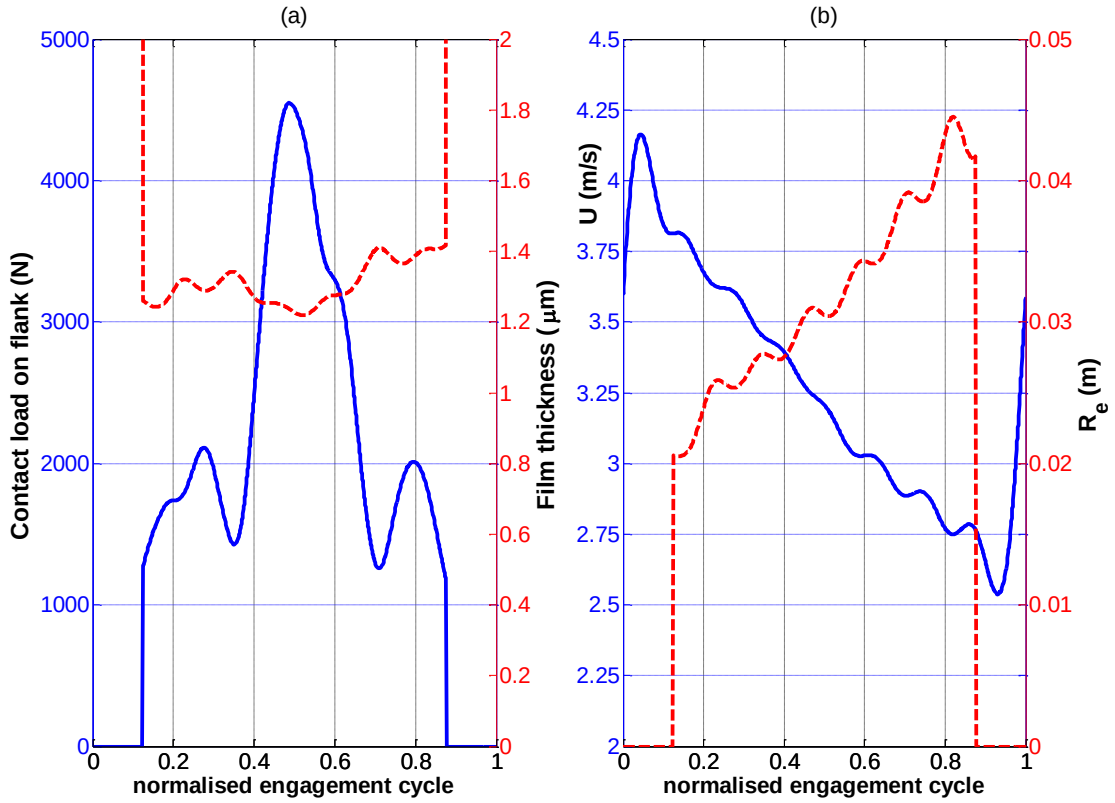

Figure 6.5- Tribological properties for two dimensional flow (Chittenden et al, 1986) at inlet lubricant temperature $\theta_{in} = 40^0 C$; (a) ——— Load (W), - - - - central film thickness (h_0), (b) ——— entraining velocity (U), - - - - radius of curvature along the entrainment direction (R_e)

Figure 6.6 (a) shows the comparison of the film thickness estimation between another two dimensional solution (Mostofi and Gohar, 1982) and Grubin (1949). The latter assumes that the flow is along the minor axis of the contact ellipse, hence neglecting considerable portion of the lubricant entrainment. This fact is reflected in the magnitude of the two solutions, with the two dimensional being almost double in magnitude; although the pattern along the meshing cycle is almost identical. Observation of the entraining velocities in Figure 6.6(b) reveals the importance of the

flow along the major axis direction. It is obvious that it represents the major contribution of the overall entraining velocity.

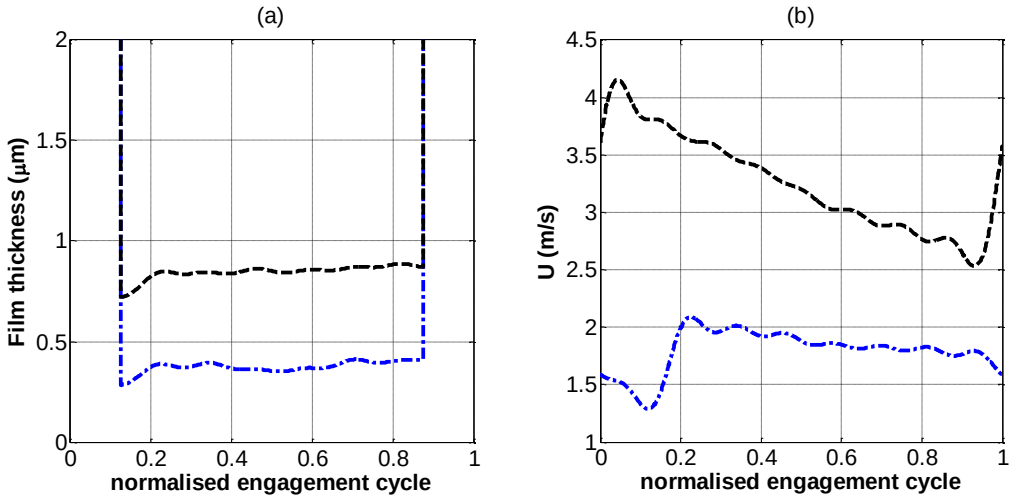

Figure 6.6- Comparison of (a) film thickness and (b) entraining velocities for inlet lubricant temperature $\theta_{in} = 40^0 C$; _ _ _ _Mostofi and Gohar (1982), __ . __Grubin (1949)

6.4 - Friction and gear pair efficiency

A graphical representation of the viscous friction force can be seen in Figure 6.7(a). In general it follows the fluctuation of the contact load; however its amplitude is one to two orders of magnitude smaller. Another observation is the absence of pure rolling conditions, since the relative sliding motion never changes direction as seen in Figure 6.8. Hence, the sign of friction is maintained constant throughout the engagement cycle.

The shear rate governing viscous frictional force is depicted in Figure 6.7(b). Throughout the engagement cycle, viscous shear is mainly affected by the lubricant film, therefore the higher rate under one-dimensional flow; the thinner films yielded by Grubin type solution result into higher shear rates and friction magnitudes. Nevertheless, the difference in force is not proportional to the shear rate since the lubricant rheology is nonlinear and follows the Eyring regime (equation (4.48)).

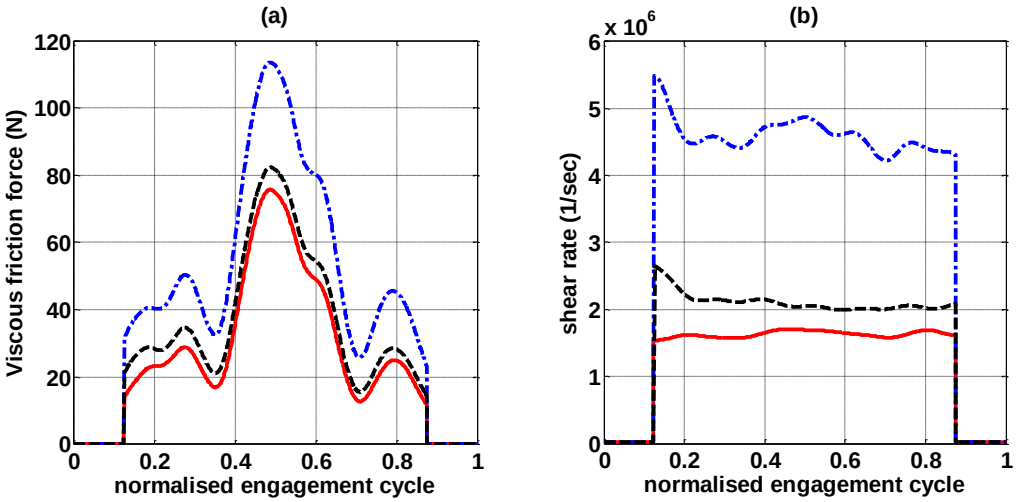

Figure 6.7--(a) Viscous friction force, (b) shear rate during an engagement cycle; ——— Chittenden et al (1986), _ _ _ _ Mostofi and Gohar (1982), __ . __ Grubin (1949)

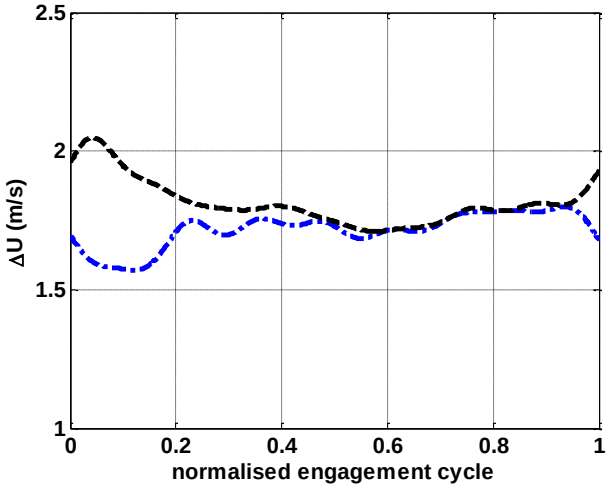

Figure 6.8- Sliding velocity; _ _ _ _two dimensional, __ . __ one dimensional flow

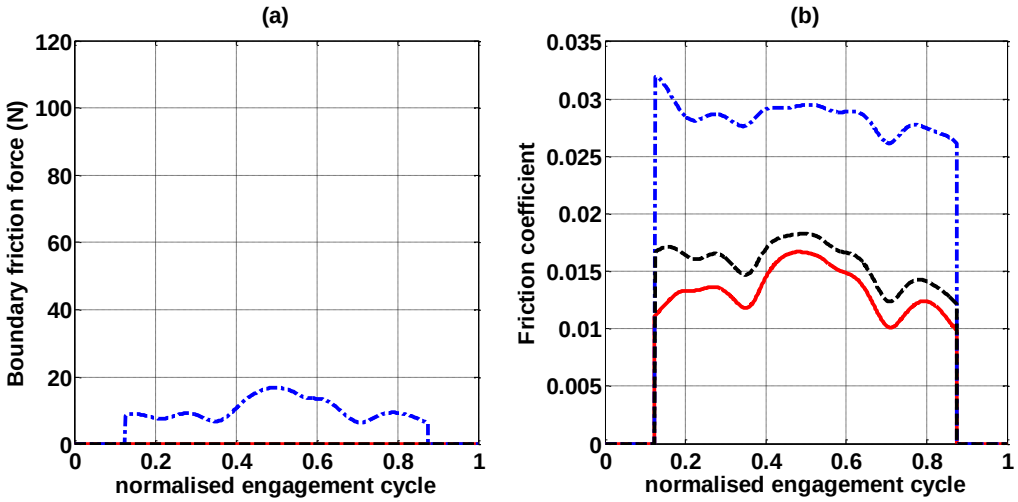

Figure 6.9- (a) Boundary friction force, (b) friction coefficient; _____Chittenden et al (1986), _ _ _ _ Mostofi and Gohar (1982), __ . __ Grubin (1949)

The film size is crucial for asperity contact and generation of boundary friction. As illustrated in Figure 6.9(a), only the Grubin type solution predicts such a case, owed to the fact that the combined root mean square roughness $\left(R_q\right)$ is equal to 0.71 μm. This value is always less than the minimum film value encountered in two-dimensional flows. The combined effect of viscous shear and asperity interaction is reflected in Figure 6.9(b), where the Grubin assumption renders the highest friction coefficient values. The two dimensional cases are ranked inversely with respect to the film thickness. The frictional torque at the pinion follows the same rule in terms of magnitude (Figure 6.10 (a)); nonetheless the latter is trivial compared to the input. If the contribution of all the flanks is summed up and the damping losses are also accounted for, the overall gear pair efficiency can be computed (Figure 6.10 (b)). The losses are mainly dominated by the friction magnitude, since the relative sliding speed becomes constant after the first quarter of the meshing cycle (Figure 6.8).

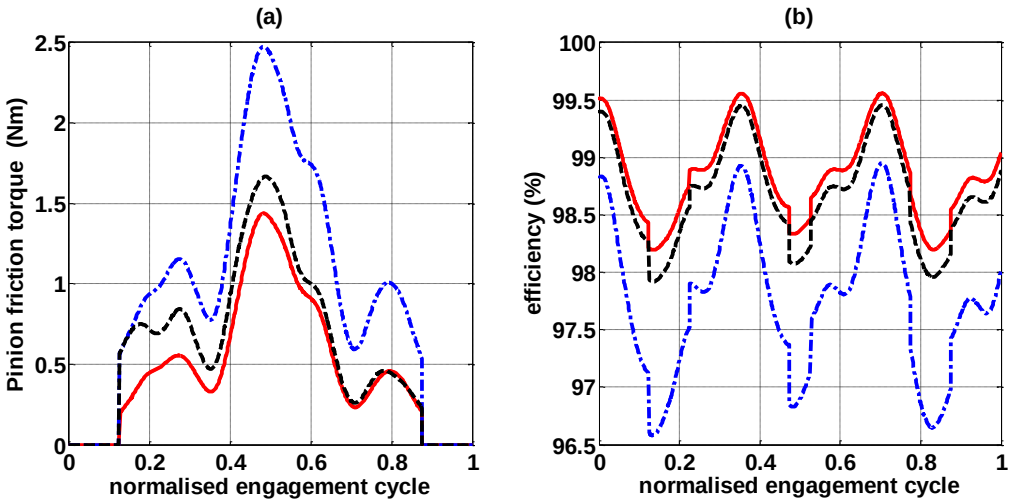

Figure 6.10-- a) Pinion frictional torque and (b) overall gear pair efficiency; _____ Chittenden et al (1986) _ _ _ _ Mostofi and Gohar (1982), __ . __ Grubin (1949)

6.5 - Heat balance

The excessive relative sliding motion between the mating flanks causes a considerable heat generation in the lubricant film, which is dissipated on the boundary surfaces. Knowledge of the temperature rise is crucial, since it can affect the effective lubricant viscosity value, which in turn determines the level of frictional forces. Figure 6.11(a) displays the temperature fluctuation of the lubricant fluid under the following main assumptions: (i) the lubricant inlet temperature remains constant and equal to $40^0 C$, hence no heat is accumulated during its recirculation and (ii) the heating of the metallic gear surfaces is neglected based on the work of Crook (1961).

This pattern is almost identical for all cases and is predominantly influenced by the contact load which alters the lubricant viscosity. In addition, the relative sliding speed plays an important role, as well as the kinematics for the estimation of the film thickness; the latter is corrected proportionally to the entraining velocity (Gohar, 2001) to accommodate the change of inlet viscosity due to the shear effect (Figure 6.11(b)). Indeed, the film thickness magnitude differences between isothermal and thermal conditions are more pronounced in the two dimensional solution types in accordance to faster oil entrainment.

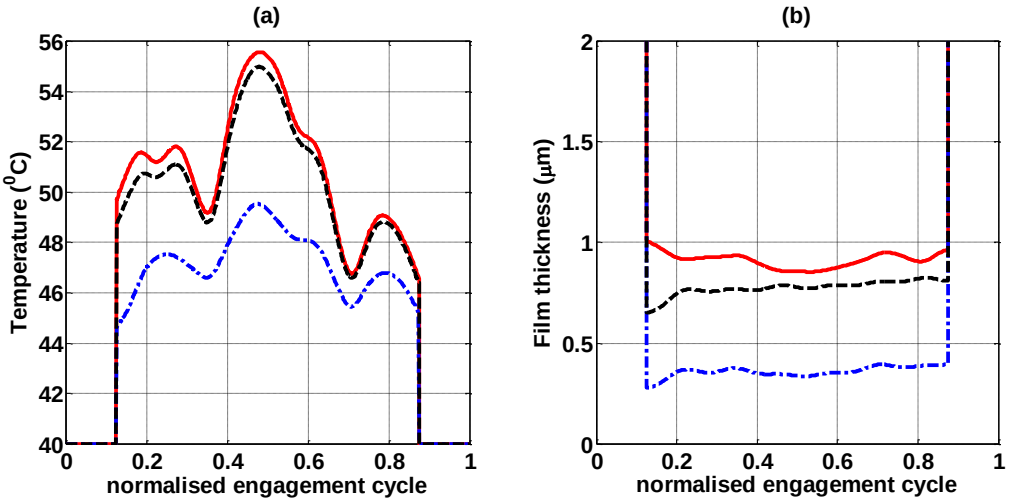

Figure 6.11- (a) Temperature and (b) film thickenss distribution across an engagement cycle $\theta_{in} = 40^0 C$ **;** ——— **Chittenden et al (1986)** – – – – **Mostofi and Gohar (1982),** — . — **Grubin (1949)**

Figure 6.12(a) shows the variation of friction coefficient which is reduced compared to the isothermal case. The temperature rise induces a drop in the lubricant effective viscosity, pushing the overall friction to lower levels (Figure 6.13). The same effect can be seen it the representation of the transmission efficiency in Figure 6.12(b) whose fluctuation is shifted to a higher threshold.

The impact of increasing the inlet lubricant temperature on the tribological properties is visualized in Figure 6.14 - Figure 6.17 by applying a Chittenden type solution. The temperature rise in the engagement cycle tends to decrease significantly (by almost 75% in the midpoint vicinity) when the inlet lubricant is heated up to $100^0 C$ (Figure 6.14(a)). The simultaneous drop in the inlet viscosity yields considerably lower magnitudes of film thickness (Figure 6.14(b) shows a noticeable reduction of nearly 66%). Normally this results into an increased shear rate, almost triple in magnitude compared to the previous inlet temperature indicated by Figure 6.15(a).

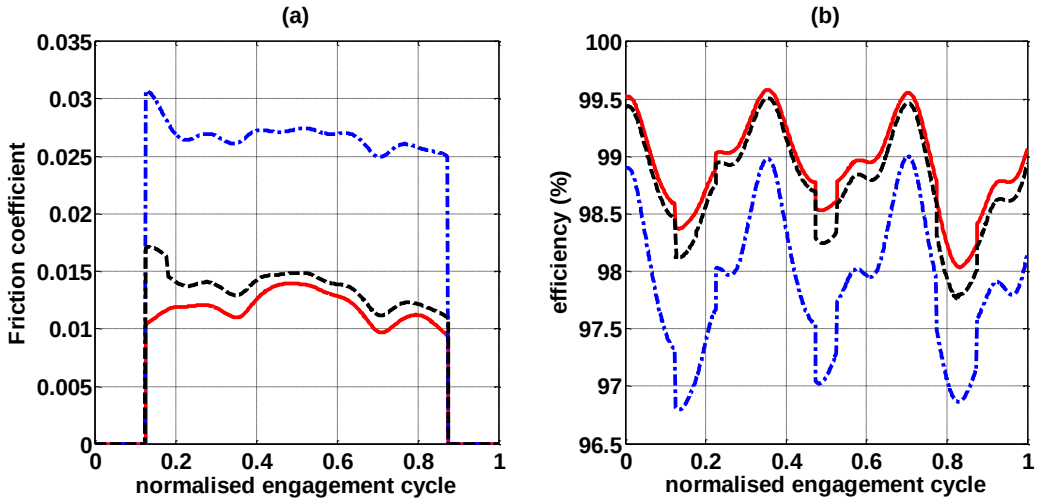

Figure 6.12- (a) Coefficient of friction and (b) overall gear pair efficiency $\theta_{in} = 40^0 C$; ——— Chittenden et al (1986) _ _ _ _ Mostofi and Gohar (1982), — . — Grubin (1949)

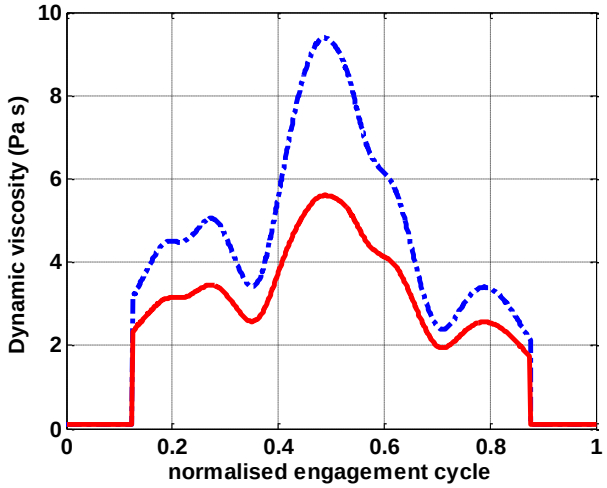

Figure 6.13- Dynamic viscosity for Chittenden solution; ——— thermal analysis, — . — isothermal conditions

Nevertheless, the mechanism producing viscous friction is also affected by the competing effective viscosity drop; the combined effect seems to cancel out since no significant difference in viscous friction can be acknowledged (Figure 6.15(b)). The shrinking of lubricant film below the combined surface roughness value will ignite asperity interactions, generating boundary friction. This fact is depicted in Figure 6.16 where boundary friction is now introduced as a significant component of the total friction force. The reflection of this outcome is seen in Figure 6.17(a) where the

friction coefficient exhibits an increase of almost 30%. Consequently, the transmission efficiency is pushed towards lower levels (Figure 6.17(b)).

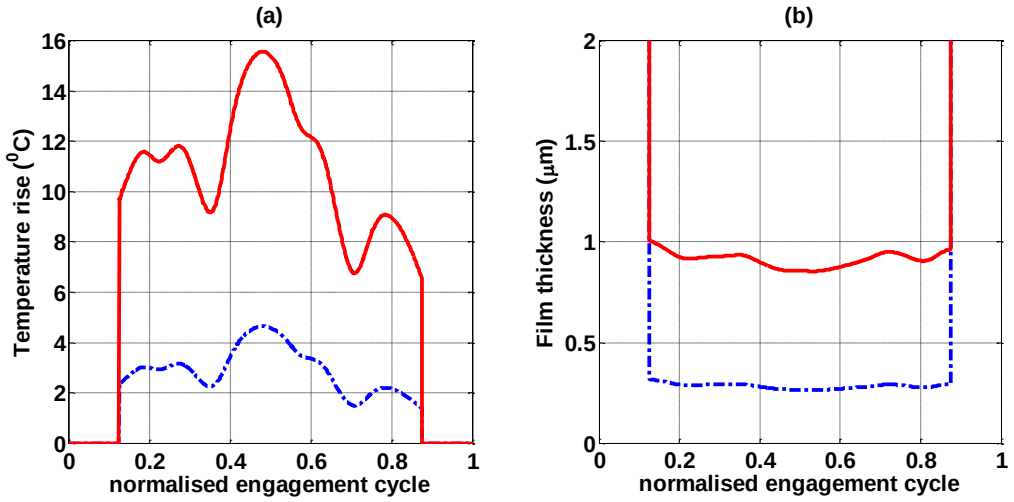

Figure 6.14- Effect of inlet lubricant temperature on (a) temperature rise (b) film thickness; ——— $\theta_{in} = 40^0 C$, — · — $\theta_{in} = 100^0 C$

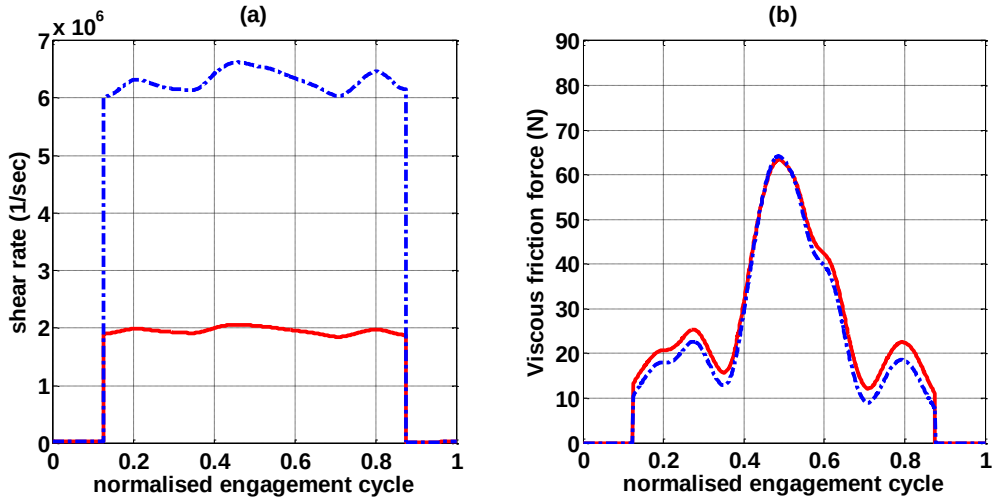

Figure 6.15- (a) Shear rate and (b) viscous friction comparison; ——— $\theta_{in} = 40^0 C$, — · — $\theta_{in} = 100^0 C$

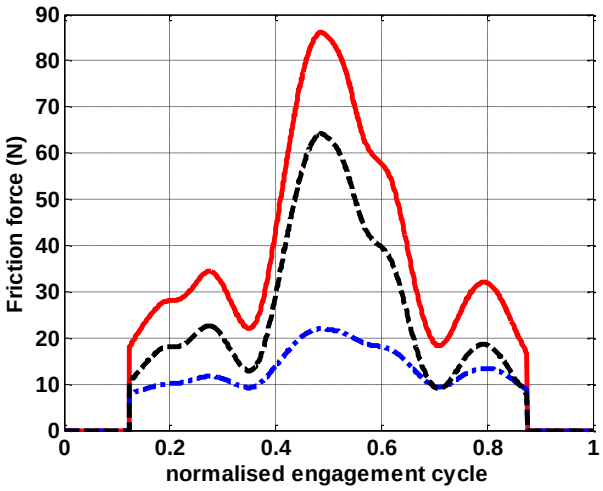

Figure 6.16- Friction distribution ($\theta_{in} = 100^0 C$); ——overall, – – – –viscous, — · — boundary

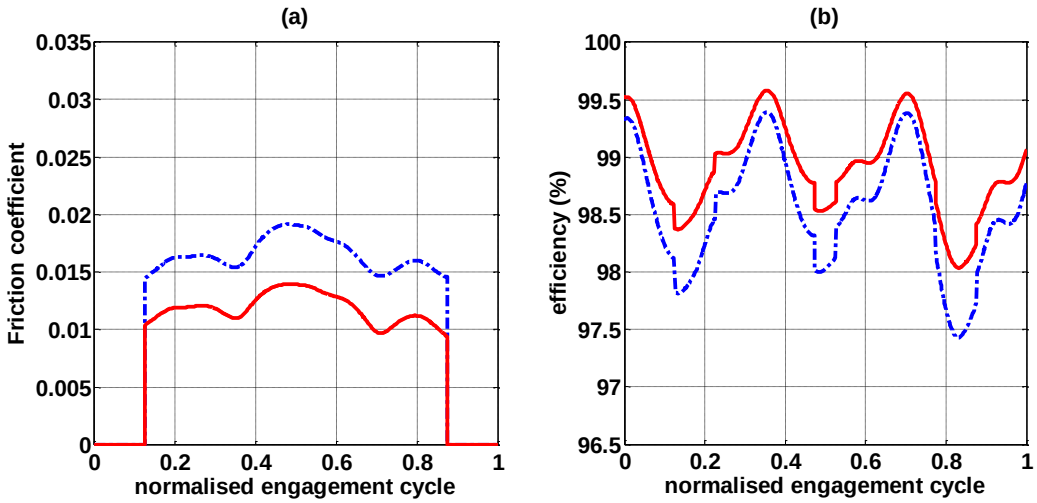

Figure 6.17- Effect of inlet lubricant temperature on (a) friction coefficient (b) transmission efficiency, $\theta_{in} = 40^0 C$, Chittenden type solution; ——$\theta_{in} = 40^0 C$, — · — $\theta_{in} = 100^0 C$

6.6 - Dynamic interaction

The influence of the dynamic consideration on the variation of tribological properties will be addressed by comparing the derived results to quasi-static conditions for cases when the fluctuations of the velocity components and the amplification of the system's response due to resonance are neglected. Figure 6.18(a) shows the variation of contact load under the two distinct cases; the difference is evident both in terms of magnitude and fluctuation pattern. The dynamic interaction induces an amplification of the overall mesh force which is transferred to each flank, indicated by

the considerable difference in the peak load value at the midpoint of the flank. The effect on the film thickness is depicted in Figure 6.18(b), illustrating only a small fluctuation around the quasi-static value. The deviation is more pronounced when considering the lubricant temperature (Figure 6.19(a)) whereas the friction coefficient seems to possess better convergence between the two cases (Figure 6.19(b)). In general, for the imposed operating conditions, the dynamic effects influence mainly the lubricant properties depending on contact pressure; the underlying tribological characteristics are affected accordingly. On the other hand, the film thickness is affected mainly by the contact kinematics; therefore, in the current case, the velocity oscillating components are not significant enough to impose any major transient behaviour.

Another important factor arising in the coupling of tribo-dynamics is the effect of teeth separation. In the previous chapter, it was observed that over a vast operation range the system dynamic behaviour is characterized by contact loss and teeth separation phenomena. Such a case will be simulated in the following set of graphs, corresponding to pinion rotation of 2246 RPM, input torque of 163.27 Nm and a cruising speed of 93.6kph while the inlet lubricant temperature is kept equal to $40^0 C$. The encountered improper mesh induces discontinuities in the dynamic response; essentially it affects the variation of the tribological properties. Figure 6.20(a) presents the distribution of contact load and film thickness. The former behaves in a manner similar to the total dynamic mesh force, in accordance to the findings of the previous chapter. Similarly, the film thickness history is shifting from typical EHL values when the gears are in mesh to the size of available clearance when contact is breached. This combined effect of zero loading capacity and extreme thick lubricant film would inflict instantaneous changes in the lubrication regime towards hydrodynamic conditions. The contact load is now applied in the form of an impulse, releasing impact energy on the flank, which is dissipated by the relative torsional motion. The thin lubricant film possesses only marginal damping capacity. Furthermore, the pressure gradients around the discontinuity points are amplified, resulting to sound wave propagation (Figure 6.21).

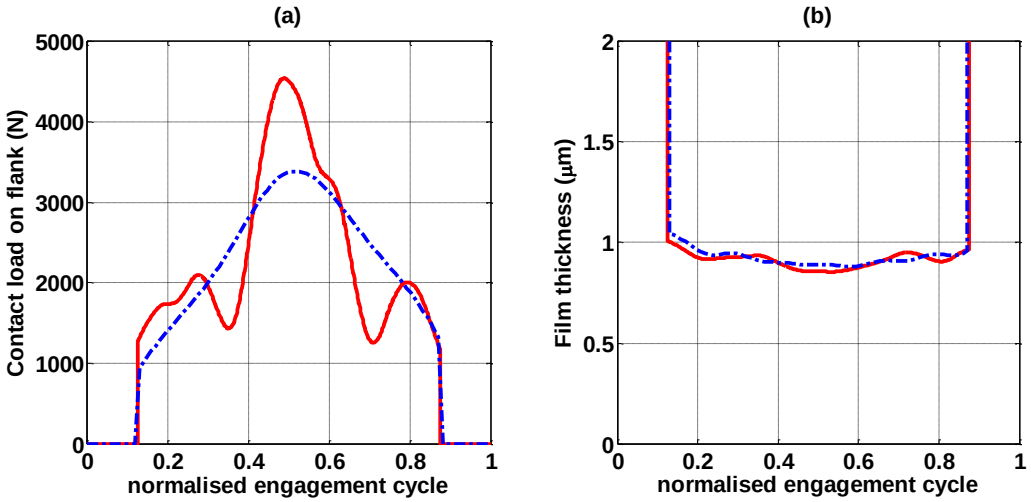

Figure 6.18- (a) Contact Load and (b) film thickness; _____dynamic analysis, _ . _quasi-static analysis

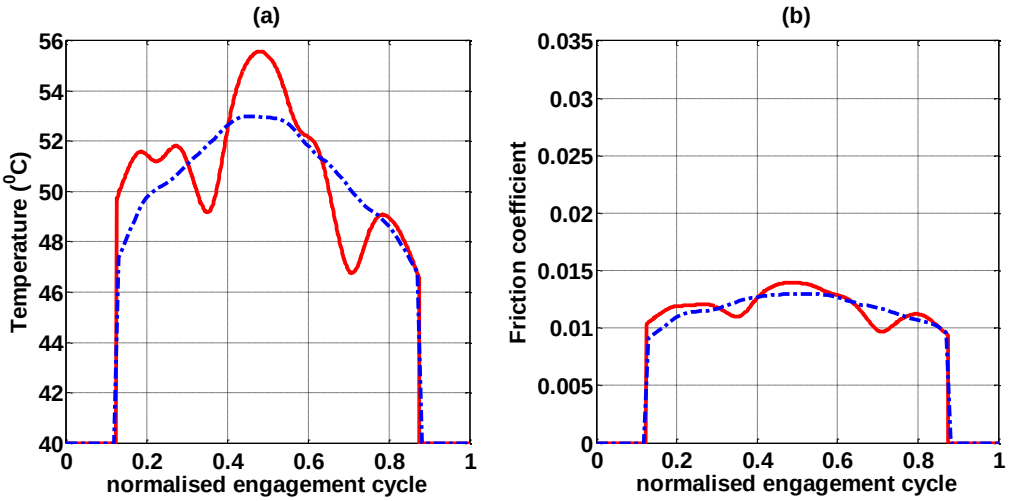

Figure 6.19- (a) Temperature and (b) friction coefficient; _____dynamic analysis, _ . _quasi-static analysis

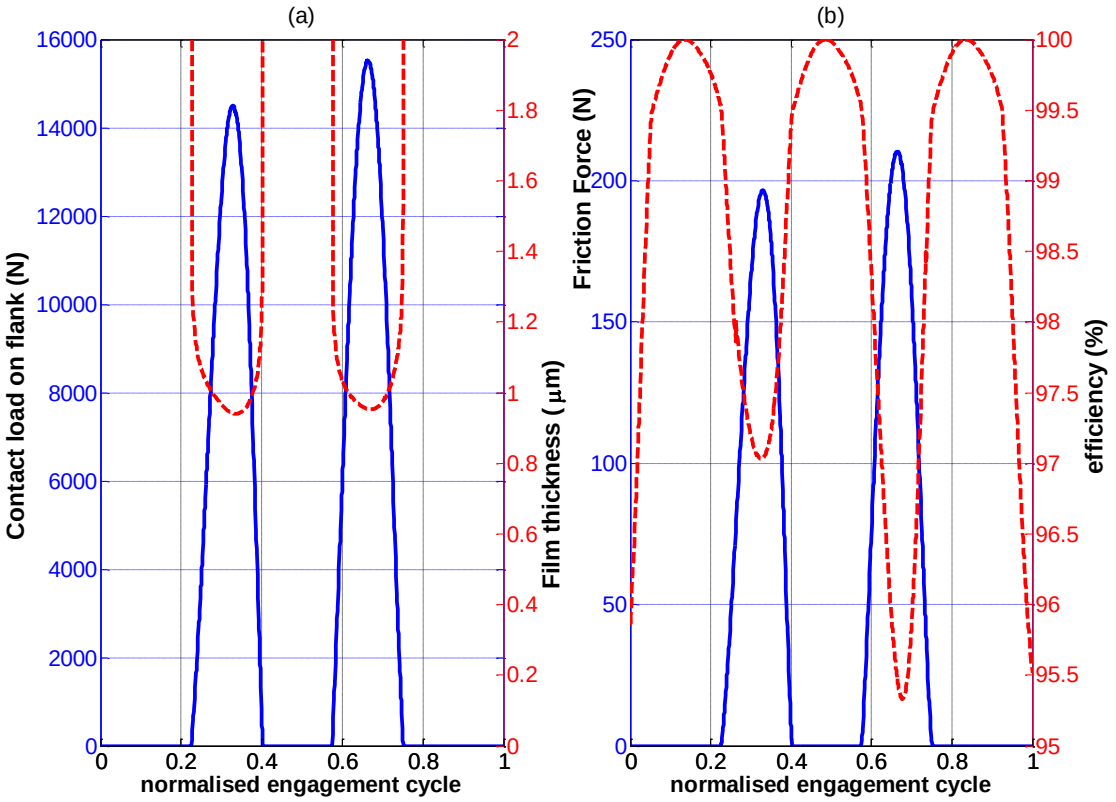

Figure 6.20- Separation effects, Chittenden solution, $\theta_{in} = 40^0 C$; (a) _____ flank contact load, - - - - film thickness, (b) _____ friction force, - - - - transmission efficiency

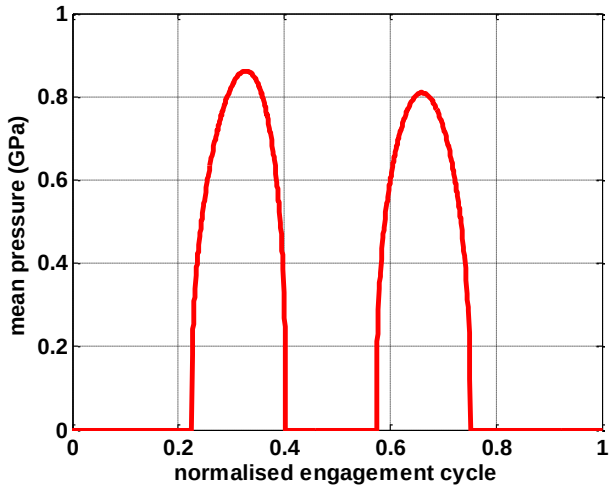

Figure 6.21- Mean contact pressure along the engagement cycle, Chittenden solution

The friction force undergoes a similar variation to the contact load; its magnitude is affected by the increased shear (higher relative angular velocities) and the increased

contact area due to the extreme loading. It acts as an impulse excitation normal to the line of action, as shown in Figure 6.20(b); hence its effect on the lateral dynamics should be investigated. Despite the load and friction impulses, the possibility of thermal shocks is also possible. The temperature distribution (not depicted) follows a similar pattern, reaching peak values over $80^{0}C$. Thus, such excessive temperature gradients can ignite undesirable heat flows towards the bounding surfaces. The mechanical efficiency is also affected, turning to lower levels due to the increased friction, although the latter is not applied for the majority of the engagement cycle. This is identical of the high energy absorption during the frictional impulses.

The previous results, showing a strong dependence of the tribological picture based on the individual operating conditions, render the need for a scan of the whole operational speed range. The results are presented in the familiar spectral form, usually by plotting extreme or mean values of the tribological properties during an engagement cycle. The variation of the flank contact load depicted in Figure 6.22(a) follows the pattern of the dynamic transmission error derived in a previous chapter. The minimum value of central film thickness is mainly influenced by the entraining motion shown in

Figure 6.23(a). However, due to the extreme discontinuity of the contact load at the vicinity of the bifurcation points, the lubricant film undergoes a small jump in those regions. Therefore, the oil film magnitude is insensitive to flank load within an engagement cycle, yet reflects the separation effect. A similar behaviour is observed for the maximum temperature rise (

Figure 6.23(b)) where the two branches now resemble to the ones of the contact loadFigure 6.24(a) shows the representation of the mean friction coefficient. In this case higher values are encountered during constant mesh rather than under separation, since in the last case the friction mechanism is idle for a vast portion of the engagement cycle. Nevertheless, the overall frictional effect induced by all the mating flanks yields a decrease on the efficiency during separation shown in Figure 6.24(b).

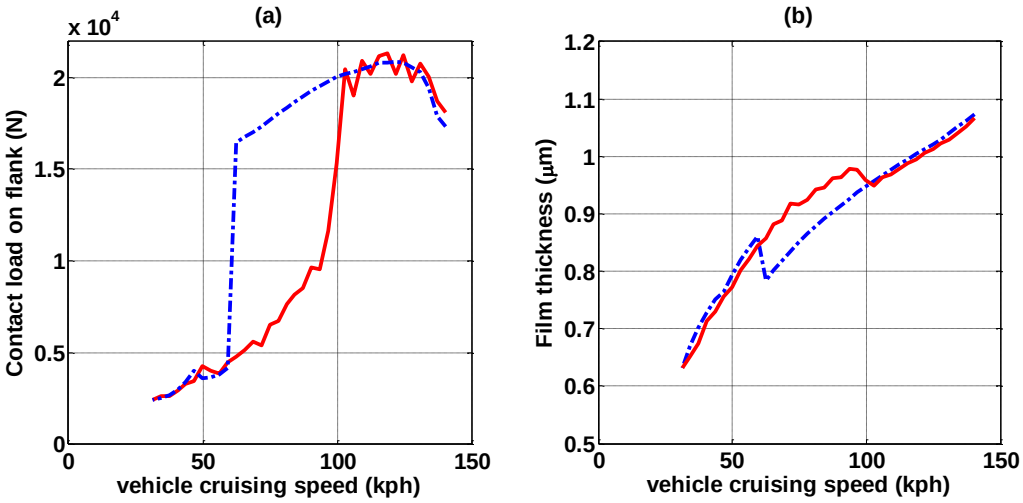

Figure 6.22- Effect of cruising speed for Chittenden solution, $\theta_{in} = 40^0 C$: (a) maximum flank load and (b) minimum value of central lubricant film; _____acceleration, _ . _ . _deceleration

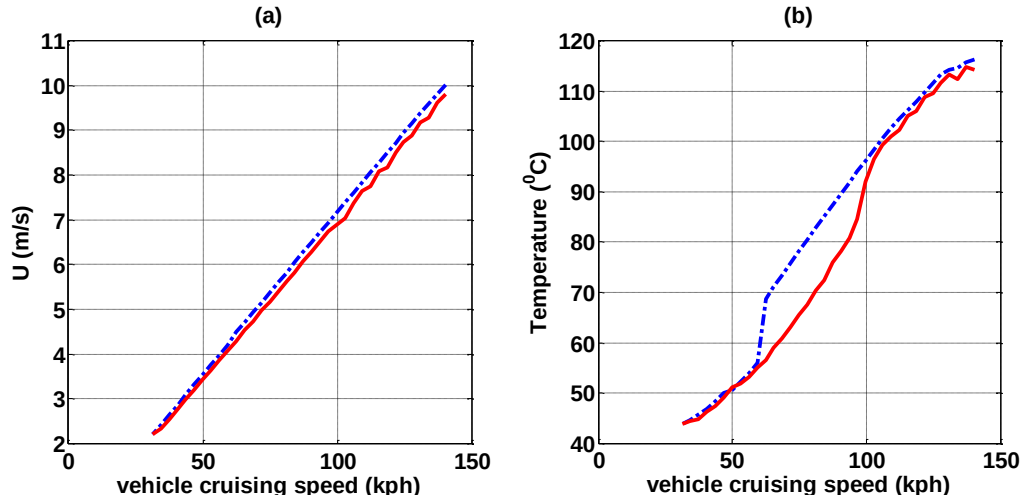

Figure 6.23- Effect of cruising speed for Chittenden solution, $\theta_{in} = 40^0 C$: (a) maximum entraining velocity and (b) maximum temperature rise; _____acceleration, _ . _ . _deceleration

Since a significant dependence of the tribological properties on the dynamic aspect of the problem has been established, it is interesting to determine to what extent the opposite relationship withholds. Therefore, correlation of response spectra and time series of the dry versus the lubricated model will be attempted. Figure 6.25 shows the comparison for acceleration and deceleration conditions. As anticipated, friction is influencing only marginally the dynamic response. This is due to its plane of action which is always perpendicular to the line of action of the mesh force. As a result, the

torsional motion is only affected by the generated frictional torque found to be insignificant compared to the input loading (Figure 6.10(a)). A graph of the time series of the nominal case seen in Figure 6.26 confirms the trivial effect of sliding friction on the relative torsional motion. A dimensionless version of the dynamic transmission error is used as abscissa, indicating that the two responses are nearly identical besides an occurring phase difference.

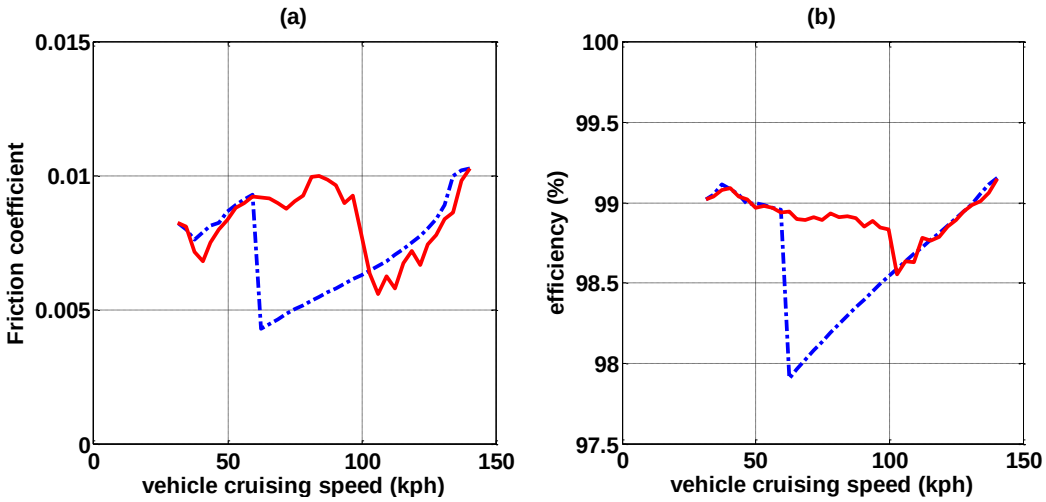

Figure 6.24- Effect of cruising speed for Chittenden solution, $\theta_{in} = 40^0 C$: (a) mean friction coefficient and (b) mean efficiency; _____acceleration, _ . _ . _deceleration

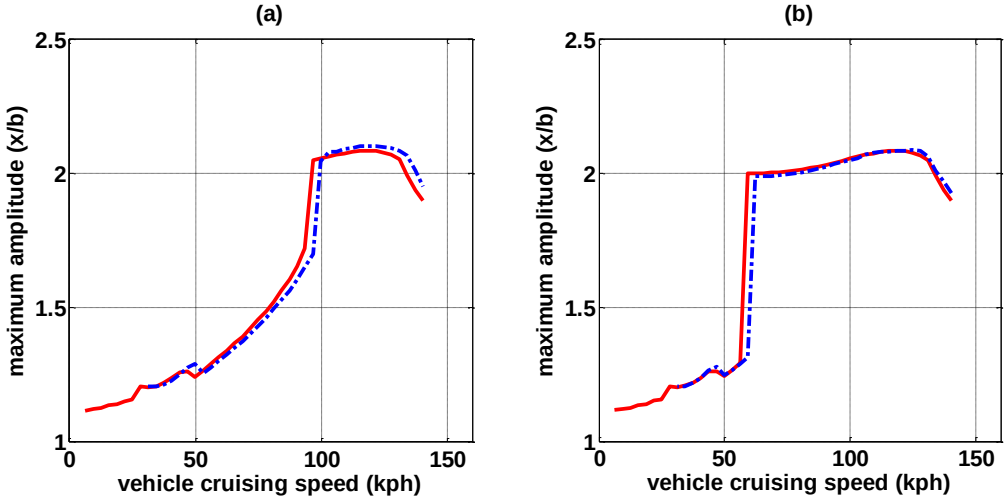

Figure 6.25- Response spectra comparison between dry and lubricated case: (a) acceleration and (b) deceleration; _____lubricated, _ . _ . _ dry model

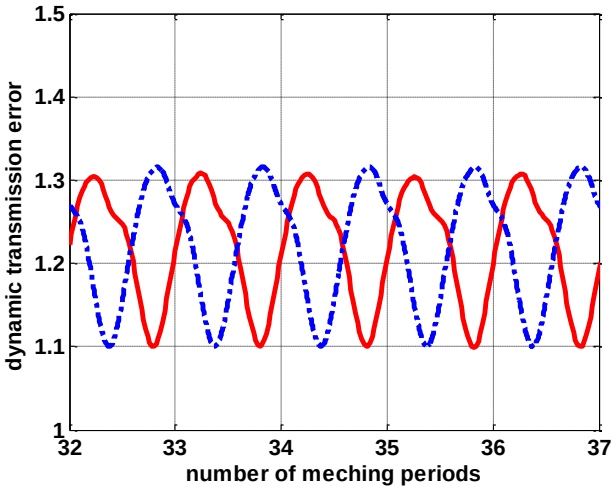

Figure 6.26- Time histories comparison between dry and lubricated case for nominal case: (a) acceleration (b) deceleration; _____lubricated, _ . _ . _ dry model

6.7 - Model Validation

As a means of validation, the friction coefficient over the operational range is correlated to two expressions available in the literature: (i) Evans and Johnson (1986) and (ii) Kolinvand and Kahraman (2010). Both expressions compute the frictional properties under Eyring regime of traction. The results are presented in Figure 6.27.

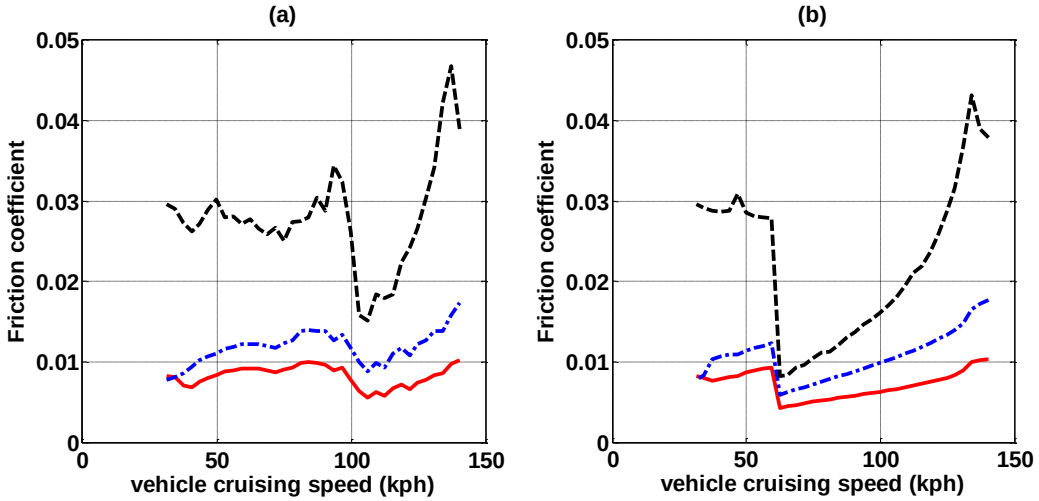

Figure 6.27- Mean friction coefficient; (a) acceleration (b) deceleration; _____current model (Chittenden solution), _ . _ . _ Kolinvand and Kahraman (2010), _ _ _ _ Evans&Johnson (1986)

The overall pattern looks similar. Under acceleration (Figure 6.27(a)) the friction coefficient for the current model and case (i) exhibit a smooth fluctuation until the beginning of the impact region, where a local maximum is reached. Case (ii) follows a more abrupt fluctuation; however all solutions undergo a sharp change when the dynamics switch to the upper branch. After this point, the friction coefficient increases continuously until the end of the operational range. The difference in magnitude is considerable between case (iii) and the other solutions. This fact can be attributed to the different application (roller), lubricant characteristics and the domain of validity of the underlying equation. However, the other two cases, corresponding to the same application and lubricant (hypoid transmission) differ only by almost a fixed offset. An explanation could be found in the method used by Kolinvand and Kahraman (2010) which neglects the side leakage, underestimating the entraining velocity magnitude. This results into thinner films, higher shear rates and friction forces. Figure 6.28 - showing the distribution along an engagement cycle - confirms the above observation in the spatial domain.

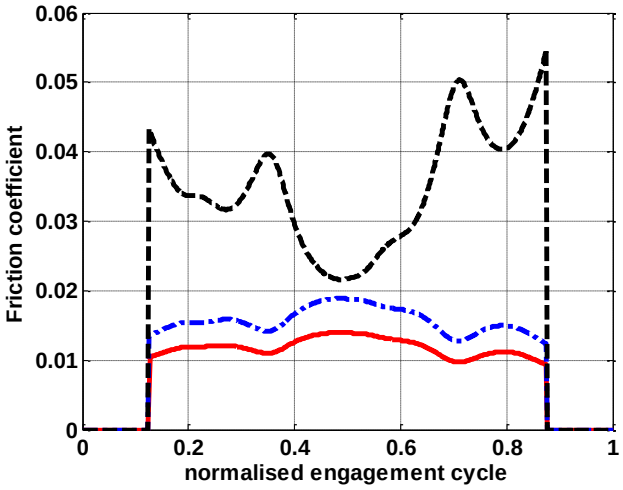

Figure 6.28- Friction coefficient over an engagement cycle; _____ current model (Chittenden solution), _ . _ . _ Kolinvand and Kahraman (2010), _ _ _ _ Evans and Johnson (1986)

6.8 - Synopsis

In this chapter, a tribological analysis was conducted on the system's dynamics. Initially, an isothermal analysis yielded the regime of lubrication and traction, confirming the initial assumption of Eyring, EHL conditions. The main tribological

properties and friction force were derived, showing the difference between one and two dimensional flows. A thermal analysis yielded the temperature rise during the engagement procedure, which affects the oil film size and transmission efficiency. The increase of inlet lubricant temperature was shown to be extremely important, resulting into further shrinking of the lubricant film, accompanied by significant asperity interaction.

The dynamic interaction showed strong dependence of the tribological characteristics on the operating conditions, resulting in the appearance of considerable discontinuities. Eventually, the torsional motion was regarded as insensitive to friction whereas the model was validated against previously published studies.

Chapter 7 - The Concept of Targeted Energy Transfer

7.1 - Introduction

The previous chapter investigated the dynamic response of the hypoid gear pair. During steady state cruising, the system behaviour was characterized by resonant conditions; at the same time, teeth contact loss inflicted single sided impacts between the mating flanks. Under coasting conditions, namely a sudden decline of the input torque due to throttle release, the system exhibited transient response associated with aggravated impact phenomena on both sides of the gear surface.

In this chapter, a passive control of the aforementioned phenomena will be attempted based on the concept of Targeted Energy Transfer (TET). The treatment will be focused on the design of a nonlinear dynamic absorber capable of absorbing energy from the main system in an irreversible manner. Parametric studies will be conducted to select the optimum design properties and the mechanism behind energy absorption will be analysed. Since friction was proven to have insignificant influence on the torsional dynamics, dry conditions will be assumed for the simplification of the numerical formulation. The implementation of such a mechanism is related with a broadband efficiency at and around resonance conditions, complying with the problem requirements witnessed in the analysis of Chapter 5.

7.2 - Dynamic Model

The modelling approach will be based on the fundamental mechanical model presented in Figures 3.1 - 3.2. The necessary addition will be a form of a Nonlinear Energy Sink (NES), as characterized by Gendelman et al (2001). The proposed configuration is shown in Figure 7.1; the NES is attached to the axle shaft by a coupling element comprising a torsional spring (k_t) and an additional damping element (c_t), where the unwanted energy will be dissipated. The essential nonlinear behaviour is introduced through the cubic nonlinearity of the torsional stiffness. The coupling between the main system (gear pair) and the NES is supposed to be weak based on previous numerical and experimental studies (Jiang et al, 2003).

The free body diagram of the NES is presented in Figure 7.2. The NES rotating motion is opposed by elastic and damping forces, induced by the coupling effect; at the same time the corresponding reaction forces are transmitted to the gear through the axle shaft and result into a pair of internal excitation torques.

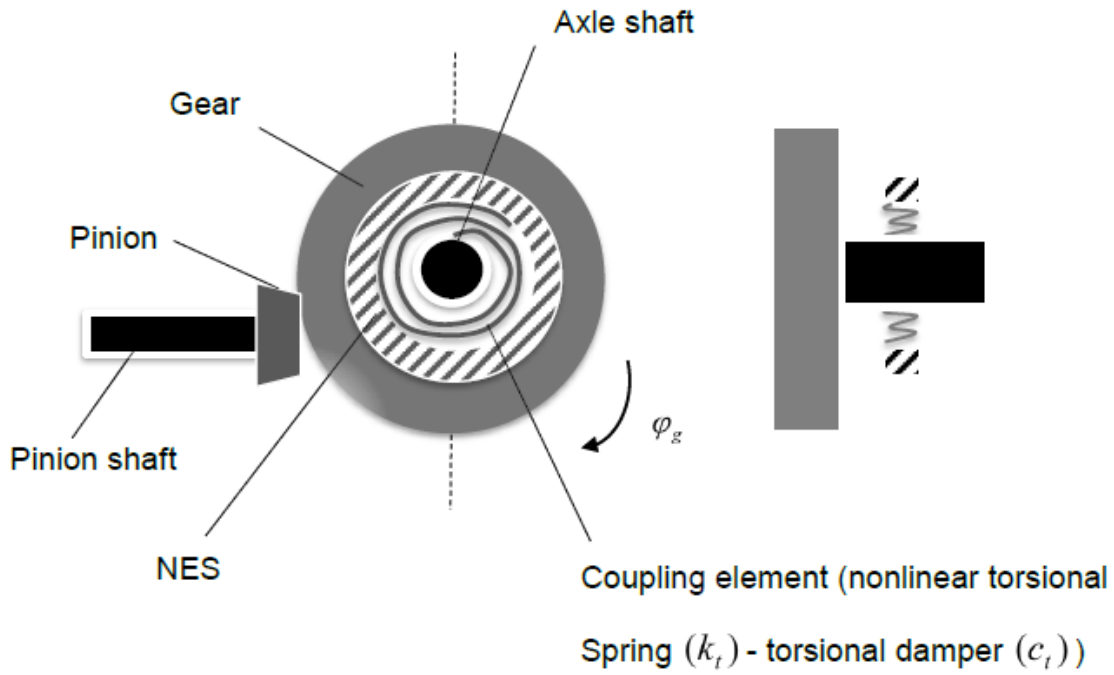

Figure 7.1- The Nonlinear Energy Sink (NES) configuration

The equations of motion are a variation of equations (3.1) – (3.9); equation (3.2) needs to be modified to reflect the effect of the nonlinear coupling and an additional expression describing the NES dynamics will be included.

Hence:

$$I_p\ddot{\varphi}_p + R_p(\varphi_p)c_m(\dot{x}) + R_p(\varphi_p)k_m(\varphi_p)f_g(x) = T_p \quad \textbf{(7.1)}$$

$$I_g\ddot{\varphi}_g - R_g(\varphi_p)c_m(\dot{x}) - R_g(\varphi_p)k_m(\varphi_p)f_g(x) = -T_g + \varepsilon\cdot(k_t\cdot u^3 + c_t\cdot\dot{u}) \quad \textbf{(7.2)}$$

$$I_u\ddot{u} + \varepsilon\cdot(k_t\cdot u^3 + c_t\cdot\dot{u}) = -I_u\ddot{\varphi}_g \quad \textbf{(7.3)}$$

In the above expressions the change of variables $u = \varphi_s - \varphi_g$ has been applied so that the relative rotational motion can be conveyed. The inertia of the NES attachment is taken as a fraction of the inertia of the differential axle. Thus:

$$I_u = \varepsilon\cdot I_g \quad \textbf{(7.4)}$$

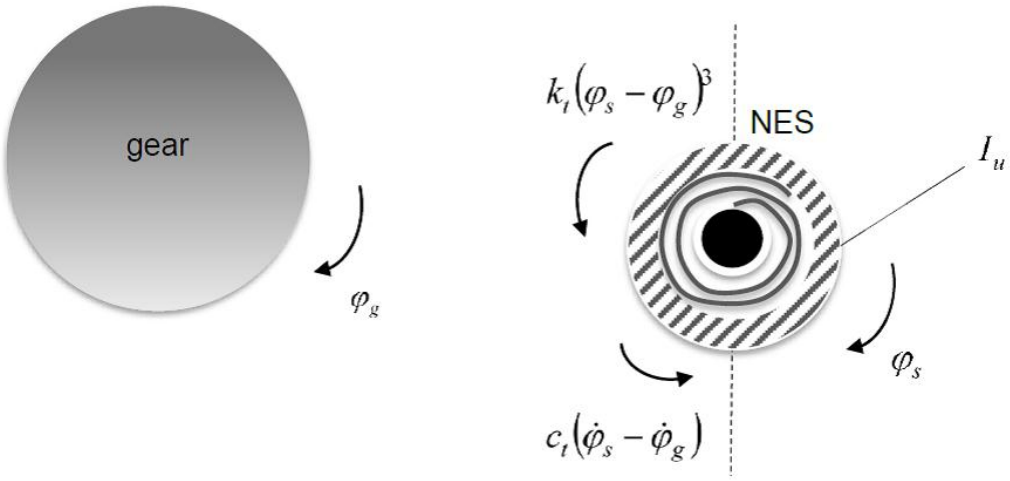

Figure 7.2: Free Body Diagram of the NES

The problem is essentially an optimization issue; an optimum NES structure must be identified by quantifying its parameters. For this reason it is essential to review the resonance and impact phenomena observed in the dynamic response of the primary system.

7.3 -Steady state resonance

7.3.1 Problem definition

The first case of unwanted motions is observed under steady state cruising conditions. In this case, an amplification of the system response is noticed due to parametric resonance; this is a consequence of the variation of system parameters with respect to the angular position (eq. (3.1) - (3.2)) and hence implicitly with time.

The response curve is illustrated in Figure 7.3. There is a region of single sided impacts between the mating flanks, associated with aggravated dynamic response. Areas of multiple solutions also appear due to the backlash nonlinearity (equation (3.6)). The analysis of a typical case is illustrated in Figure 7.4 corresponding to a cruising speed of $99kph$ and input torque of $182Nm$; the arrow in the top of Figure 7.3 indicates the corresponding point in the response spectrum.

It can be seen that the dynamic transmission error yields single sided collisions; periodic loss of contact occurs when the dimensionless quantity drops below unity. To overcome this issue, an NES attachment is introduced, following the configuration of the previous section. These types of devices have been studied previously in problems primarily involving lateral degrees of freedom and their efficiency has been well established. For impulsively excited systems, the main concept involves an irreversible energy transaction between the main structure and the NES. The occurrence or not of this energy exchange mechanism depends on the energy threshold induced by the external excitation (Vakakis, 2001). The targeted energy transfer in harmonically excited systems has been studied both for grounded (Jiang et al, 2003) and ungrounded nonlinear attachments (Gendelman et al, 2008). These applications were considering primary systems with linear characteristics. The TET in spur gear mechanisms was investigated by Scagliarini et al (2009) while considering only the parametric excitation; it was found that quasi-periodic response regimes could render significant vibration alleviation for high inertia levels of the attachment. In the current case the gear pair system is essentially a nonlinear system, excited both parametrically and externally due to the inherent harmonic terms. Furthermore, due to the variation of mesh position, the region of excessive vibrations is extended beyond the narrowband area of the fundamental resonance;

yielding the ability of NES to act as a broadband passive energy absorber extremely convenient for the purpose of alleviating the unwanted steady state peak amplitudes.

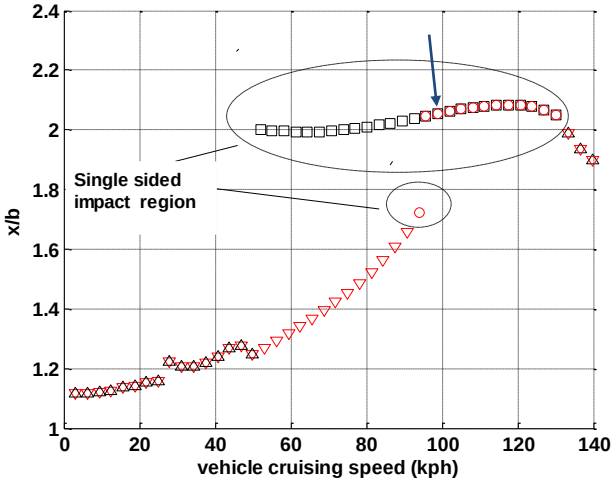

Figure 7.3: Cruising speed – Maximum Response spectra; ■single sided impacts (decelerating), ● single sided impacts (accelerating), ▲no impacts (decelerating), ▼ no impacts (accelerating)

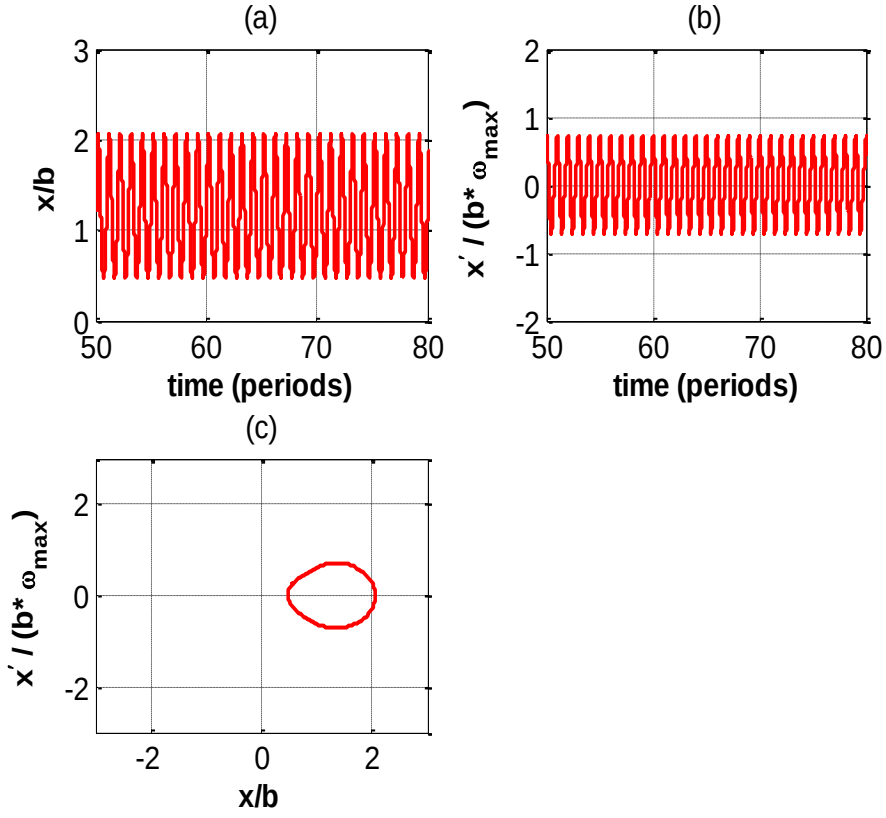

Figure 7.4- Dynamic Response for $\upsilon = 99kph$ and $T_p = 182Nm$ without NES: (a) dynamic transmission error; (b) relative velocity; (c) phase plot

7.3.2 Parametric studies

There are two main parameters affecting the performance of the NES; the inertial ratio (ε) and the nonlinear stiffness (k_t). If the main system was linear with time-invariant coefficients, the methodology presented by Starovetsy and Gendelman (2007) could be applied to locate the regions of optimised efficiency. However, the essential different characteristics of the current equations of motion indicate the employment of a formulation similar to that in Lee et al (2007). Although the latter involves transient phenomena of aeroelastic instabilities, it provides a systematic approach for treating the problem of successfully tuning the NES. Therefore, a series of numerical simulations is conducted while ensuring that sufficient time has elapsed for steady state response to evolve. Since broadband vibration attenuation is required, the whole area of multiple solutions needs to be scanned. Due to the nonlinear character of the primary system, accelerating and decelerating conditions will be accounted for by conducting speed sweeps. Therefore, the initial conditions are set based on the discussion of Chapter 5, yet currently including the NES as well.

Figure 7.5 shows the obtained parametric study results for the accelerating case. The criteria (a) and (b) are normalised (%) with respect to the original system without the presence of an NES, representing respectively the maximum reached amplitude and the number of single sided impacts between the mating flanks due to separation effects. The remaining quantities are related to the energy level of the system, expressing the work done by the mesh force and the energy damped at the NES over 100 meshing cycles. It can be seen that for accelerating conditions the NES has either no positive influence or either negative influence on the dynamics of the main system. Nevertheless, this should be not a discouraging fact in the first place; by observing the response spectra of Figure 7.3, it is obvious that aggravated dynamic response becomes an issue for nearly as much as 1/3 of the acceleration region.

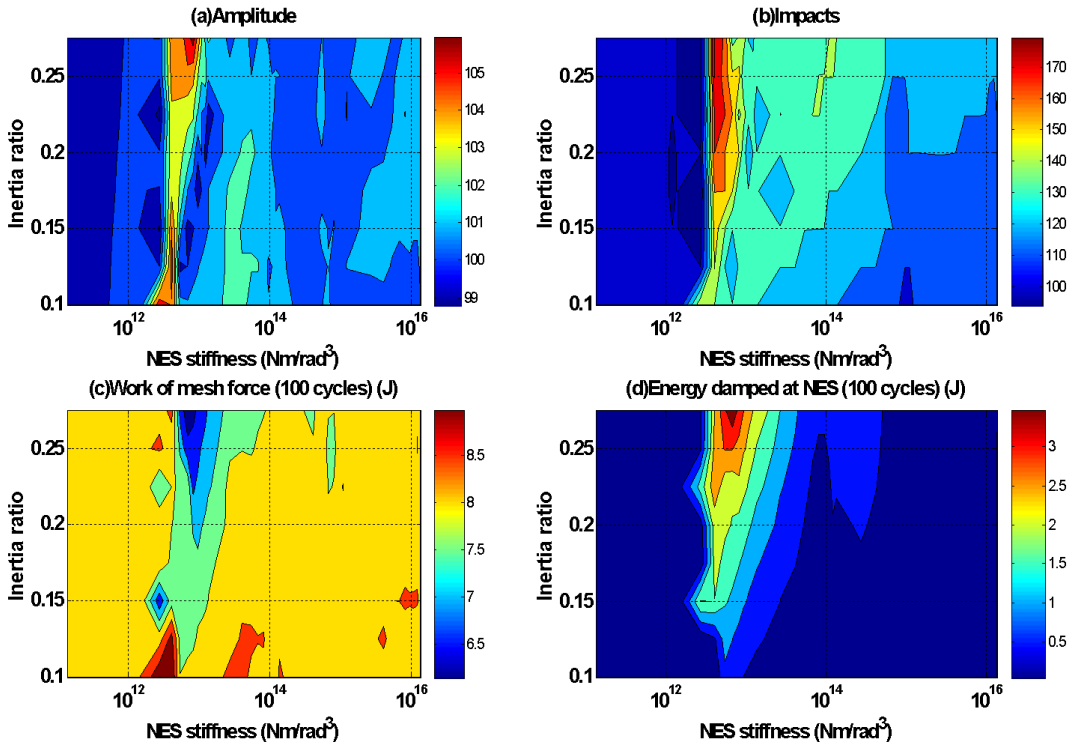

Figure 7.5- Steady state response properties for accelerating conditions (59-120kph); (a) maximum amplitude, (b) total number of single sided impacts, (c) work of mesh force, (d) energy damped at NES

Figure 7.6 illustrates the behaviour of the system under decelerating conditions. In this case, criteria (a), (b) and (c) seem to converge in terms of their minima in a certain region of the parametric map. In particular, these borders are defined by the following expressions:

$$0.1 \le \varepsilon \le 0.23,\ 5.932 \cdot 10^{12}\, Nm/rad^3 \le k_t \le 1.4808 \cdot 10^{13}\, Nm/rad^3 \qquad \textbf{(7.5)}$$

There seems to be a reduction in the peak amplitude, the number of single sided impacts and the work of mesh force in this area. It is therefore implied that the NES has a positive yet not extremely pronounced influence on alleviating the unwanted resonant motions in broadband decelerating conditions.

The contour plots presented in the previous figure summarize the NES performance in a wide set of cruising velocities. To identify the detailed picture, response spectra are constructed based on an optimum value derived by a minimum single sided impact number requirement compared to the case where no NES is attached.

Identification of this optimum couple of NES parameters is accomplished by employing an optimisation procedure based on genetic algorithms (Rahmani, 2008). After setting the parameter boundaries identical to those of $0.1 \le \varepsilon \le 0.23$, $5.932 \cdot 10^{12}\, Nm/rad^3 \le k_t \le 1.4808 \cdot 10^{13}\, Nm/rad^3$ (7.5), extensive numerical simulations are conducted within the area of interest. The sequence of selecting the next set of NES parameters in order to achieve convergence in terms of the minimum value is governed by the genetic algorithm.

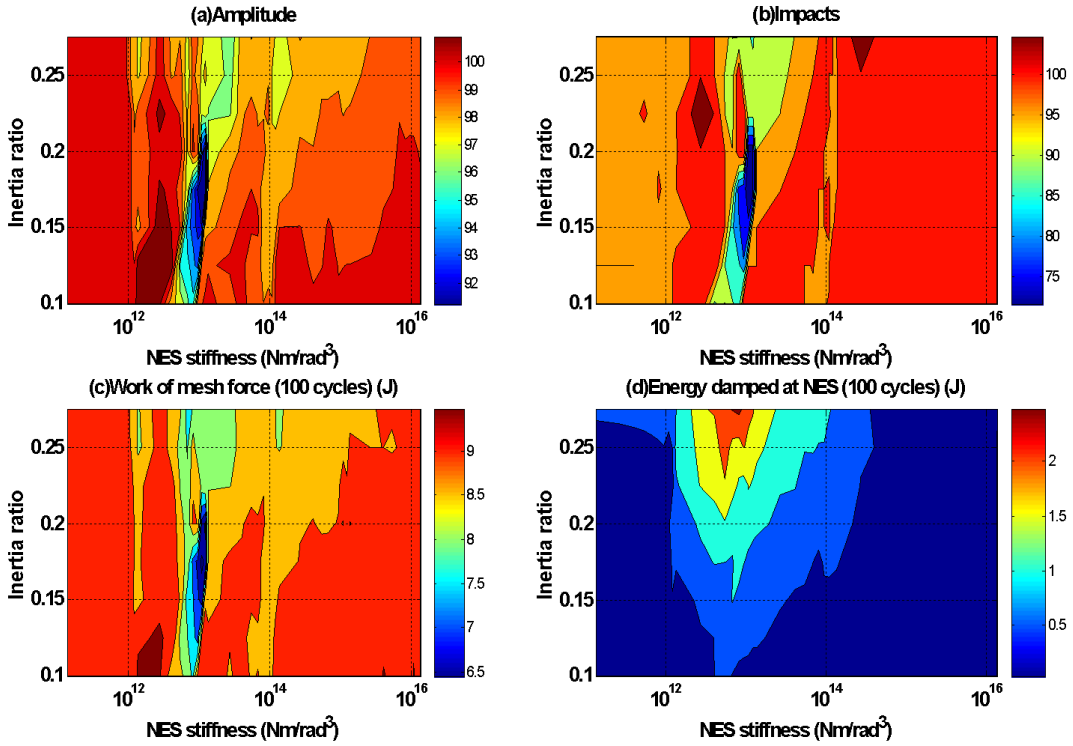

Figure 7.6- Steady state response properties for decelerating conditions (140-60kph); (a) maximum amplitude, (b) total number of single sided impacts, (c) work of mesh force, (d) energy damped at NES

7.3.3 Overview of the energy transfer mechanism

Figure 7.7 depicts the spectral behaviour of the main system when the aforementioned optimum set of NES parameters is considered ($\varepsilon = 0.181$; $k_t = 1.0411 \cdot 10^{13}\, Nm/rad^3$). The main benefit in terms of the total number of perceived impacts (Figure 7.7(a)) is restricted near the bifurcation region, where the system seems to jump on the low amplitude branch (Figure 7.7(b)) on an earlier stage when the NES is attached. Similar behaviour was observed during the

parametric studies performed in section 5.3.7 by changing the inherent parameters of system. Attaching the NES shows similar potential in terms of vibration control. Additionally, the peak to peak amplitude is reduced in the vicinity of 100kph cruising speed. The overall NES influence is concentrated in these two aforementioned regions.

The time series of the dynamic response are illustrated in Figure 7.8. The first section (a) shows the difference in the magnitude of transmission error with and without the NES attachment. Both motions are of the same frequency content and nearly in phase; however there is a notable difference in their magnitude both in terms of maximum and peak to peak values. It seems that the NES forces the system to settle in its lower branch. Similar steady state response behaviours have been presented in the work of Gendelman et al (2008), representing one of the main attractors of a linear system connected to a NES under periodic forcing. Nevertheless, the underlying mechanism needs to be addressed properly before reaching definite conclusions. The above findings should be treated as indications.

Usually, steady state motions dominate away from the primary resonance (87kph) which is in accordance with the current operating condition at the onset of backward jumps. Hence, a qualitative similarity should be noted It is true that the effect of the current configuration is limited, constrained only to almost ¼ of the overall area of interest. Nonetheless, it poses a starting point of potential further investigation.

The incurring energy exchanges derived numerically are important for understanding the TET concept. The instantaneous total energy of the system is the sum of the instantaneous kinetic and potential energies of the main system and the NES, including the non-conservative work of the mesh force:

$$E_{total}(\tau)=\left[\frac{1}{2}I_p\dot{\varphi}_p{}^2+\frac{1}{2}I_g\dot{\varphi}_g{}^2+\frac{1}{2}\varepsilon\cdot I_g\left(\dot{u}^2+\dot{\varphi}_g^2\right)\right]_{Kinetic}+\left[\frac{1}{4}\varepsilon\cdot k_t u^4\right]_{PotentialNES} \quad \textbf{(7.6)}$$

The energy dissipated by the mesh damping of the main system and the one of the NES is yielded by:

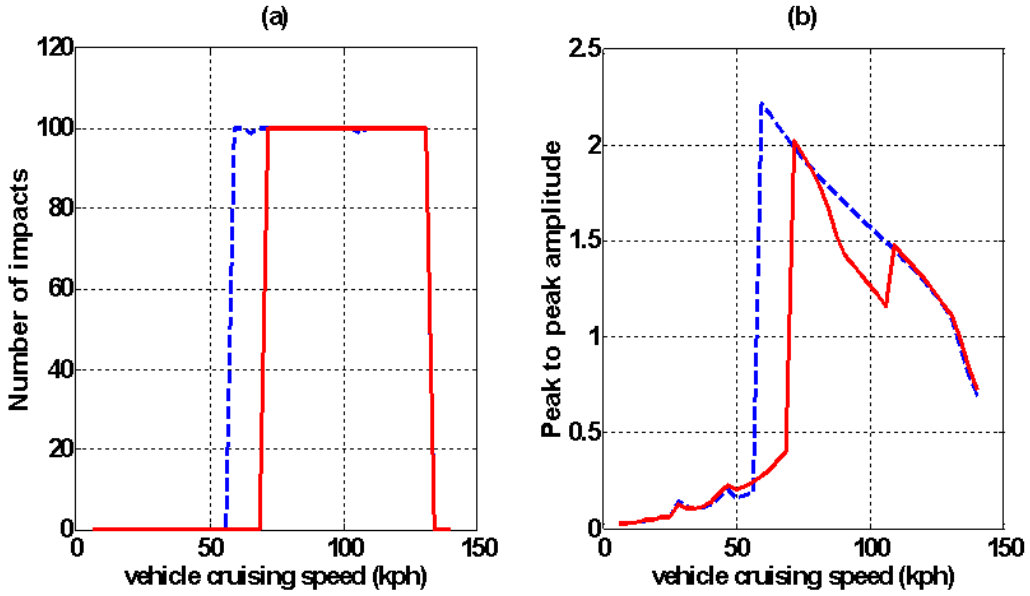

Figure 7.7- Response characteristics of the primary system ($\varepsilon = 0.181$; $k_t = 1.0411 \cdot 10^{13} Nm/rad^3$): (a) number of impacts (b) dimensionless peak to peak amplitude; - - - - without NES, ——— with NES

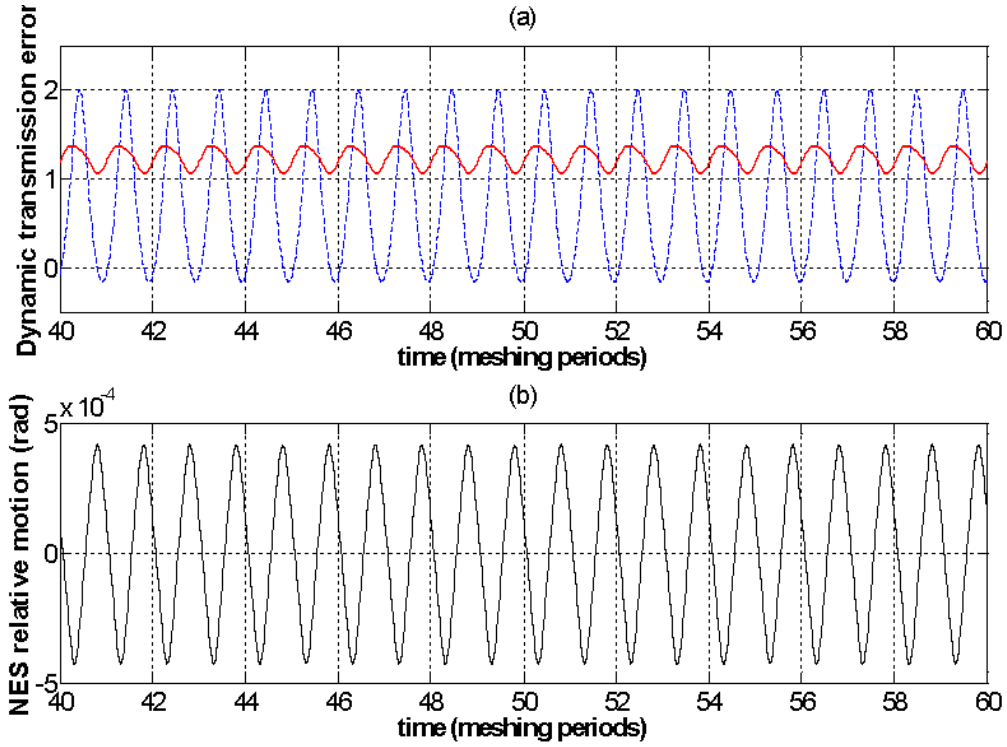

Figure 7.8- Time series of the dynamic response at 62.4kph under vibration attenuation conditions ($\varepsilon = 0.181; k_t = 1.0411 \cdot 10^{13} Nm/rad^3$): (a) Dynamic transmission error (primary system), (b) NES relative motion; - - - - without NES, ——— with NES

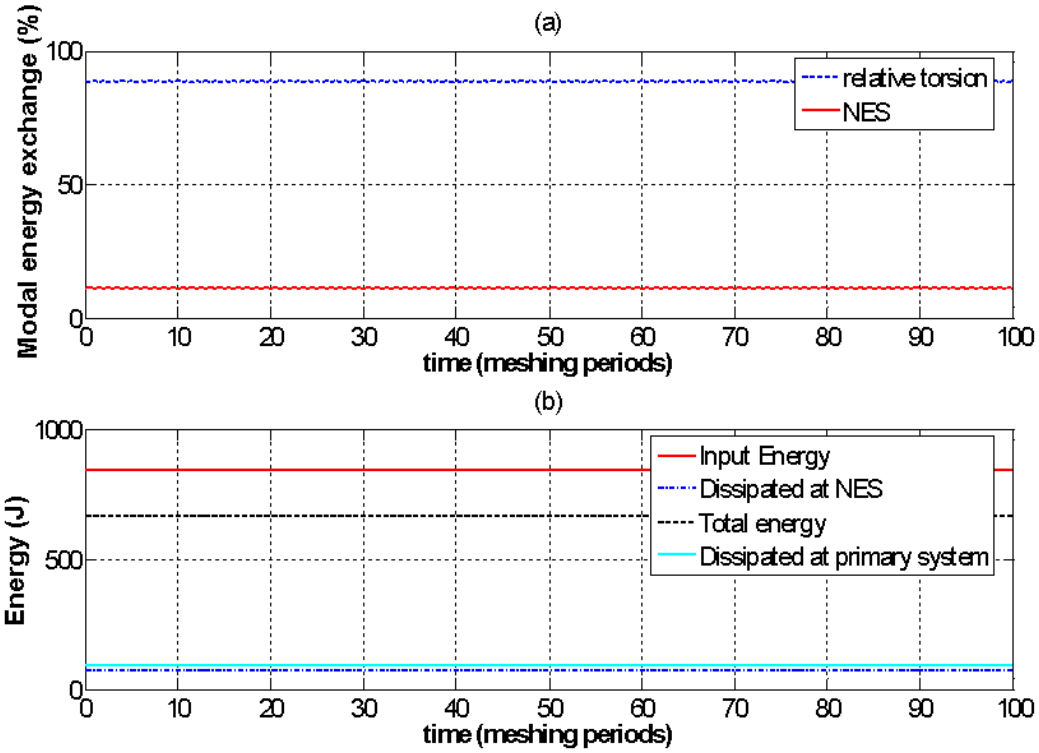

Figure 7.9- (a) Instantaneous energy exchanges between modes, (b) input energy distribution for effective vibration attenuation at 62.4kph

$$E_d(\tau) = c_m \int_0^{\tau} \dot{x}^2 dt \qquad \textbf{(7.7)}$$

$$E_{d,NES}(\tau) = \varepsilon \cdot c_t \int_0^{\tau} \dot{u}^2 dt \qquad \textbf{(7.8)}$$

The input energy is the sum of the initial energy input (initial conditions), the external forces and the non-conservative work of the mesh force:

$$E_{input}(\tau) = E_{total}(0) + \int_0^{\tau} \left(T_p \dot{\varphi}_p - T_g \dot{\varphi}_g\right) dt + \left[\int_0^{\tau} k_m(\varphi_p) f_g(x) \dot{x} dt\right]_{Non\ Conservative\ Work} \qquad \textbf{(7.9)}$$

Eventually, the instantaneous energy balance will be:

$$E_{total}(\tau) = E_{input}(\tau) - E_d(\tau) - E_{d,NES}(\tau) \qquad \textbf{(7.10)}$$

The energy exchange between the main system and the NES is seen in Figure 7.9(a). The majority of the total energy is restrained at the gear pair; this picture is analogous to the third suppression mechanism in transient aeroelastic instabilities (Lee et al, 2007) where the energy balancing is taking place in a long term basis. Nevertheless, the energy distribution of Figure 7.9(b) showing a small difference in the amount of dissipated energy between the two dampers is not highly indicative of controlled irreversible energy transfer. In order to confirm such behaviour, a case where the NES fails to comply with the criterion of impact minimisation is considered ($\varepsilon = 0.214; k_t = 1.2388 \cdot 10^{13} Nm/rad^3$). The number of impacts' spectrum in Figure 7.10(a) shows that indeed the NES attachment has no favourable influence on the flank separation range. The bifurcation point moves slightly towards the left side, hence extending the single sided impact region. The amplitude plot in Figure 7.10(b) confirms the previous findings, since no significant gain can be observed near the jump vicinity. The time series at 62.4kph (Figure 7.11) illustrate that the dynamic transmission error is now insensitive to the NES presence. The modal energy exchange of Figure 7.12(a) is similar to the previous case; however the energy distribution shows that the vast amount of input energy is dissipated at the mesh damper.

This is an extremely important finding suggesting that the energy confined at the gear pair is leading to high vibration amplitudes; thus severe separation effects. This is in contrast to the previous almost equal dissipative capacity of the NES damper. It is reasonable to correlate the difference in the dynamic response of the two cases to the previous fact. Lower vibration amplitudes and constant mesh conditions are perceived when the NES damper absorbs an increased amount of input energy. It is therefore reasonable to anticipate that an energy transfer mechanism instigated by proper NES tuning is responsible for such phenomena.

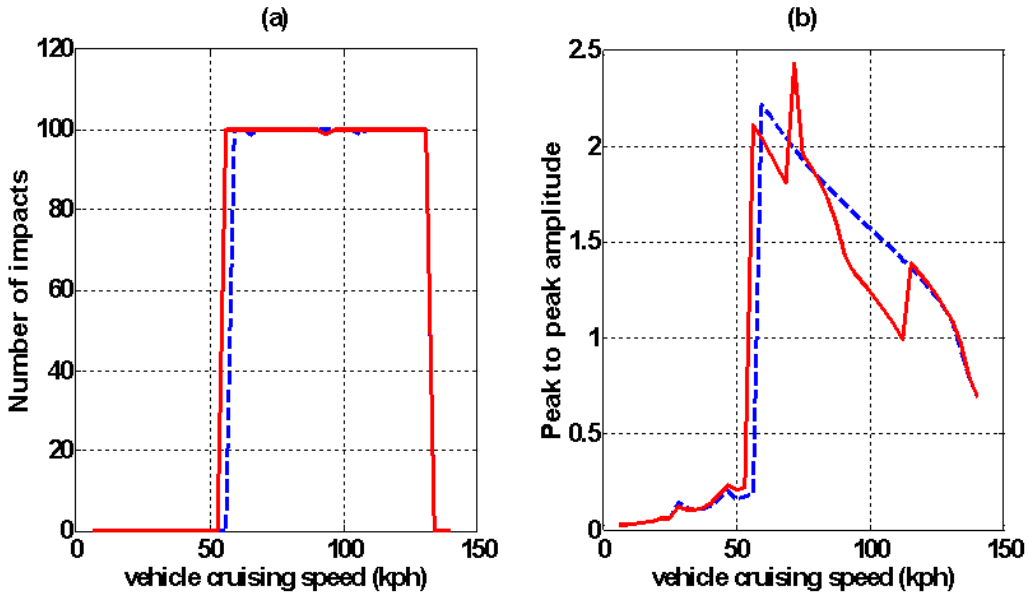

Figure 7.10- Response characteristics of the primary system ($\varepsilon = 0.214$; $k_t = 1.2388 \cdot 10^{13} Nm/rad^3$): (a) number of impacts (b) dimensionless peak to peak amplitude; - - - - without NES, ——— with NES

Besides the previous low amplitude steady-state response, another important attractor exists. It evokes a quasi-periodic set of motions characterised by a modulation of the vibration amplitude, resembling relaxation type oscillations (Gendelman et al, 2008). This response regime has been identified in previous works where NES attachments were integrated upon linear systems with periodic forcing; it was found to be related to efficient TET. It is mostly present in the proximity of the fundamental resonance and its appearance is sensitive to the initial conditions (Starovetsky and Gendelman, 2008). A potential occurrence of similar response regimes in the present case would increase the prospects of a possible application.

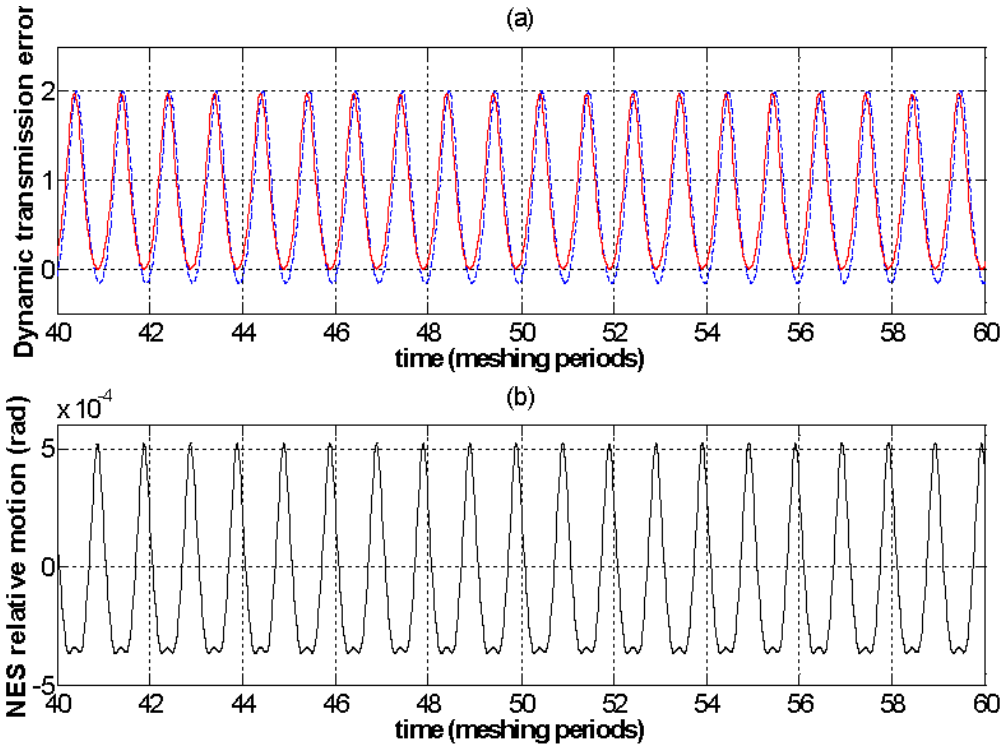

Figure 7.11- Time series of dynamic response at 62.4kph under ineffective vibration attenuation conditions ($\varepsilon = 0.214$; $k_t = 1.2388 \cdot 10^{13} Nm/rad^3$): (a) Dynamic transmission error (primary system) (b) NES relative motion; _ _ _ _ without NES, _____ with NES

The existence of strongly modulated responses (SMR) is investigated by applying the same genetic optimisation algorithm (Rahmani, 2008); however, different initial conditions are used for the NES attachment. In this case the NES is considered to be stationary in the beginning of each speed sweep. This implies an engagement mechanism capable of coupling and decoupling the main system and the nonlinear attachment. The current concern is focused on the appearance of additional response regimes connected to TET and not the practical implementation of the mechanism in a real gear pair system. The number of single sided impacts is again selected as a criterion and a range of vehicle speed around 115kph is considered.

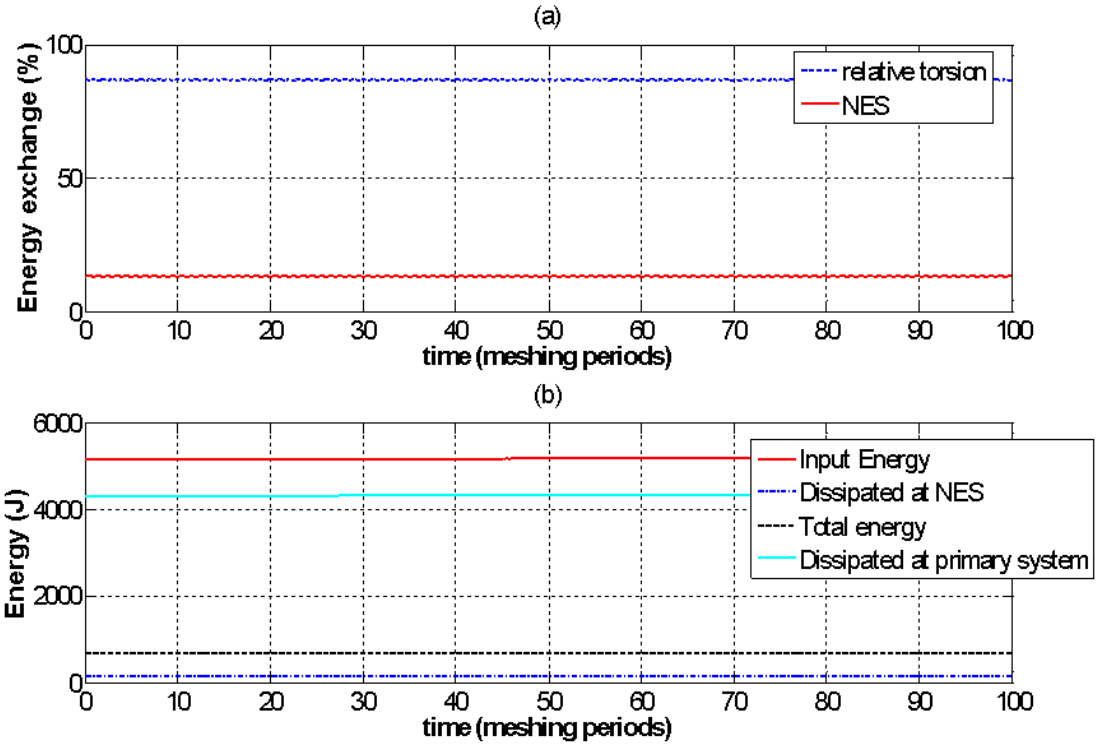

Figure 7.12- - (a) Instantaneous energy exchanges between modes, (b) input energy distribution for ineffective vibration attenuation at 62.4kph

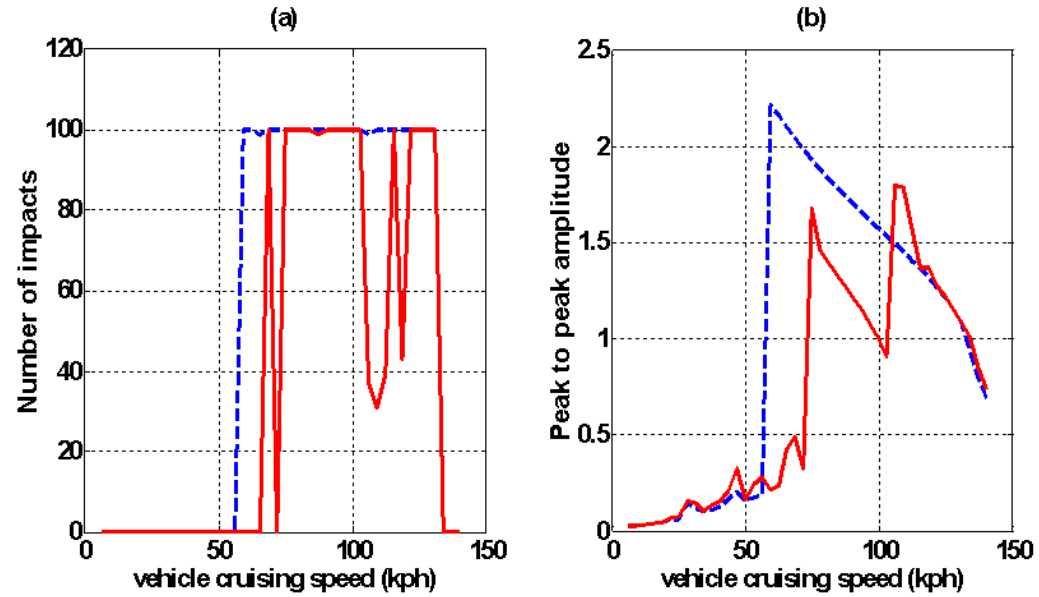

Figure 7.13- Response characteristics of the primary system ($\varepsilon = 0.31$; $k_t = 6.429 \cdot 10^{12}\, Nm/rad^3$) for $u(0) = 0, \dot{u}(0) = -\dot{\varphi}_g$: (a) number of impacts (b) dimensionless peak to peak amplitude; _ _ _ _ without NES, _____ with NES

Figure 7.13 shows the response spectra for an optimum case ($\varepsilon = 0.31$; $k_t = 6.429 \cdot 10^{12} Nm/rad^3$).The number of impacts depicted in section (a) is now affected at the speed area of interest while the positive effects near the bifurcation point are also maintained. Positive influence is also seen in the peak to peak amplitude.

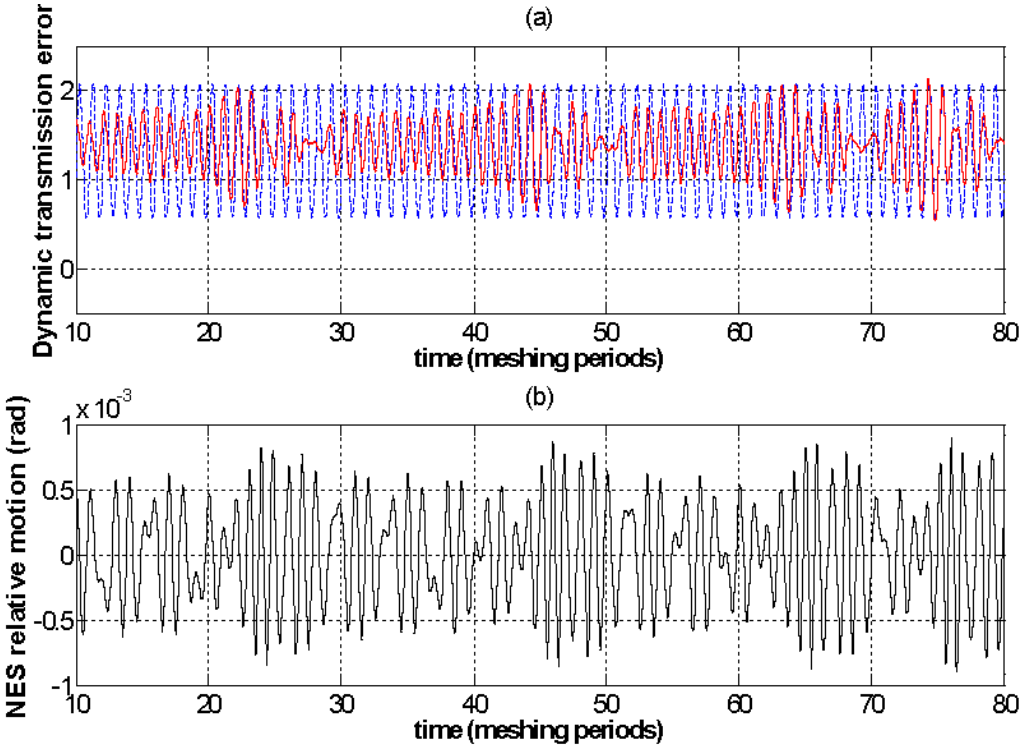

Figure 7.14-Time series of the dynamic response at 106.8kph, quasi-periodic response regime ($\varepsilon = 0.31; k_t = 6.429 \cdot 10^{12} Nm/rad^3$): (a) Dynamic transmission error (primary system) (b) NES relative motion; _ _ _ _ without NES, _____ with NES

Figure 7.14 shows the time series of the dynamic response at a cruising speed of 106.8kph. This corresponds to a local minimum of Figure 7.13(a) and a local maximum of Figure 7.10(b). The dynamic transmission error in this case Figure 7.10 is not a steady-state function; it rather exhibits a beating behaviour. The same applies for the nonlinear attachment. These motions are similar to the ones described in the analysis of Gendelman et al (2008) and Starovetsky and Gendelman (2008) when a linear primary system was considered. The favourable effect of these types of motions can be observed in Figure 7.15. The modal energy exchange shows a reduced energy level of the primary system which is now clearly

transferred to the NES. This is confirmed by Figure 7.15(b), where the majority of input energy gets dissipated in the nonlinear attachment while a reduced portion remains in the primary system. This fact implies the presence of an efficient mechanism setting an energy flow path towards the NES. This effect is reflected in the dynamic response where the single sided impacts are suppressed by almost 2/3. Although the maximum peak to peak amplitude might be slightly increased, the number of overall peaks is significantly reduced, indicating a lower energy content of the primary system. Therefore, any NES design able to undergo strongly modulated responses could be crucial towards achieving effective vibration alleviation.

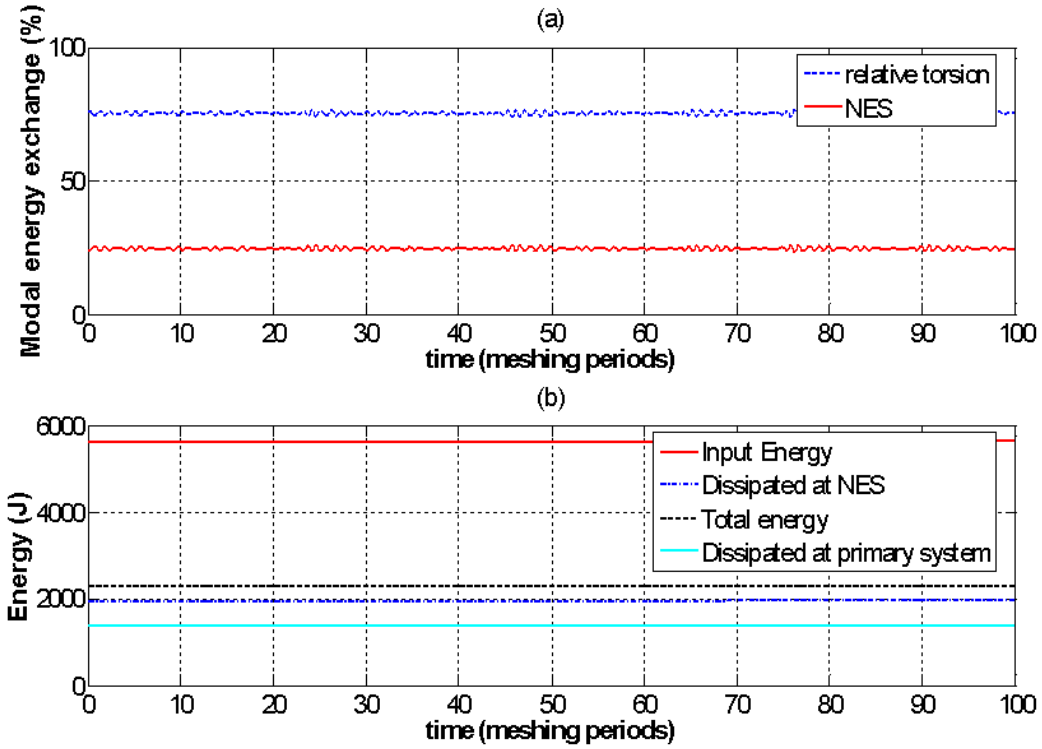

Figure 7.15- (a) Instantaneous energy exchanges between modes, (b) input energy distribution for quasi-periodic response at 106.8kph

7.4 - Breach of dynamic equilibrium

In Chapter 5, it was seen that high amplitude oscillations can be encountered when the external excitations are unbalanced. Simulations of a throttle release case indicated a deceleration of the rigid body rotation while the relative torsional mode settles to a periodic motion around a different equilibrium point. The type of this motion is significantly affected by the initial conditions at the onset of equilibrium

breach. The worst case scenario revealed the potential of repetitive double sided impacts instigating highly pronounced vibro-impact phenomena. This section will investigate the prospect of employing nonlinear attachment for accommodating the previous unwanted behaviour.

In previous analytical studies of TET, the efficiency of NES as vibration absorbers under transient conditions was related to an 1:1 internal resonance between the primary structure and the NES (Vakakis and Gendelman, 2001). These observations were confirmed by subsequent experimental studies (McFarland et al, 2005). For the current system, a violation of the balance of the external forces will cause the dynamic response to undergo a sudden transient before settling to the aforementioned periodic motion. The capability of the NES to effectively absorb energy during this transient short period could prove significant for the final exhibited periodic response.

In Chapter 5 was shown that for a certain cruising speed, the dynamic response after the throttle release depends strongly on the initial conditions at the release instant; the latter arise from the prior periodic motion. Therefore a number of initial conditions should be tried before assessing the efficiency and robustness of a NES design. A simultaneous cruising velocity sweep will yield the worst case scenario for the whole range of operating conditions. Such a procedure requires a significant amount of computational time. In order to constrain the number of simulations, the optimisation algorithm (Rahmani, 2008) is used for the same range of parameters as in the case of steady state cruising. Minimisation of the number of double sided impacts is demanded, taking the worst case scenario of 100 different initial conditions. As for the initial state of the nonlinear absorber, it is supposed to rotate with the crown gear shaft at all times.

Figure 7.16 shows the time series of the dynamic response when suppression of double sided impact phenomena is achieved. The vehicle cruising speed is set at 112.3kph while the throttle is released at 200.12 meshing periods. It should be noted that prior to this time instance, additional 10000 meshing periods have elapsed to ensure steady state conditions have been achieved. Equilibrium conditions are re-established after 400 meshing periods. Section (a) comparing the response of the main system with and without NES shows that double sided impacts are no longer

realised. The NES affects the primary system response initially during steady state reducing the peak to peak amplitude. This reduction might be crucial since it affects the initial conditions at the onset of coasting in accordance with the findings of Chapter 5.

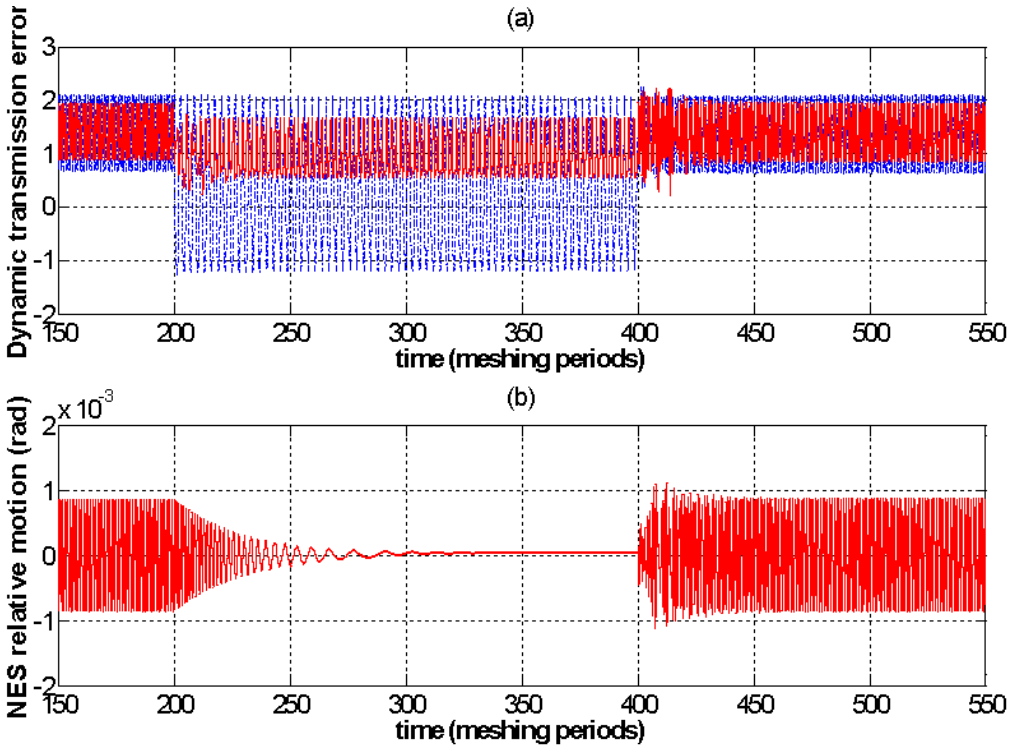

Figure 7.16- Time series of dynamic response at 112.3kph under effective vibration attenuation conditions ($\varepsilon = 0.149; k_t = 5.506 \cdot 10^{12}\, Nm/rad^3$): (a) Dynamic transmission error (primary system) (b) NES relative motion; _ _ _ _ without NES, ——— with NES

Figure 7.17 depicts the dynamic response under ineffective suppression of double sided impacts under the same conditions of Figure 7.16. The NES inertia ratio is almost identical whereas the nonlinear stiffness is reduced to a lower level. As seen in Figure 7.17(a) the NES has no influence on the dynamic response of the primary system at any stage of the motion. As a result, the relative torsion settles to periodic solution characterised by DSI as already seen in Chapter 5. Correlation of the relative motion of the NES under the two cases (Figures 7.16(b)-7.17(b)) shows a different qualitative behaviour. Under suppression of DSI (Figure 7.16(b)), the NES relative motion is almost triple in magnitude before the breach point. Moreover, it is continuous both in frequency and amplitude before and after that critical point;

oscillations exhibit a higher number of cycles compared to Figure 7.17(b). On the other hand, when the suppression mechanism is idle the NES relative motion undergoes a discontinuity at the breach point; its amplitude almost doubles. The response is followed by a finite, small number of oscillations until they finally fade.

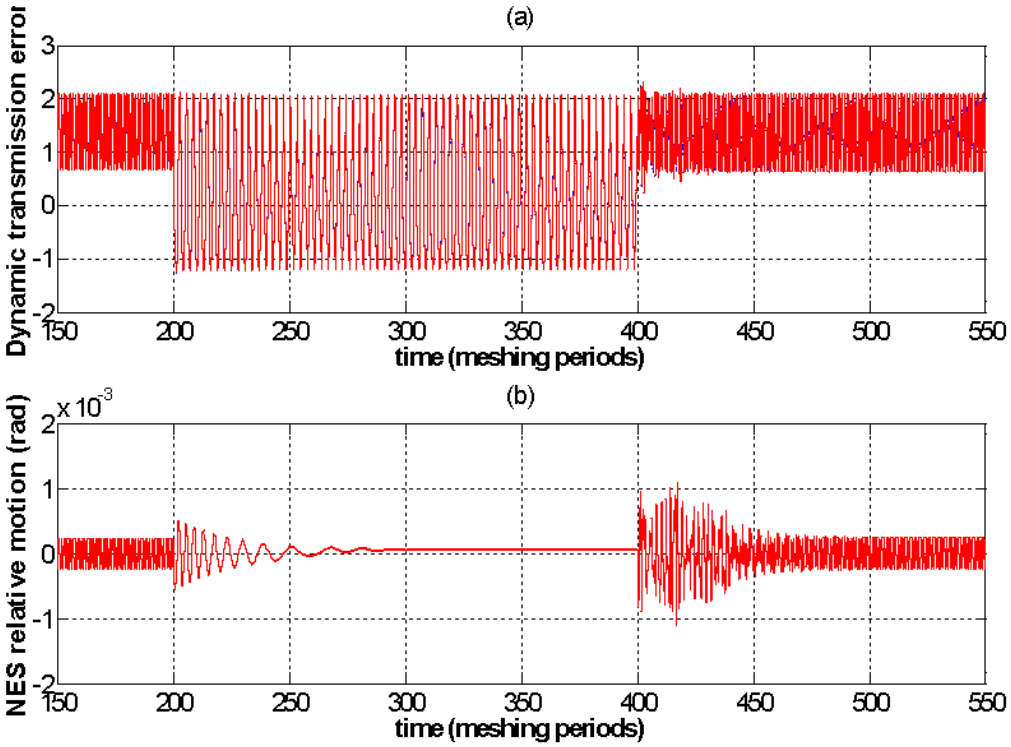

Figure 7.17- Time series of dynamic response at 112.3kph under ineffective vibration attenuation conditions ($\varepsilon = 0.15; k_t = 1.542 \cdot 10^{12}\, Nm/rad^3$): (a) Dynamic transmission error (primary system) (b) NES relative motion; _ _ _ _ without NES, _____ with NES

Interesting observations can be drawn from the wavelet analysis of the dynamic responses. Figure 7.18 shows the wavelet analysis of the relative velocity of the primary system under DSI suppression. The picture is similar to Figure 5.37 showing a frequency contribution of almost ½ mesh order during the suppression stage. The relative NES motion is analysed in Figure 7.19 where it can be seen that its instantaneous frequency undergoes a smooth transition from the 1st to ½ mesh harmonic before its oscillations start to fade.

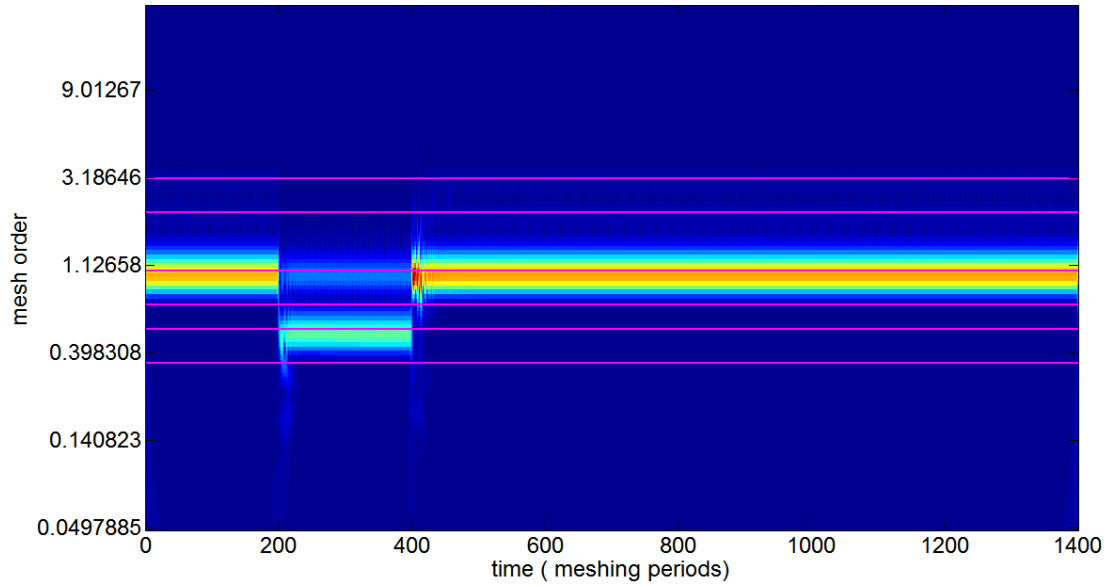

Figure 7.18- Wavelet analysis of the relative torsional velocity, DSI suppresion

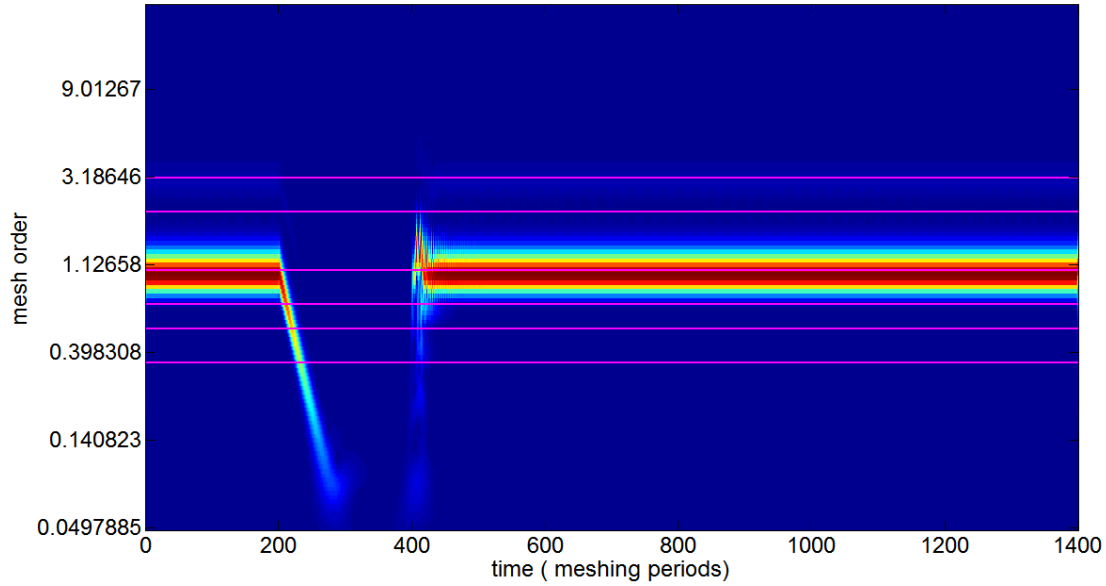

Figure 7.19- Wavelet analysis of the NES relative motion, DSI suppresion

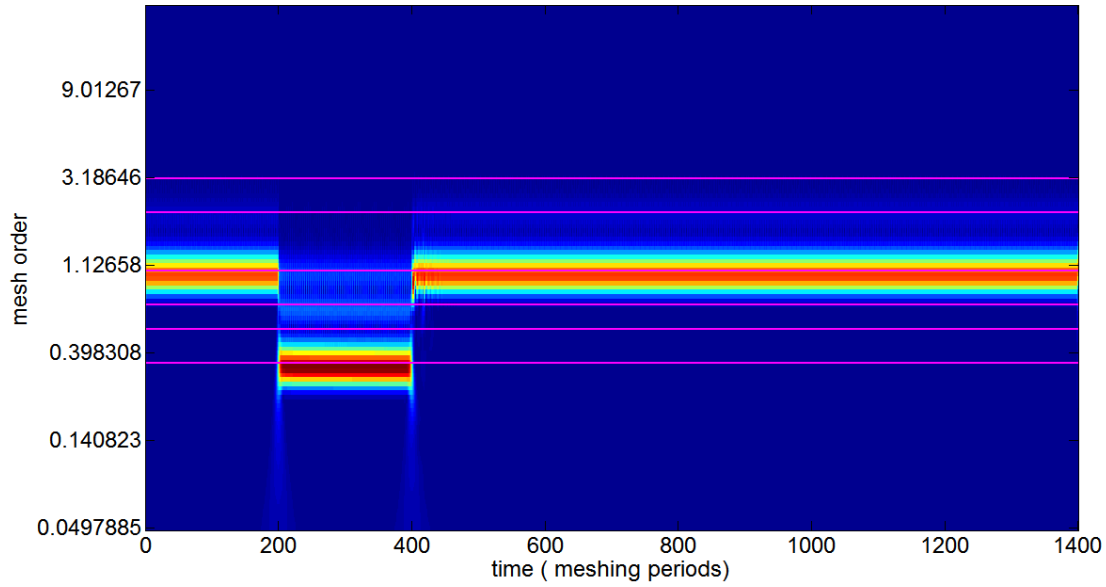

Figure 7.20- Wavelet analysis of the relative torsional velocity, no DSI suppresion

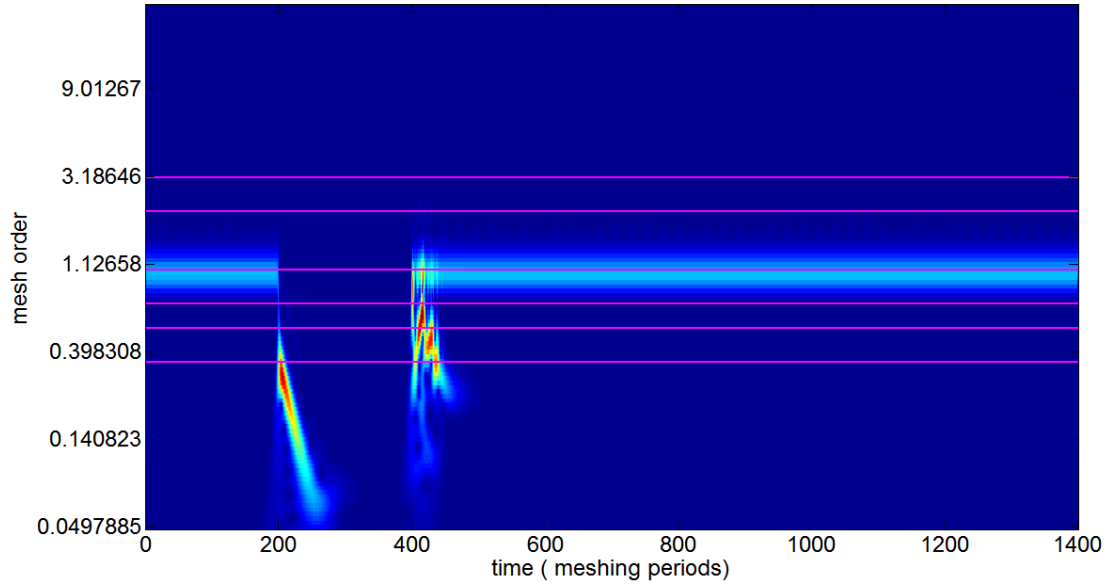

Figure 7.21- Wavelet analysis of the NES relative motion, no DSI suppression

Figure 7.20 illustrates the case of no DSI suppression for the main system; the latter now settles in a periodic motion governed by 1/3 and 2/3 mesh sub harmonics in accordance to the findings of Chapter 5. The frequency content of the NES relative

motion in this case undergoes a jump as seen in Figure 7.21; shifting impulsively from the 1st mesh order to the vicinity of the 1/3 mesh sub harmonic after the equilibrium breach. Therefore, the significant difference in the frequency characteristics of the NES signal is the discontinuity before and after the throttle release point which has been spotted in the time series of Figures 7.16(b)-7.17(b). An efficient NES is related to its ability to form a frequency bridge between the two different types of motion realised at the primary system before (mesh order) and after (mesh sub harnonics) the change in external excitation. A smooth frequency transition of the NES relative response triggers a DSI alleviation mechanism whereas a sudden jump from the mesh harmonic to a sub harmonic motion produces to viable gain.

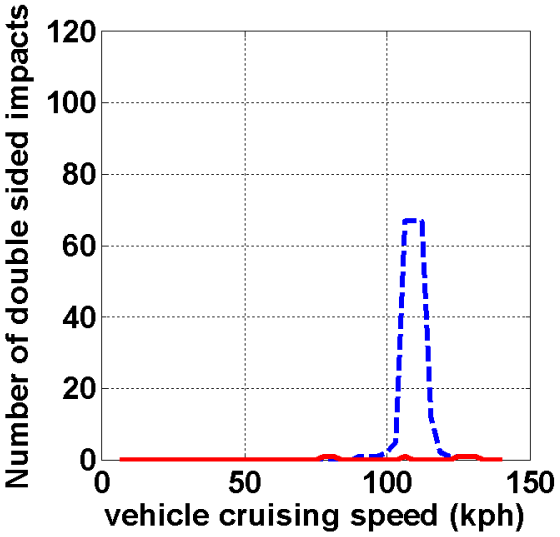

Figure 7.22- Number of double sided impacts over the vehicle speed operating range; _ _ _ _ without NES, _____ with NES

Eventually, the arising question is whether the preceding NES design is robust, concerning the whole range of operating speed. The answer is given by constructing a spectrum plot depicting the maximum number of double sided impacts for every speed of interest with and without NES presence. Figure 7.22 shows that there is a remarkable robustness in the suppression mechanism. Although the region of concern for DSI motions is quite narrowband, the NES can achieve almost complete suppression for the considered excitation conditions.

7.5 -Synopsis

The behavior of a nonlinear attachment as a method for controlling the torsional vibrations of hypoid transmissions has been investigated. These devices named nonlinear energy sinks (NES) have been already applied mostly in linear systems to achieve broadband transfer of unwanted energy. The nonlinear characteristics of the current system cause a broadband resonant behavior of the steady state motion. Furthermore, under violation of equilibrium of external forces the system dynamic response is associated to double sided impact phenomena.

NES designs showed some potential both under steady state and transient conditions. In the former case, response regimes (periodic and SMR) related to irreversible TET were identified and correlated to existing analytical studies. Numerical simulations showed a considerable gain under certain operating conditions. Treatment of transient DSI motions was also granted possible through a nonlinear attachment. The suppression mechanism was related to the formation of a frequency bridge from the NES; in a sense coupling the different type of motions exhibited by the main system before and after the equilibrium breach.

It should be noted that this is just a preliminary study aiming at highlighting the feasibility of such a design. The design is not fully optimized, nor the mechanism properly understood. The current chapter can only be regarded only in an indicative manner, showing the opportunities arising from NES implementation. A more rigorous analysis is required to gain an in depth understanding of such complex phenomena.

Chapter 8 - Overall conclusions, contribution to knowledge and suggestions for future work

8.1 - Overall conclusions

A new modeling approach was implemented in the investigation of hypoid gear torsional dynamics. The major difference lies in expressing the dynamic transmission error in integral form yielding a set of integral-differential equations that govern the motion of a hypoid transmission. Numerical simulations conveyed the existence of stable, steady state solutions compared to unbounded responses rendered by previous methodologies. Furthermore, the analysis was applied on a realistic combination of operating conditions (loading and rotational speed) corresponding to a commercial vehicle exhibiting axle whine issues. The importance of expressing the resistive torque in terms of the angular velocity of the differential was highlighted, towards achieving dynamic equilibrium conditions.

The model showed robustness in the variation of initial angular velocities of the gear members. However, a region of multiple solutions characterized by proper and improper mesh was identified. The former case is defined by constant mesh with the fundamental mesh order contributing vastly in the spectral content of the dynamic response; the latter by separation and vibro-impacts between the mating flanks while higher mesh orders become more prominent. This behavior inherent in a broadband vicinity of the vehicle speed – dynamic response spectrum was not observed in previous studies. In that instance, the multiple solution regions were confined to a narrowband area around the fundamental resonance and were realized only under lightly loaded and heavily damped cases.

The family of periodic solutions was computed by employing the numerical continuation method. A bifurcation analysis revealed the existence of multiple solutions, stable and unstable branches. Parametric studies showed the effect of various design parameters. Reduction of mesh damping contributed in the generation of a third solution branch characterized by double sided impacts and severe vibro-impact phenomena. Additionally, aggravated dynamic response is induced when the variations of mesh stiffness and contact radii are in phase and out

of phase with the kinematic transmission error. The broadband region of multiple solutions can be mainly attributed to the varying mesh point given quantified with the variation of contact radii. Higher order harmonics of the mesh properties have a dual effect both on the fundamental and on the superharmonic resonance. These findings are crucial for a designer of a differential system.

Analysis of the dynamic response under dynamic unbalance of the external excitations illustrated the existence of another type of double sided solutions. The latter are realized under coasting when the input torque is insufficient to counterbalance the resistive; for instance under a sudden release of the throttle. The dynamic response characteristics are greatly affected by the initial conditions at the ignition of the dynamic unbalance. Different frequency content is attributed to each type of possible solutions. Overall the double sided impacts are constrained at a narrowband region of the upper range of cruising speeds; nonetheless its severity cannot be overlooked.

A combined tribo-dynamic analysis conveyed that the torsional dynamics are almost insensitive to the friction generated by the relative sliding motion of the gear flanks. Nevertheless, the various properties defining the tribological conjunction are affected by the dynamics of the system due to the abrupt change in contact pressure affecting the lubricant characteristics and in the velocity magnitude of the gear flanks; these phenomena are triggered by the resonant behavior of the gear motion.

Introduction of a nonlinear dynamic absorber aiming at alleviating the torsional vibration level indicated a possible potential both under steady state and transient conditions. Response regimes correlated in literature to Targeted Energy Transfer were successfully identified. The effects of NES application were more prominent under coasting conditions, showing a deal of greater robustness, by causing almost complete elimination of DSI. Under steady state conditions the result was less pronounced; however there are large margins for further optimization considering the nature of the problem requiring broadband vibration isolation.

8.2 -Novelty – Validation

The novelty of the current work can be summarized in the development of a modeling approach which considers interacting disciplines related to hypoid gear

unique geometry and vehicle operating conditions. In specific, the geometric influence is quantified mainly in a varying form of contact radii resulting in a non holonomic constraint which defines the dynamic transmission error. The non integratable form of the latter was retained in the dynamic representation of the system yielding an enriched behavior. The operating conditions of the vehicle were included in the calculation through a resisting torque dependent on the instantaneous angular velocity. The usual nonlinearities arising in the harmonic form of kinematic transmission error and mesh stiffness were also accounted for. Additionaly, the dependence of the mean stiffness value on the external torque was included. Except for depicting the time histories under certain operating conditions, analysis was expanded to study the family of periodic solutions which has not been accomplished before for such level of complexity. Therefore, from a dynamics point of view the system was analyzed in depth.The tribological aspects of the problem were also considered by including the effect of friction as an internal excitation between the gear members. This formulation, even if it does not solve the fully transient problem is one of the first studies to investigate the effect of friction in the dynamics response and vice versa.

Experimental validation was not realized directly, however the findings of this study showed a significant qualitative correlation to previously published experimental works. Noise and peak magnitudes of acceleration received by transducers, lie within the operating vehicle speeds predicted by the current model. These regions are characterized by single or double sided impacts between the meshing gear flanks. In terms of the tribological analysis, results show agreement with the extrapolated equations produced by previous studies.

8.3 - Achievements of aims and objectives

The specific aims and objectives defined in Section 1.2 have been accomplished as follows:

I. An enhanced dynamic model was created by applying a suitable definition of the dynamic transmission error. A more enriched broadband nonlinear dynamic behaviour was captured compared to previously developed formulations while realistic operation conditions were considered.

II. The family of periodic solutions was successfully computed after employing a mathematical manipulation of the original equations of motion. Parametric studies rendered the effect of the main mesh parameters on the system dynamics.

III. A tribo-dynamic analysis was performed by coupling the global deflections and loads predicted by the dynamic model to the local flank contact problem.

IV. The dynamic response analysis revealed the existence of broadband single-sided and double-sided vibro-impacts, associated to aggravated vibration amplitudes. Numerical simulations on the effect of NES attachments revealed some potential, limited for the time being.

8.4 - Contributions to knowledge

There have been previous attempts to model the dynamic behavior of hypoid transmissions. However, the definition of the dynamic transmission error with its traditional form was not sufficient to derive realistic stable solutions. Therefore, simplifications of doubtful content were adopted. As a result, the existing models failed to predict the aggravated dynamic response encountered in experimental studies. Vibro-impact phenomena were only confined to narrow band frequency regions either to lightly loaded and highly damped cases. However, the current methodology has achieved to address the above shortcomings. A realistic formulation of the equations of motion combined to the inclusion of operating conditions based resistive torque showed the potential of separation effects under heavily loaded conditions. Analysis was enriched by the computation of the family of periodic solutions and their stability characteristics. The latter showed that by carefully designing the gear pair characteristics, the vibration severity can be addressed up to a certain extent.

A combined tribodynamic analysis, coupling the global dynamic effect to the relative motion of the individual mating flanks was yielded possible. This forms another important contribution towards the prediction of tribological properties, such as film thickness, friction coefficient and temperature rise on complex gear surfaces. The anticipation of marginal effect of frictional torque on the torsional motion was confirmed. Yet, the tribological properties exhibited a significant variation with

respect to the vehicle cruising speed; discontinuities and existence of different branches can be identified.

Vibration isolation by means of nonlinear attachments was proven to be of significant potential both under steady state and transient conditions. Response regimes reported in previous studies of linear primary systems were also identified in current case where the primary system possesses inherent nonlinearities. The governing mechanism of energy exchange was found to be dependent on the parameters of the attachment, defining regions of optimised behaviour. The benefits on the dynamics are more profound in transient conditions; nevertheless the overall picture shows promise for future work.

8.5 - Critical assessment of current work and suggestions for future work

I. Only the torsional degrees of freedom of the gear pair have been considered. Therefore, the lateral motions of the supporting shafts interacting with the surrounding bearings are overlooked. However, a more realistic approach would require the contribution of other system parameters both in lateral and in torsional motion. Future expansion of the present methodology on a multi-parametric dynamic approach could yield more realistic results and shed light into the various modal interactions with the rest of the driveline. Application of the Finite Element Method with coordinate reduction could be an effective method of analysis. Investigation of parametric resonances and noise generation modeling are some additional suggestions for possible future work.

II. The gear mesh characteristics derived by TCA are assumed to be identical under quasi-static and dynamic conditions. Additionally, the gear mesh is concentrated on a single point when solving the dynamic problem. The effect of torque on the mesh teeth stiffness has been addressed; however the influence on the contact radii was not examined. Such an attempt could identify any further complexities in the dynamic response of the system.

III. The tribodynamic approach was entirely analytical. No discretisation of the contact zone was attempted, since it would require excessive computational time.

The thermal analysis also ignored the heating on the mating solid surfaces, which was reasonably justified by previous works. Convection terms were also neglected due to the thin films encountered and the mean temperature rise was predicted. The inlet temperature of the lubricant was taken equal to the bulk one, overlooking any possible preheating effects. A more elaborate thermal model should investigate the validity of these assumptions.

IV. The investigation of a Non Linear Energy Sink (NES) as a palliative method for addressing vibro-impact problems in hypoid transmissions was only attempted on a proof of concept level. Further analysis is required both on numerical optimisation and also on understanding the energy exchanging mechanism. Such complex phenomena need to be examined thoroughly before reaching concrete conclusions.

References

Argyris, J., Fuentes, A. and Litvin, F.L. 2002, "Computerized integrated approach for design and stress analysis of spiral bevel gears", *Computer Methods in Applied Mechanics and Engineering,* vol. 191, no. 11–12, pp. 1057-1095.

Blankenship, G.W. and Kahraman, A. 1995, "Steady state forced response of a mechanical oscillator with combined parametric excitation and clearance type non-linearity", *Journal of Sound and Vibration,* vol. 185, no. 5, pp. 743-765.

Bosch, R. 2004, *Automotive handbook,* Robert Bosch GmbH.

Chaudhary, A.B. and Bathe, K. 1986, "A solution method for static and dynamic analysis of three-dimensional contact problems with friction", *Computers and Structures,* vol. 24, no. 6, pp. 855-873.

Cheng, Y. and Lim, T.C. 2001, "Vibration analysis of hypoid transmissions applying an exact geometry-based gear mesh theory", *Journal of Sound and Vibration,* vol. 240, no. 3, pp. 519-543.

Cheng, Y. and Lim, T.C. 2003, "Dynamics of Hypoid Gear Transmission With Nonlinear Time-Varying Mesh Characteristics", *Journal of Mechanical Design,* vol. 125, no. 2, pp. 373-382.

Chittenden, R.J., Dowson, D., Dunn, J.F. and Taylor, C.M. 1985, "A Theoretical Analysis of the Isothermal Elastohydrodynamic Lubrication of Concentrated Contacts. II. General Case, with Lubricant Entrainment along Either Principal Axis of the Hertzian Contact Ellipse or at Some Intermediate Angle", *Proceedings of the Royal Society of London.A.Mathematical and Physical Sciences,* vol. 397, no. 1813, pp. 271-294.

Choi, B., Yoon, J. and Oh, J. 2012, "A study on axle gear whine noise reduction with deflection test", *Proceedings of the Institution of Mechanical Engineers, Part D: Journal of Automobile Engineering,* vol. 226, no. 2, pp. 225-233.

Chung , C.(., Steyer , G., Abe , T., Clapper , M. and Shah , C. 1999, *Gear Noise Reduction through Transmission Error Control and Gear Blank Dynamic Tuning*, SAE International 1999-01-1766.

Comparin, R. and Singh, R. 1989, "Non-linear frequency response characteristics of an impact pair", *Journal of Sound and Vibration,* vol. 134, no. 2, pp. 259-290.

Crook, A.W. 1961, "The lubrication of rollers III. A theoretical discussion of friction and the temperatures in the oil film", *Philosophical Transactions of the Royal Society of London.Series A, Mathematical and Physical Sciences,* vol. 254, no. 1040, pp. 237-258.

Curtis , S., Pears , J., Palmer , D., Eccles , M., Poon , A., Kim , M., Jeon , G., Kim , J. and Joo , S. 2005, *An Analytical Method to Reduce Gear Whine Noise, Including Validation with Test Data*, SAE International 2005-01-1819.

De la Cruz, M., Theodossiades, S. and Rahnejat, H. 2010, "An investigation of manual transmission drive rattle", *Proceedings of the Institution of Mechanical Engineers, Part K: Journal of Multi-body Dynamics,* vol. 224, no. 2, pp. 167-181.

De, I.C., Theodossiades , S., Rahnejat , H. and Kelly , P. 2009, *Numerical and Experimental Analysis of Manual Transmissions - Gear Rattle*, SAE International.

Doedel, E.J. 1981, "AUTO: A program for the automatic bifurcation analysis of autonomous systems", *Congr.Numer,* vol. 30, pp. 265-284.

Donley , M.G., Lim , T.C. and Steyer , G.C. 1992, *Dynamic Analysis of Automotive Gearing Systems*, SAE International 920762.

Dudley, D.W. and Townsend, D.P. 1991, *Dudley's gear handbook,* McGraw-Hill.

Evans, C. and Johnson, K. 1986, "The rheological properties of elastohydrodynamic lubricants", *Proceedings of the Institution of Mechanical Engineers, Part C: Journal of Mechanical Engineering Science,* vol. 200, no. 5, pp. 303-312.

Eyring, H. 1936, "Viscosity, plasticity, and diffusion as examples of absolute reaction rates", *The Journal of chemical physics,* vol. 4, pp. 283.

G. Floquet, Sur les équations différentielles linéaires à coefficients périodiques, *Annales École Normale Supérieure* 12 (1883) 47–88.

Gendelman, O., Manevitch, L., Vakakis, A.F. and M'CLOSKEY, R. 2001, "Energy pumping in nonlinear mechanical oscillators: Part I: Dynamics of the underlying Hamiltonian systems", *Journal of Applied Mechanics,* vol. 68, no. 1, pp. 34-41.

Gendelman, O., Starosvetsky, Y. and Feldman, M. 2008, "Attractors of harmonically forced linear oscillator with attached nonlinear energy sink I: Description of response regimes", *Nonlinear Dynamics,* vol. 51, no. 1, pp. 31-46.

Gohar, R. 2001, *Elastohydrodynamics,* World Scientific Publishing Company.

Gohar, R. and Rahnejat, H. 2008, *Fundamentals of tribology,* World Scientific Publishing Company Incorporated.

Gosselin, C., Cloutier, L. and Nguyen, Q.D. 1995, "A general formulation for the calculation of the load sharing and transmission error under load of spiral bevel and hypoid gears", *Mechanism and Machine Theory,* vol. 30, no. 3, pp. 433-450.

Gosselin, C., Guertin, T., Remond, D. and Jean, Y. 2000, "Simulation and Experimental Measurement of the Transmission Error of Real Hypoid Gears Under Load", *Journal of Mechanical Design,* vol. 122, no. 1, pp. 109-122.

Greenwood, J. and Tripp, J. 1970, "The contact of two nominally flat rough surfaces", *Proceedings of the Institution of Mechanical Engineers,* vol. 185, no. 1, pp. 625-633.

Grubin, A. 1949, "Fundamentals of the hydrodynamic theory of lubrication of heavily loaded cylindrical surfaces", *Investigation of the Contact Machine Components,* , no. 30, pp. 115-166.

Hagino , Y., Azuma , H., Mizutani , H. and Nishiwaki , S. 1990, *A Study of Vibration Characteristics on Final Gear Unit*, SAE International 900393.

Handschuh, R.F. and Kicher, T.P. 1996, "A method for thermal analysis of spiral bevel gears", *Journal of mechanical design,* vol. 118, no. 4, pp. 580-585.

Handschuh, R.F. and Kicher, T.P. 1996, "A Method for Thermal Analysis of Spiral Bevel Gears ", *Journal of Mechanical Design,* vol. 118, no. 4, pp. 580.

He, S., Gunda, R. and Singh, R. 2007, "Inclusion of Sliding Friction in Contact Dynamics Model for Helical Gears", *Journal of Mechanical Design,* vol. 129, no. 1, pp. 48-57.

Hellinger , W., Raffel , H.C. and Rainer , G.P. 1997, *Numerical Methods to Calculate Gear Transmission Noise*, SAE International 971965.

Hirasaka , N., Sugita , H. and Asai , M. 1991, *A Simulation Method of Rear Axle Gear Noise*, SAE International 911041.

Holmes, M.J.A., Evans, H.P., Hughes, T.G. and Snidle, R.W. 2003, "Transient elastohydrodynamic point contact analysis using a new coupled differential deflection method Part 1: Theory and validation", *Proceedings of the Institution of Mechanical Engineers, Part J: Journal of Engineering Tribology,* vol. 217, no. 4, pp. 289-304.

Holmes, M., Evans, H., Hughes, T. and Snidle, R. 2003, "Transient elastohydrodynamic point contact analysis using a new coupled differential deflection method Part 2: Results",

Proceedings of the Institution of Mechanical Engineers, Part J: Journal of Engineering Tribology, vol. 217, no. 4, pp. 305-322.

Holmes, M., Evans, H. and Snidle, R. 2005, "Analysis of mixed lubrication effects in simulated gear tooth contacts", *Transactions of the ASME-F-Journal of Tribology,* vol. 127, no. 1, pp. 61-69.

Houpert, L. 1985, "New results of traction force calculations in elastohydrodynamic contacts", *Journal of tribology,* vol. 107, no. 2, pp. 241-248.

Jiang, X., McFarland, D.M., Bergman, L.A. and Vakakis, A.F. 2003, "Steady state passive nonlinear energy pumping in coupled oscillators: theoretical and experimental results", *Nonlinear Dynamics,* vol. 33, no. 1, pp. 87-102.

Johnson, K. and Greenwood, J. 1980, "Thermal analysis of an Eyring fluid in elastohydrodynamic traction", *Wear,* vol. 61, no. 2, pp. 353-374.

Johnson, K.L. 1987, *Contact Mechanics,* Cambridge University Press.

Johnson, K.L. and Gray, G.G. 1975, "Development of Corrugations on Surfaces in Rolling Contact", *Proceedings of the Institution of Mechanical Engineers,* vol. 189, no. 1, pp. 567-580.

Juang , T.B., Harvey , K.E., Burzlaff , M.W. and Rockett , P.J. 2006, *Analytical and Experimental Development to Improve Powertrain System Induced Vehicle NVH Issues*, SAE International 2006-01-1533.

Kahraman, A. and Singh, R. 1991, "Interactions between time-varying mesh stiffness and clearance non-linearities in a geared system", *Journal of Sound and Vibration,* vol. 146, no. 1, pp. 135-156.

Kahraman, A. and Singh, R. 1990, "Non-linear dynamics of a spur gear pair", *Journal of Sound and Vibration,* vol. 142, no. 1, pp. 49-75.

Kar, C. and Mohanty, A.R. 2007, "An algorithm for determination of time-varying frictional force and torque in a helical gear system", *Mechanism and Machine Theory,* vol. 42, no. 4, pp. 482-496.

Kim , H.A., Allen , M.A., Ditto , D.H. and Wickert , J.A. 1999, *Gear Noise Characterization and Reduction in Drivetrain Systems*, SAE International 1999-01-1051.

Kiyono, S., Fujii, Y. and Suzuki, Y. 1981, "Analysis of Vibration of Bevel Gears", *Bull. JSME,* vol. 24, pp. 441-446.

Kolivand, M., Li, S. and Kahraman, A. 2010, "Prediction of mechanical gear mesh efficiency of hypoid gear pairs", *Mechanism and Machine Theory,* vol. 45, no. 11, pp. 1568-1582.

Kolivand, M. and Kahraman, A. 2009, "A load distribution model for hypoid gears using ease-off topography and shell theory", *Mechanism and Machine Theory,* vol. 44, no. 10, pp. 1848-1865.

Lee , S., Go , S., Yu , D., Lee , J., Kim , S., Jo , Y. and Choi , B. 2005, *Identification and Reduction of Gear Whine Noise of the Axle System in a Passenger Van*, SAE International 2005-01-2302.

Lee , Y.E. 2007, *Axle Gear Mesh Force Prediction, Correlation and Reduction*, SAE International 2007-01-2230.

Lee , Y.E. and Kocer , F. 2003, *Minimize Driveline Gear Noise by Optimization Technique*, SAE International 2003-01-1482.

Lee, Y.S., Kerschen, G., McFarland, D.M., Joel Hill, W., Nichkawde, C., Strganac, T.W., Bergman, L.A. and Vakakis, A.F. 2007, "Suppressing aeroelastic instability using broadband passive targeted energy transfers, part 2: experiments", *AIAA Journal,* vol. 45, no. 10, pp. 2391-2400.

Lee, Y.S., Vakakis, A.F., Bergman, L.A., McFarland, D.M. and Kerschen, G. 2007, "Suppressing aeroelastic instability using broadband passive targeted energy transfers, Part 1: Theory", *AIAA Journal,* vol. 45, no. 3, pp. 693-711.

Li, S. and Kahraman, A. 2010, "Prediction of Spur Gear Mechanical Power Losses Using a Transient Elastohydrodynamic Lubrication Model", *Tribology Transactions,* vol. 53, no. 4, pp. 554-563.

Lin, C., Tsay, C. and Fong, Z. 1997, "Mathematical model of spiral bevel and hypoid gears manufactured by the modified roll method", *Mechanism and Machine Theory,* vol. 32, no. 2, pp. 121-136.

Litvin, F.L. and Fuentes, A. 2004, *Gear geometry and applied theory,* Cambridge University Press.

Litvin, F.L., Chaing, W.S., Kuan, C., Lundy, M. and Tsung, W.J. 1991, "Generation and geometry of hypoid gear-member with face-hobbed teeth of uniform depth", *International Journal of Machine Tools and Manufacture,* vol. 31, no. 2, pp. 167-181.

Litvin, F.L., Vecchiato, D., Yukishima, K., Fuentes, A., Gonzalez-Perez, I. and Hayasaka, K. 2006, "Reduction of noise of loaded and unloaded misaligned gear drives", *Computer Methods in Applied Mechanics and Engineering,* vol. 195, no. 41–43, pp. 5523-5536.

Liu, G. and Parker, R.G. 2009, "Impact of tooth friction and its bending effect on gear dynamics", *Journal of Sound and Vibration,* vol. 320, no. 4, pp. 1039-1063.

McFarland, D.M., Kerschen, G., Kowtko, J.J., Lee, Y.S., Bergman, L.A. and Vakakis, A.F. 2005, "Experimental investigation of targeted energy transfers in strongly and nonlinearly coupled oscillators", *The Journal of the Acoustical Society of America,* vol. 118, pp. 791.

Mehdigoli, H., Rahnejat, H. and Gohar, R. 1990, "Vibration response of wavy surfaced disc in elastohydrodynamic rolling contact", *Wear,* vol. 139, no. 1, pp. 1-15.

Miyauchi , Y., Fujii , K., Nishino , T., Hatamura , K. and Kurisu , T. 2001, *Introduction of Gear Noise Reduction Ring by Mechanism Analysis Including FEM Dynamic Tuning*, SAE International 2001-01-0865.

Mostofi, A. and Gohar, R. 1982, "Oil film thickness and pressure distribution in elastohydrodynamic point contacts", *Journal of Mechanical Engineering Science,* vol. 24, no. 4, pp. 173-182.

Nakayashiki , A., Kubo , K. and Imanishi , H. 1983, *One Approach on the Axle Gear Noise Generated from the Torsional Vibration*, Society of Automotive Engineers of Japan 830923.

Natsiavas, S., Theodossiades, S. and Goudas, I. 2000, "Dynamic analysis of piecewise linear oscillators with time periodic coefficients", *International Journal of Non-Linear Mechanics,* vol. 35, no. 1, pp. 53-68.

Nevzat Özgüven, H. and Houser, D.R. 1988, "Mathematical models used in gear dynamics—A review", *Journal of Sound and Vibration,* vol. 121, no. 3, pp. 383-411.

O'neil, P.V. 2011, *Advanced engineering mathematics,* Thomson Engineering.

Özgüven, H.N. 1991, "A non-linear mathematical model for dynamic analysis of spur gears including shaft and bearing dynamics", *Journal of Sound and Vibration,* vol. 145, no. 2, pp. 239-260.

Özgüven, H.N. and Houser, D.R. 1988, "Dynamic analysis of high speed gears by using loaded static transmission error", *Journal of Sound and Vibration,* vol. 125, no. 1, pp. 71-83.

Padmanabhan, C. and Singh, R. 1995, "Analysis of periodically excited non-linear systems by a parametric continuation technique", *Journal of Sound and Vibration,* vol. 184, no. 1, pp. 35-58.

Park, D. and Kahraman, A. 2009, "A surface wear model for hypoid gear pairs", *Wear,* vol. 267, no. 9, pp. 1595-1604.

Parker, R., Vijayakar, S. and Imajo, T. 2000, "Non-linear dynamic response of a spur gear pair: modelling and experimental comparisons", *Journal of Sound and Vibration,* vol. 237, no. 3, pp. 435-455.

Peng, T. 2010, *Coupled multi-body dynamic and vibration analysis of hypoid and bevel geared rotor system,* .

Rahmani, R. 2008, "*An Investigation into Analysis and Optimisation of Textured Slider Bearings with Application in Piston-Ring/Cylinder Liner Contact"*, PhD Thesis, Anglia Ruskin University.

Rahnejat, H. (1984), "*The influence of vibration on the oil film in elastohydrodynamic contacts"*, PhD Thesis, Imperial College, London.

Rahnejat, H. 1985, "Computational modelling of problems in contact dynamics", *Engineering Analysis,* vol. 2, no. 4, pp. 192-197.

Rao, S.S. "Mechanical vibrations. 2004", .

Riley, W.F., Sturges, L.D. and Morris, D.H. 1995, *Statics and mechanics of materials: an integrated approach,* Wiley.

Saunders, T. 2005, "The characterisation of rear axle whine in commercial vehicles", *MSc thesis, University of Heartfordshire.*

Scagliarini, G., Viguié, R., Kerschen, G. and Pellicano, F. 2009, "Spur Gear Vibration Mitigation by Means of Energy Pumping", *27th International Modal Analysis Conference, Orlando, 2009*.

Simon, V. 2000, "FEM stress analysis in hypoid gears", *Mechanism and machine theory,* vol. 35, no. 9, pp. 1197-1220.

Simon, V. 2007, "Load Distribution in Spiral Bevel Gears", *Journal of Mechanical Design,* vol. 129, no. 2, pp. 201-209.

Snidle, R. and Evans, H. 1997, "Elastohydrodynamics of gears", *Tribology Series,* vol. 32, pp. 271-280.

Stadtfeld, J.H. 1993, *Handbook of Bevel and Hypoid Gears: Calculation, Manufacturing, Optimization,* Rochester Institute of Technology.

Starosvetsky, Y. and Gendelman, O. 2008, "Attractors of harmonically forced linear oscillator with attached nonlinear energy sink. II: Optimization of a nonlinear vibration absorber", *Nonlinear Dynamics,* vol. 51, no. 1, pp. 47-57.

Steyer , G., Voight , M. and Sun , Z. 2005, *Balancing Competing Design Imperatives to Achieve Overall Driveline NVH Performance Objectives*, SAE International 2005 -01-2308.

Strogatz, S. 2001, "Nonlinear dynamics and chaos: with applications to physics, biology, chemistry and engineering", .

Sun , Z., Ranek , M., Voight , M. and Steyer , G. 2005, *Variation Reduction of Axle System NVH*, SAE International 2005-01-2309.

Sun , Z., Schankin , D., Braun , W. and Ley , J. 2011, *Attenuation of Driveline Vibrations through Tuning of Propeller Shaft Liners*, SAE International 2011-01-1547.

Sun , Z., Steyer , G.C., Meinhardt , G. and Ranek , M. 2003, *NVH Robustness Design of Axle Systems*, SAE International 2003-01-1492.

Teodorescu, M., Taraza, D., Henein, N.A. and Bryzik, W. 2003, "Simplified elasto-hydrodynamic friction model of the cam-tappet contact", *SAE transactions,* vol. 112, no. 3, pp. 1271-1282.

Theodossiades, S., Tangasawi, O. and Rahnejat, H. 2007, "Gear teeth impacts in hydrodynamic conjunctions promoting idle gear rattle", *Journal of Sound and Vibration,* vol. 303, no. 3, pp. 632-658.

Theodossiades, S. and Natsiavas, S. 2001, "On geared rotordynamic systems with oil journal bearings", *Journal of Sound and Vibration,* vol. 243, no. 4, pp. 721-745.

Theodossiades, S. and Natsiavas, S. 2001, "Periodic and chaotic dynamics of motor-driven gear-pair systems with backlash", *Chaos, Solitons and Fractals,* vol. 12, no. 13, pp. 2427-2440.

Theodossiades, S. and Natsiavas, S. 2000, "Non-linear dynamics of gear-pair systems with periodic stiffness and backlash", *Journal of Sound and Vibration,* vol. 229, no. 2, pp. 287-310.

Vaishya, M. and Singh, R. 2001, "Sliding friction-induced non-linearity and parametric effects in gear dynamics", *Journal of Sound and Vibration,* vol. 248, no. 4, pp. 671-694.

Vaishya, M. and Singh, R. 2001, "Analysis of periodically varying gear mesh systems with coulomb friction using Floquet theory", *Journal of Sound and Vibration,* vol. 243, no. 3, pp. 525-545.

Vaishya, M. and Singh, R. 2003, "Strategies for Modeling Friction in Gear Dynamics", *Journal of Mechanical Design,* vol. 125, no. 2, pp. 383-393.

Vakakis, A.F. and Gendelman, O. 2001, "Energy pumping in nonlinear mechanical oscillators: Part II: Resonance capture", *Journal of Applied Mechanics,* vol. 68, no. 1, pp. 42-48.

Vakakis, A.F., Manevitch, L., Gendelman, O. and Bergman, L. 2003, "Dynamics of linear discrete systems connected to local, essentially non-linear attachments", *Journal of Sound and Vibration,* vol. 264, no. 3, pp. 559-577.

Vakakis, A. 2001, "Inducing passive nonlinear energy sinks in vibrating systems", *Transactions-American society of mechanical engineers journal of vibration and acoustics,* vol. 123, no. 3, pp. 324-332.

Velex, P. and Maatar, M. 1996, "A mathematical model for analyzing the influence of shape deviations and mounting errors on gear dynamic behaviour", *Journal of Sound and Vibration,* vol. 191, no. 5, pp. 629-660.

Velex, P. and Sainsot, P. 2002, "An analytical study of tooth friction excitations in errorless spur and helical gears", *Mechanism and machine theory,* vol. 37, no. 7, pp. 641-658.

Velex, P. and Cahouet, V. 2000, "Experimental and Numerical Investigations on the Influence of Tooth Friction in Spur and Helical Gear Dynamics", *Journal of Mechanical Design,* vol. 122, no. 4, pp. 515-522.

Velex, P. and Sainsot, P. 2002, "An analytical study of tooth friction excitations in errorless spur and helical gears", *Mechanism and Machine Theory,* vol. 37, no. 7, pp. 641-658.

Vijayakar, S. 1991, "A combined surface integral and finite element solution for a three-dimensional contact problem", *International Journal for Numerical Methods in Engineering,* vol. 31, no. 3, pp. 525-545.

Vijayakar, S. 1998, Tooth Contact Analysis Software: CALYX, Advanced Numerical Solutions, Hilliard, OH.

Wang, Y., Li, H., Tong, J. and Yang, P. 2004, "Transient thermoelastohydrodynamic lubrication analysis of an involute spur gear", *Tribology International,* vol. 37, no. 10, pp. 773-782.

Wang, J., Lim, T.C. and Li, M. 2007, "Dynamics of a hypoid gear pair considering the effects of time-varying mesh parameters and backlash nonlinearity", *Journal of Sound and Vibration,* vol. 308, no. 1–2, pp. 302-329.

Wani , N.Y. and Singh , V.K. 2005, *Design Evaluations On IRS Axle System NVH Through Analytical Studies*, SAE International 2005-01-2289.

Wesley Blankenship, G. and Singh, R. 1995, "Dynamic force transmissibility in helical gear pairs", *Mechanism and Machine Theory,* vol. 30, no. 3, pp. 323-339.

Xu, H. and Kahraman, A. 2007, "Prediction of friction-related power losses of hypoid gear pairs", *Proceedings of the Institution of Mechanical Engineers, Part K: Journal of Multi-body Dynamics,* vol. 221, no. 3, pp. 387-400.

Yoon, J.H., Choi, B.J., Yang, I.H. and Oh, J.E. 2011, "Deflection test and transmission error measurement to identify hypoid gear whine noise", *International Journal of Automotive Technology,* vol. 12, no. 1, pp. 59-66.

Appendix

The notation followed in the Appendix is consistent to Chapter 5. The main objective is the representation of the system with a single variable, in the form of the dynamic transmission error (x). The corresponding differential equation is in the form of equation $\ddot{x} = \dot{R}_p(\varphi_p)\dot{\varphi}_p + R_p(\varphi_p)\ddot{\varphi}_p - \dot{R}_g(\varphi_p)\dot{\varphi}_g + R_g(\varphi_p)\ddot{\varphi}_g - \ddot{e}(\varphi_p)$ (5.16):

$$\ddot{x} = \dot{R}_p\dot{\varphi}_p + R_p\ddot{\varphi}_p - \dot{R}_g\dot{\varphi}_g - R_g\ddot{\varphi}_g - \ddot{e}$$

Therefore, all the quantities involving angular rotations and their derivarives need to be replaced by functions of (x) and its derivatives.

From equations $I_p\ddot{\varphi}_p + R_p(\varphi_p)c_m(\dot{x}) + R_p(\varphi_p)k_m(\varphi_p)f_g(x) = T_p$

(3.3) and $I_g\ddot{\varphi}_g + R_g(\varphi_p)c_m(\dot{x}) + R_g(\varphi_p)k_m(\varphi_p)f_g(x) = -T_g$

(3.4) respectively, the angular accelerations can be expressed in terms of the dynamic transmission error:

$$\ddot{\varphi}_p = \frac{1}{I_p}\left[-R_p\left(k_m f_g(x) + c\dot{x}\right) + T_p\right] \qquad \textbf{(A.1)}$$

$$\ddot{\varphi}_g = \frac{1}{I_g}\left[R_g\left(k_m f_g(x) + c\dot{x}\right) - T_{g0} - a_1\dot{\varphi}_g{}^2\right] \qquad \textbf{(A.2)}$$

In the above expression, a_1 is a constant arising from the definition of angular velocity dependent resistive torque $T_e\frac{i_{tot}}{r}\eta_{tot} = mgf\cos a + mg\sin a + em\mathrm{a} + c_w A\frac{\rho}{2}\upsilon^2$ (3.8)). The next step is to repeat the same process for the angular velocities. In this case equations $\dot{x} = R_p(\varphi_p)\dot{\varphi}_p - R_g(\varphi_p)\dot{\varphi}_g - \dot{e}(\varphi_p)$ (5.6

$\ddot{x} = \dot{R}_p(\varphi_p)\dot{\varphi}_p + R_p(\varphi_p)\ddot{\varphi}_p - \dot{R}_g(\varphi_p)\dot{\varphi}_g + R_g(\varphi_p)\ddot{\varphi}_g - \ddot{e}(\varphi_p)$ (5.16) can be treated as a system with angular velocities as uknowns:

$$\dot{x} + \dot{e} = R_p \dot{\varphi}_p - R_g \dot{\varphi}_g \qquad \textbf{(A.3)}$$

$$\ddot{x} + \ddot{e} = \dot{R}_p \dot{\varphi}_p + R_p \ddot{\varphi}_p - \dot{R}_g \dot{\varphi}_g - R_g \ddot{\varphi}_g \qquad \textbf{(A.4)}$$

Combination of equations (A.2), (A.3) and (A.4) will yield the angular velocities with respect to (x) and its derivatives:

$$\dot{\varphi}_p = \frac{\dot{x} + \dot{e} + R_g \dot{\varphi}_g}{R_p} \qquad \textbf{(A.5)},$$

while the angular velocity of the gear is yielded by the ensuing quadratic algebraic equation:

$$A_2 \dot{\varphi}_g{}^2 + A_1 \dot{\varphi}_g + A_0 = 0 \qquad \textbf{(A.6)}$$

In the above expression:

$$A_2 = \frac{R_g a_1}{I_g},$$

$$A_1 = \frac{\dot{R}_p R_g}{R_p},$$

$$A_0 = \left[\ddot{x} + \ddot{e} + R_g \left(\frac{R_g}{I_g} k_m f_g(x) + \frac{R_g}{I_g} c\dot{x} - \frac{T_{g0}}{I_g} \right) - \dot{R}_p \frac{\dot{x} + \dot{e}}{R_p} \right]$$

Eventually solution of (A.6) renders a pair of solutions of which only the positive has a physical meaning:

$$\dot{\varphi}_g = \frac{-A_1 + \sqrt{A_1^{\,2} - 4A_2A_0}}{2A_2} \qquad \textbf{(A.7)}$$

Until now, through expressions (A.1), (A.2), (A.5) and (A.7), the angular velocities and accelerations can be substituted in terms of (x) and its derivatives. However, solution of the dynamic problem requires the differentiation of equation (5.16). The new equation will be integrated numerically while substituting all the terms involving angular rotations with respect to dynamic transmission error:

$$\dddot{x} = R_p\dddot{\varphi}_p - R_g\dddot{\varphi}_g + 2\dot{R}_p\ddot{\varphi}_p - 2\dot{R}_g\ddot{\varphi}_g + \ddot{R}_p\dot{\varphi}_p - \ddot{R}_g\dot{\varphi}_g \qquad \textbf{(A.8)}$$

In the above formula the third derivatives of the angular rotations can be yielded by differentiating expressions (A.1) and (A.2). All the other terms are complex functions of (x) ; hence implicit substitution can be employed to solve numerically the differential equation. Comparison of solutions verifies the equivalence of the two approaches.